

As hundreds of single cells are connected in parallel and series to compose a battery pack and provide energy that can meet the requirements of an application like a smart grid or EV, a whole battery pack model is required. The similarity principle cannot be simply implemented from a single cell to the battery pack because of cell inconsistencies and mechanical integrity influences [37]. If cell inconsistencies are considered, describing every individual cell with its unique ECM and parameters is desirable. However, it takes time to experiment on every individual cell to fit a precise ECM, and a complete model for a large number of cells would become quite complex. The approach presented in [37] uses a Thevenin ECM for every single cell in an array of more than 90 series-connected cells, and this model is used to identify the internal resistance of each cell. Similarly, in [38] a Thevenin model that uses two different branches (for charge and discharge) is connected in series n times to represent n cells in a series-connected battery pack. Russu et al. in [38] present the model equations for n cells, and these equations are included as a single system by using Equations (1) and (2)

4. Methods for SoC Estimation

SoC represents the available battery capacity that can be withdrawn from the battery and is used to prevent its over-discharge or over-charge as well as to operate the battery in such a manner that aging effects are reduced. SoC estimation has drawn the attention of many researchers, and many different methods have been proposed [18]. To make a classification of the methods is not an easy task because most approaches point to the combination of two or more methods and the inclusion of different heuristic or deterministic mathematical tools. This review will show that it is common to find a mix of both open circuit voltage (OCV) and coulomb counting (CC) methods. It is common for these combinations to involve a variety of improvements in the initial and online SoC estimation since methods applied separately can suffer from some inaccuracies. For example, [8] combined the algorithm OCV method, a full charge detector/dynamic load observer, and, as the key function, the CC method with robust extended Kalman filter algorithm (REKF). These combinations make it harder to sort out each approach into a specific method classification. However, based on the classification made in [4], and from the published literature on this topic in the last five years, this review proposes two categories (direct and indirect methods), and several subcategories that summarize trends in SoC estimation. Figure 3 displays a summary of these categories with their main drawbacks.

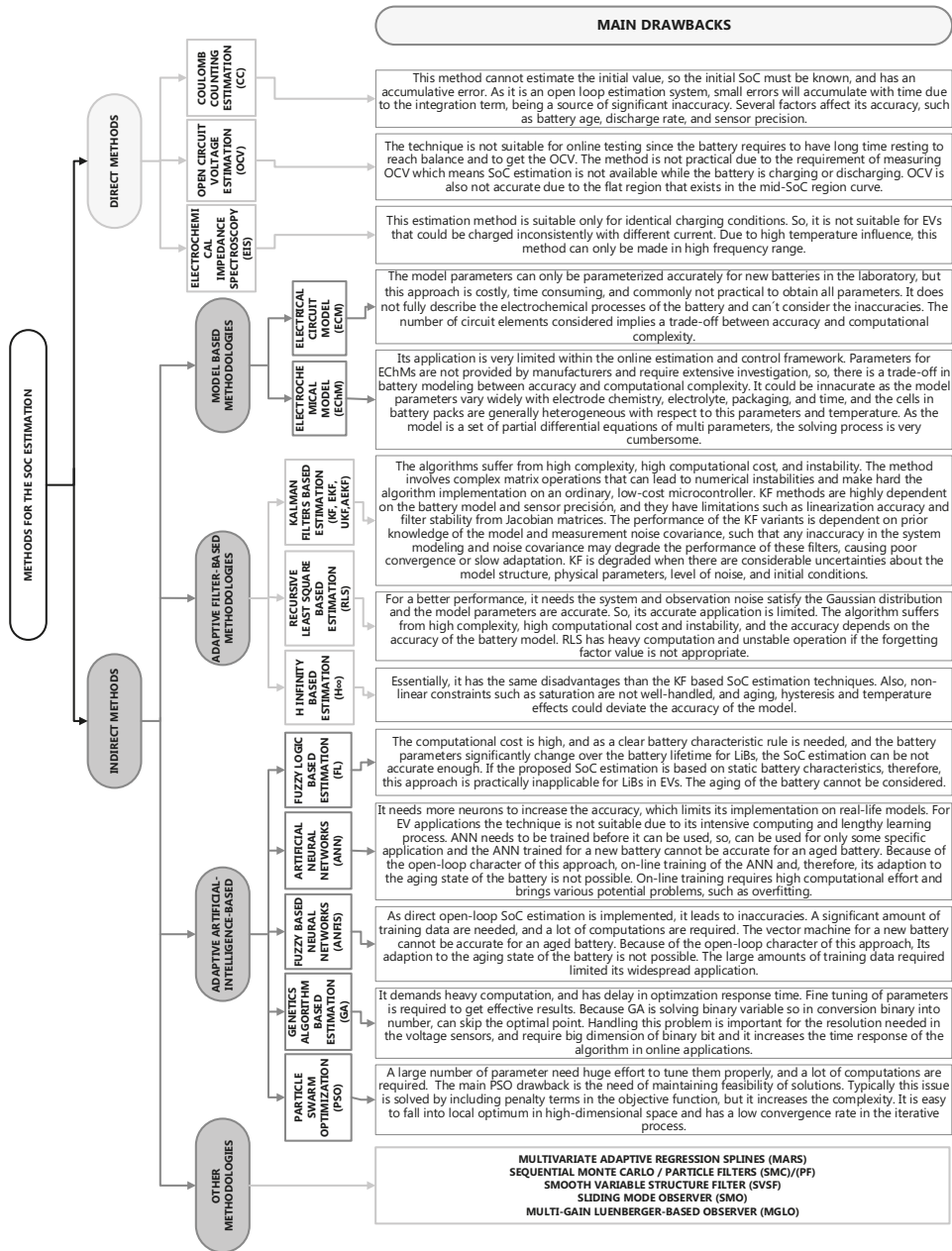


Figure 3. Summary of methods for the SoC estimation and main disadvantages.

4.1. Direct Methods

Direct SoC estimation methods use and measure physical battery properties such as voltage, current, and temperature, and then, by using an equation or relationship, the SoC can be estimated.

4.1.1. Coulomb Counting Estimation (CC)

CC has been standardized in the industry as an SoC estimation method [39]. At present, the CC method (also known as the ampere-hour balancing method), is the most used method for SoC estimation since it is the most accurate technique for short-term calculations. The CC method defines SoC as [8]:

$$SoC(t) = SoC(t_0) + \frac{1}{C_n} \int_{t_0}^{t_0+t} I_{bat}(d\tau) \times 100\%, \quad (5)$$

where $SoC(t_0)$ is the initial SoC, C_n the nominal capacity, and I_{bat} is the charging/discharging current. CC is a simple method, but has problems such as an initial value error and accumulated errors, so it is necessary to take into account the following issues: The measurement of battery current can contain measurement errors and abundant measurement noise. Errors due to noise and the wide range in sensors' resolution or rounding lead to accumulated errors and Equation (5) will gradually lose precision, so supporting algorithms are necessary. The initial SoC may not be known in practice and to define the SoC of a battery is only feasible when the battery system is in thermodynamic equilibrium [40].

CC is calculated by charge and discharge current time integral, and it is necessary to know the initial SoC value. If not known, this is usually assumed. This method is unable to eliminate cumulative error and is sensitive to the initial SoC value. If the initial SoC value is inaccurate, it will affect all estimates and error will accumulate during the whole estimation process. Despite being widely used in recent years, CC is not a method that is usually used as a sole tool for estimating SoC but is commonly used in combination with other techniques. A few publications, like [41], use the CC technique as the only tool to calculate the SoC. This work uses CC as a unique method for the SoC estimation since it incorporates a procedure that allows an on-line adaptive parameter estimation of a source-dependent ECM like will be described in Section 4.2.1.

4.1.2. Open Circuit Voltage-Based Estimation (OCV)

SoC estimation methods commonly impose a characterization of the OCV curve (mainly through a polynomial or a look-up table), as they use either a direct OCV curve inversion method (if the application permits cell steady state voltage measurement), or a cell model-based methods [42]. Making voltage measurements to determine the SoC for the cell allows us to define the relation:

$$SoC = f^{-1}(OCV). \quad (6)$$

In the OCV method, the cell's voltage is continuously measured, and the corresponding SoC is obtained from a table. The method has inherent difficulties in practical applications: the sensors need high resolution to measure voltage accurately, and sufficient time is required for equilibrium. The OCV method can be very accurate, but as it needs a rest time to estimate the SoC, it cannot be used in real time. Also, the OCV-SoC relationship differs among cells and, therefore results in unacceptable error. However, the OCV method is used to calibrate the CC method expressed in Equation (5) [40], in combination with noise-filtering and other adaptive techniques, as is described in Section 4.2.2.

To understand why the OCV-SoC curve cannot be used directly to estimate SoC, we must analyze Figure 4, which was obtained from the experimental data. This figure displays 10 curves obtained under different C-rates charging processes for a LiNiCoMnO₂ battery. In the figure, it can be seen that, as the amount of charging current increases in each cycle, the curve shifts upward. This behavior gives to the charging process the following features: (1) When the battery receives a large amount of current, the charging process reaches the upper limit voltage faster than when it receives less current; (2) At the same open OCV, the battery has different SoC values depending on the amount of current it is receiving, with SoC values being larger when the charging process is developed under small values of current. If the behavior of the discharging process were presented, opposite features to the charging process could be seen. This OCV curve is fairly flat over the operational SoC range. Thus, even the

smallest error in the OCV obtained from a battery model can lead to divergence of SoC from the actual value. To compensate for the mentioned shortcomings, the OCV method has to be mixed with other approaches. In [40,43] the SoC has been estimated by inferring the remaining cell voltage from an OCV using the OCV–SoC curve and Equation (6).

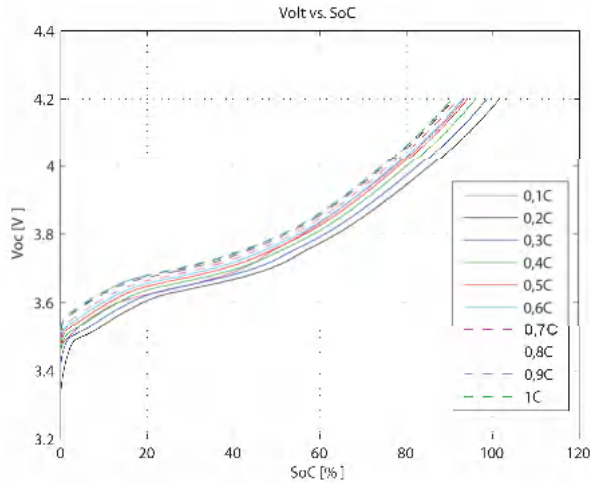


Figure 4. OCV vs. SoC during the charge process at different current values.

The changes of the OCV curve of each cell due to battery aging and performance degradation distort the estimation technique if nothing is done to adjust the curve. Therefore, OCV–SoC curve correction is required and in [42,44] it is implemented by comparing the capacity error with the CC and look-up table methods or by polynomial parametrization for the OCV curve. The OCV method compensates for both parameter and temperature variations in SoC estimation method presented in [20]. In [20] the OCV–SoC characteristic is represented by a controlled sources circuit, where a voltage-controlled source bridges SoC to OCV.

OCV is a common tool for supporting other methods. For example, in [45] a discontinuous discharging method to establish OCV–SoC characterization is used to calculate the internal resistance of the model battery and, in combination with an ECM and an extended Kalman observer, estimates the SoC. In [46,47], it is also used for determining the parameters of an ECM of a cell. The curve is used as part of the circuit model in [48–50] to consider the hysteresis phenomenon, which shows a difference in the equilibrium OCV between the charge and discharge processes of batteries.

4.1.3. Impedance Measurement-Based Estimation

An impedance measurement system is obtained from sinusoidal excitations at different excitation frequencies in which both voltage and current are recorded, and their complex quotient is computed as the cell impedance. The impedance spectroscopy of a battery cell can be approximated with two circles on the Nyquist plane [51]. In recent years, methods based on electrochemical impedance spectroscopy (EIS) have found application for accurate analysis of occurring electrochemical processes and diagnosis of LiBs, as the cell chemistry has a strong effect on the curve of the impedance spectrum [52,53]. An experimental lifetime model that can predict the internal resistance increase at various temperatures and SoC levels was developed and parameterized in [54].

In [52] the battery model is established using a simple ECM whose parameters are determined by the impedance measured data, presented as a Nyquist plot. The measured impedance (at frequencies between 100 mHz and 100 KHz) is decomposed with the help of a phase angle in a real part (x axis)

and an imaginary part (y axis), which are plotted against each other. Once the parameters of the model are known, the SoC can be estimated. A similar process is developed in [55] for finding the internal resistance growth model of the LiB cell. As this method needs a sinusoidal source, it is not suitable for online applications. The research developed in [56] uses an approach of the EIS for the online estimation of a LiB by decomposing the impulse signal used for getting the impulse response of the circuit model into the corresponding Fourier series factors. With this different frequencies sinusoidal signal, an online spectral analysis is made to obtain the impedance. The works presented in [57,58] introduce an EIS approach where the Nyquist plot impedance spectra is divided into high, mid, and low frequency sections. This division allows us to simplify the ECM parameter estimation and then, by using OCV correction and a fractional Kalman filter, estimate SoC.

4.2. Indirect Methods

These methods propose connecting the measured battery signals (voltage, current, and temperature) with the battery SoC employing a battery model. A high-fidelity battery model is required to capture the characteristics of the real-life battery and predict its behavior under a wide variety of conditions. In a BMS algorithm, using the signals as model inputs, the model can be used to calculate the SoC and other states of the battery.

4.2.1. Model-Based Estimation Methods

Model-based estimation techniques have become more common as they surmount the disadvantages of the direct estimation methods. Model-based methods deploy a battery model with advanced algorithms to estimate the states of a battery from its measured parameters such as voltage, current, and temperature. Although there are different approaches presented in the literature for estimating SoC directly using a battery model, this section just reviews electrical and electrochemical models because they are the base for most of the other methods of battery modeling. For example, the model technique displayed in [59] presents the so-called fractional order impedance model, which is inferred by mixing EIS technique and a first-order equivalent circuit model that will be described in the following. To estimate the SoC of a LiB, [59] deduces a fractional order Kalman filter and establishes a battery model that cannot be classified into the next two categories, but it is based on the two techniques presented here.

(1) Electrical Circuit Model-Based Estimation (ECM)

There are three different ECMs of a LiB widely adopted because of their excellent dynamic performance, described in [36]. The first is known as the Thevenin model and is a first-order RC model that consists of a nonlinear voltage source V_{OCV} as a function of SoC, a capacitor to model polarization capacitance and diffusion effects within the battery, C_{p1} , a diffusion resistance, R_{p1} , an internal resistance, R_t , a charge/discharge current, I_b , and a battery terminal voltage, V_t . The second model adds a capacitor in series with the voltage source V_{OCV} to characterize the capacity of store charge of the battery and to describe the changes in the OCV over time. This review calls this second model the first-order ECM. Similarly, the third one is obtained by adding in series an RC network (a parallel R_{p2}/C_{p2}) to simulate concentration and electrochemical polarizations. This review calls this model the second-order ECM. Figure 5 shows the second-order ECM.

An increase in the number of parallel RC networks can enhance the accuracy of dynamic battery response prediction. However, the coupling of SoC and time constants with cycle number and temperature leads to high prediction errors for estimating the SoC [60]. In [36], the discretization equations of each of the three mentioned models are presented and used in combination with an extended Kalman filter (EKF) and the CC estimation method to estimate the SoC. Wang et al. in [36] show that the second-order ECM is the most accurate and has the best dynamic performance, but is also the most complex of these three models. The work presented in [61] makes a comparison between continuous-time and discrete-time equations of the second-order ECM and concludes that discrete-time

identification methods are less robust due to undesired sensitivity issues in transformation of discrete domain parameters. The parameters of the second-order ECM can be calculated with different datasets depending on the scenario where the model is going to be used, like in [62].

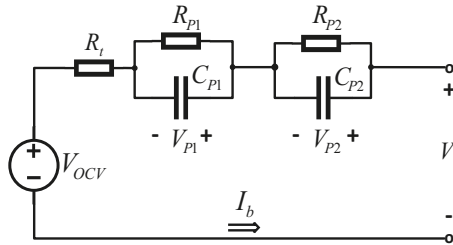


Figure 5. Second-order ECM.

By employing a simple ECM, like the Thevenin ECM, the SoC can be directly calculated by the transformation of the model equations [38,63–65]. The advantage of this approach is its simplicity, which enables easy implementation on a low-cost target microcontroller. In [5], Thevenin model and second-order ECM were used for SoC estimation and compared with three other enhanced ECMs. The difference between these models is the way the SoC equations are calculated. In this approach, the equation model considers an SoC_{surf} based on electrochemical analysis rather than the average SoC (Equation (5)), to reflect the real-time particle surface concentration. This approach shows better performance in a low SoC range compared with the one that uses the average SoC for the ECM.

A fourth typical ECM originally proposed in [66] is presented in [6]. This model is quite accurate and could significantly increase the battery’s nonlinear dynamic behavior identification. The model is shown in Figure 6. The OCV–SoC behavior of the battery is modeled by a self-discharge resistance R_d , a battery storage capacitor C_c , and a current-dependent current source. Likewise, the voltage–current characteristics are modeled as a second-order ECM but replacing the voltage source with a voltage-dependent voltage source to relate SoC to OCV. This ECM and the voltage–current dynamic mathematical equations are presented in [6], where V_{p1} and V_{p2} are the state variables, I_b is the input, and V_t is the output. In [10], by using this ECM, a procedure is developed that performs a real-time comparison between measured and calculated values of the battery voltage, while a PI-based observer is used to provide the SoC actual values. The second-order model has also been used in [60] for predicting SoC over a complete drive cycle in EV applications, but it uses a three time-constant model for modeling the transient behavior of the terminal voltage. For this reason, it uses a third RC network in series with the existing two. This ECM has been used as a part of the electrochemical model presented in [67].

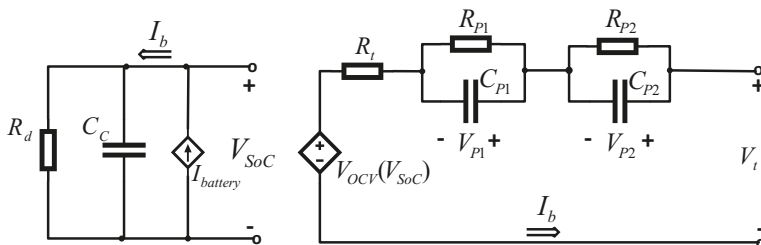


Figure 6. Source-dependent ECM.

In practical, all the parameterization values of the resistances and capacitors depend on the particular operating point of the battery, so they vary with time, temperature, power demand, SoC, and SoH. In the four mentioned models, the battery SoC is directly incorporated into the model using its relationship with the battery OCV. If the scope of the model is to simulate dynamics slower than 1 s, it is possible to use an ECM like the described Thevenin model [51]. A possible variation is not to incorporate the battery SoC in the equations, but to estimate the battery OCV using the model and then use another technique to estimate the SoC from the OCV, like the approach presented in [68,69]. In [68] an improved Thevenin model that includes the hysteresis phenomenon in its equations is used for obtaining the voltage of the cell and then, by using Equation (5) and a multiple model Kalman filter (KF) in one case, and an autovariance least squares technique in the other, estimates the SoC. In [70], a Thevenin ECM is used to obtain the OCV and then, a linear fitting of a portion of the OCV–SoC curve is used to obtain the SoC. A similar process is followed in [71] to obtain the SoC, but this approach uses a simple ECM that considers just a voltage source and an internal resistance.

SoC estimation methods mix the second-order ECM of a LiB with other techniques such as an improved KF, like in [72,73], or with a kinetic model capable of predicting the circuit characteristics and the nonlinear effects under dynamic loads accurately, like in [74,75] (in these approaches, SoC estimation is replaced with the state of energy, SoE, calculation). However, it was not used in SoC estimation directly; the second-order ECM is coupled with a thermal model by heat generation equations in [76]. As this model gives accurate predictions of the temperature distribution through the cell surface and the voltage behavior under various operating conditions, it could be used in enhanced SoC estimation procedures.

By using second-order ECM plus an EKF and Equation (5), the approach presented in [7] can estimate the SoC and shows that it does not rely on the initial SoC and is immune to parameter errors. The approach displayed in [77] uses the second-order ECM presented in [7] to obtain the voltage circuit using the SoC and current as inputs. Then, another partial least squares battery-based model is used to estimate the same circuit voltage. Both calculations are compared with the terminal voltage of reference and the algorithm selects the model whose output has the minimum difference compared to the measured terminal voltage. This algorithm uses model free adaptive control to calculate ΔI , utilizing the terminal voltage errors; with this enhanced value, the algorithm calculates the SoC correction. Despite the mixed algorithm making the estimation process simple and effective, it increases the computational burden and the fusion mechanism, and the proposed methods with limited samples under various conditions still need further research [77]. In [78] a second-order ECM equation whose parameters are dependent on SoC, or deep of discharge (DoD), charging or discharge rate, and temperature, is used to estimate the SoC, and three different optimization techniques are used to estimate the parameters of the ECM and the feasibility of these techniques are evaluated by the accuracy of the predicted model and the rate of convergence in prediction.

Another ECM different than the conventional four mentioned is presented in [79]. In this approach, the architecture and components of the proposed circuit model capture the diffusion characteristics and the resulting overpotential by way of segment-wise diffusion modeling and based on the chemical mass transport mechanism. An approach that considers a second-order ECM as a base to add a thermal generation and thermal transfer equations is presented in [80] for real-time SoC estimation. In [80], electrical and thermal equations are coupled into a single model, and then an EKF is used for SoC estimation.

(2) Electrochemical Model-Based Estimation (EChM)

Electrochemical models (EChMs) use the equations that describe physicochemical phenomena like diffusion, intercalation, and electrochemical kinetics occurring in a battery. The definition of these equations involves a specialized knowledge of electrochemistry, hence their exploitation in the field of electrical and electronics engineering is not common. These models are typically computationally challenging owing to a system of coupled time-varying partial differential equations. They are known

to be computationally prohibitive, and thus their employment in BMS is hard. For example, a simple EChM like that presented in [81] involves six nonlinear partial differential equations that need a numerical solution. This complexity not only prevents the implementation of monitoring algorithms on low-cost target microcontrollers but also reduces the number of model parameters that can be adapted on-line to the present states of the battery [82]. For this reason, such models are best suited for optimization of the physical and material design aspects of internal electrodes and electrolytes [60]. The review presented in [83] is a brief updated literature revision of approaches using electrochemical models to estimate different states in batteries.

Several publications propose EChMs that could be used for SoC and other battery states estimation but do not present the SoC estimation process [67,83–87]. For example, [84] presents the full equation descriptions and model algorithm of an EChM based on the absolute nodal coordinate formulation approach, and also a brief model order reduction techniques review for EChMs. Most methods that use EChMs develop reduced-order models and use an estimator. The work developed in [88] fully describes a reduced order EChM. The model reduction and observer design process are intimately intertwined; simpler models ease estimation design at the expense of fidelity. Moura et al. in [83] present a state estimation scheme for a reduced EChM by deriving a single-particle model (SPM) with electrolyte. Tran et al. in [87] present equations of a three-parameter SPM and their Matlab simulation.

The approaches presented in [89–92] specifically develop EChMs for SoC estimation. Zou et al. in [89] propose a model composed of four submodels that capture the electrochemical, thermal, electrical, and aging dynamics in a set of partial differential equations. As one of the outputs of the full model is the SoC, it can be directly estimated by solving the system equations. Barlett et al. in [90] present a reduced-order electrochemical model for different Li ion chemistries that are used in dual-nonlinear observers (KF, fixed interval Kalman smoother and particle filter), to estimate the cell SoC and loss of cyclable lithium over time. The research presented in [91] described an EChM where a set of discretized equations are used to estimate the SoC directly, and then SoC is compared with an approach where the EChM is written as a linearly spatially interconnected system. Here, by exploiting the resulting semi-separable structure, the method uses an EKF to optimize the calculations for the SoC estimation. The technique presented in [88] introduces EChM parameters estimation by a noninvasive optimization strategy at any state of battery life. This technique is used in [92] for SoC estimation.

The advantage of EChMs is that they inherently include the dependence of the battery behavior on SoC and temperature, while electrical models must store their parameters as look-up tables for various SoC and temperature combinations. The disadvantage of EChMs is their high complexity. As has been stated, the parameter values of a battery model vary with temperature, so SoC estimation values directly depend on battery thermal behavior. Excessive temperature can greatly accelerate the battery aging process, and even cause a fire or explosion in the battery pack in severe cases. On the other hand, the battery electrical properties, such as usable capacity, internal resistance, and power delivery ability, all depend on the battery's internal temperature [80]. The battery's internal temperature can reach critical a lot quicker than the surface temperature. Thus, the surface temperature measurement alone might be not sufficient to ensure safe battery operation. This is why, for enhanced security and more accurate SoC estimation, the parameter values of the ECMs should be continually updated. This can be achieved with the adaptive methods described below. In EChMs, since they include temperature as one of their variables, this may not be necessary.

Most of the battery degradation literature consists of empirical-based studies with results extracted from experimental tests in laboratories [93]. Ahmadian et al. in [93] present the most prominent degradation models and the effects of degradation factors on LiBs' performance. Bashash et al. in [94] state that there is an exponential relation between calendar aging and SoC. This relationship shows that battery internal resistance increases as SoC increases. Thus, battery degradation increases if it is kept at high SoCs. Also, the average SoC maintained during battery cycling has an influence on the degradation rate, and a higher average SoC leads to faster degradation [93]. So, storing a battery

at full charge may be considered misuse. As the aging of batteries is reflected directly in the model parameters, the parameter values of the models should be continually updated, and the adaptive SoC methods described below can be used try to reach this condition.

4.2.2. Adaptive Filter-Based Estimation Methods

Adaptive techniques combine the direct and model-based methods, and are adaptive and self-designing systems that can automatically adjust to changing systems. Adaptive systems usually use feedback to change the current output according to the varying input [13].

(1) Kalman Filter-Based Estimation

KF theory can be applied by viewing each cell in the battery pack as a dynamic system whose inputs include the current and temperature of the cell and whose output is the terminal voltage. The way KF is used for SoC estimation is based on the explanation of the technique in [95]. As the parameters of Equations (1) and (2) depend on the cell model used, the idea is to include the desired unknown quantities into state vector x_k and the KF will automatically compute the best estimate of its present values. In this case, SoC has to be included as a state in the vector x_k . For deriving the filter equations, w_k and v_k are assumed to be mutually uncorrelated white Gaussian random processes, with zero mean and covariance matrices $\Sigma_w \Sigma_v$ with known values $E[w_n w_k^T] = \begin{cases} \Sigma_w & n = k \\ 0 & n \neq k \end{cases}$;

$$\text{and } E[v_n v_k^T] = \begin{cases} \Sigma_v & n = k \\ 0 & n \neq k \end{cases}.$$

$E[\cdot]$ is the statistical expectation operator, and T is the matrix transpose. The KF problem is then: Use the observed data $\{u_0, u_1, \dots, u_k\}$ and $\{y_0, y_1, \dots, y_k\}$ to find the minimum mean squared error while at the same time estimating \hat{x}_k of the state x_k . So, with w_k and v_k , and an observable system modeled, solve: $\hat{x}_k = \arg \min E[(x_k - \hat{x})^T (x_k - \hat{x}) | u_0, u_1, \dots, u_k, y_0, y_1, \dots, y_k]$; with $\hat{x} \in R^n$.

KF gives a set of computationally efficient recursive relationships that involve both an estimate of the state itself, and also the covariance matrix $\Sigma_{\tilde{x},k} = E[\tilde{x}_k \tilde{x}_k^T]$ of the state estimate error $\tilde{x}_k = x_k - \hat{x}_k$. A covariance matrix of the error, $\Sigma_{\tilde{x},k}$, with large singular values indicates a high level of uncertainty in the state estimate, and one with small singular values indicates confidence in the estimate. The KF algorithm is depicted in Figure 7. The algorithm is initialized with the best available information on the state and error covariance: $\hat{x}_0^+ = E[x_0]$; $\Sigma_{\tilde{x},0}^+ = E[(x_0 - \hat{x}_0^+)(x_0 - \hat{x}_0^+)^T]$. Usually these quantities are not known, so initialization can be performed in an ad hoc manner, and the KF will quickly converge to the actual values as it runs. Later, the KF repeatedly performs two steps at each measurement interval: (1) It *predicts* the value of the present state, system output, and error covariance: $\hat{x}_k^-, \hat{y}_k, \Sigma_{\tilde{x},k}^-$ respectively. These values are predicted by propagating the system input through the system model dynamics (Equation (2)), assuming the expected process noise w_k of zero: $\hat{x}_k^- = A_{k-1} \hat{x}_{k-1}^+ + B_{k-1} u_{k-1}$; $\Sigma_{\tilde{x},k}^- = A_{k-1} \Sigma_{\tilde{x},k-1}^+ A_{k-1}^T + \Sigma_w$; and $\hat{y}_k = C_k \hat{x}_k^- + D_k u_k$; (2) Using a measurement of the physical system output, it *corrects* the state estimate and error covariance to \hat{x}_k^+ and $\Sigma_{\tilde{x},k}^+$: $\hat{x}_k^+ = \hat{x}_k^- + L_k [y_k - \hat{y}_k]$. It can be seen in these equations that the error between the output measurement y_k and the output estimation \hat{y}_k is weighted by Kalman gain vector L_k , which is defined as $L_k = \Sigma_{\tilde{x},k}^- C_k^T [C_k \Sigma_{\tilde{x},k}^- C_k^T + \Sigma_v]^{-1}$. The covariance correction step is $\Sigma_{\tilde{x},k}^+ = (I - L_k C_k) \Sigma_{\tilde{x},k}^-$. The covariance matrix indicates the uncertainty of the state estimate, and it always decreases due to the new information provided by the measurement. The uncertainty value of SoC is reduced by the KF algorithm because the recursive equations are repeatedly evaluated during system operation [96].

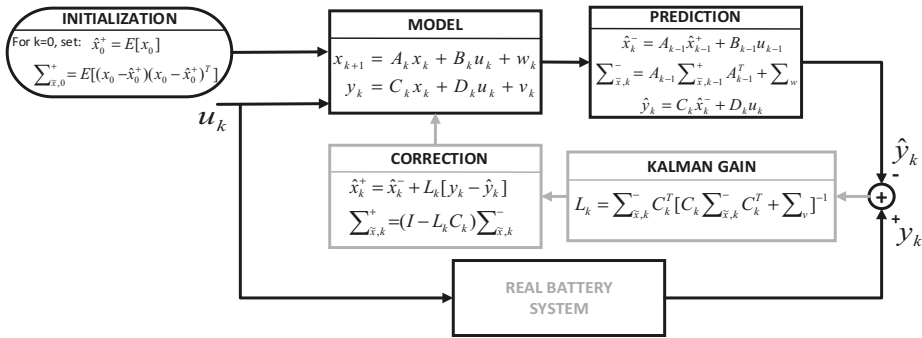


Figure 7. Kalman filter iteration diagram.

Recently, the EKF has attracted increasing attention and become one of the most commonly used methods to estimate the battery SoC even when the initial SoC is unknown [97]. KF is the optimum state estimator for linear systems. If the system is nonlinear, a linearization process can be used at every time step to approximate the nonlinear system with a linear time varying (LTV) system. This LTV system is then utilized in the KF, resulting in an EKF on the real nonlinear system. Using a nonlinear model such as that presented in Equations (3) and (4), and taking into account the same considerations for w_k and v_k , at each time step, $f(x_k, u_k)$ and $g(x_k, u_k)$ are linearized by a first-order Taylor-series expansion. Assuming that $f(x_k, u_k)$ and $g(x_k, u_k)$ are differentiable at all operating points (x_k, u_k) : $f(x_k, u_k) \approx f(\hat{x}_k, u_k) + \left. \frac{\partial f(x_k, u_k)}{\partial x_k} \right|_{x_k = \hat{x}_k} (x_k - \hat{x}_k)$; $g(x_k, u_k) \approx g(\hat{x}_k, u_k) + \left. \frac{\partial g(x_k, u_k)}{\partial x_k} \right|_{x_k = \hat{x}_k} (x_k - \hat{x}_k)$. Combining these two equations with Equations (3) and (4), the linearized equations that describe the real system state as a function of itself (known inputs u_k and \hat{x}_k , and the unmeasurable noise inputs w_k and v_k), we have: $x_{k+1} \approx \hat{A}_k x_k + f(\hat{x}_k, u_k) - \hat{A}_k \hat{x}_k + w_k$; $y_k \approx \hat{C}_k x_k + g(\hat{x}_k, u_k) - \hat{C}_k \hat{x}_k + v_k$, where $\hat{A}_k = \left. \frac{\partial f(x_k, u_k)}{\partial x_k} \right|_{x_k = \hat{x}_k^+}$, $\hat{C}_k = \left. \frac{\partial g(x_k, u_k)}{\partial x_k} \right|_{x_k = \hat{x}_k^-}$. With this linearization, the EKF iterative algorithm is similar to that presented for the KF and is described in Figure 8.

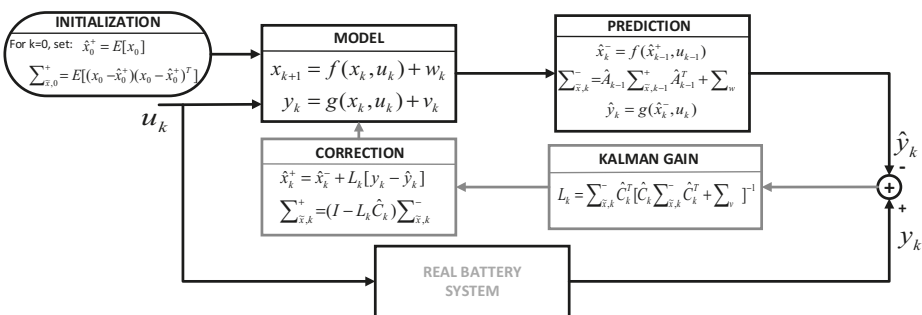


Figure 8. Extended Kalman filter iteration diagram.

The linearization process made in EKF uses the first- or second-order terms of the Taylor series expansion to approximate a nonlinear model, which degrades the SOC estimation accuracy. To overcome this, instead of local linearization, the unscented Kalman filter (UKF) captures the statistical distribution characteristics of a nonlinear system according to a series of sigma points [98]. The UKF based on unscented transform not only does not require the calculation of a Jacobian matrix

but has a higher order of accuracy in the noise statistics estimation than the EKF, such as the mean and error covariance of the state vector of the battery system [97]. Figure 9 shows the UKF algorithm. The sigma points and weighted coefficients calculations, as well as the covariance matrix of the error factors included in the Kalman gain, can be seen in [98,99].

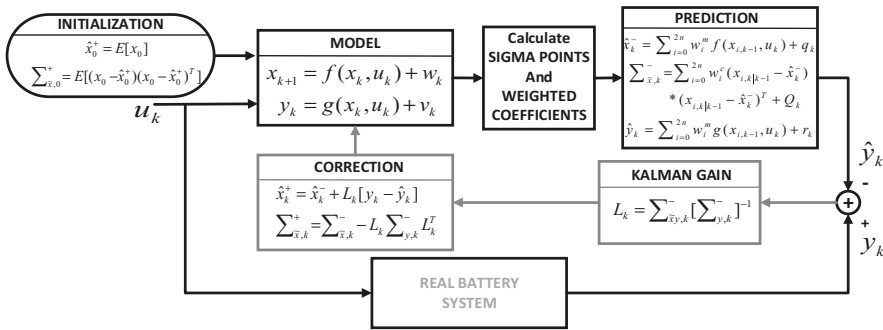


Figure 9. Unscented Kalman filter iteration diagram.

In [100] a KF is introduced to extract an OCV value in a noisy environment, and then to estimate SoC based on the OCV–SoC mapping. As the KF has the observability of the system as a requirement, a virtual-measurement-based method can be implemented to account for a local loss of observability, like is presented in [91]. This approach uses the iterative process of the KF described in Figure 8 for estimating not only SoC but also other battery parameters, like the KF implemented in [96] estimates both SoC and SoH. It is common to find a combination of CC or OCV methods with the KF method to estimate SoC value, as is presented in [58,101].

Some good examples of how to apply and run an EKF algorithm (as depicted in Figure 9) for SoC estimation are presented in [7,21,91,102]. Due to the electrochemical and thermal models of the batteries being highly nonlinear, EKF is used for estimating its parameters, followed by SoC [45,80,90]. The EKF method is also used in combination with CC and/or OCV, as proposed in [11,45,50,103]. The works presented in [47,68,104] use a multiple model approach that uses a bank of EKFs to estimate the SoC of the battery. Each filter represents a particular operational condition of the battery, and is used to enhance the accuracy of the SoC EKF estimation by accounting for the unknown measurement noise covariance. Additionally, any errors in the model can also be compensated for by an increase in the measurement noise covariance. The state estimate is provided through a sum of each filter’s estimate weighted by the likelihood of the unknown elements conditioned on the measurement sequence.

KF and EKF work well when the system model and noise statistics are known a priori. Wrong assumptions or changes during operation may lead to a degradation of filter estimates. Fleischer et al. in [8] implement an REKF, which is more robust to uncertainties in the system equation, in the measurement equation, and in the noise covariances. It also provides the estimation error bounds dynamically. This approach uses the same algorithm depicted in Figure 8 but adds a tuning parameter that guarantees that the relation between process/measurement noise and estimation error is lower than this parameter value. Fleischer et al. in [8] use a state space linear circuit model where the output is the OCV, and the SoC is one of the state variables. An improvement to the measurement noise due to a harsh electromagnetic environment, like the present in EVs, is to add a wavelet transform matrix (WTM) that can analyze and denoise the nonstationary current and voltage signals. Zhang et al. in [9] developed a SoC estimation approach that uses this improvement in the measurement noise treatment and, by correcting the covariance matrix error in the depicted EKF, builds an adaptive EKF (AEKF) that can reduce the estimation error when the measurements are passed through WTM.

Another common improvement to the KF algorithm for finding SoC is UKF, which is used in [97,105]. In [105], the equations of an ECM with two RC branches are written in the form of Equations (4) and (5). Here, an adaptive adjustment of the noise covariances is implemented using a technique of covariance matching to estimate the noise statistics in this iterative process adaptively; see the estimation process presented in Figure. It allows for obtaining better accuracy both in battery model parameters estimation and in the battery SoC estimation. This method is known as adaptive UKF (AUKF) and is employed here for online model parameter identification of the ECM at each sampling time. Subsequently, based on the updated model parameters, SoC estimation is conducted using the AUKF method. Since the temperature variation affects the performance of the battery, it is important to compensate for temperature effects to improve the model’s predictive capability and SoC estimation. UKF is implemented in [98] to estimate SoC using a modification of ECM (a resistance and a capacitor correction factor), to include the impact of different current rates and SoC on the battery internal resistance, and the impact of different temperatures and current rates on the battery capacity. To deal with the variation of battery parameters due to temperature changes [106,107], we propose a SoC estimation approach and online parameter updating using a dual square root UKF based on unit spherical unscented transform. A relatively simple modification to the depicted UKF is the double UKF algorithm used in [72]. It introduces the use of two UKF filters that work together to calculate the real value of SoC and ohmic resistance to obtain a final SoH value.

(2) Recursive Least Squares-Based Estimation (RLS)

The least squares method calculates system parameter values that minimize the least squares error between the measured output signal and the estimated output signal by assuming that the system is disturbed by white noise. The recursive least squares (RLS) method is used in adaptive filters to find the filter coefficients that allow for obtaining the minimum square of the error signal (defined as the difference between the desired signal and the signal produced at the output of the filter). The RLS algorithm makes this process recursively and updates its estimated parameter values by incorporating new information from every sampling time. RLS with a single fixed forgetting factor is a parameter identification method that is described in Figure 10. In this figure, e_k is the output estimation error, P_k is the covariance matrix of the parameter estimates, λ is the forgetting factor, and K_k is the RLS gain. The forgetting factor allows the algorithm to tune its parameters to a time-varying system. The tuning speed depends on the asymptotic memory length N , which means that information is forgotten with a time constant of N sample intervals [108]: $\lambda = 1 - \frac{1}{N}$. When all information is preserved, the memory length $N = \infty$, which means $\lambda = 1$. When information dies away with a time constant of one sampling interval, the forgetting factor becomes 0.

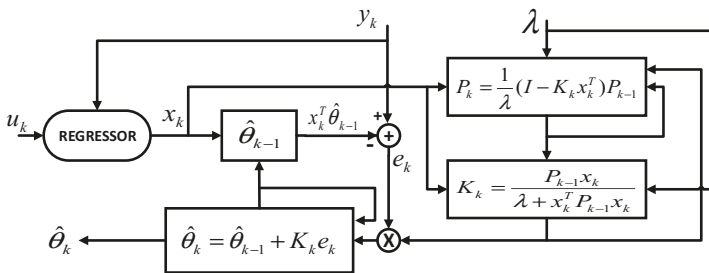


Figure 10. Recursive least squares algorithm.

The approach presented in [109], seeking to solve the problems related to model accuracy, sensor precision, data saturation, and heavy computation in the EKF-based methods [110], uses the RLS method to improve an adaptive EKF to estimate online the SoC and the battery model parameters.

Also, a RLS for estimating the circuit parameters was used in [111,112]. A RLS filter is employed in [112] to dynamically estimate in real time the parameters of a Thevenin ECM. Next, the model parameters are used to estimate the battery’s OCV and hence its SoC via the fading KF. Shen et al. in [111] use a single forgetting factor RLS like that presented in Figure to obtain the second-order ECM parameters and an EKF for the final SoC estimation procedure. Rozaqi and Rijanto in [108] present multiple fixed forgetting factors RLS, where OCV and internal resistance of a Thevenin ECM are used as the main parameters to be estimated by the algorithm, and then to estimate SoC. Lotfi et al. in [82] use an observer-based reduced-order EChM to estimate SoC by using an RLS with exponential forgetting parameter identification routine to compensate for the reduced-order model uncertainties. In [82], an RLS algorithm was coupled with a Luenberger-like observer for the estimation of the states of the model.

(3) H Infinity-Based Estimation (H∞)

H infinity (H∞) theory is a powerful tool to restrict the effect of exogenous disturbances on output. The H∞-based method is to guarantee that the norm from the system and measurement noises to the SoC estimation error are less than a given attenuation level, which can still ensure SoC estimation accuracy in the worst cases [113]. The H∞ filter is robust in the presence of parameter uncertainties and modeling errors [114], and its general procedure is displayed in Figure 11.

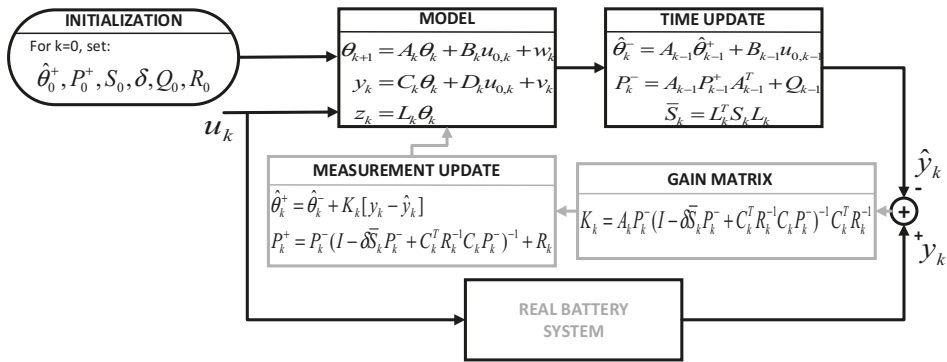


Figure 11. H-infinity filter algorithm.

In Figure, θ_k is the state vector of the model, y_k is the output, and z_k represents the SoC. P is the covariance matrix, δ is the constraint boundary, and S is a user-defined positive definite matrix that will affect the gain matrix. Also L is a user-defined matrix. Q and R are the covariances of the process noise w_k and measurement noise v_k , respectively. Xiong et al. in [114] present a time-saving method to obtain the OCV–SoC relationship through any existing current and voltage measurements by using the H∞ filter in the absence of the time-intensive OCV test. Here, the parameters and OCV of a Thevenin ECM are obtained by using the procedure depicted in Figure, and OCV–SoC relationships are extracted from standardized characterization tests. Then, the method obtains the SoC using another H∞ filter and considering a linearized state space model like that depicted in Figure 2, and establishing the relationship $z_{s,k} = L_{s,k} x_k$.

In the SoC estimation process, the variation of the model parameter under different aging levels and operation conditions is a critical issue that is addressed by using a dual H∞ filter in [115]. This strategy uses a first H∞ filter to overcome the drawback of its sensitivity to their initial noise information, and the second part of the filter is an adaptive H∞ filter that employs a covariance matching approach to estimate SoC. H∞ provides the most consistent estimates concerning different uncertainties, compared with EKF and UKF [116]. However, the variability of the estimation errors is

larger for batteries with a strong correlation between SoC and OCV. Fridholm et al. in [116] describe the H_∞ technique by using a Thevenin ECM in two different battery chemistries. Yu et al. in [117] use the H_∞ procedure to trace the parameters online according to the working conditions, and utilizes an UKF for the final SoC estimation. The strategy presented in [118] displays the H_∞ technique at both cell and pack levels. Lin et al. in [119] propose a multi-model probability fusion SoC estimation using H-infinity algorithm. Here, the H_∞ technique is employed to develop online SoC estimators for the Thevenin, second-, and third-order ECMs. Another battery model like the electromotive force model presented in [113] is used, combined with the H_∞ algorithm, to estimate SoC.

4.2.3. Adaptive Artificial-Intelligence-Based Techniques Estimation

A short (13 references) review of adaptive techniques including the KF, Artificial Neural Networks (ANNs), and Fuzzy Logic (FL) systems was presented [13].

(1) Fuzzy-Logic-Based Estimation (FL)

FL is a problem-solving methodology that simplifies all the noisy, vague, ambiguous, and imprecise input data by using objective rules to find the real value of the input. The operating principle of a FL technique can be structured into four simple stages [13]: (1) Fuzzification: in this stage the measured system values are converted into linguistic fuzzy sets, and classified into membership functions. Fuzzy sets specify the degree of belonging to each logical set; (2) Fuzzy rule base: a fuzzy rule base is designed using professional experience and system operating method; (3) Inference Engine: through this stage all the fuzzy rules are transformed into fuzzy linguistic outputs; (4) Defuzzification: translates the linguistic fuzzy rules into analog output values.

FL systems can generalize any system using cycle number estimation because in some of the battery tests it will be easier to describe the state of the battery (High, Low) rather than getting a precise number. The approach presented in [120] uses a fuzzy rule-based system to compute the nonlinear gain of a KF that estimates SoC, and a Genetic Algorithm (GA) is used to evolve the definition of the rule base. In [121] a Thevenin ECM in a weighted combination with the CC method is adopted by the fuzzy logic control scheme to obtain a static SoC estimation. Then the dynamic battery SoC is precisely estimated on the basis of static SoC using an ANN.

Fuzzy technique can be used to model a battery with high accuracy and consider the degradation process in the model [122]. This model could be used for other approaches to the SoC estimation process or to improve the performance of other SoC estimation techniques like in [123], which presents an improved fuzzy adaptive KF method, or like in [102], where a fuzzy controller is applied to online adjust the measurement noise variance. Cheng et al. in [102] designed a fuzzy self-adjusting controller where, according to fuzzy inference rules, the error covariance matrix elements of KF are adjusted online and in real time for every step of the KF iterations. In [124], the polarization resistance of the battery model is modeled using fuzzy rules that are a function of both SoC and the current. Despite the fact that this approach does not directly use the FL technique for the SoC estimation process, the model presented can be adapted to this task. Similarly, [125] uses FL by fuzzy self-tuning algorithms to update the model parameters of a second-order ECM that is used with an adaptive UKF to obtain SoC values. Hametner and Jakubek in [126] present a SoC estimation technique based on a purely data-driven model and a nonlinear fuzzy observer that uses KF theory for each local linear state space model. Then, the technique uses linear combinations of the local filters to derive a global filter and estimate SoC.

A few publications directly calculate SoC from FL [127,128]. Zheng et al. in [128] estimate SoC and cell capacities by comparing cell voltages at the beginning and end of charging. This approach calls the technique the "FL Dissipative Cell Equalization" algorithm. Sheng and Xiao in [127] use a least squares support vector machine by applying fuzzy inference and nonlinear correlation measurement. This allows an improvement in the SoC estimation process due to the effects of the samples with low confidence being reduced.

(2) Artificial Neural Networks-Based Estimation (ANN)

ANN relies on an input layer and output layer consisting of neurons that contain system-specific normalized input and output information. The mathematical junction between the input and the output layer is realized by a hidden layer and its neurons, where the neurons are interconnected as in Figure 12. Every neuron except the inputs consist of a sum of the products of the output O_{pred} of the neurons in the predecessor layer and a particular weight $W_{pred,actual}$ between the neurons of the predecessor and the actual layer [129]: $\varphi_{actual} = \sum_{i=1}^l (O_{pred} * W_{pred,actual})$. Those cumulated outputs and weights φ_{actual} are arguments for a sigmoidal activation function $sig(\varphi_{actual})$ to determine an output O_{actual} for every neuron in the actual layer: $O_{actual} = sig(\varphi_{actual}) = \frac{1}{1+e^{-\varphi_{actual}}}$. Those outputs are further distributed to the successor neurons in the next layer, whether a hidden or an output layer.

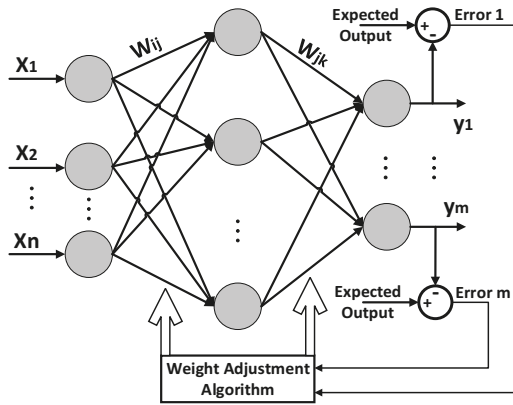


Figure 12. Topology structure of ANN model.

There are two basic architectures of ANNs: feed-forward networks and feedback (recurrent) networks. Meanwhile, there are three main training scenarios for ANNs: supervised, unsupervised, and hybrid. A feed-forward neural network (FFNN) has no feedback and the input signals propagate through the network forward from the input layer to output layer. In the back propagation neural network model (BPNN) feedback and learning take place during the propagation of input patterns from the input neurons to the output neurons. The outputs are compared with the desired target values, and error is produced. Then the weights are adapted to minimize the error. The initial values of weights are assumed to be zero, and the weight between the actual neuron and the output of the predecessor neuron is defined as $W_{pred,actual}$. The weight adaptation equation is given by [130]: $W_{pre,act}(t_n) = W_{pre,ac}(t_{n-1}) - \frac{\alpha E(t_n)}{W_{pre,ac}(t_{n-1})} \Delta W_{pre,ac}(t_{n-1})$, where $0 < \alpha < 1$; $E = \frac{1}{2} * \sum (y_i - O_{actual})^2$; $i = 1 \dots n$; and y_i is the expected output.

In [129] a BPNN was used for the SoC determination based on frequency domain data. Here, the real and imaginary parts of the measured impedance, plus the frequency of each measurement are used as X1, X2, and X3 inputs of a three-input BPNN like that presented in Figure. The corresponding output layer provides with its neurons the dedicated SoC classes $\{c_i\}$ corresponding to the SoC specific impedance spectra. The neuron with the determined SoC will remain after execution with the binary value one, and all the others will remain with the value zero. Two different architectures of BPNN are used for calculating SoC in [131]. Unlike these traditional BPNNs, [132] does not take into account the equivalent inner resistance of the battery and makes a single improvement to the weight adjustment algorithm of its BPNN that can significantly reduce the SoC estimation error. In [133] a simple radial basis ANN is used just to identify the ECM parameters and then, using SoC as one of the state-space variables and employing EKF, SoC is estimated. In [133] the inputs of the ANN

are SoC and the current and voltage measured, and the output is the OCV. A similar strategy is used in [43,134–136], where, after modeling the battery system by an ANN model and a state space model as presented in Section 3, SoC is calculated using a dual EKF or other adaptive filter-based estimator. Wang et al. in [137] use a four-input, one-output BPNN. Its only output is SoC estimation in an EV. The four inputs are the current at times $[k]$ and $[k - 1]$, and the voltage at times $[k]$ and $[k - 1]$. This method uses an extensive dataset of charging and discharging experimental LiB voltage and current, obtained at different standardized driving conditions, and trains the network offline. The approach reports that the inclusion of previous time points allows the ANN to better understand the relation of current and voltage drops to SoC. Other approaches can estimate online the battery SoC directly from an ANN [6,138–142]. In [138] the inputs for a topology like in Figure are separated depending on the behaviors of a battery while charging, idling, and discharging. Yan and Wang in [142] utilize a simple two-input, one-output, and one hidden layer BPNN structure. Yan and Wang in [142] used as inputs the current and terminal voltage of the battery, and SoC as the output variable.

The main disadvantage of ANN is that it needs more neurons to increase the accuracy, which limits its implementation in real-life models. In addition, each ANN needs to be trained before it can be used and numerous iterations may be required to train it. For this reason, the trained ANN can be used for only one specific application. For example, in a HEV, the input conditions are always changing and simulating these inputs will be hard. On the other hand, ANN is not effective in extrapolation, which limits its ability to calculate the remaining charge time of a battery [13].

(3) Fuzzy-Based Neural Network Estimation

In general, two types of fuzzy-based neural networks are used in the literature for the estimation of SoC: the adaptive neuro-fuzzy inference system (ANFIS) and the local linear model tree [8]. In all cases, direct open-loop SoC estimation is implemented. ANFIS combines the advantages of fuzzy systems and adaptive networks in one hybrid intelligent paradigm. The flexibility and subjectivity of fuzzy inference systems, when added to the optimization strength and learning capability of adaptive networks, give ANFIS its remarkable power of modeling, approximation, nonlinear mapping, and pattern recognition. ANFIS can be used to model cell characteristics [143], to online correct other SoC estimation techniques for reaching high accuracy [144], or to directly obtain the SoC estimated value [145].

An offline model for power systems applications using ANFIS is developed in [143] for SoC estimation in LiBs. In this publication, based on the manufacturer data on LiBs, the ANFIS battery model is trained offline and developed to yield the cell SoC at any given temperature and OCV within the training range. The cell SoC is estimated while the battery is at rest, and the CC approach is adopted at the cell level. The fact that the ANFIS model is based on the data supplied by manufacturer makes this approach inefficient due to most of the manufacturers not supplying battery data. On the other hand, to take into account the cell degradation, it is required to add a mechanism that guarantees accurate SoC estimation over time. Dai et al. in [144] utilize a KF to estimate the SoC by using a second-order ECM. Then, the ANFIS method is used to correct the SoC obtained by KF. Here, the ANFIS technique is comprised of two steps: the first step is the acquirement of the fuzzy inference system knowledge base based on ANFIS using the experimental data offline, and the next step is the online correction of the pack's SoC estimation results. Dai et al. in [144] present the elaboration of the building, training, and optimizing of the ANFIS model. In [145] a Thevenin ECM is used to obtain the OCV. This output voltage is used as an input of an ANFIS system whose output is the SoC. Despite the tests being performed with a NiMH battery, they are applicable to other chemistries.

Another ANFIS application is presented in [8]. It uses a combination of several algorithms to determine the battery state variables. In this approach, among other SoC boundary estimation methods, a robust EKF is implemented for recalibration of the CC method. Then, the method uses ANFIS to estimate the state of available power. Since ANFIS is known to suffer from the curse of dimensionality, the large number of inputs is likely to hinder the estimation performance. Extensive

experimentation is sometimes required to obtain the ANFIS training dataset [143]. The approach of ANFIS estimation is basically the same as that of the direct SoC estimation using ANNs and, therefore, has the same disadvantages.

(4) Genetic Algorithm-Based Estimation (GA)

Genetic Algorithm (GA) is an optimization technique where the variables of interest of the system to be optimized are characterized in the form of strings called chromosomes. In SoC estimation applications, the chromosome is a vector that has as elements the parameters of the battery model used. SoC can be an element of this vector. The algorithm is initiated by creating a random set of chromosomes in the search space followed by an iterative process of selection, crossover, and mutation to find the optimal solution, as depicted in Figure 13. The stop criterion is defined by an objective function that minimizes the error between the voltages defined in the chromosome and the actual measured voltage. This criterion selects the best population in each iteration.

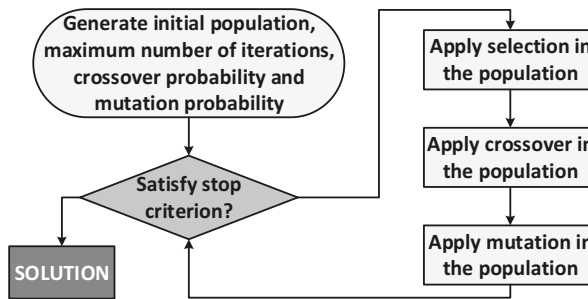


Figure 13. GA algorithm.

GA is used as an optimization technique to estimate different states of the battery. The approaches presented in [59,146] use a GA to identify time constant and other parameters of the battery model (fractional order and EIS-based model [59], and Thevenin ECM [146]). Despite these proposals utilizing a UKF-based SoC and EKF-based SoC estimation, respectively, the model parameter estimation using the GA is crucial, and accounts for the high accuracy of the methods. In [5], a classic GA was used to identify the parameters of five different ECMs and, thus, estimate the SoC. In [78] a GA is used as one of the optimization techniques to estimate the second-order ECM equation parameters that are dependent on SoC, and so to estimate the SoC. The objective of this optimization process was to find the values of polynomial coefficients of parameters equations, which produce a OCV–SoC characteristic that best fits the characteristic curve obtained from the manufacturer’s battery data. As the model fitness function is defined as the absolute of the difference between model output and catalog values at each sample point, the absence of battery data supplied by the manufacturer may cause this method to be unsuitable for many applications. Rozaqi and Rijanto in [108] apply a RLS algorithm for battery SoC estimation by using a Thevenin ECM of a LiB. Here OCV and the internal resistance are the parameters to be estimated, and the optimum values of RLS are determined using a GA.

Several variations in GA applications for SoC estimation processes can be found in the literature. One of them is just to use the algorithm to identify the initial SoC, like the procedure presented in [147]. This approach uses a Thevenin ECM, and SoC estimation is finally made by a modified OCV method. Yan and Wang in [142] use a GA for optimizing the weights and thresholds of a one hidden layer BPNN that has SoC as the only output. In [112], OCV is calculated based on a Thevenin ECM, and then, by using it, SoC is estimated through a fading KF where the fading factors that optimize the KF are calculated by the means of a GA.

(5) Particle Swarm Optimization Algorithm-Based Estimation (PSO)

Particle swarm optimization (PSO) is a swarm intelligence-based meta-heuristic optimization technique inspired by intelligent movement depicted by the population of different species. The algorithm consists of a population of particles randomly initialized in the search space. Initially, it produces a random population and then generates the next population based on an objective function. In this process, the PSO algorithm is similar to GA, but PSO does not need reproduction or mutation to produce the next generation. Thus, PSO is faster at finding solutions than GA [148]. The initiated population works collectively through velocity: $v_i^{t+1} = wv_i^t + c_1.rand.(p_{b_i} - x_i^t) + c_2.rand.(g_b - x_i^t)$; and position: $x_i^{t+1} = x_i^t + v_i^{t+1}$; to find the optimal solution [78]. In these equations, w is the inertia weight factor, c_j is an acceleration coefficient, $rand$ is a random number between 0 and 1, v_i^t is the velocity of particle i at iteration t , and x_i^t is the current position of particle i at iteration t . Each particle moves iteratively in the solution space with movement depending on global best position (g_b) of the swarm and its personal best solution (p_{b_i}).

In SoC estimation applications the process of iterative update of the position of the particles is continued until the stop criterion is met, and this criterion is given by an objective function that evaluates the relation OCV–SoC in a direct or indirect way like in [78,149], where a PSO method is used to determine the unknown parameters of a second-order ECM to obtain the OCV. Then these approaches estimate SoC using a lookup table. In [150], instead of a lookup table, the CC method is used for estimating SoC. Ismail and Toha in [148] develop the same process but uses a Thevenin ECM. Huachun et al. in [151] calculated the parameters of a Thevenin ECM using a PSO algorithm and, by using a technique called second-order sliding mode observer, estimated SoC. The approach presented in [152] uses the PSO algorithm to estimate the second-order ECM parameters, but SoC is calculated using two different methods: EKF and the smooth variable structure filter (SVSF). The approach presented in [153] uses a version of the second-order ECM where the voltage source is replaced by a SoC-dependent capacitance and an RC parallel network is added as a third time constant. The values of all intrinsic parameters of this ECM are estimated using a PSO algorithm, and instead of assuming any predefined nonlinear relationships between intrinsic parameters and SoC, the PSO algorithm takes the response of all intrinsic parameters, as well as SoC, into account in the parameter estimation without treating SoC as an independent variable. Antón et al. in [154] present a statistical learning technique for SoC estimation called multivariate adaptive regression splines (MARS), whose optimal parameters are calculated using PSO.

4.2.4. Other Estimation Techniques

The methods presented above can suffer from one or several drawbacks like sensor drifts and precision, modeling mismatches and lack of model accuracy, data saturation, heavy computation, or specific input information requirements. These aspects are key factors that influence the accuracy of the SoC estimation method, so the authors are still working on innovative proposals to overcome those error sources in the SoC estimation process. Although some approaches do not fit into any of the previously presented categories, it is important to list some of those new proposals in this review.

Statistical learning theory addresses the problem of finding a predictive function based on data. The goal is to learn a general rule that maps input variables to outputs. In [154], the MARS statistical learning method was applied to estimate the SoC of a high-capacity battery cell for a simple data profile (constant-current constant-voltage charge, and constant-current discharge) and a limited range of SoC. The fact that MARS parameters are difficult to estimate generates some limitations in the technique. Another statistical approach is presented in [155], which uses a particle filter (PF) or sequential Monte Carlo (SMC) method for SoC estimation of a LiB battery pack for an EV. SMC is a set of genetic-type particle Monte Carlo methodology to solve filtering problems arising from signal processing and Bayesian statistical inference. The filtering problem consists of estimating the internal states in dynamical systems when partial observations are made; random perturbations are present in the sensors as well as in the dynamical system. This proposal utilizes both Gaussian and non-Gaussian

distributed noise models. PF utilizes particles (weighted random samples) to approximate the posterior distribution sampled by the Monte Carlo method.

Afshari et al. in [152] use a second-order ECM and a smooth variable structure filter (SVSF) to estimate the SoC. The SVSF benefits from the robustness of variable structure systems in which it is guaranteed that the measurement error (innovation sequence) remains norm-bounded. The stability and convergence of the SVSF method are proven in this publication. The filter is formulated in a predictor–corrector form, and its corrective gain is designed to force the states to remain within a subspace of true states. This paper shows that this filter is robust to a wider range of modeling inaccuracies and parametric uncertainties. SVSF is implemented to alleviate the effects of different factors on SoC estimation like inaccuracies in modeling a cell, deviations of a battery’s parameters from their nominal values due to aging, unpredictable temperature variations, and measurement and environmental noises. The publication states that the SVSF method is more robust to modeling and for parametric uncertainties, and demonstrates the superiority of the SVSF over the EKF for SoC estimation under uncertain conditions.

Huanchun et al. in [151] propose an approach based on second-order sliding mode observer (SMO) for battery SoC estimation. The PSO technique is utilized to estimate the Thevenin ECM parameters. The estimation technique has a robust tracking capability in SoC estimation with high accuracy for both known and unknown initial SoC, and showed that SoC could be determined with high accuracy based on only the measurements of the battery voltage and current.

Tang et al. in [110] present a multi-gain Luenberger-based (MGL) observer that is robust to modeling inaccuracy and sensor drifts to estimate SoC. The gains of the observer are switched by a classifier, which categorizes the errors between the real voltage measurement and model output into different groups. Correspondingly, different observing strategies are designed for different groups for better SoC estimation robustness and accuracy.

5. Technical Challenges in the SoC Estimation Process

The factors affecting battery SoC are many and complicated. Scholars have proposed many methods to estimate SoC, but these still do not guarantee accuracy and practicability. There are two overall challenges in this field: (1) To enhance the SoC estimation accuracy, robustness, and effectiveness without increasing the complexity of the models and estimation procedures; (2) To simplify the complexity of the estimation process, and therefore facilitate its implementation in low-cost hardware. The solutions for the two challenges are closely related and cannot be disconnected from each other. The goal is to find a trade-off in the SoC estimation procedures between accuracy and computational complexity in compliance with the motto “simple is better.” To achieve this, it is necessary to propose strategies to nullify or minimize sources of error in the SoC estimation methodologies.

In this review, the main SoC estimation error sources are: (1) Zero-mean sensing noise is inevitable in practical cases for both current and voltage sensors; (2) Battery modeling error or inaccuracies in the models; (3) The parameters that are assumed such as covariance and noise type, initial SoC, and search spaces in optimization processes; (4) Other unknown error sources that may have been caused by some unknown reasons or the combination of errors noted above. For example, the drifting of the current sensor can cause a large SoC estimation error in the current integral method after a long period of error accumulation; however, the influence is negligible when the time is short.

Now the two main mentioned challenges become more specific: To deal with the probabilistic tendency to model the sensing noise with models closer to the real phenomenon; to find less complex and more accurate battery models that include aging and thermal behavior; to define methodologies to establish initial values; and to identify and characterize other possible error sources. The last three can be solved by overcoming the drawbacks of the battery modeling by including the battery strong nonlinearity, time-varying features, and temperature effects on the behavior. The principal concern in the thermal control of LiBs is the considerable temperature rise that happens during charging and discharging, which may cause thermal runaway. Therefore, understanding the discharge behavior

of a lithium ion battery is very important as well as using correction factors in the models according to temperature variations, or other approaches that guarantee the inclusion of thermal restrictions and also variations of thermal and electric behaviors between cells within a battery pack. A fully efficient battery model can quantitatively characterize battery nonlinearities such as open-circuit voltage, internal resistance, and transient voltage response. Such a model enables designers to gain a thorough understanding of battery behaviors under different operating situations and will allow accurate battery performance prediction and the optimization not only of the safe control of the battery but also the extension of its useful life thanks to the optimum management of all its capacity. This kind of model would simplify and optimize the design of the BMS. The information contained in the current i and voltage v variables are related to microscopic behavior within each battery cell, and they embrace all the internal dynamics of a battery. This review proposes that at a given instant k , i_k , and v_k are the result of the performance of all the internal chemistry of the battery under conditions such as aging, temperature, hysteresis, self-discharge, rates of charge and discharge, and even noise present in the battery as a system (except the noise of the DAQ systems). The challenge is to take these data, extract the information, and build a system free from the constraints and limitations presented by existing methods.

6. Conclusions

This paper critically reviews SoC estimation methodologies presented by scholars in the last five years, presenting the fundamentals and main drawbacks of each method. The approaches that have not been extensively used during recent years have not been cited here. From the review of the different approaches, it can be concluded that the hardest part of obtaining a battery SoC estimation is to build a model that reflects the reality inside the battery, including the impact of temperature dependencies on internal resistance and capacity fading. It can also be concluded that the accuracy of SoC estimation may be affected by factors such as modeling imperfections, parametric uncertainties, sensor inaccuracies, and measurement noise. There are also some other factors that affect the battery performance (and therefore, the estimation method), including self-discharging, aging effects, imbalance between cells, capacity fade, and temperature effects. No matter the method, there must always be a trade-off in battery modeling between accuracy and computational complexity. The literature shows that the aging of LiBs is influenced by temperature, time, SoC, cycle number, charge rate, and depth of discharge. Also, the SoC estimation accuracy is affected by the inclusion or not of these parameters into the battery models. Those SoC estimation techniques that continuously update the model parameters can address the aging phenomenon. The review shows that the temperature makes model parameters vary. So the inclusion of thermal behavior in the model used for SoC estimation is needed for better SoC estimation accuracy.

For real-time EV application, the model has to be as simple as possible, keeping the accuracy of SoC estimation within a reasonable range. ECM is regarded as the most appropriate for online estimation and, based on this type of model the adaptive filter-based and artificial-intelligence-based approaches are presented to estimate the SoC with high precision. However, the lack of physical-chemical explanation for the microscopic movements in the battery is the main drawback of this model. Meanwhile, the electrochemical model, which could illustrate the charge transfer between two electrodes and reveal the electrochemical mechanism, is reported as too complicated to be used for online calculation. From the review, it is clear that adaptive filter-based algorithms are more suitable for EV applications, and those based on artificial intelligence are not suitable for this application due to its intensive computing and/or offline learning process requirements. For solving the optimization problem in filter-based techniques, the trend is to use artificial-intelligence-based optimization techniques because of their simplicity, flexibility, derivation-free mechanism, and local optima avoidance.

As the battery modeling is a fundamental process to establish an accurate SoC estimation algorithm, and due to the battery modeling methods proposed by literature not being accurate enough

under specific conditions and having several restrictions on aging assessment to continually update the models, it is necessary to perform more research in this field. The building of practical battery and the application of the adaptive control technology, the expert system theories, and artificial intelligence in the modeling process are required. It is important to consider that none of the reviewed methods is entirely efficient and reliable, and although it may be complete and accurate for an application under certain conditions, it may be inaccurate for others. Therefore, the selection of the appropriate algorithm is up to the designer, mainly depending on his or her knowledge of the addressed application. To this aim, the information provided earlier can help with choosing the most convenient approach.

Acknowledgments: We would like to thank the Administrative Department of Science, Technology, and Innovation of the Colombian government, COLCIENCIAS, for supporting this work, and the University Politécnico Colombiano Jaime Isaza Cadavid for covering the costs to publish in this journal. The authors also want to thank Universidad de Antioquia for the support of the project CODI 2015-7747.

Author Contributions: All authors contributed to the paper. Nicolás Muñoz-Galeano was the director of the research project; Juan Pablo Rivera-Barrera was responsible for collecting the information and analyzing the different methodologies; Henry Omar Sarmiento-Maldonado was the advisor of the project. All authors were responsible for organizing and revising the whole paper and for classifying the different methodologies.

Conflicts of Interest: The authors declare no conflict of interest.

References

1. Rahimi-Eichi, H.; Ojha, U.; Baronti, F.; Chow, M.Y. Battery management system: An overview of its application in the smart grid and electric vehicles. *IEEE Ind. Electron. Mag.* **2013**, *7*, 4–16. [[CrossRef](#)]
2. Yu, H.; Duan, J.; Du, W.; Xue, S.; Sun, J. China's energy storage industry: Develop status, existing problems and countermeasures. *Renew. Sustain. Energy Rev.* **2017**, *71*, 767–784. [[CrossRef](#)]
3. Chen, J.; Ouyang, Q.; Xu, C.; Su, H. Neural network-based state of charge observer design for lithium-ion batteries. *IEEE Trans. Control Syst. Technol.* **2017**, *PP*, 1–9. [[CrossRef](#)]
4. Waag, W.; Fleischer, C.; Sauer, D.U. Critical review of the methods for monitoring of lithium-ion batteries in electric and hybrid vehicles. *J. Power Sources* **2014**, *258*, 321–339. [[CrossRef](#)]
5. Liu, G.; Lu, L.; Hong, F.; Hua, J.; Li, J.; Ouyang, M.; Wang, Y.; Xue, S.; Chen, P. A comparative study of equivalent circuit models and enhanced equivalent circuit models of lithium-ion batteries with different model structures. In Proceedings of the 2014 IEEE Conference and Expo Transportation Electrification Asia-Pacific (ITEC Asia-Pacific), Beijing, China, 31 August–3 September 2014; pp. 1–6.
6. Chaoui, H.; Ibe-Ekeocha, C.C.; Gualous, H. Aging prediction and state of charge estimation of a lifepo4 battery using input time-delayed neural networks. *Electr. Power Syst. Res.* **2017**, *146*, 189–197. [[CrossRef](#)]
7. Chen, Z.; Fu, Y.; Mi, C.C. State of charge estimation of lithium-ion batteries in electric drive vehicles using extended kalman filtering. *IEEE Trans. Veh. Technol.* **2013**, *62*, 1020–1030. [[CrossRef](#)]
8. Fleischer, C.; Waag, W.; Bai, Z.; Sauer, D.U. Adaptive on-line state of available power prediction of lithium-ion batteries. *J. Power Electron.* **2013**, *13*, 516–527. [[CrossRef](#)]
9. Zhang, Z.L.; Cheng, X.; Lu, Z.Y.; Gu, D.J. Soc estimation of lithium-ion batteries with aekf and wavelet transform matrix. *IEEE Trans. Power Electron.* **2017**, *32*, 7626–7634. [[CrossRef](#)]
10. Cacciato, M.; Nobile, G.; Scarella, G.; Scelba, G. Real-time model-based estimation of soc and soh for energy storage systems. *IEEE Trans. Power Electron.* **2017**, *32*, 794–803. [[CrossRef](#)]
11. Jingshan, L.; Shiyu, Z.; Yehui, H. Recent research on battery diagnostics, prognostics, and uncertainty management. In *Advances in Battery Manufacturing, Service, and Management Systems*; Wiley-IEEE Press: Hoboken, NJ, USA, 2017; p. 416.
12. Feng, Y.; Cao, Z.; Shen, W.; Yu, X.; Han, F.; Chen, R.; Wu, J. Intelligent battery management for electric and hybrid electric vehicles: A survey. In Proceedings of the 2016 IEEE International Conference on Industrial Technology (ICIT), Taipei, Taiwan, 14–17 March 2016; pp. 1436–1441.
13. Khayat, N.; Karami, N. Adaptive techniques used for lifetime estimation of lithium-ion batteries. In Proceedings of the 2016 Third International Conference on Electrical, Electronics, Computer Engineering and their Applications (EECEA), Beirut, Lebanon, 21–23 April 2016; pp. 98–103.

14. Hannan, M.A.; Lipu, M.S.H.; Hussain, A.; Mohamed, A. A review of lithium-ion battery state of charge estimation and management system in electric vehicle applications: Challenges and recommendations. *Renew. Sustain. Energy Rev.* **2017**, *78*, 834–854. [[CrossRef](#)]
15. Xiong, R.; Tian, J.; Mu, H.; Wang, C. A systematic model-based degradation behavior recognition and health monitoring method for lithium-ion batteries. *Appl. Energy* **2017**. [[CrossRef](#)]
16. Cuma, M.U.; Koroglu, T. A comprehensive review on estimation strategies used in hybrid and battery electric vehicles. *Renew. Sustain. Energy Rev.* **2015**, *42*, 517–531. [[CrossRef](#)]
17. Meng, J.; Ricco, M.; Luo, G.; Swierczynski, M.; Stroe, D.I.; Stroe, A.I.; Teodorescu, R. An overview of online implementable soc estimation methods for lithium-ion batteries. In Proceedings of the 2017 International Conference on Optimization of Electrical and Electronic Equipment (OPTIM) & 2017 Intl Aegean Conference on Electrical Machines and Power Electronics (ACEMP), Brasov, Romania, 25–27 May 2017; pp. 573–580.
18. Tang, X.; Liu, B.; Gao, F. State of charge estimation of lifepo4 battery based on a gain-classifier observer. *Energy Procedia* **2017**, *105*, 2071–2076. [[CrossRef](#)]
19. Cai, Y.; Wang, Q.; Qi, W. D-ukf based state of health estimation for 18650 type lithium battery. In Proceedings of the 2016 IEEE International Conference on Mechatronics and Automation, Harbin, China, 7–10 August 2016; pp. 754–758.
20. Chaoui, H.; Gualous, H. Adaptive state of charge estimation of lithium-ion batteries with parameter and thermal uncertainties. *IEEE Trans. Control Syst. Technol.* **2017**, *25*, 752–759. [[CrossRef](#)]
21. Couto, L.D.; Schorsch, J.; Nicotra, M.M.; Kinnaert, M. Soc and soh estimation for li-ion batteries based on an equivalent hydraulic model. Part I: Soc and surface concentration estimation. In Proceedings of the 2016 American Control Conference (ACC), Boston, MA, USA, 6–8 July 2016; pp. 4022–4028.
22. He, H.; Xiong, R.; Fan, J. Evaluation of lithium-ion battery equivalent circuit models for state of charge estimation by an experimental approach. *Energies* **2011**, *4*, 582–598. [[CrossRef](#)]
23. Beir, M.D.; Calado, M.d.R.A.; Pombo, J.A.N.; Mariano, S.J.P.S. Balancing management system for improving li-ion batteries capacity usage and lifespan. In Proceedings of the 2016 IEEE 16th International Conference on Environment and Electrical Engineering (EEEIC), Florence, Italy, 7–10 June 2016; pp. 1–6.
24. Cao, J.; Schofield, N.; Emadi, A. Battery balancing methods: A comprehensive review. In Proceedings of the 2008 IEEE Vehicle Power and Propulsion Conference, Harbin, China, 3–5 September 2008; pp. 1–6.
25. Evzelman, M.; Rehman, M.M.U.; Hathaway, K.; Zane, R.; Costinett, D.; Maksimovic, D. Active balancing system for electric vehicles with incorporated low-voltage bus. *IEEE Trans. Power Electron.* **2016**, *31*, 7887–7895. [[CrossRef](#)]
26. Kim, M.Y.; Kim, J.W.; Kim, C.H.; Cho, S.Y.; Moon, G.W. Automatic charge equalization circuit based on regulated voltage source for series connected lithium-ion batteries. In Proceedings of the 2011 IEEE 8th International Conference on Power Electronics and ECCE Asia (ICPE & ECCE), Jeju, Korea, 30 May–3 June 2011; pp. 2248–2255.
27. Rehman, M.M.U.; Evzelman, M.; Hathaway, K.; Zane, R.; Plett, G.L.; Smith, K.; Wood, E.; Maksimovic, D. Modular approach for continuous cell-level balancing to improve performance of large battery packs. In Proceedings of the 2014 IEEE Energy Conversion Congress and Exposition (ECCE), Pittsburgh, PA, USA, 14–18 September 2014; pp. 4327–4334.
28. Zhang, Z.; Gui, H.; Gu, D.J.; Yang, Y.; Ren, X. A hierarchical active balancing architecture for lithium-ion batteries. *IEEE Trans. Power Electron.* **2016**, *32*, 2757–2768. [[CrossRef](#)]
29. Liu, P.; Zhu, H.-H.; Chen, J.; Li, G.-Y. A distributed management system for lithium ion battery pack. In Proceedings of the 2016 Chinese Control and Decision Conference (CCDC), Yinchuan, China, 28–30 May 2016; pp. 3997–4002.
30. Abdeltawab, H.H.; Mohamed, Y.A.R.I. Market-oriented energy management of a hybrid wind-battery energy storage system via model predictive control with constraint optimizer. *IEEE Trans. Ind. Electron.* **2015**, *62*, 6658–6670. [[CrossRef](#)]
31. Abdul-Hak, M.; Al-Holou, N. Its based predictive intelligent battery management system for plug-in hybrid and electric vehicles. In Proceedings of the 2009 IEEE Vehicle Power and Propulsion Conference, Dearborn, MI, USA, 7–10 September 2009; pp. 138–144.
32. Mahamadi, A.; Sastry, S. Model predictive controller for battery management systems. In Proceedings of the 2015 International Conference on Computing, Control, Networking, Electronics and Embedded Systems Engineering (ICCNEEE), Khartoum, Sudan, 7–9 September 2015; pp. 21–26.

33. Watrin, N.; Blunier, B.; Miraoui, A. Review of adaptive systems for lithium batteries state-of-charge and state-of-health estimation. In Proceedings of the 2012 IEEE Transportation Electrification Conference and Expo (ITEC), Dearborn, MI, USA, 18–20 June 2012; pp. 1–6.
34. Tanim, T.R. *Lithium Ion Battery Modeling, Estimation, and Aging for Hybrid Electric Vehicle Applications*; The Pennsylvania State University: State College, PA, USA, 2015.
35. Zou, Z.; Xu, J.; Mi, C.; Cao, B.; Chen, Z. Evaluation of model based state of charge estimation methods for lithium-ion batteries. *Energies* **2014**, *7*, 5065–5082. [[CrossRef](#)]
36. Wang, Q.; Wang, J.; Zhao, P.; Kang, J.; Yan, F.; Du, C. Correlation between the model accuracy and model-based soc estimation. *Electrochim. Acta* **2017**, *228*, 146–159. [[CrossRef](#)]
37. Zheng, Y.; Han, X.; Lu, L.; Li, J.; Ouyang, M. Lithium ion battery pack power fade fault identification based on shannon entropy in electric vehicles. *J. Power Sources* **2013**, *223*, 136–146. [[CrossRef](#)]
38. Rusu, F.A.; Livint, G. Estimator for a pack of lithium-ion cell. In Proceedings of the 2016 20th International Conference on System Theory, Control and Computing (ICSTCC), Sinaia, Romania, 13–15 October 2016; pp. 573–577.
39. Lashway, C.R.; Mohammed, O.A. Adaptive battery management and parameter estimation through physics-based modeling and experimental verification. *IEEE Trans. Transp. Electrification* **2016**, *2*, 454–464. [[CrossRef](#)]
40. Truchot, C.; Dubarry, M.; Liaw, B.Y. State-of-charge estimation and uncertainty for lithium-ion battery strings. *Appl. Energy* **2014**, *119*, 218–227. [[CrossRef](#)]
41. Ali, D.; Mukhopadhyay, S.; Rehman, H. A novel adaptive technique for li-ion battery model parameters estimation. In Proceedings of the 2016 IEEE National Aerospace and Electronics Conference (NAECON) and Ohio Innovation Summit (OIS), Dayton, OH, USA, 25–29 July 2016; pp. 23–26.
42. Lavigne, L.; Sabatier, J.; Francisco, J.M.; Guillemard, F.; Noury, A. Lithium-ion open circuit voltage (ocv) curve modelling and its ageing adjustment. *J. Power Sources* **2016**, *324*, 694–703. [[CrossRef](#)]
43. Dang, X.; Yan, L.; Xu, K.; Wu, X.; Jiang, H.; Sun, H. Open-circuit voltage-based state of charge estimation of lithium-ion battery using dual neural network fusion battery model. *Electrochim. Acta* **2016**, *188*, 356–366. [[CrossRef](#)]
44. Cheng, M.W.; Lee, Y.S.; Liu, M.; Sun, C.C. State-of-charge estimation with aging effect and correction for lithium-ion battery. *IET Electr. Syst. Transp.* **2015**, *5*, 70–76. [[CrossRef](#)]
45. Mejdoubi, A.E.; Oukaour, A.; Chaoui, H.; Gualous, H.; Sabor, J.; Slamani, Y. State-of-charge and state-of-health lithium-ion batteries' diagnosis according to surface temperature variation. *IEEE Trans. Ind. Electron.* **2016**, *63*, 2391–2402. [[CrossRef](#)]
46. Savanth, P.; Shailesh, K.R. Reduction of parameters in a lithium ion cell model by experimental validation of relationship between ocv and soc. In Proceedings of the 2016 Online International Conference on Green Engineering and Technologies (IC-GET), Coimbatore, India, 19 November 2016; pp. 1–5.
47. Nejad, S.; Gladwin, D.T.; Stone, D.A. On-chip implementation of extended kalman filter for adaptive battery states monitoring. In Proceedings of the IECON 2016—42nd Annual Conference of the IEEE Industrial Electronics Society, Florence, Italy, 23–26 October 2016; pp. 5513–5518.
48. Kim, T.; Qiao, W.; Qu, L. Hysteresis modeling for model-based condition monitoring of lithium-ion batteries. In Proceedings of the 2015 IEEE Energy Conversion Congress and Exposition (ECCE), Montreal, QC, Canada, 20–24 September 2015; pp. 5068–5073.
49. Wei, C.; Benosman, M. Extremum seeking-based parameter identification for state-of-power prediction of lithium-ion batteries. In Proceedings of the 2016 IEEE International Conference on Renewable Energy Research and Applications (ICRERA), Birmingham, UK, 20–23 November 2016; pp. 67–72.
50. Nejad, S.; Gladwin, D.T.; Stone, D.A. Enhanced state-of-charge estimation for lithium-ion iron phosphate cells with flat open-circuit voltage curves. In Proceedings of the IECON 2015—41st Annual Conference of the IEEE Industrial Electronics Society, Yokohama, Japan, 9–12 November 2015; pp. 3187–3192.
51. Barcellona, S.; Grillo, S.; Piegari, L. A simple battery model for ev range prediction: Theory and experimental validation. In Proceedings of the 2016 International Conference on Electrical Systems for Aircraft, Railway, Ship Propulsion and Road Vehicles & International Transportation Electrification Conference (ESARS-ITEC), Toulouse, France, 2–4 November 2016; pp. 1–7.
52. Westerhoff, U.; Kroker, T.; Kurbach, K.; Kurrat, M. Electrochemical impedance spectroscopy based estimation of the state of charge of lithium-ion batteries. *J. Energy Storage* **2016**, *8*, 244–256. [[CrossRef](#)]

53. Shili, S.; Sari, A.; Hijazi, A.; Venet, P. Online lithium-ion batteries health monitoring using balancing circuits. In Proceedings of the 2017 IEEE International Conference on Industrial Technology (ICIT), Toronto, ON, Canada, 22–25 March 2017; pp. 484–488.
54. Stroe, D.I.; Swierczynski, M.; Kær, S.K.; Teodorescu, R. A comprehensive study on the degradation of lithium-ion batteries during calendar ageing: The internal resistance increase. In Proceedings of the 2016 IEEE Energy Conversion Congress and Exposition (ECCE), Milwaukee, WI, USA, 18–22 September 2016; pp. 1–7.
55. Guha, A.; Patra, A.; Vaisakh, K.V. Remaining useful life estimation of lithium-ion batteries based on the internal resistance growth model. In Proceedings of the 2017 Indian Control Conference (ICC), Guwahati, India, 4–6 January 2017; pp. 33–38.
56. Yang, Z.; Patil, D.; Fahimi, B. Online estimation of capacity fade and impedance of lithium-ion batteries based on impulse response technique. In Proceedings of the 2017 IEEE Applied Power Electronics Conference and Exposition (APEC), Tampa, FL, USA, 26–30 March 2017; pp. 1229–1235.
57. Xu, J.; Mi, C.C.; Cao, B.; Cao, J. A new method to estimate the state of charge of lithium-ion batteries based on the battery impedance model. *J. Power Sources* **2013**, *233*, 277–284. [[CrossRef](#)]
58. Ma, Y.; Zhou, X.; Li, B.; Chen, H. Fractional modeling and soc estimation of lithium-ion battery. *IEEE/CAA J. Autom. Sin.* **2016**, *3*, 281–287.
59. Mu, H.; Xiong, R.; Zheng, H.; Chang, Y.; Chen, Z. A novel fractional order model based state-of-charge estimation method for lithium-ion battery. *Appl. Energy* **2017**. [[CrossRef](#)]
60. Cao, Y.; Kroeze, R.C.; Krein, P.T. Multi-timescale parametric electrical battery model for use in dynamic electric vehicle simulations. *IEEE Trans. Transp. Electrification* **2016**, *2*, 432–442. [[CrossRef](#)]
61. Xia, B.; Zhao, X.; Callafon, R.D.; Garnier, H.; Nguyen, T.; Mi, C. Accurate lithium-ion battery parameter estimation with continuous-time system identification methods. In Proceedings of the 2016 IEEE Energy Conversion Congress and Exposition (ECCE), Milwaukee, WI, USA, 18–22 September 2016; pp. 1–8.
62. Yang, J.; Xia, B.; Shang, Y.; Huang, W.; Mi, C. Improved battery modeling approach considering operating scenarios for hev /ev applications. In Proceedings of the 2017 IEEE Applied Power Electronics Conference and Exposition (APEC), Tampa, FL, USA, 26–30 March 2017; pp. 1216–1222.
63. Anyaegbunam, I. *The Development of a Battery Management System with Special Focus on Capacity Estimation and Thermal Management*; University of Texas: Austin, TX, USA, 2016.
64. Zhou, X.; Cheng, L.; Tang, Y.; Pan, Z.; Sun, Q. Model identification of lithium-ion batteries in the portable power system. In Proceedings of the 2016 IEEE International Conference on Prognostics and Health Management (ICPHM), Ottawa, ON, Canada, 20–22 June 2016; pp. 1–5.
65. Jiang, B.; Dai, H.; Wei, X.; Zhu, L.; Sun, Z. Online reliable peak charge/discharge power estimation of series-connected lithium-ion battery packs. *Energies* **2017**, *10*, 390. [[CrossRef](#)]
66. Min, C.; Rincon-Mora, G.A. Accurate electrical battery model capable of predicting runtime and i-v performance. *IEEE Trans. Energy Convers.* **2006**, *21*, 504–511.
67. Madani, S.S.; Swierczynski, M.J.; Kær, S.K. The discharge behavior of lithium-ion batteries using the dual-potential multi-scale multi-dimensional (msmd) battery model. In Proceedings of the 2017 Twelfth International Conference on Ecological Vehicles and Renewable Energies (EVER), Monte Carlo, Monaco, 11–13 April 2017; pp. 1–14.
68. Din, M.S.E.; Abdel-Hafez, M.F.; Hussein, A.A. Enhancement in li-ion battery cell state-of-charge estimation under uncertain model statistics. *IEEE Trans. Veh. Technol.* **2016**, *65*, 4608–4618.
69. Jiang, J.; Zhang, C.; Wen, J.; Zhang, W.; Sharkh, S.M. An optimal charging method for li-ion batteries using a fuzzy-control approach based on polarization properties. *IEEE Trans. Veh. Technol.* **2013**, *62*, 3000–3009. [[CrossRef](#)]
70. Parvini, Y.; Vahidi, A.; Fayazi, S.A. Heuristic versus optimal charging of supercapacitors, lithium-ion, and lead-acid batteries: An efficiency point of view. *IEEE Trans. Control Syst. Technol.* **2017**, *PP*, 1–14. [[CrossRef](#)]
71. Raszmann, E.; Baker, K.; Shi, Y.; Christensen, D. Modeling stationary lithium-ion batteries for optimization and predictive control. In Proceedings of the 2017 IEEE Power and Energy Conference at Illinois (PECI), Champaign, IL, USA, 23–24 February 2017; pp. 1–7.
72. Qiuting, W.; Yinzhu, J.; Yunhao, L. State of health estimation for lithium-ion battery based on d-ukf. *Int. J. Hybrid Inf. Technol.* **2015**, *8*, 55–70.

73. Zhang, Z.; Cheng, X.; Lu, Z.Y.; Gu, D.J. Soc estimation of lithium-ion battery pack considering balancing current. *IEEE Trans. Power Electron.* **2017**, *PP*, 1. [[CrossRef](#)]
74. Li, K.; Soong, B.H.; Tseng, K.J. A high-fidelity hybrid lithium-ion battery model for soe and runtime prediction. In Proceedings of the 2017 IEEE Applied Power Electronics Conference and Exposition (APEC), Tampa, FL, USA, 26–30 March 2017; pp. 2374–2381.
75. Li, K.; Tseng, K.J. An electrical model capable of estimating the state of energy for lithium-ion batteries used in energy storage systems. In Proceedings of the 2016 IEEE 2nd Annual Southern Power Electronics Conference (SPEC), Auckland, New Zealand, 5–8 December 2016; pp. 1–8.
76. Jaguemont, J.; Nikolian, A.; Omar, N.; Goutam, S.; Mierlo, J.V.; Bossche, P.V.d. Development of a 2d-thermal model of three battery chemistries considering entropy. *IEEE Trans. Energy Convers.* **2017**, *PP*, 1.
77. Luo, G.; Meng, J.; Ji, X.; Cai, X.; Gao, F. A data driven model for accurate soc estimation in evs. In Proceedings of the 2017 IEEE International Conference on Industrial Technology (ICIT), Toronto, ON, Canada, 22–25 March 2017; pp. 352–357.
78. Sangwan, V.; Sharma, A.; Kumar, R.; Rathore, A.K. Equivalent circuit model parameters estimation of li-ion battery: C-rate, soc and temperature effects. In Proceedings of the 2016 IEEE International Conference on Power Electronics, Drives and Energy Systems (PEDES), Trivandrum, India, 14–17 December 2016; pp. 1–6.
79. Payyappilly, B.; John, V. A generic in-circuit modeling approach for electrochemical batteries. In Proceedings of the 2016 IEEE International Conference on Power Electronics, Drives and Energy Systems (PEDES), Trivandrum, India, 14–17 December 2016; pp. 1–6.
80. Zhang, C.; Li, K.; Deng, J.; Song, S. Improved realtime state-of-charge estimation of liFePO₄ battery based on a novel thermoelectric model. *IEEE Trans. Ind. Electron.* **2017**, *64*, 654–663. [[CrossRef](#)]
81. Subramanian, V.R.; Tapriyal, D.; White, R.E. A boundary condition for porous electrodes. *Electrochem. Solid-State Lett.* **2004**, *7*, A259–A263. [[CrossRef](#)]
82. Lotfi, N.; Landers, R.G.; Li, J.; Park, J. Reduced-order electrochemical model-based soc observer with output model uncertainty estimation. *IEEE Trans. Control Syst. Technol.* **2017**, *PP*, 1–14. [[CrossRef](#)]
83. Moura, S.J.; Argomedeo, F.B.; Klein, R.; Mirtabatabaei, A.; Krstic, M. Battery state estimation for a single particle model with electrolyte dynamics. *IEEE Trans. Control Syst. Technol.* **2017**, *25*, 453–468. [[CrossRef](#)]
84. Limoge, D.W.; Bi, P.Y.; Annaswamy, A.M.; Krupadanam, A. A reduced-order model of a lithium-ion cell using the absolute nodal coordinate formulation approach. *IEEE Trans. Control Syst. Technol.* **2017**, *PP*, 1–14. [[CrossRef](#)]
85. Shen, W.J.; Li, H.X. A sensitivity-based group-wise parameter identification algorithm for the electric model of li-ion battery. *IEEE Access* **2017**, *5*, 4377–4387. [[CrossRef](#)]
86. Yi, J.; Koo, B.; Shin, C.B.; Han, T.; Park, S. Modeling the effect of aging on the electrical and thermal behaviors of a lithium-ion battery during constant current charge and discharge cycling. *Comput. Chem. Eng.* **2017**, *99*, 31–39. [[CrossRef](#)]
87. Tran, N.T.; Vilathgamuwa, M.; Farrell, T.; Choi, S.S. Matlab simulation of lithium ion cell using electrochemical single particle model. In Proceedings of the 2016 IEEE 2nd Annual Southern Power Electronics Conference (SPEC), Auckland, New Zealand, 5–8 December 2016; pp. 1–6.
88. Ahmed, R.; Sayed, M.E.; Arasaratnam, I.; Tjong, J.; Habibi, S. Reduced-order electrochemical model parameters identification and soc estimation for healthy and aged li-ion batteries part i: Parameterization model development for healthy batteries. *IEEE J. Emerg. Sel. Top. Power Electron.* **2014**, *2*, 659–677. [[CrossRef](#)]
89. Zou, C.; Manzie, C.; Nešić, D. A framework for simplification of pde-based lithium-ion battery models. *IEEE Trans. Control Syst. Technol.* **2016**, *24*, 1594–1609. [[CrossRef](#)]
90. Bartlett, A.; Marcicki, J.; Onori, S.; Rizzoni, G.; Yang, X.G.; Miller, T. Electrochemical model-based state of charge and capacity estimation for a composite electrode lithium-ion battery. *IEEE Trans. Control Syst. Technol.* **2016**, *24*, 384–399. [[CrossRef](#)]
91. Corno, M.; Bhatt, N.; Savaresi, S.M.; Verhaegen, M. Electrochemical model-based state of charge estimation for li-ion cells. *IEEE Trans. Control Syst. Technol.* **2015**, *23*, 117–127. [[CrossRef](#)]
92. Ahmed, R.; Sayed, M.E.; Arasaratnam, I.; Tjong, J.; Habibi, S. Reduced-order electrochemical model parameters identification and state of charge estimation for healthy and aged li-ion batteries—Part II: Aged battery model and state of charge estimation. *IEEE J. Emerg. Sel. Top. Power Electron.* **2014**, *2*, 678–690. [[CrossRef](#)]

93. Ahmadian, A.; Sedghi, M.; Elkamel, A.; Fowler, M.; Golkar, M.A. Plug-in electric vehicle batteries degradation modeling for smart grid studies: Review, assessment and conceptual framework. *Renew. Sustain. Energy Rev.* **2017**. [[CrossRef](#)]
94. Bashash, S.; Moura, S.J.; Forman, J.C.; Fathy, H.K. Plug-in hybrid electric vehicle charge pattern optimization for energy cost and battery longevity. *J. Power Sources* **2011**, *196*, 541–549. [[CrossRef](#)]
95. Plett, G.L. Extended kalman filtering for battery management systems of lipb-based hev battery packs. *J. Power Sources* **2004**, *134*, 252–261. [[CrossRef](#)]
96. Topan, P.A.; Ramadan, M.N.; Fathoni, G.; Cahyadi, A.I.; Wahyunggoro, O. State of charge (soc) and state of health (soh) estimation on lithium polymer battery via kalman filter. In Proceedings of the 2016 2nd International Conference on Science and Technology-Computer (ICST), Yogyakarta, Indonesia, 27–28 October 2016; pp. 93–96.
97. Peng, S.; Chen, C.; Shi, H.; Yao, Z. State of charge estimation of battery energy storage systems based on adaptive unscented kalman filter with a noise statistics estimator. *IEEE Access* **2017**, *5*, 13202–13212. [[CrossRef](#)]
98. Tian, Y.; Xia, B.; Sun, W.; Xu, Z.; Zheng, W. A modified model based state of charge estimation of power lithium-ion batteries using unscented kalman filter. *J. Power Sources* **2014**, *270*, 619–626. [[CrossRef](#)]
99. Julier, S.J.; Uhlmann, J.K. Unscented filtering and nonlinear estimation. *Proc. IEEE* **2004**, *92*, 401–422. [[CrossRef](#)]
100. Lin, N.; Ci, S.; Wu, D. A novel low-cost online state of charge estimation method for reconfigurable battery pack. In Proceedings of the 2016 IEEE Applied Power Electronics Conference and Exposition (APEC), Long Beach, CA, USA, 20–24 March 2016; pp. 3189–3192.
101. Jung-Hyo, B.; Bai, Z. The development of technology on reduces the soc error rate using hybrid kalman filter(hkf) and the demonstration its performance using bms platform. In Proceedings of the 2016 IEEE Transportation Electrification Conference and Expo, Asia-Pacific (ITEC Asia-Pacific), Busan, Korea, 1–4 June 2016; pp. 661–665.
102. Cheng, P.; Zhou, Y.; Song, Z.; Ou, Y. Modeling and soc estimation of lifepo4 battery. In Proceedings of the 2016 IEEE International Conference on Robotics and Biomimetics (ROBIO), Qingdao, China, 3–7 December 2016; pp. 2140–2144.
103. Liu-Henke, X.; Scherler, S.; Jacobitz, S. Verification oriented development of a scalable battery management system for lithium-ion batteries. In Proceedings of the 2017 Twelfth International Conference on Ecological Vehicles and Renewable Energies (EVER), Monte Carlo, Monaco, 11–13 April 2017; pp. 1–7.
104. Xia, X.; Wei, Y. Lithium-ion batteries state-of-charge estimation based on interactive multiple-model extended kalman filter. In Proceedings of the 2016 22nd International Conference on Automation and Computing (ICAC), Colchester, UK, 7–8 September 2016; pp. 204–207.
105. Partovibakhsh, M.; Liu, G. An adaptive unscented kalman filtering approach for online estimation of model parameters and state-of-charge of lithium-ion batteries for autonomous mobile robots. *IEEE Trans. Control Syst. Technol.* **2015**, *23*, 357–363. [[CrossRef](#)]
106. Aung, H.; Low, K.S. Temperature dependent state-of-charge estimation of lithium ion battery using dual spherical unscented kalman filter. *IET Power Electron.* **2015**, *8*, 2026–2033. [[CrossRef](#)]
107. Aung, H.; Low, K.S.; Goh, S.T. State-of-charge estimation of lithium-ion battery using square root spherical unscented kalman filter (sqrt-ukfst) in nanosatellite. *IEEE Trans. Power Electron.* **2015**, *30*, 4774–4783. [[CrossRef](#)]
108. Rozaqi, L.; Rijanto, E. Soc estimation for li-ion battery using optimum rls method based on genetic algorithm. In Proceedings of the 2016 8th International Conference on Information Technology and Electrical Engineering (ICITEE), Yogyakarta, Indonesia, 5–6 October 2016; pp. 1–4.
109. Xiong, R.; Sun, F.; Gong, X.; Gao, C. A data-driven based adaptive state of charge estimator of lithium-ion polymer battery used in electric vehicles. *Appl. Energy* **2014**, *113*, 1421–1433. [[CrossRef](#)]
110. Tang, X.; Liu, B.; Lv, Z.; Gao, F. Observer based battery SOC estimation: Using multi-gain-switching approach. *Appl. Energy* **2017**, *204*, 1275–1283. [[CrossRef](#)]
111. Shen, P.; Ouyang, M.; Lu, L.; Li, J.; Feng, X. The co-estimation of state of charge, state of health and state of function for lithium-ion batteries in electric vehicles. *IEEE Trans. Veh. Technol.* **2017**, *PP*, 1. [[CrossRef](#)]
112. Lim, K.; Bastawrous, H.A.; Duong, V.-H.; See, K.W.; Zhang, P.; Dou, S.X. Fading kalman filter-based real-time state of charge estimation in lifepo4 battery-powered electric vehicles. *Appl. Energy* **2016**, *169*, 40–48. [[CrossRef](#)]

113. Liu, C.Z.; Zhu, Q.; Li, L.; Liu, W.Q.; Wang, L.Y.; Xiong, N.; Wang, X.Y. A state of charge estimation method based on H ∞ observer for switched systems of lithium-ion nickel–manganese–cobalt batteries. *IEEE Trans. Ind. Electron.* **2017**, *64*, 8128–8137. [[CrossRef](#)]
114. Xiong, R.; Yu, Q.; Wang, L.Y.; Lin, C. A novel method to obtain the open circuit voltage for the state of charge of lithium ion batteries in electric vehicles by using h infinity filter. *Appl. Energy* **2017**. [[CrossRef](#)]
115. Chen, C.; Sun, F.; Xiong, R.; He, H. A novel dual h infinity filters based battery parameter and state estimation approach for electric vehicles application. *Energy Procedia* **2016**, *103*, 375–380. [[CrossRef](#)]
116. Fridholm, B.; Nilsson, M.; Wik, T. Robustness comparison of battery state of charge observers for automotive applications. *IFAC Proc. Vol.* **2014**, *47*, 2138–2146. [[CrossRef](#)]
117. Yu, Q.; Xiong, R.; Lin, C. Online estimation of state-of-charge based on the h infinity and unscented kalman filters for lithium ion batteries. *Energy Procedia* **2017**, *105*, 2791–2796. [[CrossRef](#)]
118. He, F.; Shen, W.X.; Kapoor, A.; Honnery, D.; Dayawansa, D. H infinity observer based state of charge estimation for battery packs in electric vehicles. In Proceedings of the 2016 IEEE 11th Conference on Industrial Electronics and Applications (ICIEA), Hefei, China, 5–7 June 2016; pp. 694–699.
119. Lin, C.; Mu, H.; Xiong, R.; Shen, W. A novel multi-model probability battery state of charge estimation approach for electric vehicles using h-infinity algorithm. *Appl. Energy* **2016**, *166*, 76–83. [[CrossRef](#)]
120. Sanchez, L.; Couso, I.; Viera, J.C. Online soc estimation of li-fepo4 batteries through a new fuzzy rule-based recursive filter with feedback of the heat flow rate. In Proceedings of the 2014 IEEE Vehicle Power and Propulsion Conference (VPPC), Coimbra, Portugal, 27–30 October 2014; pp. 1–6.
121. Zhang, S.; Yang, L.; Zhao, X.; Qiang, J. A ga optimization for lithium–ion battery equalization based on soc estimation by nn and flc. *Int. J. Electr. Power Energy Syst.* **2015**, *73*, 318–328. [[CrossRef](#)]
122. Ma, L. Lithium-ion battery life evaluation method based on fuzzy nonlinear accelerated degradation process. In Proceedings of the 2016 10th International Conference on Software, Knowledge, Information Management & Applications (SKIMA), Chengdu, China, 15–17 December 2016; pp. 309–313.
123. Yan, X.; Yang, Y.; Guo, Q.; Zhang, H.; Qu, W. Electric vehicle battery soc estimation based on fuzzy kalman filter. In Proceedings of the 2013 2nd International Symposium on Instrumentation and Measurement, Sensor Network and Automation (IMSNA), Toronto, ON, Canada, 23–24 December 2013; pp. 863–866.
124. Burgos-Mellado, C.; Orchard, M.E.; Kazerani, M.; Cárdenas, R.; Sáez, D. Particle-filtering-based estimation of maximum available power state in lithium-ion batteries. *Appl. Energy* **2016**, *161*, 349–363. [[CrossRef](#)]
125. Li, Y.; Wang, C.; Gong, J. A combination kalman filter approach for state of charge estimation of lithium-ion battery considering model uncertainty. *Energy* **2016**, *109*, 933–946. [[CrossRef](#)]
126. Hametner, C.; Jakubek, S. State of charge estimation for lithium ion cells: Design of experiments, nonlinear identification and fuzzy observer design. *J. Power Sources* **2013**, *238*, 413–421. [[CrossRef](#)]
127. Sheng, H.; Xiao, J. Electric vehicle state of charge estimation: Nonlinear correlation and fuzzy support vector machine. *J. Power Sources* **2015**, *281*, 131–137. [[CrossRef](#)]
128. Zheng, Y.; Ouyang, M.; Lu, L.; Li, J.; Han, X.; Xu, L. On-line equalization for lithium-ion battery packs based on charging cell voltages: Part 2. Fuzzy logic equalization. *J. Power Sources* **2014**, *247*, 460–466. [[CrossRef](#)]
129. Jansen, P.; Gebel, T.; Renner, D.; Vergossen, D.; John, W.; Götze, J. An approach to determine the state of charge of a lithium iron phosphate cell using classification methods based on frequency domain data. In Proceedings of the 8th IET International Conference on Power Electronics, Machines and Drives (PEMD 2016), Glasgow, UK, 19–21 April 2016; pp. 1–6.
130. Zuchang, G.; Chin, C.S.; Wai Lok, W.; Junbo, J.; Wei Da, T. Genetic algorithm based back-propagation neural network approach for fault diagnosis in lithium-ion battery system. In Proceedings of the 2015 6th International Conference on Power Electronics Systems and Applications (PESA), Hong Kong, China, 15–17 December 2015; pp. 1–6.
131. Hussein, A.A. Capacity fade estimation in electric vehicle li-ion batteries using artificial neural networks. *IEEE Trans. Ind. Appl.* **2015**, *51*, 2321–2330. [[CrossRef](#)]
132. Guo, Y.; Zhao, Z.; Huang, L. Soc estimation of lithium battery based on improved bp neural network. *Energy Procedia* **2017**, *105*, 4153–4158. [[CrossRef](#)]
133. Shahriari, M.; Farrokhi, M. Online state-of-health estimation of vrla batteries using state of charge. *IEEE Trans. Ind. Electron.* **2013**, *60*, 191–202. [[CrossRef](#)]
134. Bai, G.; Wang, P.; Hu, C. A self-cognizant dynamic system approach for prognostics and health management. *J. Power Sources* **2015**, *278*, 163–174. [[CrossRef](#)]

135. Wang, Y.; Yang, D.; Zhang, X.; Chen, Z. Probability based remaining capacity estimation using data-driven and neural network model. *J. Power Sources* **2016**, *315*, 199–208. [[CrossRef](#)]
136. Dong, G.; Zhang, X.; Zhang, C.; Chen, Z. A method for state of energy estimation of lithium-ion batteries based on neural network model. *Energy* **2015**, *90*, 879–888. [[CrossRef](#)]
137. Ismail, M.; Dlyma, R.; Elrakaybi, A.; Ahmed, R.; Habibi, S. Battery state of charge estimation using an artificial neural network. In Proceedings of the 2017 IEEE Transportation Electrification Conference and Expo (ITEC), Chicago, IL, USA, 22–24 June 2017; pp. 342–349.
138. Tong, S.; Lacap, J.H.; Park, J.W. Battery state of charge estimation using a load-classifying neural network. *J. Energy Storage* **2016**, *7*, 236–243. [[CrossRef](#)]
139. He, W.; Williard, N.; Chen, C.; Pecht, M. State of charge estimation for li-ion batteries using neural network modeling and unscented kalman filter-based error cancellation. *Int. J. Electr. Power Energy Syst.* **2014**, *62*, 783–791. [[CrossRef](#)]
140. Hussein, A.A. Derivation and comparison of open-loop and closed-loop neural network battery state-of-charge estimators. *Energy Procedia* **2015**, *75*, 1856–1861. [[CrossRef](#)]
141. Kang, L.; Zhao, X.; Ma, J. A new neural network model for the state-of-charge estimation in the battery degradation process. *Appl. Energy* **2014**, *121*, 20–27. [[CrossRef](#)]
142. Yan, Q.; Wang, Y. Predicting for power battery soc based on neural network. In Proceedings of the 2017 36th Chinese Control Conference (CCC), Dalian, China, 26–28 July 2017; pp. 4140–4143.
143. Awadallah, M.A.; Venkatesh, B. Accuracy improvement of soc estimation in lithium-ion batteries. *J. Energy Storage* **2016**, *6*, 95–104. [[CrossRef](#)]
144. Dai, H.; Guo, P.; Wei, X.; Sun, Z.; Wang, J. Anfis (adaptive neuro-fuzzy inference system) based online soc (state of charge) correction considering cell divergence for the ev (electric vehicle) traction batteries. *Energy* **2015**, *80*, 350–360. [[CrossRef](#)]
145. Fotouhi, A.; Propp, K.; Auger, D.J. Electric vehicle battery model identification and state of charge estimation in real world driving cycles. In Proceedings of the 2015 7th Computer Science and Electronic Engineering Conference (CEEC), Colchester, UK, 24–25 September 2015; pp. 243–248.
146. Lin, C.; Zhang, X.; Xiong, R.; Zhou, F. A novel approach to state of charge estimation using extended kalman filtering for lithium-ion batteries in electric vehicles. In Proceedings of the 2014 IEEE Conference and Expo Transportation Electrification Asia-Pacific (ITEC Asia-Pacific), Beijing, China, 31 August–3 September 2014; pp. 1–6.
147. Yang, R.; Xiong, R.; He, H.; Mu, H.; Wang, C. A novel method on estimating the degradation and state of charge of lithium-ion batteries used for electrical vehicles. *Appl. Energy* **2017**. [[CrossRef](#)]
148. Ismail, N.H.F.; Toha, S.F. State of charge estimation of a lithium-ion battery for electric vehicle based on particle swarm optimization. In Proceedings of the 2013 IEEE International Conference on Smart Instrumentation, Measurement and Applications (ICSIMA), Kuala Lumpur, Malaysia, 25–27 November 2013; pp. 1–4.
149. Aung, H.; Low, K.S.; Soon, J.J. State-of-charge estimation using particle swarm optimization with inverse barrier constraint in a nanosatellite. In Proceedings of the 2015 IEEE 10th Conference on Industrial Electronics and Applications (ICIEA), Auckland, New Zealand, 15–17 June 2015; pp. 1–6.
150. Kim, T.; Qiao, W.; Qu, L. Online state of charge and electrical impedance estimation for multicell lithium-ion batteries. In Proceedings of the 2013 IEEE Transportation Electrification Conference and Expo (ITEC), Detroit, MI, USA, 16–19 June 2013; pp. 1–6.
151. Huachun, H.; Haiping, X.; Zengquan, Y.; Yingjie, Z. State of charge estimation of li-ion battery in evs based on second-order sliding mode observer. In Proceedings of the 2014 IEEE Conference and Expo Transportation Electrification Asia-Pacific (ITEC Asia-Pacific), Beijing, China, 31 August–3 September 2014; pp. 1–5.
152. Afshari, H.H.; Attari, M.; Ahmed, R.; Farag, M.; Habibi, S. Modeling, parameterization, and state of charge estimation of li-ion cells using a circuit model. In Proceedings of the 2016 IEEE Transportation Electrification Conference and Expo (ITEC), Dearborn, MI, USA, 27–29 June 2016; pp. 1–6.
153. Wang, W.; Chung, H.S.H.; Zhang, J. Near-real-time parameter estimation of an electrical battery model with multiple time constants and soc-dependent capacitance. In Proceedings of the 2014 IEEE Energy Conversion Congress and Exposition (ECCE), 14–18 September 2014; pp. 3977–3984.

154. Antón, J.C.Á.; Nieto, P.J.G.; Gonzalo, E.G.; Pérez, J.C.V.; Vega, M.G.; Viejo, C.B. A new predictive model for the state-of-charge of a high-power lithium-ion cell based on a pso-optimized multivariate adaptive regression spline approach. *IEEE Trans. Veh. Technol.* **2016**, *65*, 4197–4208. [[CrossRef](#)]
155. Zahid, T.; Qin, F.; Li, W.; Xu, K.; Zhou, Y. Sequential monte carlo based technique for soc estimation of lifepo4 battery pack for electric vehicles. In Proceedings of the 2016 IEEE International Conference on Information and Automation (ICIA), Ningbo, China, 1–3 August 2016; pp. 1308–1312.



© 2017 by the authors. Licensee MDPI, Basel, Switzerland. This article is an open access article distributed under the terms and conditions of the Creative Commons Attribution (CC BY) license (<http://creativecommons.org/licenses/by/4.0/>).

Article

Small Signal Stability of a Balanced Three-Phase AC Microgrid Using Harmonic Linearization: Parametric-Based Analysis

Atta Ur Rahman ^{*,†}, Irtaza Syed and Mukhtar Ullah

Electrical Engineering Department, National University of Computer and Emerging Sciences, Islamabad 44000, Pakistan; irtaza.syed@nu.edu.pk (I.S.); mukhtar.ullah@nu.edu.pk (M.U.)

* Correspondence: atta.rahman@nu.edu.pk; Tel.: +92-334-355-9900

† Current address: Electrical Engineering Department, National University of Computer and Emerging Sciences, Islamabad 44000, Pakistan.

Received: 31 October 2018; Accepted: 17 December 2018; Published: 21 December 2018

Abstract: The growth of power-electronic-based components is inescapable in future distribution grids (DGs). The introduction of these non-linear components poses many challenges, not only in terms of power quality, but also in terms of stability. These challenges become more acute when active loads are behaving as generators and power is flowing in reverse direction. The frequency-domain-based impedance modeling methods are preferred for small signal stability analysis (SSSA) of DGs involving such non-linear components. The harmonic linearization method can be used for impedance estimation, and afterwards, the Nyquist stability criterion can be used for stability analysis. In this paper, a parametric-based stability analysis of grid-connected active loads at the point of common coupling (PCC) is done by changing the parallel clustering distance and size of active loads. The results verify a positive impact on the stability of increasing parallel clustering and distance from the PCC and a negative impact of increasing the size of individual active loads.

Keywords: DC-AC power converters; frequency-domain analysis; impedance-based model; Nyquist stability analysis; small signal stability analysis; harmonic linearization

1. Introduction

Electrical energy is the global source of energy, and every device in the future will eventually switch to the electric source of energy. It is necessary to not only utilize every possible resource of energy, but also make the transmission system as efficient, reliable, and stable as possible. The worldwide integration of renewables and other power electronic (PE)-based resources at distribution grids (DGs) is an effort to meet this ever-increasing energy demand [1–3].

The PE-based components, which are non-linear devices and draw/deliver constant power, have a dominant role in the future DGs [4–7]. It is expected from the PE-based active loads to give support to the grid under the IEEE-1547 grid integration code [8]. These PE-based non-linear devices behave as negative impedances and have a constant power nature, so traditional stability methods are unable to deal with these [9–13]. The growth and clustering of these new PE-based components at or near the point of common coupling (PCC) may lead to the instability of DGs [14–19].

In the frequency domain, the impedance-based modeling methods are used for small signal stability analysis (SSSA), where the impedances are estimated at the PCC to apply the stability criterion. Two frequency domain impedance-based SSSA modeling methods are harmonic linearization (HL) [20–22] and the impedance estimation method used for balanced three-phase system transformation into the synchronous reference frame (SRF) [23–27]. A comparative analysis for different stability analysis techniques is given in Table 1.

Table 1. Comparative analysis of different stability techniques [20,28–33]. SRF, synchronous reference frame.

Model	Disadvantages	Reference
Lyapunov Methods (Time Domain)	A detailed system modeling is required for this method, so it does not work well for complex large systems. Its converter model is unable to capture the harmonic effect.	[28,29,31,33]
Probabilistic Methods (Time Domain)	It requires huge computational effort, so this method is very time consuming. Inaccurate first approximation may lead to faulty conclusions. Not all applied schemes work for complex large systems.	[32]
Phasor Model	It is often not differentiable due to significantly higher dimensions.	[20]
Bifurcation Theory	It is slow in the time domain and more complicated in the frequency domain for a higher order system.	[30]
SRF Method	Limited to only balanced three-phase systems.	[20,33]

In the SRF method, the balanced three-phase shunt current perturbation is used for impedance estimation [24,34–36] with the automated unit as presented in [36,37]. The impedance can be measured in real time with negligible additional cost [21,22,25,38–43] by this method. The limitation of the SRF method is that it can only be used to extract the impedances for balanced three-phase systems. This method is unable to capture harmonic effects. This method does not work for a system that is a combination of single- and a three-phase system. Furthermore, this method cannot be used for such a three-phase system in which one specific phase is heavily loaded as compared to the other phases or for an unbalanced system when a fault or other abnormal conditions occur [20,33]. In these scenarios, the zero-axis component is not zero, so the model cannot be linearized by using the SRF method to extract the impedances [20].

HL can be used without the limitations of SRF and is generally applicable to all kinds of AC systems. It can be used for a balanced three-phase system, a single-phase system, an unbalanced three-phase system having harmonics, and a three-phase system having one phase heavily loaded as compared to the other phases [20,33]. This method decomposes the AC system into linear and time-invariant symmetrical components without cross-coupling between them. Here, HL has many advantages over the other methods.

In this paper, the three-phase harmonic shunt-current-injection technique is used to introduce harmonic current perturbation at the PCC. The resultant harmonic voltage and harmonic current components on the source side and load side respectively are used to estimate the source and load side impedances by using the HL technique.

2. System Modeling Using HL

In this technique, the impedances of the non-linear system are extracted by superimposing a specific harmonic component. Superimposing a specific harmonic component involves two steps: firstly, harmonic perturbation is introduced into the system at the PCC, and secondly, the system response is monitored by using symmetrical components (positive, negative, and zero components).

To estimate the impedances, the perturbation source is switched in at the PCC to inject the perturbations into the system. This perturbation source should have a perturbation magnitude significantly higher than the magnitude level PCC to have an impact at the PCC. Current perturbations are usually preferred because these are used in shunt configuration (as shown in Figure 1) as compared to voltage perturbations used in series configuration [24,34]. There are two basic methods, one based on electronic circuits and the other based on wound rotor induction machines, to switch in shunt current perturbations' source for practical impedance estimation [34]. After injecting the perturbations at the PCC, the corresponding change in the source side and load side parameters (voltages and currents) is measured.

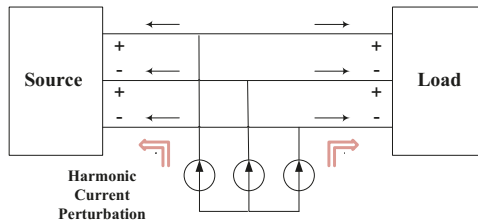


Figure 1. Current perturbation injection in the shunt configuration.

The Nyquist stability criterion (NSC) and/or Bode plot stability criteria are applied after developing the impedance-based model for the stability analysis in the frequency domain. Mostly, NSC is applied to verify the stability of the interconnected systems after extracting the impedances of both sides at the PCC.

The HL technique can deal with the positive and negative components of symmetrical components separately by using the property of linear time-invariant (LTI) systems. The system is stable only if all the components of the sequence domain are stable.

In the HL technique, specific harmonic perturbations are injected at a specific point, usually at the PCC. The old and new values of voltages and currents are measured both at the source side and load side. From the ratio of voltages and currents, the impedances are extracted from both the source and the load side.

This technique estimates the stability of the overall system at the PCC after extracting impedances through symmetrical components by developing a linear model (along a periodically time-varying operation trajectory) of the AC system having non-linear components. This operation trajectory may consist of any single harmonic or a collection of multiple odd harmonics for impedance extraction. The corresponding impedances in the sequence domain are extracted by using the harmonic balance principle [44] and small-signal approximation, assuming that the harmonic perturbation is sufficiently small.

To ensure the power quality and grid stability, it is necessary that the grid interconnection of active loads be carefully examined. The objective of this work is to estimate and establish the pattern of small signal stability (SSS) in relation to the varying sizes, penetration level, and distances of the active loads from the PCC (as shown in Figure 2) to assess the stability of the distribution grid. Figure 2 describes how the size, distance, or penetration is changed for comparative stability analysis.

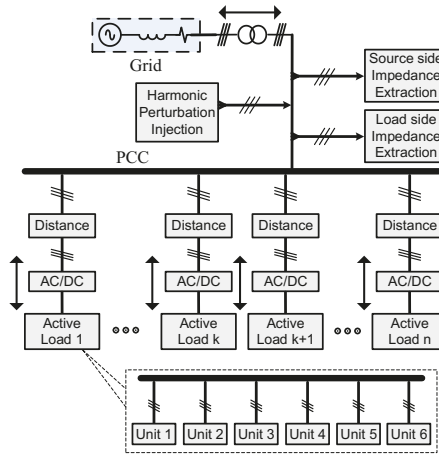


Figure 2. Comparative stability analysis of grid-connected active loads at the point of common coupling (PCC) with changing size, distance, and penetration.

3. Mathematical Modeling of the Impedances at the PCC

By applying the concept of the feedback control system on the simplified power system shown in Figure 3, the transfer function with $V_I(s)$ as output, $V_s(s)$ as input, $Z_1(s)$ as forward gain, and $Z_s(s)$ as reverse gain is given in (1).

$$\frac{[V_I(s)]}{[V_s(s)]} = \frac{1}{1 + [Z_1(s)][Z_s(s)]^{-1}} \tag{1}$$

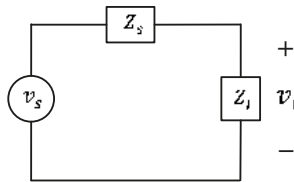


Figure 3. Simplified power system as a feedback control system.

The open loop gain, $L(s)$ can be extracted by rearranging (1) as given in (2).

$$V_I(s) = [1 + [Z_1(s)][Z_s(s)]^{-1}]^{-1}[V_s(s)] \tag{2}$$

The stability can be determined by applying the NSC and only observing the Nyquist contour of the open loop transfer function, as given in (3).

$$L(s) = [Z_1(s)][Z_s(s)]^{-1} \tag{3}$$

The transfer function of this power system can be determined in terms of input voltage V_s and output voltage V_I , as shown in (4), where the term 012 (zero-positive-negative) represents that the quantities are in the HL.

$$\frac{V_{I(012)}(s)}{V_{s(012)}(s)} = \frac{1}{1 + [Z_{I(012)}(s)][Z_{s(012)}(s)]^{-1}} \tag{4}$$

This can be rearranged as given by (5) to extract the open loop gain $L(s)$ to apply the NSC on the open loop gain in (3).

$$V_{l(012)}(s) = \frac{V_{s(012)}(s)}{1 + [Z_{l(012)}(s)][Z_{s(012)}(s)]^{-1}} \tag{5}$$

Since the HL technique uses the symmetrical components for stability analysis, therefore relations are expressed in terms of the symmetrical components.

By increasing the parallel clustering of the active loads, at a specific frequency, the effective value of the load side impedance decreases at the PCC as shown in Figure 4 and as given by (6), where Z_a is the impedance of non-linear active loads connected at the PCC.

$$\frac{1}{Z_a} = \frac{1}{Z_{a1}} + \frac{1}{Z_{a2}} + \frac{1}{Z_{a3}} + \frac{1}{Z_{a4}} + \dots + \frac{1}{Z_{an}} \tag{6}$$

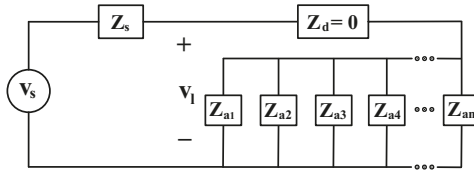


Figure 4. The effect of increasing penetration on load side impedance.

The total load side impedance Z_l can be expressed as given by (7).

$$Z_l = Z_d + Z_a \tag{7}$$

On the other hand, by increasing serial clustering (size) at the PCC, at a specific frequency, the effective value of load side impedance Z_l increases, as shown in Figure 5 and as given by (8).

$$Z_l = Z_{a1} + Z_{a2} + Z_{a3} + Z_{a4} + \dots + Z_{an} + Z_d \tag{8}$$

If (8) is compared with (7), it is clear that the value of $Z_a = Z_{a1} + Z_{a2} + Z_{a3} + Z_{a4} + \dots + Z_{an}$ is increasing with size while Z_d remains constant.

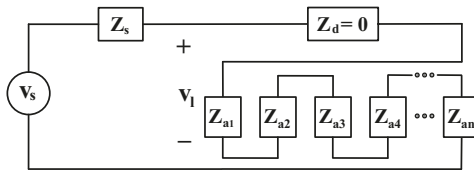


Figure 5. Effect of increasing the size on load side impedance.

Finally, by increasing the distance from the PCC, at a specific frequency, the effective value of the load side impedance Z_l decreases. This is because as the distance increases, the contribution of non-linear active load impedance in total series impedance decreases, as shown in Figure 6 and as given by (9).

$$Z_l = Z_{d1} + Z_{d2} + Z_{d3} + Z_{d4} + \dots + Z_{dn} + Z_a \tag{9}$$

If (9) is compared with (7), it is clear that the value of $Z_d = Z_{d1} + Z_{d2} + Z_{d3} + Z_{d4} + \dots + Z_{dn}$ is increasing with distance, while Z_a remains constant.

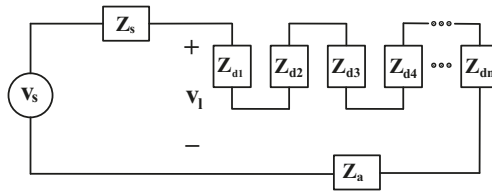


Figure 6. Effect of increasing distance from the PCC on load side impedance.

In the impedance-based method, the perturbations are injected into the distribution system with the perturbation injection point dividing the system into two parts. The part with larger AC sources is called the source side, and the other part is called the load side.

The first step to determine the impedance is to superimpose the harmonic perturbation over the fundamental carrier signal. Then, the second step is to determine the resultant change in the response of that specific harmonic component at the frequency of interest. The fundamental or any other single harmonic, as well as multiple harmonics can be superimposed on the original power wave to extract the impedances. The current perturbations are injected into the system in shunt, as shown in Figure 1. Three-phase AC voltage and current are converted into symmetrical components at the point of injection. The source and load impedances are then extracted using the ratio of voltage and current at the extraction point. The impedance extracted from the ratio of symmetrical components of voltage and currents can be directly used for stability analysis. A typical impedance measurement setup is shown in Figure 7.

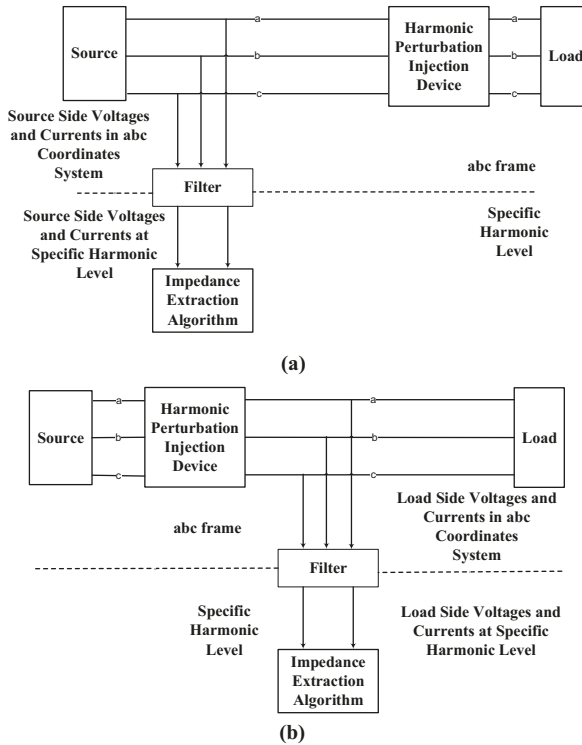


Figure 7. Impedance measurement setup for the (a) source side and (b) load side.

The load and source side impedance matrix in symmetrical components are given by (10) and (11):

$$\left[Z_{l(012)} \right]_{3 \times 3} = \begin{bmatrix} Z_{l(00)} & Z_{l(01)} & Z_{l(02)} \\ Z_{l(10)} & Z_{l(11)} & Z_{l(12)} \\ Z_{l(20)} & Z_{l(21)} & Z_{l(22)} \end{bmatrix} \quad (10)$$

$$\left[Z_{s(012)} \right]_{3 \times 3} = \begin{bmatrix} Z_{s(00)} & Z_{s(01)} & Z_{s(02)} \\ Z_{s(10)} & Z_{s(11)} & Z_{s(12)} \\ Z_{s(20)} & Z_{s(21)} & Z_{s(22)} \end{bmatrix} \quad (11)$$

The relation between voltage and current in symmetrical components on the load side is given by (12) for a balanced three-phase system.

$$\left[V_{l(012)} \right]_{3 \times 1} = \left[Z_{l(012)} \right]_{3 \times 3} \left[I_{l(012)} \right]_{3 \times 1} \quad (12)$$

The perturbations are introduced at the PCC to build nine full equations based on a 3×3 impedance matrix for both the source side and the load side. A single perturbation can generate only three equations (for both the source and load side) [45]. At least three perturbations are introduced to build full 3×3 impedance matrices for the source and the load side. Voltages on the load side in HL after first perturbation are given by (13):

$$\left[V_{l(012)}^1 \right]_{3 \times 1} = \left[Z_{l(012)} \right]_{3 \times 3} \left[I_{l(012)}^1 \right]_{3 \times 1} \quad (13)$$

The voltages in HL on the load side after the second perturbation are given by (14):

$$\left[V_{l(012)}^2 \right]_{3 \times 1} = \left[Z_{l(012)} \right]_{3 \times 3} \left[I_{l(012)}^2 \right]_{3 \times 1} \quad (14)$$

The voltages in HL on the load side after the third perturbation are given by (15):

$$\left[V_{l(012)}^3 \right]_{3 \times 1} = \left[Z_{l(012)} \right]_{3 \times 3} \left[I_{l(012)}^3 \right]_{3 \times 1} \quad (15)$$

Equations (13)–(15) can be written in combined form as (16).

$$\left[V_{l(012)} \right]_{3 \times 3} = \left[Z_{l(012)} \right]_{3 \times 3} \left[I_{l(012)} \right]_{3 \times 3} \quad (16)$$

Rearranging (16) results in (17),

$$\left[Z_{l(012)} \right]_{3 \times 3} = \left[V_{l(012)} \right]_{3 \times 3} \left[I_{l(012)} \right]_{3 \times 3}^{-1} \quad (17)$$

Similarly, for the source side, (17) can be rewritten as (18):

$$\left[Z_{s(012)} \right]_{3 \times 3} = \left[V_{s(012)} \right]_{3 \times 3} \left[I_{s(012)} \right]_{3 \times 3}^{-1} \quad (18)$$

The unknown impedances can be found through simulation or the experiment-based impedance method.

4. Simulation Results

The Simulink model of the grid-connected PV systems (shown in Figure 8) was used for stability analysis.

The detail of the system parameters is tabulated in Table 2. In this model, different PV systems, each having a rating of 100 kW, were integrated with PCC. In this configuration, each unit of the PV system consisted of 100 kW, and the size of the active load may consist of multiple units. To achieve the objective of comparative analysis, it was assumed that all the PV systems were working at the same temperature and receiving the same amount of irradiance. The stability at the PCC was evaluated against three different indices. These three indices were;

1. First, stability was assessed by changing the parallel clustering (penetration) of grid-connected active loads.
2. Then, the stability was evaluated by changing the distance of active loads from the PCC.
3. Afterwards, the stability at the PCC was assessed by changing the serial clustering (size) of active loads.

These parameters were changed one by one, and the corresponding change in load side impedance at the PCC was recorded. Then, NSC was applied on the load side and source side impedance in each of the above cases. The corresponding Nyquist plots were drawn against different specific values of these parameters. The objective was to assess how varying these parameter affected the stability at the PCC.

Table 2. Parameters at the PCC for different penetrations of active loads.

Parameter	Symbol	Value	Symbol	Value
Power Source	P	2500 MVA	V	120 kV
Line Section	$R[r_1]$	[0.1153]	$L[r_1]$	$[1.05 \times 10^{-3}]$
Line Section	$R[r_0]$	[0.413]	$L[r_0]$	$[3.32 \times 10^{-3}]$
Industrial Load	P	30 MW	Q	2 MVar
Residential Load 1	P	2 MW	Q	0
Residential Load 2	P	100 kW	Q	0

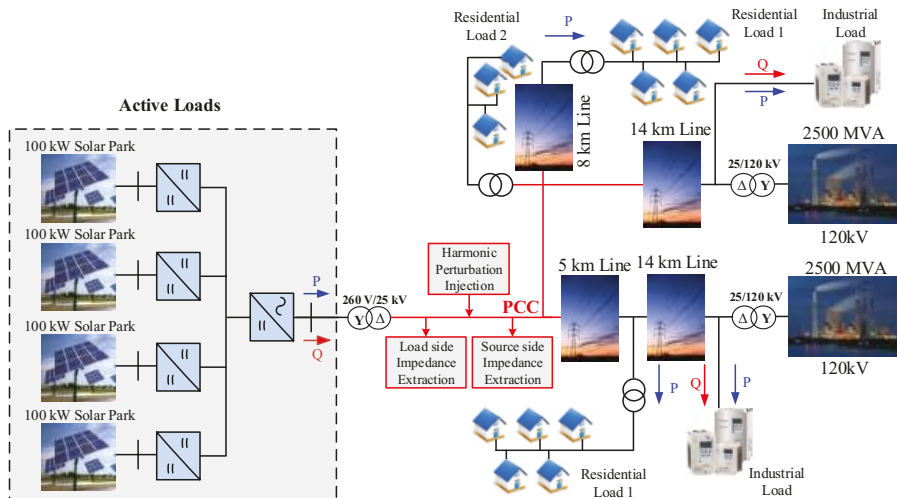
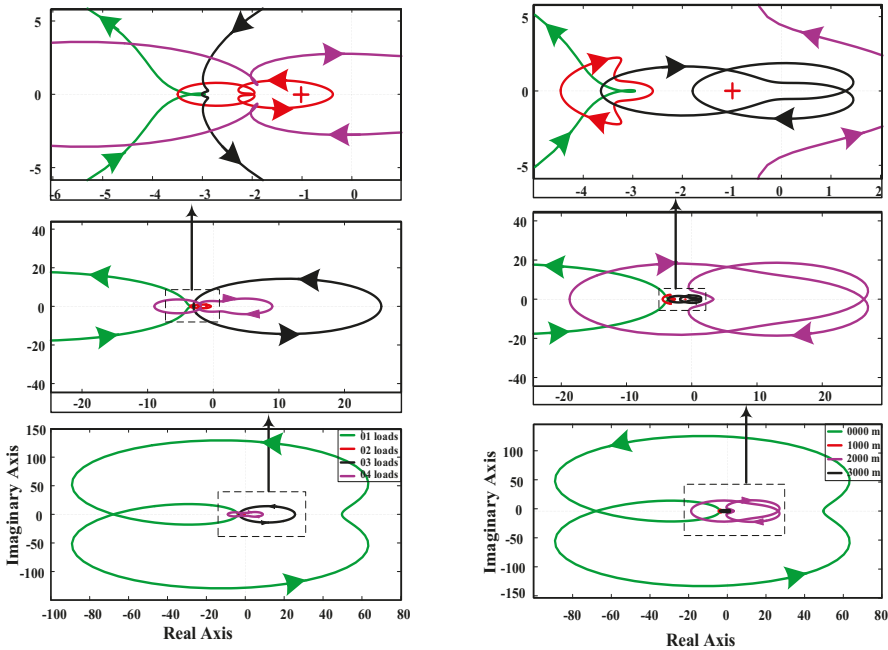


Figure 8. Simulink model of grid-connected active Loads.

The dynamic models of grid-connected active loads were developed and designed in MATLAB Simulink. The block diagram of the grid-connected active loads is shown in Figure 2 where PCC was working at a 25-kV voltage rating. Figure 2 describes how the size, distance, or penetration was changed for comparative stability analysis.

4.1. Effect of Penetration

The first objective was to check the stability pattern at the PCC against various penetrations. The penetration of active loads was varied in a systematic way, and the corresponding change in load side impedance was recorded. The resultant Nyquist plots for different values of parallel clustering by keeping the distance and size constant are shown in a single plot in Figure 9a.



(a) Nyquist plot for different penetrations. (b) Nyquist plot for different distances from PCC.

Figure 9. Nyquist plot for different penetrations and distances.

It is clear from these plots that as the parallel clustering increased, the anti-clockwise encirclements of -1 vanished. The anti-clockwise encirclements of -1 depicted the total number of closed loop poles in the right half plane, which caused the instability of the system. When the anti-clockwise encirclements of -1 vanished, the system became stable. The microgrid system was designed in such a way that the PCC was working at a stability boundary for different indices. Therefore, as the system indices were changed near the PCC, the system changed from unstable to stable or vice versa. Not all of the Nyquist plot is clearly visible to the naked eye, so the selected parts of the lower Nyquist plots are zoomed-in and shown above for better and clear understanding of the Nyquist plots. The system at the PCC was unstable when only a single active load (of size 700 kW i.e., seven units) was connected at the PCC (distance = 0 km). The Nyquist plot of one active load depicted an anti-clockwise encirclement, as shown in the lower part of Figure 9a. Similarly, the system at the PCC was still unstable when two and three active loads were connected respectively at the PCC in parallel configuration, as shown in the zoomed-in version of Figure 9a. When the parallel clustering reached the four active loads,

keeping size and distance unchanged, the system at the PCC became stable. The stability would further improve by increasing the penetration at the PCC by keeping the distance and size constant.

4.2. Effect of Distance from PCC

To check the effect of the distance of active loads from the PCC to the stability at the PCC, the distance of active load was varied by keeping the penetration and size constant. The objective of selecting a specific penetration and a specific size was to keep the PCC near the stability boundary. The penetration of one active load and the size of seven units (700 kW) were chosen in this case. The load side impedance was recorded by changing the distance from the PCC by keeping the penetration and size constant in all the cases. The NSC was applied on the load and the source side impedances to get the Nyquist plot for different values of distances, as shown in Figure 9b.

The results show that the system was unstable at the PCC when the distance was 0 km because there was a pole in the right half plane (anti-clockwise encirclement of -1). As the distance was increased to 1 km, the anti-clockwise encirclement vanished (as shown in the zoomed-in version of the Nyquist plots), so the system became stable at the PCC. This stability further improved as the distance increased to 2 km and 3 km, respectively, by keeping the size and penetration constant.

4.3. Effect of the Sizes of Active Loads

To check the effect of changing the size of an active load on the stability at the PCC, the size was varied by keeping the distance and penetration constant. A single active load was connected at the PCC in this case, so the distance was 0 km and the penetration was one active load. The load side impedance changed by changing the size. Different Nyquist plots were obtained when NSC was applied on different values of load side impedances and the same value of source side impedance. These Nyquist plots, each corresponding to different sizes of an active load, are shown in Figure 10.

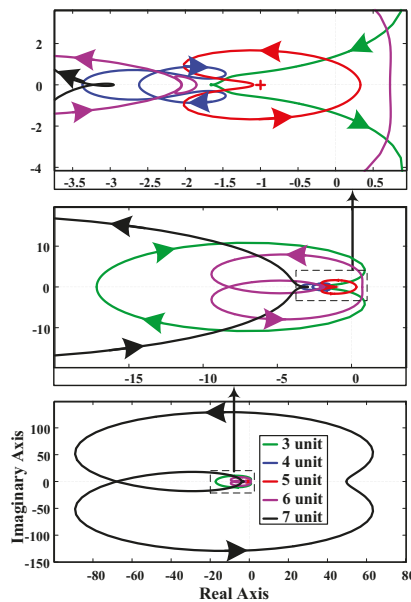


Figure 10. Nyquist plot for different sizes of active loads.

Initially, the system was stable at the PCC, as there were no anti-clockwise encirclements of -1 , which depicts that there were no poles in the right half plane. The system remained stable when the

size of active loads was equal to or less than four units (400 kW). As the size of the system reached five units (500 kW), the system became unstable, and there was an anti-clockwise encirclement of -1 , which depicts a pole in the right half plane. The stability further deteriorated as the size was increased further.

The summary of the above three cases is given in Table 3. According to this table, when the size was increased by keeping other parameters constant, the stability at the PCC deteriorated. When the distance was increased from the PCC by keeping other parameters constant, the stability at the PCC improved.

When the penetration was increased at the PCC by keeping the distance and size constant, the stability at the PCC improved. The stability behavior at the PCC by changing the size, distance, and penetration is given in Figure 11. Figure 11 depicts the stability region in connection with size, distance, and penetration. Firstly, keeping distance (=0 km) and penetration (=1) constant, the instability boundary for size was six units. As the size decreased, the stability improved. The direction of the arrow shows the stability behavior (from the unstable to stable region and from the stable to more stable region). Secondly, keeping distance (=0 km) and size (=7 units) constant, the instability boundary for penetration was one active load. The direction of the arrow shows the stability behavior, so as the penetration increased, the stability improved further. Finally, keeping size (=7 units) and penetration (=1) constant, the instability boundary for distance was 0 km. As the distance increased, the stability improved further. These results verified that there was a strong relation between these parameters and the stability at the PCC. Changing any other system components, the stability boundary would shift, but the behavior of the stability and the relation to these parameters will remain the same.

Table 3. Effect of different parameters on stability.

Penetration	Distance at PCC	Size	Effect on Stability
Increasing	Constant	Constant	Improve
Constant	Increasing	Constant	Improve
Constant	Constant	Increasing	Deteriorate

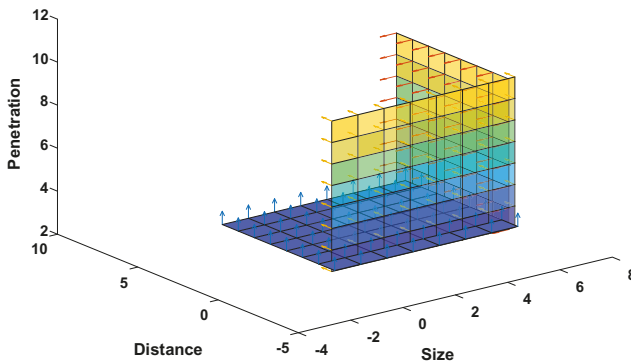


Figure 11. The stability behavior at the PCC for different sizes, distances, and penetrations.

The simulation results presented were near the stability boundary. These results and stability boundaries were only specific for the system designed for simulation. Changing the system would change the stability boundary because impedance would change. However, the relation of different parameters with the Nyquist stability would remain the same.

5. Conclusions

In this paper, the SSSA at the PCC was done by varying one of three parameters (size distance and penetration) and keeping the other two constant. The results show that the stability pattern of NSC changes in a systematic way in response to a systematic change in any of these parameters. The impact of increasing penetration and increasing distance from the PCC was positive on the stability at the PCC, while the impact of increasing the size (while keeping the other parameters constant) was negative on the stability at the PCC. Thus, a change in any of these parameters will play a significant role in deciding the stability at the PCC.

The design and composition, as well as the distance from the PCC of active loads play an important role in the SSS of an AC microgrid. These parameters must be thoroughly assessed before deploying active loads at the PCC.

Author Contributions: Conceptualization, A.U.R. and I.S.; Methodology, A.U.R. and I.S.; Software, A.U.R. and M.U.; Validation, A.U.R. and M.U.; Formal analysis, A.U.R. and I.S.; Investigation, A.U.R.; Writing original draft preparation, A.U.R.; Writing review and editing, I.S. and M.U.; Supervision, I.S.; Project administration, M.U.

Funding: This research received no external funding.

Conflicts of Interest: The authors declare no conflict of interest.

References

1. Siddique, M.N.; Ahmad, A.; Nawaz, M.K.; Bukhari, S.B.A. Optimal integration of hybrid (wind-solar) system with diesel power plant using HOMER. *Turk. J. Electr. Eng. Comput. Sci.* **2015**, *23*, 1547–1557. [\[CrossRef\]](#)
2. Matos, E.O.D.; Soares, T.M.; Bezerra, U.H.; De Tostes, L.M.E.; Rodrigo, A.; Manito, A.; Cordeiro, B.C., Jr. Using linear and non-parametric regression models to describe the contribution of non-linear loads on the voltage harmonic distortions in the electrical grid. *IET Gener. Transm. Distrib.* **2016**, *10*, 1825–1832. [\[CrossRef\]](#)
3. Li, Y.W.; He, J. Distribution System Harmonic Compensation Methods: An Overview of DG-Interfacing Inverters. *IEEE Ind. Electron. Mag.* **2014**, *8*, 18–31. [\[CrossRef\]](#)
4. Bhattacharyya, S.; Cobben, S.; Ribeiro, P.; Kling, W. Harmonic emission limits and responsibilities at a point of connection. *IET Gener. Transm. Distrib.* **2012**, *6*, 256–264. [\[CrossRef\]](#)
5. Wildrick, C.; Lee, F.; Cho, B.; Choi, B. A method of defining the load impedance specification for a stable distributed power system. In Proceedings of the IEEE Power Electronics Specialist Conference PESC '93, Seattle, WA, USA, 20–24 June 1993; pp. 826–832.
6. Khaligh, A.; Rahimi, A.; Emadi, A. Negative Impedance Stabilizing Pulse Adjustment Control Technique for DC/DC Converters Operating in Discontinuous Conduction Mode and Driving Constant Power Loads. *IEEE Trans. Veh. Technol.* **2007**, *56*, 2005–2016. [\[CrossRef\]](#)
7. Emadi, A.; Ehsani, M. Negative impedance stabilizing controls for pwm Dc-Dc converters using feedback linearization techniques. In Proceedings of the 35th Intersociety Energy Conversion Engineering Conference and Exhibit (Cat. No.00CH37022), Las Vegas, NV, USA, 24–28 July 2000; Volume 1, pp. 613–620.
8. Preda, T.; Uhlen, K.; Nordgård, D.E. An overview of the present grid codes for integration of distributed generation. In Proceedings of the CIRED 2012 Workshop: Integration of Renewables into the Distribution Grid, Lisbon, Portugal, 29–30 May 2012; pp. 1–4.
9. Sudhoff, S.; Corzine, K.; Glover, S.; Hegner, H.; Robey, H. DC link stabilized field oriented control of electric propulsion systems. *IEEE Trans. Energy Convers.* **1998**, *13*, 27–33. [\[CrossRef\]](#)
10. Emadi, A.; Khaligh, A.; Rivetta, C.; Williamson, G. Constant Power Loads and Negative Impedance Instability in Automotive Systems: Definition, Modeling, Stability, and Control of Power Electronic Converters and Motor Drives. *IEEE Trans. Veh. Technol.* **2006**, *55*, 1112–1125. [\[CrossRef\]](#)
11. Feng, X.; Liu, J.; Lee, F. Impedance Specifications for Stable DC Distributed Power Systems. *IEEE Trans. Power Electron.* **2002**, *17*, 157–162. [\[CrossRef\]](#)
12. Belkhat, M.; Cooley, R.; Witulski, A. Large Signal Stability Criteria For Distributed Systems with Constant Power Loads. In Proceedings of the PESC '95 - Power Electronics Specialist Conference, Atlanta, GA, USA, 18–22 June 1995; pp. 1333–1338.

13. Liserre, M.; Teodorescu, R.; Blaabjerg, F. Stability of photovoltaic and wind turbine grid-connected inverters for a large set of grid impedance values. *IEEE Trans. Power Electron.* **2006**, *21*, 263–272. [[CrossRef](#)]
14. Liu, J.; Feng, X.; Lee, F.; Boroyevich, D. Stability margin monitoring for DC distributed power systems via current/voltage perturbation. In Proceedings of the Sixteenth Annual IEEE Applied Power Electronics Conference and Exposition APEC 2001 (Cat. No.01CH37181), Anaheim, CA, USA, 4–8 March 2001; Volume 2, pp. 745–751.
15. Grigore, V.; Hatonen, J.; Kyyra, J.; Suntio, T. Dynamics of a buck converter with a constant power load. In Proceedings of the PESC 98 Record. 29th Annual IEEE Power Electronics Specialists Conference (Cat. No.98CH36196), Fukuoka, Japan, 22 May 1998; Volume 1, pp. 72–78.
16. Chen, M.; Sun, J. Low-Frequency Input Impedance Modeling of Boost Single-Phase PFC Converters. *IEEE Trans. Power Electron.* **2007**, *22*, 1402–1409. [[CrossRef](#)]
17. Prodic, A. Compensator Design and Stability Assessment for Fast Voltage Loops of Power Factor Correction Rectifiers. *IEEE Trans. Power Electron.* **2007**, *22*, 1719–1730. [[CrossRef](#)]
18. Mithulananthan, N.; Kumar Saha, T.; Chidurala, A. Harmonic impact of high penetration photovoltaic system on unbalanced distribution networks—Learning from an urban photovoltaic network. *IET Renew. Power Gener.* **2016**, *10*, 485–494.
19. He, J.; Li, Y.W.; Munir, M.S. A Flexible Harmonic Control Approach Through Voltage-Controlled DG-Grid Interfacing Converters. *IEEE Trans. Ind. Electron.* **2012**, *59*, 444–455. [[CrossRef](#)]
20. Sun, J. Small-signal methods for AC distributed power systems—A review. *IEEE Trans. Power Electron.* **2009**, *24*, 2545–2554.
21. Cespedes, M.; Sun, J. Adaptive Control of Grid-Connected Inverters Based on Online Grid Impedance Measurements. *IEEE Trans. Sustain. Energy* **2014**, *5*, 516–523. [[CrossRef](#)]
22. Roinila, T.; Vilkkko, M.; Sun, J. Online Grid Impedance Measurement Using Discrete-Interval Binary Sequence Injection. *IEEE J. Emerg. Sel. Top. Power Electron.* **2014**, *2*, 985–993. [[CrossRef](#)]
23. Belkhaty, M. Stability Criteria for AC Power Systems with Regulated Loads. Ph.D. Thesis, Purdue University, West Lafayette, IN, USA, 1997.
24. Francis, G.; Burgos, R.; Boroyevich, D.; Wang, F.; Karimi, K. An Algorithm and Implementation System for Measuring Impedance in the D-Q Domain. In Proceedings of the 2011 IEEE Energy Conversion Congress and Exposition, Phoenix, AZ, USA, 17–22 September 2011; pp. 3221–3228.
25. Wen, B.; Dong, D.; Boroyevich, D.; Burgos, R.; Mattavelli, P.; Shen, Z. Impedance-Based Analysis of Grid-Synchronization Stability for Three-Phase Paralleled Converters. *IEEE Trans. Power Electron.* **2016**, *31*, 26–38. [[CrossRef](#)]
26. Valdivia, V.; Lazaro, A.; Barrado, A.; Zumel, P.; Fernandez, C.; Sanz, M. Black-Box Modeling of Three-Phase Voltage Source Inverters for System-Level Analysis. *IEEE Trans. Ind. Electron.* **2012**, *59*, 3648–3662. [[CrossRef](#)]
27. Rygg, A.; Molinas, M.; Zhang, C.; Cai, X. A Modified Sequence-Domain Impedance Definition and Its Equivalence to the dq-Domain Impedance Definition for the Stability Analysis of AC Power Electronic Systems. *IEEE J. Emerg. Sel. Top. Power Electron.* **2016**, *4*, 1383–1396. [[CrossRef](#)]
28. Kundur, P. *Power System Stability and Control*; McGraw-Hill: New York, NY, USA, 1994.
29. Yao, Z.; Therond, P.G.; Davat, B. Stability analysis of power systems by the generalised nyquist criterion. In Proceedings of the 1994 International Conference on Control Control '94, Coventry, UK, 21–24 March 1994; pp. 739–744.
30. Guanrong, C.; Moiola, J.L. *Hopf Bifurcation Analysis: A Frequency Domain Approach*; World Scientific: Singapore, 1996.
31. Sanchez, S. Stability Investigation of Power Electronics Systems: A Microgrid Case. Ph.D. Thesis, Norwegian University of Science and Technology, Trondheim, Norway, 2015.
32. Xu, Q.; Member, S.; Ma, F.; Luo, A.; Member, S. Analysis and Control of M3C based UPQC for Power Quality Improvement in Medium/High Voltage Power Grid. *IEEE Trans. Power Electron.* **2016**, *31*, 8182–8194. [[CrossRef](#)]
33. Amin, M.; Molinas, M. Small-Signal Stability Assessment of Power Electronics based Power Systems: A Discussion of Impedance and Eigenvalue-based Methods. *IEEE Trans. Ind. Appl.* **2017**, *53*, 5014–5030. [[CrossRef](#)]
34. Familant, Y.A.; Huang, J.; Corzine, K.A.; Belkhaty, M. New Techniques for Measuring Impedance Characteristics of Three-Phase AC Power Systems. *IEEE Trans. Power Electron.* **2009**, *24*, 1802–1810. [[CrossRef](#)]

35. Valdivia, V.; Lázaro, A.; Barrado, A.; Zumel, P.; Fernández, C.; Sanz, M. Impedance Identification Procedure of Three-Phase Balanced Voltage Source Inverters Based on Transient Response Measurements. *IEEE Trans. Power Electron.* **2011**, *26*, 3810–3816. [[CrossRef](#)]
36. Shen, Z.; Jaksic, M.; Mattavelli, P.; Boroyevich, D.; Verhulst, J.; Belkhat, M. Design and implementation of three-phase AC impedance measurement unit (IMU) with series and shunt injection. In Proceedings of the 2013 Twenty-Eighth Annual IEEE Applied Power Electronics Conference and Exposition (APEC), Long Beach, CA, USA, 17–21 March 2013; pp. 2674–2681.
37. Shen, Z.; Jaksic, M.; Mattavelli, P.; Boroyevich, D.; Verhulst, J. Three-phase AC system impedance measurement unit (IMU) using chirp signal injection. In Proceedings of the 2013 Twenty-Eighth Annual IEEE Applied Power Electronics Conference and Exposition (APEC), Long Beach, CA, USA, 17–21 March 2013; pp. 2666–2673.
38. Wen, B.; Boroyevich, D.; Burgos, R.; Mattavelli, P.; Shen, Z. Small-Signal Stability Analysis of Three-Phase AC Systems in the Presence of Constant Power Loads Based on Measured D-Q Frame Impedances. *IEEE Trans. Power Electron.* **2015**, *30*, 5952–5963. [[CrossRef](#)]
39. Dong, D.; Wen, B.; Boroyevich, D.; Mattavelli, P.; Xue, Y. Analysis of Phase-Locked Loop Low-Frequency Stability in Three-Phase Grid-Connected Power Converters Considering Impedance Interactions. *IEEE Trans. Ind. Electron.* **2015**, *62*, 310–321. [[CrossRef](#)]
40. Cespedes, M.; Sun, J. Impedance Modeling and Analysis of Grid-Connected Voltage-Source Converters. *IEEE Trans. Power Electron.* **2014**, *29*, 1254–1261. [[CrossRef](#)]
41. Wen, B.; Boroyevich, D.; Burgos, R.; Mattavelli, P.; Shen, Z. Analysis of D-Q Small-Signal Impedance of Grid-Tied Inverters. *IEEE Trans. Power Electron.* **2016**, *31*, 675–687. [[CrossRef](#)]
42. Hoffmann, N.; Fuchs, F.W. Minimal Invasive Equivalent Grid Impedance Estimation in Inductive-Resistive Power Networks Using Extended Kalman Filter. *IEEE Trans. Power Electron.* **2014**, *29*, 631–641. [[CrossRef](#)]
43. Xiao, P.; Venayagamoorthy, G.K.; Corzine, K.A.; Huang, J. Recurrent Neural Networks Based Impedance Measurement Technique for Power Electronic Systems. *IEEE Trans. Power Electron.* **2010**, *25*, 382–390. [[CrossRef](#)]
44. Gelb, A.; Velde, W.E.V. *Multiple-Input Describing Functions and Nonlinear System Design*; McGraw-Hill: New York, NY, USA, 1968.
45. Shen, Z.; Jaksic, M.; Zhou, B.; Mattavelli, P.; Boroyevich, D.; Verhulst, J.; Belkhat, M. Analysis of Phase Locked Loop (PLL) influence on dq impedance measurement in three-phase AC systems. In Proceedings of the 2013 Twenty-Eighth Annual IEEE Applied Power Electronics Conference and Exposition (APEC), Long Beach, CA, USA, 17–21 March 2013; pp. 939–945.



© 2018 by the authors. Licensee MDPI, Basel, Switzerland. This article is an open access article distributed under the terms and conditions of the Creative Commons Attribution (CC BY) license (<http://creativecommons.org/licenses/by/4.0/>).

Article

Energy Management and Switching Control of PHEV Charging Stations in a Hybrid Smart Micro-Grid System

Tariq Kamal ^{1,2,*}, Murat Karabacak ², Syed Zulqadar Hassan ³, Luis M. Fernández-Ramírez ¹, Muhammad Tanveer Riaz ³, Muhammad Abbas Khan ⁵ and Laiq Khan ⁶

¹ Research Group in Electrical Technologies for Sustainable and Renewable Energy (PAIDI-TEP-023), Department of Electrical Engineering, University of Cadiz, Higher Polytechnic School of Algeciras, 11202 Algeciras (Cadiz), Spain; luis.fernandez@uca.es

² Department of Electrical and Electronics Engineering, Sakarya University, 54050 Sakarya, Turkey; muratkarabacak@sakarya.edu.tr

³ State Key Laboratory of Power Transmission Equipment and System Security and New Technology, School of Electrical Engineering, Chongqing University, 400044 Chongqing, China; syedzulqadar.hassan.pk@ieee.org (S.Z.H.); tanveer.riaz@ieee.org (M.T.R.)

⁴ Department of Electrical Engineering, Lahore University of Management Sciences (LUMS), 54792 Lahore, Pakistan; hussnainriaz8@gmail.com

⁵ School of Electronics and Information Engineering, Changchun University of Science and Technology, Jilin 130022, China; engineerabbaskhan111@gmail.com

⁶ Department of Electrical Engineering, COMSATS Institute of Information Technology, 22060 Abbottabad, Pakistan; laiq@ciit.net.pk

* Correspondence: tariq.kamal.pk@ieee.org; Tel.: +90-536-6375731

Received: 30 June 2018; Accepted: 20 August 2018; Published: 22 August 2018

Abstract: In this study, the energy management and switching control of plug-in hybrid electric vehicles (PHEVs) in a hybrid smart micro-grid system was designed. The charging station in this research consists of real market PHEVs of different companies with different sizes. The rate of charging of PHEVs is managed via switching control to receive maximum benefits from renewable energy sources and reduce the consumption of electricity from the grid. To support the optimum utilization of sustainable power, charging time and network stability, seven scenarios were developed for different interaction among the proposed micro-grid system and PHEVs. The proposed hybrid smart micro-grid system consists of three renewable energy sources: photovoltaic (PV) array controlled via an intelligent fuzzy control maximum power point subsystem, a fuel cell stack and a microturbine set controlled by proportional integral differential/proportional integral subsystems. A hybrid energy storage system (super-capacitor, battery storage bank and hydrogen) and residential load are also included in the proposed architecture. The hybrid smart micro-grid system is checked in terms of voltage regulation, frequency deviation and total harmonic distortion (THD). It was found that these are in limits according to the international standards. The simulations verify the feasibility of the proposed system and fulfill the requirement of vehicle-to-grid and grid-to-vehicle operations in a smart grid environment.

Keywords: plug-in hybrid electric vehicles; power management system; renewable energy sources; fuzzy; smart micro-grid

1. Introduction

Due to environmental concerns, depletion of fossil fuels, and advances in battery storage system, PHEVs have received a great amount of attention in the transportation sector [1,2]. These days, the

world is looking towards renewable energy sources such as solar, wind and biomass to produce green energy. This green energy can be utilized by vehicles which are considered the main sources of environmental pollution. For example, 33.7% of greenhouse gas emissions were released by the transportation sector to the environment in 2012 [3]. Similarly, many American Lung Association projects have stated [4] that the transportation sector is responsible for numerous lung diseases in America. Consequently, transport industries have introduced low emission vehicles such as PHEVs to directly address these problems. Therefore, each year, the purchase of PHEV increases worldwide. In the future, many Electric Vehicles (EVs) will be available in the transportation sector. For example, in 2015, approximately one million PHEVs were on US roads and 425,000 PHEVs were sold [5,6]. Furthermore, the Electric Power Research Institute have concluded that the PHEVs market share may reach up to 62% by 2050 in the US [7]. In the US, there are about 250 million registered vehicles. Using a moderate scenario since 2020, if the US vehicle fleet is 10% PHEVs and each vehicle uses 25 kWh battery capacity, the total 625 GWh would be a potential threat to today's utility.

The first electric vehicle was sold in Turkey in 2012 [8]. The electric vehicle market in Turkey is now growing very rapidly. According to the Ministry of Science, Industry and Technology of Turkey, PHEVs will become the dominant vehicle choice on the road soon in Turkey. The increasing of PHEVs could burden the existing utility, which can result power losses at the customers end. Specifically, uncontrolled charging can cause grid stability problems on the local scale. Pakistan under Rahmat Group company has signed an agreement with two different Chinese companies to introduce EVs in Pakistan [9]. In the initial stage, the companies will introduce electric buses in the transport market, and in the second phase, a factory would be established at the complex in Jamshoro District of Sindh, Pakistan to produce electric cars and two-wheelers. According to the Energy Conservation Center belonging to the Ministry of Water and Power of Pakistan, the transport sector represents 28% of the total energy consumption in Pakistan. In the Pakistan scenario reported on 30 June 2015, the gap between electricity demand and supply was 5201 MW [10]. Currently, Pakistan is suffering from severe energy crisis, where urban and rural areas are not powered by proper electricity for 8–12 h and 18 h per day, respectively. There is a growing risk that the proliferation of EVs will trigger extreme surges in demand in Pakistan. This cannot be ignored, especially in Pakistan, and therefore, it is imperative to design a Charging Station (CS) setup powered from Renewable Energy Sources (RESs) coupled with smart charging strategies.

Generally, vehicles are supposed to stay for at least 5 h per day in workplace [11]. Hence, making electric CS in a given workplace is beneficial, but the result would be some overloading issues particularly at the distribution level. Since the upgrading of transformer is an inflexible and a quite expensive option, this concern needs close concentration. Many authors in the literature have studied the effect of PHEVs charging on the distribution transformer [12–14]. In [12], the authors discussed the impact of PHEVs on distribution networks, but there is no analytical calculation in the paper. In [13], the authors analyzed the concerns due to the integration of PHEV on the residential distribution networks; however, in this study, the number of PHEVs per distribution transformer was limited to two. The authors concluded in [14] that the power management of the EV battery charge profile can help manage the loss of life of the distribution transformer. However, not much work has been done to charge the PHEVs from several RESs in a smart micro-grid.

Although there are a few published papers about CSs for PHEV supplied by PV [15–18], they present certain limitations. For instance, the control of the PV system was not studied in [15–18]. Further, in all these papers, the authors designed the CSs based on the control of DC-link voltage, but the DC-link voltage has its own limitation and the authors did not consider the control of DC-link voltage when it reaches its maximum limit. Similarly, several authors focused on the residential distribution networks [19–21]. In [22,23], the authors described the overall peak demand due to the charging of EVs. They suggested that it should be managed effectively with proper load management. Smart control strategies that can open the paths for PV systems and EVs to integrate with the current power systems are suggested in [24]. The charging of PHEVs from PV system and its co-benefits are discussed in [25]. The study explains that PV provides an auspicious source of mid-day generation power for PHEVs while PHEVs perform as a

dispatchable load. In another paper, the authors showed that high scale integration of EVs in the existing utility would be possible through management and scheduling [26]. The significance of EVs operating as an energy storage source is studied in [27]. There are three types of charging methods for PHEVs/EVs: Alternating Current (AC) level-1, AC level-2 and Direct Current (DC) level-3 charging. DC charging allows boosting the overall efficiency and providing the opportunity of fast charging [28–30]. The same concept is also supported in [31,32]. This sets it up appropriately to mix distributed renewable power generations such as PV, fuel cells, wind and other energy storage devices such as super-capacitor (SC) using the DC distribution bus (bus is an electrical node, which can be in DC or AC, where two or more electrical elements, such as loads, generators, etc., meet). Different DC charging station infrastructures have been presented by many authors [33,34].

The integration of PHEVs in municipal parking deck using smart energy management system is developed in [35]. The energy management system is there to control provision of energy to the vehicle battery chargers through real time monitoring to secure the maximum consumption of available power from sustainable energy and charging time. None of the papers reviewed provide an intelligent control, power electronics interface and power management of PHEVs in smart micro-grid system, where the primary energy source is controlled efficiently. None of those reviewed studies consider the real weather characteristics, but many researchers have developed charging station using virtual generated weather patterns. Moreover, the intelligent control of a renewable energy source is very important for a stable DC bus voltage. For instance, fluctuations in bus voltage cause power imbalance that originate from different sources of disturbances such as sudden change in solar irradiance or temperature, and abrupt change in PHEVs load. Such a power imbalance results an extra energy. The above-mentioned papers do not discuss the control of photovoltaic in their charging station which is essential for maximum efficiency.

This paper intends a proper power management for different PHEV models in a hybrid smart micro-grid system where the required power for the PHEVs charging is smartly managed from solar, hydrogen energy (fuel cell), natural gas (micro-turbine), SC, battery and grid. The operation of the charging algorithm is performed using dynamic power switches of the power converters controlled via proportional integral differential/proportional integral subsystems. The highly intermittent nature of PV in the proposed hybrid smart micro-grid system is addressed by an isolated intelligent fuzzy inference subsystem. The intelligent fuzzy inference subsystem contributes to minimize the stress on the DC bus and ensures quality and regulated output power to CS. If the power sent by the PV is in excess of the requirement of the PHEVs charging, the remaining power will be supplied to charge the battery and then the SC. If still there is an excess power, then it will be used to produce hydrogen for fuel cell or sent to a national grid. Correspondingly, if the net power provided by the PV is less than the demand, the battery and then the SC will be used to deliver the required power provided their SoC > 20%. If the requirement surpasses the power provided by the combination of PV/SC/battery, the difference is provided by the fuel cell. If there is still a need, the difference will be covered by the Micro-turbine (MT), followed by the national grid. In addition, the proposed CS also comprises of a Battery Storage System (BSS) as supplementary power sources to store the power in off peak hours, which can be used in rush hours to charge the PHEVs or provide to the grid.

This work is arranged as follows: Section 2 gives the description of the proposed hybrid smart micro-grid system. The control of the systems components is described in Section 3. The problem formulation of the proposed work is presented in Section 4. Section 5 deals with the proposed power management. Section 6 supports the performance of the proposed system via simulations, followed by a conclusion in Section 7.

2. System Description

Figure 1 shows the proposed system configuration combining PV system, FC system, SC module and battery bank to form a combine DC bus line by four different non-isolated DC-DC converters. The PV system is taken as the primary power source; SC module and battery bank serves as a short-term storage system; and the Solid Oxide Fuel Cell (SOFC) is used as a backup and long-term storage system [36]. The additional power with respect to the load requirement is used for the battery,

SC charging and hydrogen production for later use in the SOFC. The output of the DC bus link is combined through a three-phase main inverter to supply the desired power to the grid if only one source is accessible. On the other hand, the PHEVs/EVs CS, MT, residential load and utility grid are integrated to form an AC bus line. The MT also behaves as a backup to take full advantage of RESs, while the CS acts as either load under the Grid-to-Vehicle (G2V) concept or distributed sources of energy under the Vehicle-to-Grid (V2G) revenue opportunity [37]. The MT interface consists of a rectifier followed by a unidirectional hysteresis current control inverter. A bidirectional inverter is used for power sending and receiving from the CS towards an AC bus link. The CS is designed to charge five PHEVs and BSS. The PHEVs are selected from five different companies. The grid attachment is used to accomplish any charging demand more than the RESs output. The development of all energy sources are according to Table 1 and taken from [38–42].

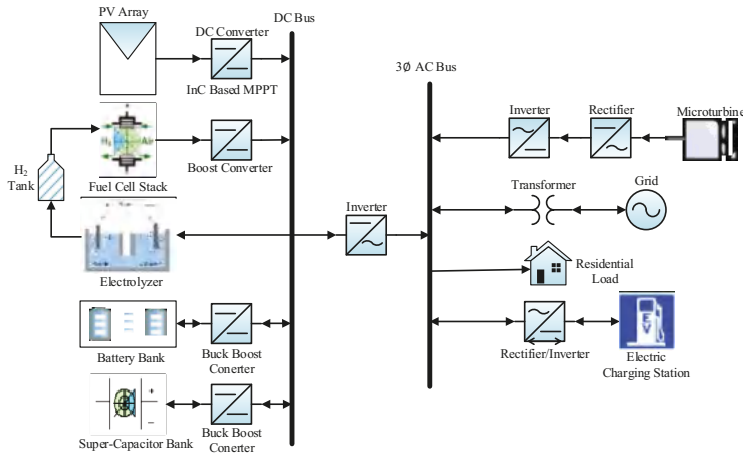


Figure 1. Proposed hybrid smart micro-grid system.

Table 1. RESs and their power converter parameters [36,38,42–44].

PV Array		Battery	
Type	SunPower SPR-305-WHT	Type	CINCO FM/BB12100T
Module	305 W @ 1 kW/m ² , 25 °C	Capacity	50 Ah
Number of series/string	13	Single module voltage	12 V
Number of parallel strings	66	No of series connected modules	34
Power Rating	305 × 13 × 66 ≈ 262 kW	Rated Voltage	12 × 34 ≈ 400 V
Supercapacitor		Fuel Cell Array	
Type	Maxwell Boost Cap BMOD0165-48.6VUC	Type	Bloom Energy USA ES-5700
Capacitance	165 F	Number of cells in series in the stack	768
Number of series capacitors	50	SOFC Stack	4 kW
Number of parallel capacitors	20	SOFC Array	5 × 10 = 50
No of modules	12	SOFC Array Power Rating	50 × 4 kW = 200 kW
Rated Voltage	12 × 48.6 ≈ 584 V		
Electrolyzer		Microturbine	
Type	QualeanQL-85000	Type	Ingersoll Rand MT250
Rated Power	30 kW	Rated Power	200 kVA, 160 kW
Rated Voltage	380 V	Rated Voltage	440 V
Number of Cells in Stack	30	Rated Frequency	50 Hz
Utility Grid		Main Inverter	
Phase Voltage	11 kV	Type	Zhejiang, China CHZIRI-2VF
Rated Power	10 MVA	Rated Power	400 kW
Phase Frequency	50 Hz	Rated Voltage	200/540 V

3. Architecture and Control of the Proposed Charging Station

Figure 2 illustrates a detailed structure of the proposed CS, which is located in Pakistan. The major components of CS are the PHEVs, BSS, power converters and the power management controller. A Power Management System (PMS) monitors all the PHEVs and BSS. The algorithm implemented in the PMS senses the State of Charge (SOC), rated charging power of the PHEVs batteries, the peak and off-peak hours, and controls the power flow in the CS, as given in Figure 2. The SoC level provides information about the charging and discharging of the PHEVs/EVs and BSS.

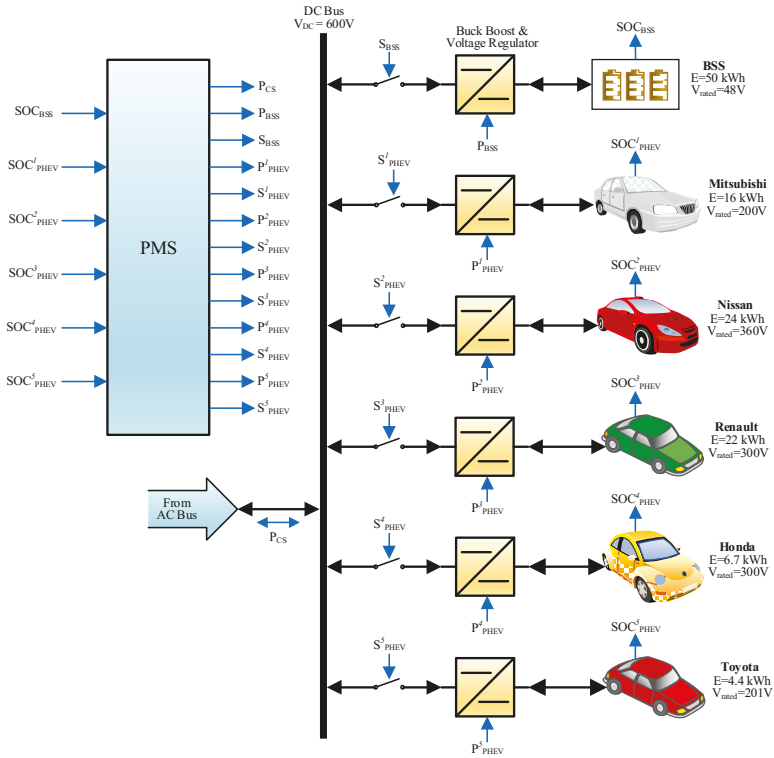


Figure 2. Structure of electric charging station.

The PMS also consists of a Battery Management System (BMS) which prevents the PHEVs and BSS from getting overcharged. The BSS also supports the charging of the PHEVs when there is no power available from the AC bus link. The battery bank in the BSS can be charged from the AC bus link during off peak hours.

Five different types of PHEVs/EVs are considered: Mitsubishi i-MiEV, Kangoo Z.E, Toyota Prius plug-in, Nissan leaf, Honda Accord Hybrid and Renault. Their respective usable battery capacity and charging information is listed in Table 2. Since the PHEVs/EVs are from different automobile manufacturers, their control approach and BSS are based on the charging requirements of each PHEV and BSS. Each PHEV and BSS must have an autonomous buck-boost converter fitted in each charge point in the proposed CS. All the buck-boost converters of the CS are controlled by conventional Proportional Integral Differential (PID) controllers, as shown in Figure 3, and their parameters are given in Table 3.

Table 2. PHEVs technical details [45–49].

Company Name	Vehicle Name	Battery Type	Battery Capacity (kWh)	Range (km)	Charging Rate (kW)		Rated Voltage (V)	Charging Time	
					Slow	Fast		Slow	Fast
Mitsubishi	MiEV	Li-ion	16.0	160	3	50	20	7 h	30 min
Nissan	Leaf	Li-ion	24.0	160	6.6	50	360	4 h	30 min
Renault	Kangoo Z.E.	Li-ion	22.0	170	3	43	300	6 h	30 min
Honda	Civic hybrid	Li-ion	6.7	150	2.2	13.4	300	3 h	30 min
Toyota	Prius	Li-ion	4.4	16	1	8	201	5 h	30 min

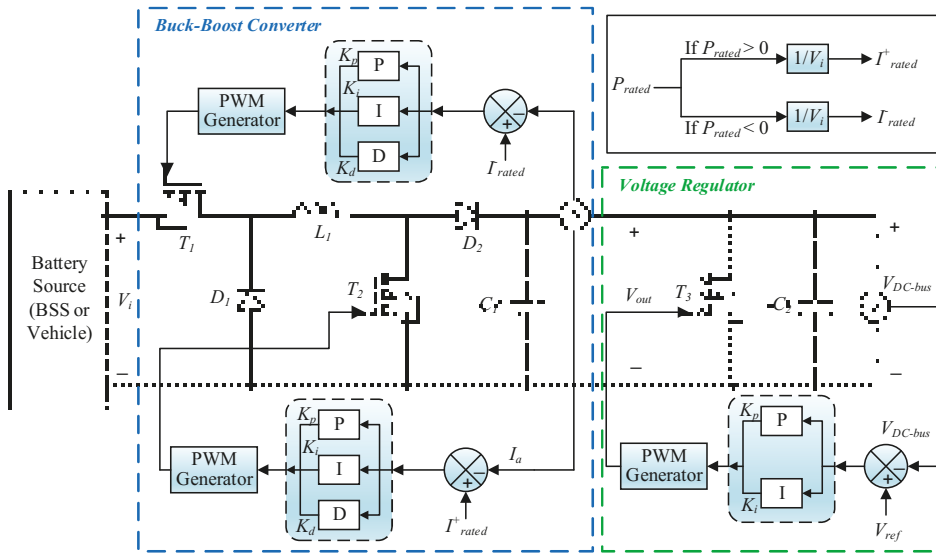


Figure 3. Schematic diagram of a buck boost converter/voltage regulator.

The output of the overall charging station is coupled to the AC bus via a bidirectional inverter-controlled hysteresis current control embedded with PI controllers, as illustrated in Figure 4, whose parameters are shown in Table 1. The PI controllers try to reduce the error to adjust the desired active and the reactive powers. It is assumed that all vehicles have equal market penetration and the analysis is considered for a 24-h cycle for a typical summer day in Pakistan. The proposed architecture is flexible and multiple PHEVs can be charged by increasing the corresponding charging points. Furthermore, the DC-DC boost converter based on the intelligent fuzzy controller is used to exactly track the MPP of the PV, as shown in Figure 5. The intelligent fuzzy controller is modeled using expert knowledge and many inputs. Based on those inputs, the fuzzy rules are defined in the Fuzzy Logic Controller (FLC). A FLC operates in three steps: a fuzzifier to express the crisp value of inputs into their respective fuzzy sets, an inference system to generate appropriate output also in the form of fuzzy sets, and a De-fuzzifier to give the original crisp value through conversion theorems (i.e., center of area). Similarly, a DC-DC boost converter based on PI control is used to control the FC voltage.

Table 3. Buck boost/voltage regulator parameters of the charging station.

Parameter	Representation	Values
CS DC Buck Boost Converter		
Model Type	NCP1136	
V_{rated}	Rated Voltage	10/700 V
C_1	Converter Capacitance	2200 μ F
L_1	Converter Inductance	1 mH
K_p, K_i, K_d	PID Gains (T_1)	1.5, 1, 1
K_p, K_i, K_d	Proportional Gain (T_2)	1.5, 1, 1
f	Rated Switching Frequency	10 kHz
CS DC Voltage Regulator		
Model Type	MC33363ADWG	
V_{rated}	Rated Voltage	10/700 V
C_2	Converter Capacitance	4700 μ F
K_p	Proportional Gain	0.0005
K_i	Integral Gain	0.15
f	Rated Switching Frequency	10 kHz
CS Converter		
Model Type	Zhejiang, China CHZIRI-2VF	
P_{rated}	Rated Power	220 kW
V_{rated}	Rated Voltage	220/1140 V
f_c	Carrier Frequency	10 k Ω
f_{out}	Frequency of Output Voltage	50 Hz
C_s	Snubber Capacitance	100 k Ω
R_s	Snubber Resistance	10 k Ω
L	Inductance L-Filter	2.6 μ H

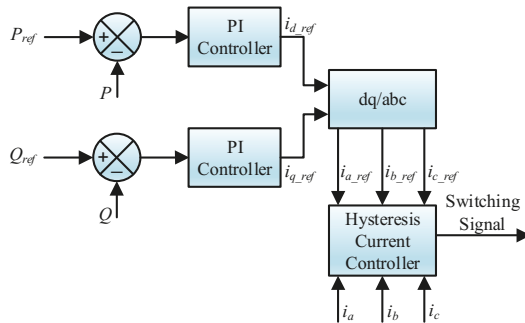


Figure 4. Schematic diagram of charging station converter control.

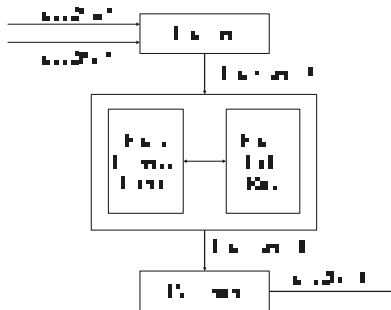


Figure 5. Fuzzy logic controller model.

4. Problem Formulation

In this paper, the objective is to design a decision-making control algorithm for the PHEVs CS by using the available resources (renewable energy, utility grid) for the PHEVs charging, while reducing the stress on the utility grid and satisfying the required demand of all PHEVs and BSS. Equation (1) represents the formulation for the PHEVs CS. According to Equation (1), the actual power level of all vehicles and BSS must reach their reference level within the desired time provided the charging constraints of all PHEVs/EVs and BSS according to Table 2. The power quality and network constraints are according to international standards such as IEC61000 and IEEE 519-2014. Pakistan’s LV power network is considered in this work.

$$\begin{aligned}
 & \cup \left[\begin{array}{l} PHEV_{i=5} \\ BSS \end{array} \right] \Big|_{t \rightarrow \infty} \left[\begin{array}{l} P_{PHEV_{i=5}}(t) \rightarrow P_{PHEV_{i=5_ref}}(t) \\ P_{BSS}(t) \rightarrow P_{BSS_ref}(t) \end{array} \right] \\
 & \text{s.t :} \\
 & \quad SOC_{i,\min} \leq SOC_i(t) \leq SOC_{i,\max} \\
 & \quad 0 \leq |SOC(t+1) - SOC(t)| \leq \Delta SOC_{i,\max} \\
 & \quad V_{\min-load(rms)} \leq V_{load(rms)} \leq V_{\max-load(rms)} \\
 & \quad THD_{\min-vload} \leq THD_{vst}, THD_{\min-iload} \leq THD_{ist} \\
 & \quad f_{\min-vfund} < f_{vload} < f_{\max-vfund}
 \end{aligned} \tag{1}$$

where $SOC_{i,\min}$ and $SOC_{i,\max}$ are the user-defined minimum and maximum battery SOC limits for the i th PHEV/EV. Once SOC_i reaches $SOC_{i,\max}$, the i th battery charger switches to a stand-by mode to avoid the overcharging of the PHEV/EV battery. To prevent large variations in the charging rate over consecutive time slots, the SoC ramp rate is bounded by the constraint $\Delta SOC_{i,\max}$. $V_{loadrms}$ is the RMS voltage at the customer side; THD_{vst} and THD_{ist} are the acceptable value of total harmonic distortion in voltage and current, respectively; and $f_{\min-vfund}$ and $f_{\max-vfund}$ are the allowable limits in the load voltage frequency deviation.

5. Proposed Power Management System for PHEVs/EVs

There are two main buses: DC and AC bus. The PHEVs/EVs CS is the major part of the AC bus. Therefore, the bidirectional power flow between the CSs and the rest of the system, especially with the grid, occurs via AC bus. The overall PMS consists of seven possible scenarios considered for a 24-h cycle as depicted in Figure 6. Five PHEVs/EVs and BSS are the main actors which take part in the PMS. Before explaining the PMS, one must know the following points which are considered during the simulation.

- For the PHEVs charging, the PMS must to take power from BSS rather than the AC bus.
- Similarly, in the case of discharging of PHEVs, first BSS then the AC bus is used to take power from the PHEVs.
- The PHEV owner will decide how much power he wants to transfer or receive.

5.1. Proposed Scenarios for the Charging Station PMS

To develop a proper power management at a CS, several possible scenarios are taken for one complete day depending on the user preference and interest, as shown in Table 4. In a real-time scenario, the power flow between grid and PHEVs depend upon the mutual understanding between them.

Table 4. Possible scenarios.

Scenario	Description
1	No Cars in the CS (Empty CS)
2	Vehicles to AC bus
3	AC bus to Vehicles
4	BSS to AC bus
5	AC bus to BSS
6	BSS to Vehicles
7	Vehicles to BSS

5.1.1. Scenario 1 (No Cars in the CS or Empty CS)

This scenario was considered the normal situation. PHEVs are not present in the CS for charging and BSS is fully charged.

5.1.2. Scenario 2 (Vehicles to AC Bus Line)

This case is the most likely and creates a promising opportunity in the form of V2G or Vehicle-to-Home (V2H). In this scenario, the PMS first checks the availability of the charged PHEVs and the BSS. If the charged PHEVs are available and are programmed to discharge their power and the SoC of BSS is also greater than 90%, then the controller will allow the PHEVs to discharge to the AC bus. This power is further transmitted to the grid or to the load. The owners of the PHEVs will decide how much they discharge their PHEVs, which is automatically accomplished by the controller.

5.1.3. Scenario 3 (AC Bus to Vehicles)

In this situation, the controller first checks the SoC of the BSS. If the BSS is not available for PHEV charging, then the AC bus power is used to charge the PHEVs. It is imperative to show that the maximum power for the AC bus comes from RESs.

5.1.4. Scenario 4 (BSS to AC Bus)

It is also possible that there are no PHEVs in the CS and BSS is charged. The PMS controller will allow the charged BSS to supply its power to the AC bus. Depending upon the choice, the power could be transmitted to the grid or directly to the residential load. Regardless, it will reduce the overall stress on the grid.

5.1.5. Scenario 5 (AC Bus to BSS)

This case is considered for the off-peak time. According to the proposed PMS, if there are no PHEVs and all other loads are satisfied, then the AC bus will supply power to the BSS. The charged BSS will reduce the burden on the grid during peak times.

5.1.6. Scenario 6 (BSS to Vehicles)

Those PHEVs that want to be charged from the BSS are covered in this mode. The proposed PMS will allow the charged BSS to satisfy the required demands of the PHEVs.

5.1.7. Scenario 7 (Vehicles to BSS)

In this case, the controller will allow the PHEV to transfer power to the BSS. All seven scenarios are explained well during simulation.

6. Simulation Results

To evaluate the proposed PMS, simulations were performed in MATLAB/Simulink and the modes of operation are verified. The simulation started at midnight and finished at midnight the next day, on 22 July 2017, in Islamabad, Pakistan. The simulation was performed on an hourly basis for the energy available from the RESs, utility grid and accordingly manages the charging demand of PHEVs/EVs and demand of residential load. The goal was to observe the response of the proposed system over a long period of time including day and night cases. The PHEV/EV battery SOC was used to calculate the charging time and charging energy when the vehicles enter the charging station.

It is important to mention that level 3 (DC fast charging) was used to charge the PHEVs/EVs in this simulation. On fast charging, the vehicle battery takes approximately 30 min to fully charge. The data used for simulation are shown in Table 2. The PV output power obtained by the fuzzy controller is shown in Figure 7. The individual powers available from the PV, SOFC, MT, SC module and the battery bank are shown in Figure 8. The total available power from the different energy sources and the total demand including residential load, CS load and utility grid are shown in Figure 9. To make the discussion simple, the net power available from the PV, SOFC, MT, SC module and the battery bank is represented by P-RESs.

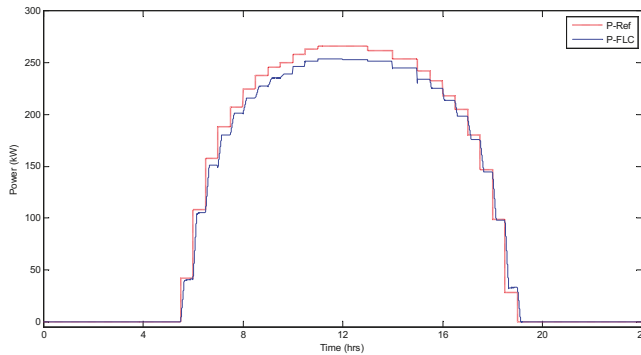


Figure 7. PV output power.

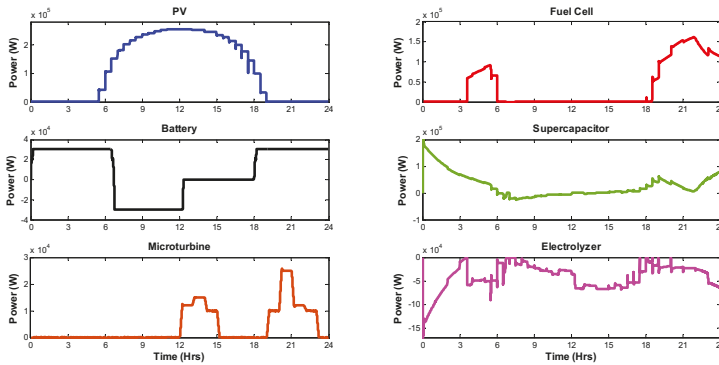


Figure 8. Individual powers of RESs.

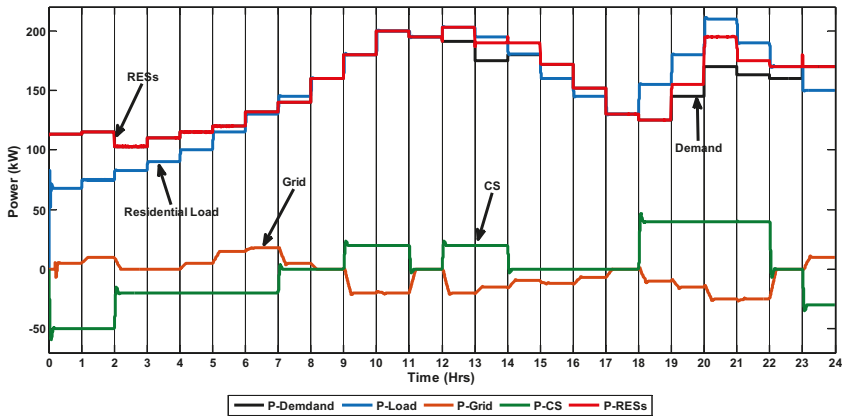


Figure 9. Power of all the energy sources and total demand in the proposed micro-grid.

During $t = 0-2$ h, it is obvious that the power delivered by the RESs exactly satisfies the total demand. The CS is receiving power from both the RESs and grid, but a higher share of power comes from the RESs, viz., the total demand of the CS in this interval is 100 kW in which the RESs' share is 85 kW, while the utility grid provides 15 kW. In addition, it is noticeable that at this interval there is no PHEVs/EVs present for the charging, therefore the total power received from the AC bus is used to charge the BSS through DC-DC converter and its SOC increases from 40% to 60% (Scenario 5) as shown in Figures 10a and 11. The charged BSS could help to reduce the stress on the grid during the peak times. During $t = 2-4$ h, the CS need 40 kW power which is completely provided by RESs. This power is utilized to charge the Mitsubishi i-MiEV and Nissan leaf vehicles and their batteries' SoCs go from 50% to 65% and 30% to 90%, respectively (Scenario 3, Figure 10b,c). Most of the vehicles come for charging at night due to the normal or low electricity price which could be used in rush hours under the V2G scheme, e.g., during $t = 4-7$ h, Toyota Prius plug-in, Honda Accord Hybrid and Renault Kangoo Z.E vehicles are charged from the AC bus. A total of 60 kW power is utilized to charge all these three vehicles. Among 60 kW, the RESs contribute 38 kW, while the grid provides 22 kW.

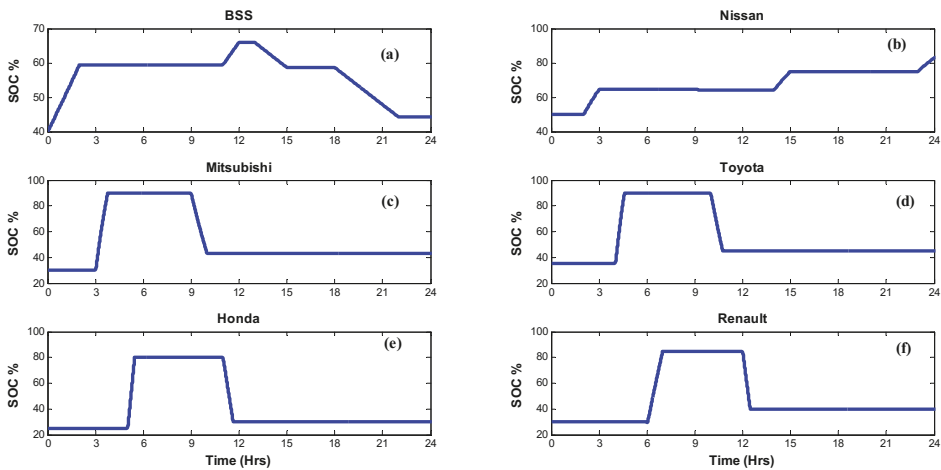


Figure 10. State of charge of the BSS and PHEVs.



Figure 11. SOC of the BSS/PHEVs and CS power using the proposed PMS.

The charging station demand is zero during $t = 7-9$ h (Scenario 1), hence, both the RESs and utility grid are used to meet the residential load demand. Some of the discharged PHEVs/EVs want to discharge under the revenue opportunity scheme during peak times. For example, during $t = 9-11$ h, Mitsubishi i-MiEV and Toyota Prius plug-in supply 40 kW power combined to the AC bus (Scenario 2), which is then transferred to the grid through the CS inverter, as shown in Figure 10b,c and Figure 11.

Similarly, Renault Kangoo Z.E provides 20 kW to the AC bus during $t = 12-13$ h, which is completely transferred to the utility grid because the RESs satisfy the residential load, as shown in Figure 9. During $t = 13-14$ h, the residential demand increases and needs 5 kW. According to the PMS, the required power is provided from the BSS. A total of 20 kW is transferred from the BSS to the AC bus and thus the SoC decreases from 66% to 62% (Scenario 5). Out of 20 kW, the residential load utilizes 5 kW, while the remaining 15 kW is sent to the utility grid via the CS inverter and thus the total demand decreases.

Those PHEVs that want to be charged from the BSS are covered during $t = 14-15$ h, viz., Nissan leaf has received power from the BSS (Scenario 6) and it increases from 65% to 75%, as shown in Figure 10a,b and Figure 11. In this interval, the RESs first satisfy the residential load demand while the remaining 10 kW power is sent to the utility grid. The demand of the CS is zero during $t = 15-18$ h, therefore the RESs meet the residential load while the remaining excess power, i.e., 19 kW, is sent to the utility grid. Figure 9 shows that the peak hours occur during $t = 18-22$ h, viz., the residential load is at peak, the utility grid cannot provide the power due to the rush hours, and the RESs cannot meet the residential load; therefore, the BSS provides 160 kW power to the AC bus. The AC bus then provides 85 kW to the grid while the remaining 75 kW power is utilized to satisfy the residential load demand. Similarly, Scenarios 1 and 3 are repeated during $t = 22-23$ h and $t = 23-24$ h, respectively.

The power quality and grid stability parameters such as RMS load voltage, load frequency and net power at AC bus are shown in Figures 12 and 13. The net power on the AC bus is zero, which indicates that the overall system and grid are stable. The RMS load voltage, load frequency deviation and DC bus voltage deviation are in limits according to the IEC61000 and IEEE 519-2014 standards.

The proposed PMS based on FLC is also compared with that based on PID controllers. Figure 14 illustrates the changes in the DC bus voltage obtained by both PMSs. The simulation results show that the proposed FLC (denoted as black) has a faster response, smaller overshoot and maintains better DC bus voltage compared to the standard PID controller (denoted as red).

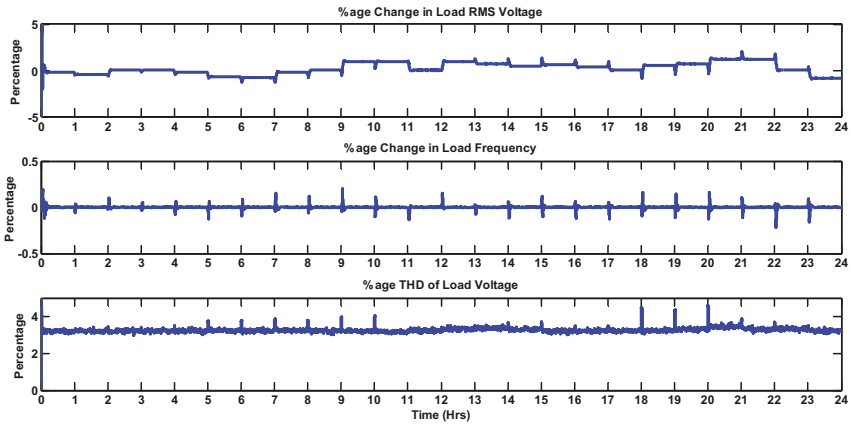


Figure 12. Power quality parameters.

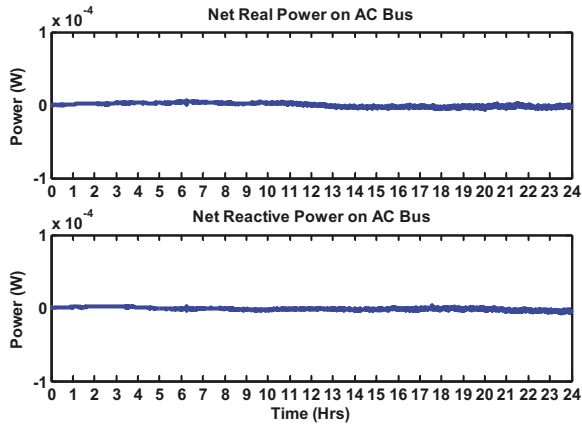


Figure 13. Grid stability parameters.

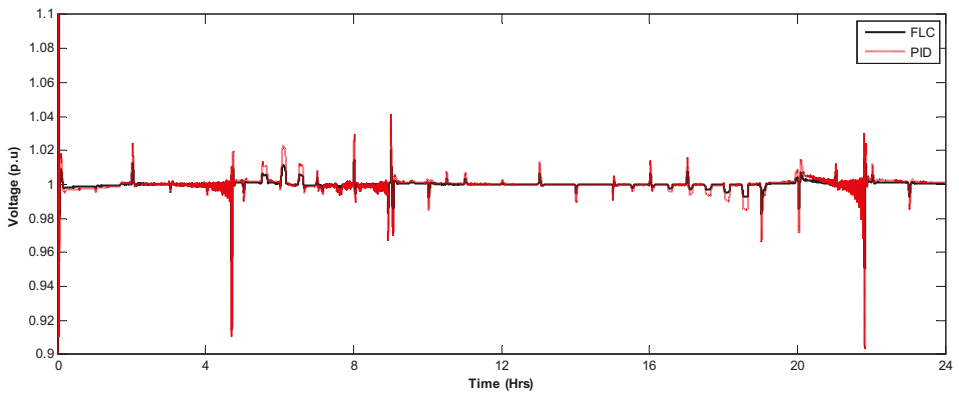


Figure 14. DC bus voltage deviation: PMS based on FLC versus PMS based on PID controllers.

7. Conclusions

Without proper management, the penetration of PHEVs in the transportation sector can cause a burden on the distribution systems, especially when many PHEVs are connected to the grid at peak-hours. To face this concern, the distribution system requires to be improved to carry new loads. The enhancement of conventional grids to smart grids will create a proper management system to control the PHEVs charging and avoid the distribution transformer from being overloaded. To further increase the benefits of PHEVs, it is essential to take power from the RESs for the PHEVs charging. This paper proposes a PHEVs/EVs CS structure using a high share of power from the RESs and proper power management strategies. The proposed PMS managed the PHEVs charging in such a way that their charging does not become a burden on the utility during peak hours. The paper also provides the integration and coordination of different RESs. This paper shows that the PHEV charging demand does not disturb the grid stability and power quality parameters of the proposed system.

Author Contributions: T.K., and L.K. designed the algorithm in this work. S.Z.H., M.H.R., M.T.R. and M.A.K. were responsible for the preparation of required material. M.K. and L.M.F.-R. analyzed the results. All authors contributed at different stages.

Funding: This work was partially funded by the Turkish government under “Türkiye Bursları 2015–2020”.

Acknowledgments: Thanks to University of Cadiz, Spain for providing technical support under the framework of the Erasmus program of the European Commission.

Conflicts of Interest: The authors declare no conflict of interest.

References

1. Clarke, A.D.; Makram, E.B. An Innovative Approach in Balancing Real Power Using Plug in Hybrid Electric Vehicles. *J. Power Energy Eng.* **2014**, *2*, 1–8. [[CrossRef](#)]
2. Anumolu, P.; Banhazl, G.; Hilgeman, T.; Pirich, R. Plug-in hybrid vehicles: An overview and performance analysis. In Proceedings of the 2008 IEEE Long Island Systems, Applications and Technology Conference, Farmingdale, NY, USA, 2 May 2008; pp. 1–4.
3. Tie, S.F.; Tan, C.W. A review of energy sources and energy management system in electric vehicles. *Renew. Sustain. Energy Rev.* **2013**, *20*, 82–102. [[CrossRef](#)]
4. Cowell, R. Global Energy Justice: Problems, Principles, and Practices. *J. Environ. Plan. Policy Manag.* **2016**, *18*, 253–255. [[CrossRef](#)]
5. Nurre, S.G.; Bent, R.; Pan, F.; Sharkey, T.C. Managing operations of plug-in hybrid electric vehicle (PHEV) exchange stations for use with a smart grid. *Energy Policy* **2014**, *67*, 364–377. [[CrossRef](#)]
6. Su, W.; Chow, M.-Y. An intelligent energy management system for PHEVs considering demand response. In Proceedings of the 2010 FREEDM Annual Conference, 2010. Available online: <http://citeseerx.ist.psu.edu/viewdoc/download?doi=10.1.1.455.8086&rep=rep1&type=pdf> (accessed on 15 May 2018).
7. Su, W.; Zeng, W.; Chow, M.-Y. A digital testbed for a PHEV/PEV enabled parking lot in a smart grid environment. In Proceedings of the 2012 IEEE PES Innovative Smart Grid Technologies (ISGT), Washington, DC, USA, 16–20 January 2012; pp. 1–7.
8. Yılmaz, S.; Ustaoglu, M. Electric Vehicles Production in Turkish Automotive Industry and Sectoral PEST Analysis. *Proced. Soc. Behav. Sci.* **2013**, *75*, 10–17. [[CrossRef](#)]
9. Khan, A.S. Big Bets Coming on Local Assembly of Electric Cars. Available online: <https://www.dawn.com/news/1413157> (accessed on 18 May 2018).
10. Kamran, M. Current status and future success of renewable energy in Pakistan. *Renew. Sustain. Energy Rev.* **2018**, *82*, 609–617. [[CrossRef](#)]
11. National Household Travel Survey (NHTS). Summary of Travel Trends-2009. Available online: <https://nhts.ornl.gov/2009/pub/stt.pdf> (accessed on 12 May 2018).
12. Green, R.C.; Wang, L.; Alam, M. The impact of plug-in hybrid electric vehicles on distribution networks: A review and outlook. *Renew. Sustain. Energy Rev.* **2011**, *15*, 544–553. [[CrossRef](#)]

13. Shao, S.; Pipattanasomporn, M.; Rahman, S. Challenges of PHEV penetration to the residential distribution network. In Proceedings of the 2009 IEEE Power & Energy Society General Meeting, Calgary, AB, Canada, 26–30 July 2009; pp. 1–8.
14. Rutherford, M.J.; Yousefzadeh, V. The impact of electric vehicle battery charging on distribution transformers. In Proceedings of the 2011 Twenty-Sixth Annual IEEE Applied Power Electronics Conference and Exposition (APEC), Fort Worth, TX, USA, 6–11 March 2011; pp. 396–400.
15. Nagarajan, A.; Shireen, W. Grid connected residential photovoltaic energy systems with Plug-In Hybrid electric Vehicles (PHEV) as energy storage. In Proceedings of the IEEE PES General Meeting, Providence, RI, USA, 25–29 July 2010; pp. 1–5.
16. Preetham, G.; Shireen, W. Photovoltaic charging station for plug-in hybrid electric vehicles in a smart grid environment. In Proceedings of the 2012 IEEE PES Innovative Smart Grid Technologies (ISGT), Washington, DC, USA, 16–20 January 2012; pp. 1–8.
17. Goli, P.; Shireen, W. PV Integrated Smart Charging of PHEVs Based on DC Link Voltage Sensing. *IEEE Trans. Smart Grid* **2014**, *5*, 1421–1428. [[CrossRef](#)]
18. Goli, P.; Shireen, W. PV powered smart charging station for PHEVs. *Renew. Energy* **2014**, *66*, 280–287. [[CrossRef](#)]
19. Zhao, J.; Kucuksari, S.; Mazhari, E.; Son, Y.-J. Integrated analysis of high-penetration PV and PHEV with energy storage and demand response. *Appl. Energy* **2013**, *112*, 35–51. [[CrossRef](#)]
20. Oviedo, R.J.M.; Fan, Z.; Gormus, S.; Kulkarni, P.; Kaleshi, D. Residential energy demand management in smart grids. In Proceedings of the PES T&D 2012, Orlando, FL, USA, 7–10 May 2012; pp. 1–8.
21. Erol-Kantarci, M.; Mouftah, H.T. Management of PHEV batteries in the smart grid: Towards a cyber-physical power infrastructure. In Proceedings of the 2011 7th International Wireless Communications and Mobile Computing Conference, Istanbul, Turkey, 4–8 July 2011; pp. 795–800.
22. Heydt, G.T. The Impact of Electric Vehicle Deployment on Load Management Strategies. *IEEE Trans. Power Appar. Syst.* **1983**, 1253–1259. [[CrossRef](#)]
23. Heider, A.; Haubrich, H.-J. Impact of wide-scale EV charging on the power supply network. In Proceedings of the IEE Colloquium on Electric Vehicles—A Technology Roadmap for the Future, London, UK, 5 May 1998.
24. Zhang, Q.; Tezuka, T.; Ishihara, K.N.; Mclellan, B.C. Integration of PV power into future low-carbon smart electricity systems with EV and HP in Kansai Area, Japan. *Renew. Energy* **2012**, *44*, 99–108. [[CrossRef](#)]
25. Denholm, P.; Kuss, M.; Margolis, R.M. Co-benefits of large scale plug-in hybrid electric vehicle and solar PV deployment. *J. Power Sources* **2013**, *236*, 350–356. [[CrossRef](#)]
26. Ma, Z.; Callaway, D.; Hiskens, I. Decentralized charging control for large populations of plug-in electric vehicles: Application of the Nash certainty equivalence principle. In Proceedings of the 2010 IEEE International Conference on Control Applications, Yokohama, Japan, 8–10 September 2010; pp. 191–195.
27. Hota, A.R.; Juvvanapudi, M.; Bajpai, P. Issues and solution approaches in PHEV integration to smart grid. *Renew. Sustain. Energy Rev.* **2014**, *30*, 217–229. [[CrossRef](#)]
28. Hamilton, C.; Gamboa, G.; Elmes, J.; Kerley, R.; Arias, A.; Pepper, M.; Shen, J.; Batarseh, I. System architecture of a modular direct-DC PV charging station for plug-in electric vehicles. In Proceedings of the IECON 2010—36th Annual Conference on IEEE Industrial Electronics Society, Glendale, AZ, USA, 7–10 November 2010; pp. 2516–2520.
29. Bauer, P.; Zhou, Y.; Doppler, J.; Stembridge, N. Charging of electric vehicles and impact on the grid. In Proceedings of the 13th Mechatronika 2010, Trencianske Teplice, Slovakia, 2–4 June 2010; pp. 121–127.
30. Arancibia, A.; Strunz, K. Modeling of an electric vehicle charging station for fast DC charging. In Proceedings of the 2012 IEEE International Electric Vehicle Conference, Greenville, SC, USA, 4–8 March 2012; pp. 1–6.
31. Kelly, N.A.; Gibson, T.L. Solar photovoltaic charging of high voltage nickel metal hydride batteries using DC power conversion. *J. Power Sources* **2011**, *196*, 10430–10441. [[CrossRef](#)]
32. Gibson, T.L.; Kelly, N.A. Solar photovoltaic charging of lithium-ion batteries. In Proceedings of the 2009 IEEE Vehicle Power and Propulsion Conference, Dearborn, MI, USA, 7–10 September 2009; Volume 195, pp. 3928–3932. [[CrossRef](#)]
33. Gamboa, G.; Hamilton, C.; Kerley, R.; Elmes, S.; Arias, A.; Shen, J.; Batarseh, I. Control strategy of a multi-port, grid connected, direct-DC PV charging station for plug-in electric vehicles. In Proceedings of the 2010 IEEE Energy Conversion Congress and Exposition, Atlanta, GA, USA, 12–16 September 2010; pp. 1173–1177.

34. Aggeler, D.; Canales, F.; Zelaya, H.; La Parra, D.; Coccia, A.; Butcher, N.; Apeldoorn, O. Ultra-fast DC-charge infrastructures for EV-mobility and future smart grids. In Proceedings of the 2010 IEEE PES Innovative Smart Grid Technologies Conference Europe (ISGT Europe), Gothenberg, Sweden, 11–13 October 2010; pp. 1–8.
35. Kulshrestha, P.; Wang, L.; Chow, M.-Y.; Lukic, S. Intelligent energy management system simulator for PHEVs at municipal parking deck in a smart grid environment. In Proceedings of the 2009 IEEE Power & Energy Society General Meeting, Calgary, AB, Canada, 26–30 July 2009; pp. 1–6.
36. Nehrir, M.H. Power Management of a Stand-Alone Wind/Photovoltaic/Fuel Cell Energy System. *IEEE Trans. Energy Convers.* **2008**, *23*, 957–967. [[CrossRef](#)]
37. Drude, L.; Pereira Junior, L.C.; R  ther, R. Photovoltaics (PV) and electric vehicle-to-grid (V2G) strategies for peak demand reduction in urban regions in Brazil in a smart grid environment. *Renew. Energy* **2014**, *68*, 443–451. [[CrossRef](#)]
38. Onar, O.C.; Uzunoglu, M.; Alam, M.S. Modeling, control and simulation of an autonomous wind turbine/photovoltaic/fuel cell/ultra-capacitor hybrid power system. *J. Power Sources* **2008**, *185*, 1273–1283. [[CrossRef](#)]
39. Li, C.-H.; Zhu, X.-J.; Cao, G.-Y.; Sui, S.; Hu, M.-R. Dynamic modeling and sizing optimization of stand-alone photovoltaic power systems using hybrid energy storage technology. *Renew. Energy* **2009**, *34*, 815–826. [[CrossRef](#)]
40. Uzunoglu, M.; Alam, M.S. Dynamic Modeling, Design, and Simulation of a Combined PEM Fuel Cell and Ultracapacitor System for Stand-Alone Residential Applications. *IEEE Trans. Energy Convers.* **2006**, *21*, 767–775. [[CrossRef](#)]
41. El-Shatter, T.F.; Eskandar, M.N.; El-Hagry, M.T. Hybrid PV/fuel cell system design and simulation. *Renew. Energy* **2002**, *27*, 479–485. [[CrossRef](#)]
42. Zhu, Y.; Tomsovic, K. Development of models for analyzing the load-following performance of microturbines and fuel cells. *Electr. Power Syst. Res.* **2002**, *62*, 1–11. [[CrossRef](#)]
43. Hajizadeh, A.; Golkar, M.A. Intelligent Control of Fuel Cell Distributed Generation Systems. In Proceedings of the 2007 International Conference on Intelligent Systems Applications to Power Systems, Niigata, Japan, 5–8 November 2007; pp. 1–7.
44. Khan, M.J.; Iqbal, M.T. Analysis of a small wind-hydrogen stand-alone hybrid energy system. *Appl. Energy* **2009**, *86*, 2429–2442. [[CrossRef](#)]
45. Prius Plug-in Hybrid. 2014. Available online: <http://www.toyota.com/prius-plug-in/features.html#!/mechanical/1235/1237> (accessed on 25 March 2017).
46. Mitsubishi. Mitsubishi i-MiEV Technical Specifications Consulted. 2011. Available online: <http://www.mitsubishi-motors.com/special/ev/whatis/index.html> (accessed on 20 March 2017).
47. Nissan. Nissan Leaf Technical Specifications. Consulted. 2011. Available online: <http://www.nissan.co.uk/vehicles/electricvehicles/leaf.htm#vehicles/electricvehicles/leaf/leaf-engine/specifications> (accessed on 30 March 2018).
48. Renault. Renault Kangoo Z.E. Technical Specification. Consulted. 2011. Available online: <http://www.renault.com/en/vehicules/renault/pages/kangoo-express-ze.aspx> (accessed on 22 March 2018).
49. Accord Plug-in. 2014. Available online: <http://automobiles.honda.com/accord-plug-in/> (accessed on 15 March 2018).



   2018 by the authors. Licensee MDPI, Basel, Switzerland. This article is an open access article distributed under the terms and conditions of the Creative Commons Attribution (CC BY) license (<http://creativecommons.org/licenses/by/4.0/>).

Article

A Variable Speed Pumped Storage System Based on Droop-Fed Vector Control Strategy for Grid Frequency and AC-Bus Voltage Stability

Girmaw Teshager Bitew ^{1,*}, Minxiao Han ¹, Sifrash Amogne Mekonnen ² and Patrobers Simiyu ¹

¹ State Key Laboratory of Alternate Electrical Power System with Renewable Energy Sources, School of Electrical and Electronics Engineering, North China Electric Power University, Beijing 102206, China; hanminxiao@ncepu.edu.cn (M.H.); simiyupr@yahoo.com (P.S.)

² Social Science and Humanity College, Debre Markos University, Debre Markos 269, Ethiopia; gbitew1983@yahoo.com (S.A.M.)

* Correspondence: 1154300005@ncepu.edu.cn; Tel.: +86-155-1026-0077

Received: 7 May 2018; Accepted: 3 July 2018; Published: 7 July 2018

Abstract: Harnessing wind energy is the most rapidly growing amongst renewable energy sources. However, because of its intermittency in nature, wind power results in unfavorable influences on power system control, operation and stability. The voltage sag and flicker and grid frequency fluctuation are significant in this regard. To minimize the effect of wind power fluctuations and other contingencies on the grid frequency and AC-bus voltage, this paper presents a droop-fed vector control strategy based variable speed pumped storage (VSPS) system comprising the doubly fed induction machine. Modelling of the system is undertaken based on a phasor model technique. The case study is made by considering the droop-controlled VSPS plant in a grid containing conventional synchronous machines for hydropower and thermal power plants and an induction machine wind farm. The performance is validated and analyzed using a MATLAB/Simulink platform. The proposed droop-fed control model is compared with the conventional control strategy (without being droop-fed) and tested to wind power fluctuations, start-up transients, load variations and three-phase fault. The results show that the droop-fed vector control strategy of the VSPS plant achieves better dynamic and steady state controlling responses for grid frequency and AC-bus voltage in the power system than the conventional vector control scheme during wind power fluctuations and contingencies.

Keywords: variable speed pumped storage system; droop control; vector control; phasor model technique

1. Introduction

Due to increasing environmental concerns and energy markets, wind power generation has undergone rapid growth. In 2013, the world wind power production capacity was 318 GW and is forecasted to reach 712 GW, 1480 GW, 2089 GW and 2672 GW by 2020, 2030, 2040, and 2050, respectively, in a moderate scenario. China records the fastest growth in this regard [1,2].

Wind energy production is eco-friendly, sustainable, space efficient, incredible domestic potential, has low operational cost, revitalizing to rural economies, etc. However, the major drawback of wind power is its intermittency in nature over time, hence, significant wind power fluctuations can be observed. For a power system even with moderate wind power penetration, the fluctuations should be mitigated, otherwise this may lead to substantial deviations in the grid frequency [3], voltage sag and flicker at the grid buses [4], steady state voltage deviation, even equipment damage and system collapse at large. A study in [5] shows that the variable speed pumped storage (VSPS) system can improve the steady state operations and dynamic stability of the power system. Having dependable

features, the VSPS plant can play a key role in stabilizing the dynamics and transients of the grid affected by wind power fluctuations and other contingencies [6–11].

So far, many works have been done on the control strategies doubly fed induction machine in doubly fed induction machine (DFIM) based applications. Vector control strategy is predominantly taken into account in this regard. According to the references [8,9,12–16], the very common applicable vector control strategies implemented in DFIM are field oriented control (FOC) and direct torque control (DTC).

Based on the concept of the DTC, the direct power control (DPC) strategy is adopted. DPC is applied in an electrical machine field and has been widely studied. In DPC, the control of the real and reactive instantaneous power is independent, direct and simple [17,18]. It is noted that DPC has noble features than FOC particularly in the variable speed application [13,16,19]. Moreover, a comparative study between DPC and FOC strategies for doubly fed induction generator (DFIG) has been conducted in [19] and attempts to assure having lower computational complexity and machine model dependency, direct controllability of active and reactive powers, very good transitory response and lower overall implementation complexity than FOC. DPC is also characterized by its fast dynamic response against parameter variations and it does not utilize a rotor current control loops. In the DPC strategy, the estimations of active and reactive powers are carried out using current measurements, and directly controlled with hysteresis controllers and a switching table [12,14].

On the other hand, DPC has drawbacks compared to the FOC strategy. It has high ripples of active and reactive powers, high switching frequency which presents a high harmonic distortion of the generated currents, and provides warming-up of the silicon switchers [16]. Based on the comparative study in [16], it is hardly to state on the superiority of DPC versus FOC owing to the balance of the merits of them.

Regardless of its types, DPC or FOC, vector control confirms the higher level performance improvements in grid frequency and AC-bus voltage regulation with the implementation of the phasor model technique. However, the study of vector control in DFIM based VSPS application with the implementation of the phasor model technique is limited. The frequency regulator based on DPC implemented in a full-size converter fed synchronous machine was, for example, conducted in [8], but DFIM would be better advantages than synchronous machine in the implementation of VSPS plant for its efficiency and control [20]. The reference [13] also attempts to explore DPC in DFIG based wind power system. The DPC in [11] was also studied for the application of DFIM-based VSPS system with emphasis on converter topology study. Implementing an H-bridge cascaded multilevel converter for VSPS based on a stator voltage FOC strategy has been presented in [9] for suppressing the effect of a wind farm power fluctuations. Moreover, power filtering algorithm solution control approach was proposed in [3] to regulate the deviations of the grid frequency caused by wind power fluctuations. DPC is also studied in [11–16,19] and FOC is in [16,19] as well. The aforementioned works have not considered the phasor model simulation technique as significantly important in the large power system stability and control analysis where simulation time and computational storage are very critical. Since the electromagnetic transients are not of interest, the dynamic simulation time is highly reduced in the phasor model technique because the sinusoidal voltages and currents are replaced with phasors expressed in polar form. Implementing a phasor model in any linear system is also an advantage in that since the studies of a small-signal stability are based on eigenvalue analysis of the linearized power system, the eigenvalue analysis is complemented with dynamic simulations of the non-linear system [21,22]. Nevertheless, when implementing a phasor model technique in the DFIM application, grid frequency controlling is challenging. In the phasor model technique, the grid frequency is fixed to a constant value. It is difficult to develop a phasor locked loop which is used to synthesize the frequency. Thus, the grid frequency control is made through the active power control strategy which is an open loop control scheme for the frequency as shown in Figure 1. As a result, the responses in the grid frequency lack dynamic performances especially during contingencies [23].



Figure 1. Open-loop frequency and AC-bus voltage control through the power control strategy.

On the other hand, the frequency has a droop characteristic with active power in the converter system. Due to the imposed frequency droop, the converter will respond to the decrement of the frequency by increasing the inverted power or by reducing the rectified power. So, the frequency droop is estimated per unit increment of rectified power to be fed to the closed control system. Since a change in the converter power results in a change in DC voltage level, a frequency decrement will be manifested as decrement in DC voltage level in an AC/DC interface system which in turn results in demanding a power flow compensation [24]. Therefore, this problem can be resolved by incorporating a synchronous machine in the power grid system helping to get the measured and estimated frequency to the VSPS control system since the rotor speed of the synchronous machine is the same as the grid frequency with a proportion factor.

Regarding voltage regulation, the AC voltage can be controlled either by reactive power control or constant voltage control. Considering the reactive power PI control, the steady state deviation of AC voltage can be observed. For a constant voltage control strategy, generating or absorbing reactive power by the VSC converter is distorted during disturbances, hence leading to significant voltage sag and flicker and steady state voltage magnitude deviations. Therefore, combining these strategies together provides droop based power control resulting in fast dynamic control response and minimized error in steady state values. Therefore, droop controllers are to be incorporated as the input of reactive power PI control (outer loop controller) of the conventional vector control strategy.

Hence, this paper presents a droop-fed vector control strategy based VSPS system for the reduction of wind power fluctuation and other contingencies impact on grid frequency and AC-bus voltage to resolve the steady state and dynamic performance problems stated in the aforementioned papers. The converter employed is the three-level neutral point clamped voltage sourced converter (NPC-VSC). Due to its novel features to the VSPS plant, the DFIM is deployed. To validate the performance of the proposed system, a phasor model simulation technique is developed and analyzed in a MATLAB/Simulink platform. The performances of the proposed system are made by comparison with the conventional method. The VSPS grid connected system consisting of hydropower and thermal power with synchronous machine and wind farm with induction generator is presented for a case study. The results show that the proposed VSPS control strategy achieves better performances in the dynamic and steady state responses of the grid frequency and AC voltage than the conventional strategy.

2. Materials and Methods

2.1. Basic Concepts of Droop Vector Control System

2.1.1. The Vector Control

Vector control is strictly defined as a variable frequency drive control method in which the stator currents of a three-phase AC electric motor are identified as two orthogonal components that can be visualized with a vector [25]. One of the two components states the torque and the other magnetic flux of the machine. From the flux and torque references, the drive control system calculates the corresponding current component references. To keep the measured current components at their reference values, typically PI controllers are used. A single-variable scalar (V/f) control will be universally displaced by the vector control strategy due to increase of the microprocessors vector control computational power. It is applicable to both induction and synchronous machines.

The very common applicable control strategies named FOC and DTC are categorized under vector control scheme [8,16]. They are different on the operation principle but their objectives are the same. Both of them aim to control effectively the machine torque and flux, and have been successfully implemented [16]. The FOC controllers move the stator field so that it is perpendicular to the rotating rotor field. The FOC is an attractive control method but it also has a drawback. The precise knowledge of the motor parameters are, for example, mandatory. It is particularly difficult to measure precisely with a varying temperature. The DTC, which is a more robust control scheme, provides for estimating the stator flux and electric torque of the machine from terminal measurements in the stationary reference frame. The DPC strategy adopted based DTC was initially developed in 1998 [26] and implemented to DFIG in 2006 [12]. A DPC is characterized by its fast dynamic response against parameter variations and it does not utilize a rotor current control loops. The DPC also has drawbacks with high ripples of active and reactive powers, high switching frequency of which presents a high harmonic distortion of the generated currents, and provides warming-up of the silicon switchers [16].

2.1.2. The Droop Control

The main concept of droop control is to build an additional VSC-DC link frequency and AC voltage control on top of the state-of-the-art frequency and AC voltage control approach to provide virtual reserve through VSC-DC link systems. In case of the power change due to load or supply variation, the droop characteristics of grid frequency and AC voltage is observed in the VSC-DC link based system performance as is strongly related to change of power.

The frequency control structure given in Figure 2 provides a governor like droop behavior through active power loop. If there are generating units in the power system, the load sharing is determined by the frequency droop of each power generating unit, which is defined as $R = \Delta\omega / \Delta P$. For two power generating units with frequency droops R_1 and R_2 , the following relationship is established for the power output ΔP_1 and ΔP_2 :

$$\frac{\Delta P_1}{\Delta P_2} = \frac{R_2}{R_1} \quad (1)$$

The power generating unit with smaller frequency droop shares more loads in the power system. Accordingly, the frequency droop of the VSC-DC link with the proposed frequency controller can be expressed as

$$\Delta f = \frac{1}{K_f} (P_{ref} - P) \quad (2)$$

where K_f is the droop constant.

Likewise, if two or more alternating-voltage-controlling units are connected to a common bus in the power system, the alternating voltage controls should be coordinated to avoid hunting between the units. The transformer used in the application of VSC is to transform the grid or load bus voltage to a suitable voltage. Nevertheless, the VSC-based system performance is affected due to voltage droops of the transformer [27]. Thus, instead of controlling the alternating voltage of the point-of common-coupling (PCC), the VSC-DC link and the synchronous generator both control voltages between their own terminal/filter-bus voltages and the voltage of the PCC to give a droop characteristic to their alternating-voltage controls. So, the virtual inertia is provided through the reactive power or AC voltage control loop of the VSC system. Since the voltage is strongly related to the reactive power generation or absorption, its droop needs to be compensated via a reactive power control loop as shown Figure 2.

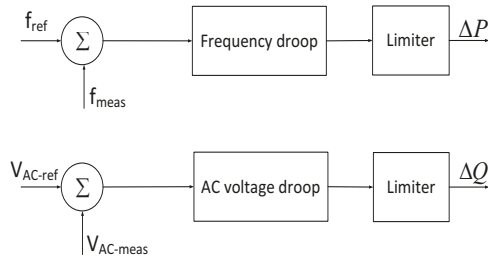


Figure 2. The block diagram of the droop control.

2.2. The Proposed System Modelling

The structure of the proposed system in this paper is illustrated in Figure 3. As shown in the figure, the DFIM of the VSPS is configured in such a way that the rotor is connected with the rotor side NPC-VSCr and the stator is connected with the grid, whereas the grid side NPC-VSCg is connected with the grid through the coupling inductor. Details are explained in [23]. The wind farm is also connected to the grid with the conventional machine. The control structure is hierarchical having inner loops (current PI controllers), outer loops (power PI controllers) and droop controllers (frequency droop controller and AC voltage droop controller).

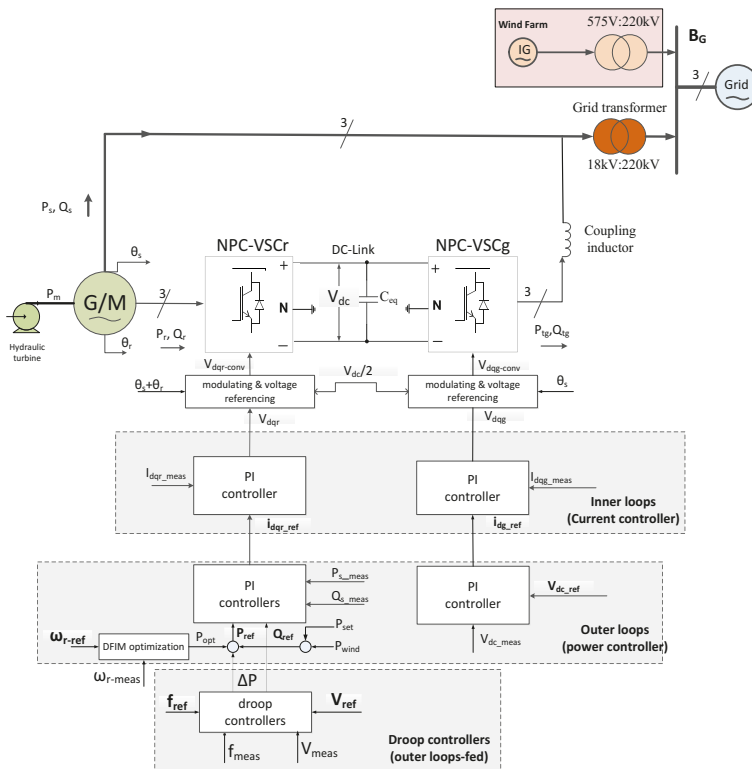


Figure 3. Structure of droop-fed vector control strategy for the NPC-VSC topology of the VSPS-wind-grid integrated system.

2.3. Machine and Converter Modelling

Detailed modelling of the hydraulic-turbine, the DFIM and the NPC-VSC is presented in [23] and the wind farm also in [15] by the same authors. This paper focuses on developing the control strategy of the VSPS in the wind-grid-integrated system for analyzing the dynamic behavior and performance of controlling the grid frequency and AC-bus voltage during the fluctuation of wind energy and other contingencies.

2.4. Control Modelling in MATLAB Platform for Dynamic and Steady State Analysis

Referring to [15,23], we have the stator power equations and the dynamics equations of the induction machine fluxes in (3) and (4) respectively.

$$\begin{aligned} P_s &= 1.5(v_{qs}i_{qs} + v_{ds}i_{ds}) \\ Q_s &= 1.5(v_{qs}i_{ds} - v_{ds}i_{qs}) \end{aligned} \tag{3}$$

$$\begin{aligned} \frac{d\Psi_{ds}}{dt} &= V_{ds} - R_s i_{ds} - \omega_s \Psi_{qs} \\ \frac{d\Psi_{qs}}{dt} &= V_{qs} - R_s i_{qs} + \omega_s \Psi_{ds} \\ \frac{d\Psi_{dr}}{dt} &= V_{dr} - R_r i_{dr} + (\omega_s - \omega_r) \Psi_{qr} \\ \frac{d\Psi_{qr}}{dt} &= V_{qr} - R_r i_{qr} - (\omega_s - \omega_r) \Psi_{dr} \end{aligned} \tag{4}$$

Based on the detail works in [23], from (3) and (4), the stator power (P_s, Q_s) is determined and expressed as a function of the rotor dq-axis current.

$$\begin{aligned} P_s &= 1.5V_s(L_m/L_s)i_{qr} \\ Q_s &= 1.5V_s[(\Psi_s/L_s) - (L_m/L_s)i_{dr}] \end{aligned} \tag{5}$$

Equation in (5) implies the independent control of the real power and reactive power in the application of a DFIM-based VSPS system, and equations in (6) have been also derived based on the assumptions taken; a voltage drop across stator resistor being very small compared to the grid voltage and a magnitude of stator flux fairly constant.

$$\begin{aligned} V_{qr} &= R_r i_{qr} + L_r^* \frac{di_{qr}}{dt} + (\omega_s - \omega_r)(L_r i_{dr} + L_m i_{ds}) \\ V_{dr} &= R_r i_{dr} + L_r^* \frac{di_{dr}}{dt} - (\omega_s - \omega_r)(L_r i_{qr} + L_m i_{qs}) \end{aligned} \tag{6}$$

where $L_r^* = L_r - (L_m^2/L_s)$ and V_{qr} and V_{dr} are feed-forward voltages to the controller.

Thus, the dynamics of the rotor dq-axes currents are controlled by developing the PI control loops from (6) which in turn are used to control the stator active power which is the function of rotor dq-axes current as equated in (5). However, dynamics of i_{dr} and i_{qr} are coupled due to the presence of the terms $L_r(\omega_s - \omega_r)$ in (6). Since the VSC controls the DFIM rotor terminal voltage, as stated in (6), i_{qr} and i_{dr} are to be related to the new control inputs u_{qr} and u_{dr} . To decouple the dynamics, the new control inputs are introduced and is redefined as in (7).

$$\begin{aligned} u_{qr} &= V_{qr} - (\omega_s - \omega_r)(L_r i_{dr} + L_m i_{ds}) \\ u_{dr} &= V_{dr} + (\omega_s - \omega_r)(L_r i_{qr} + L_m i_{qs}) \\ \text{where } u_{dr} &= L_r^* \frac{di_{dr}}{dt} + R_r i_{dr} \\ u_{qr} &= L_r^* \frac{di_{qr}}{dt} + R_r i_{qr} \end{aligned} \tag{7}$$

On the other hand, in the grid side of NPC-VSCg converter, the PI control of DC voltage in the DC link is deployed for regulating the proper active power exchange between the converter and the grid on the outer loop whereas PI current controller is used on the inner loop. But, reactive power

exchange is usually set to zero [28]. The mathematical model design is made by the equation in (5) denoting the voltage equations across the coupling inductor.

$$\begin{aligned} V_{dg} &= Ri_{dg} + L \frac{di_{dg}}{dt} - \omega_s Li_{qg} + V_{ds} \\ V_{qg} &= Ri_{qg} + L \frac{di_{qg}}{dt} + \omega_s Li_{dg} + V_{qs} \end{aligned} \quad (8)$$

where R and L are the coupling inductor resistance and inductance respectively; and V_{dqg} and V_{dqs} are control inputs and disturbance inputs respectively.

Similarly, i_{qg} and i_{dg} are to be related to the new control inputs u_{qg} and u_{dg} and (9) is redefined as

$$\begin{aligned} u_{dg} &= V_{dg} + \omega_s Li_{qg} - V_{ds} \\ u_{qg} &= V_{qg} - \omega_s Li_{dg} - V_{qs} \\ \text{where } u_{dg} &= L \frac{di_{dg}}{dt} + Ri_{dg} \\ u_{qg} &= L \frac{di_{qg}}{dt} + Ri_{qg} \end{aligned} \quad (9)$$

Thus, from (7) and (9), the rotor and grid current control loops (inner loops) are developed. Both current controllers are supported by feed forward terms predicting V_{dqr} and V_{dqg} . The dynamics of the DC voltage in the DC link is defined by (10). The converters and DC-link are assumed to be lossless.

$$\frac{dV_{dc}}{dt} = \frac{1}{C} i_{dc} = \frac{1}{CV_{dc}} (P_r - P_g) \quad (10)$$

where C and V_{dc} are the DC link capacitance and DC voltage respectively. P_g and P_r are active power flow in the grid and rotor side of the converters respectively.

The power equations of (3) also hold for a grid side power flow and denoted by (11).

$$\begin{aligned} P_{ig} &= 1.5(v_{qg}i_{qg} + v_{dg}i_{dg}) \\ Q_{tg} &= 1.5(v_{qg}i_{dg} - v_{dg}i_{qg}) \end{aligned} \quad (11)$$

2.5. Control of Active and Reactive Power for Rotor Side Converter

Active or reactive power is controlled by the rotor side converter which connects rotor windings and DC link. This converter offers a proper AC excitation for the windings of the rotor that provides the stator windings proper active power.

2.5.1. Active Power Control

Controlling of active power can ensure controlling of system frequency. So as to keep the grid frequency constant, synchronous generators, for example, can have a permanent droop control loop in the turbine control. It is dedicated to adjust the active power balance between the production and the consumption of the system. On the other hand, implementing the primary frequency control in the DFIM-based VSPS unit, which is critically important, controls the active power flow of the system. In this application, a vector control strategy is employed to have fast dynamic response and lets the control system compensate effectively during contingencies. Even if this is a limited control scheme that is placed in the VSPS unit, the significant output that is an adjustable and nearly constant power flow can be seen from the network of the power system as far as the VSPS operates within the specified limits. The power command P_{opt} of the control system of the VSPS is determined from the capacity of the VSPS unit and its efficiency. An external set point, P_{set} which is the input to the power control system, in this regard, should be assumed for the VSPS. The set point depends on the VSPS capacity and the situation of the power grid. The value of this set point is dedicated to optimize the system energy balance and update relatively with slow rate. The main concern is, however, to control the contingencies and regulate the VSPS power for mitigating the impact on the grid stability.

As illustrated in Figure 3, the rotor-side converter control is modelled in two stages. The first stage is power (PQ) control (the outer loop) in that the active/reactive power tracks the respective reference. This loop provides dq-axis reference currents for the second stage (the inner loop). The inner loop is technically a current control offering dq-axis reference voltage for modulation and injected to the converter. PI controllers with limiters are applied in both control stages.

The model design of the active power control of the rotor side converter is presented as follows. Referring to the voltage equations in (4), we have the mathematical equations of (6). From (6), the rotor electrical dynamics model is determined based on the system equations and representing two decoupled, first-order subsystems. It can control i_{dqr} by u_{dqr} , in turn, u_{dqr} can be delivered by corresponding PI compensators. The compensators process the current errors and provides u_{dqr} . The control plants in dq-axis current-control loops are identical. Therefore, the corresponding compensators can also be identical. Thus, the compensator can be a simple proportional-integral (PI) compensator, $K_i(s)$ to enable tracking of a respective reference. The compensator is defined by

$$K_i(s) = \frac{P_i s + I_i}{s} \tag{12}$$

Thus, the loop gain becomes

$$\ell(s) = \left(\frac{P_i}{L_r^*} \right) \frac{s + I_i/P_i}{s + R_r/L_r^*} \tag{13}$$

Due to the plant pole at $s = -R_r/L_r^*$, which is fairly close to the origin, the magnitude and the phase of the loop gain start to drop from a relatively low frequency. Thus, the plant pole is first canceled by the compensator zero $s = -I_i/P_i$, and the loop gain assumes the form $\ell = P_i/L_r^*$. Then, based on the plant function, $G_i(s) = 1/(L_r^*s + R_r)$ developed from (7) and considering the compensator $K_i(s)$ in, the closed-loop transfer function becomes;

$$\frac{I_{dqr}(s)}{I_{dqr-ref}(s)} = G_{ic}(s) \approx \frac{1}{\tau^*s + 1} \text{ if } P_i = L_r^*/\tau^* \text{ and } I_i = R_r/\tau^* \tag{14}$$

where P_i and I_i are proportional and integral gains and $\tau^* = L_r^*/R_r$. The gains are determined and tuned based on the control stability theory. The control structure of the inner loop is illustrated in Figure 5a.

From Equation (14), the q-axis rotor current as a function of its own reference value is obtained.

$$I_{qr}(s) = G_{ic}(s)I_{qr-ref}(s) \tag{15}$$

Multiplying both sides of (15) by $1.5 V_s L_m / L_s$, we get

$$1.5V_s L_m / L_s I_{qr}(s) = G_{ic}(s)1.5V_s L_m / L_s I_{qr-ref}(s) \tag{16}$$

Therefore, based on Equation (5), from (16), we can deduce (17).

$$P_s(s) = G_p(s)P_{s-ref}(s) \tag{17}$$

From these relationship, we can have the block diagram of Figure 4.

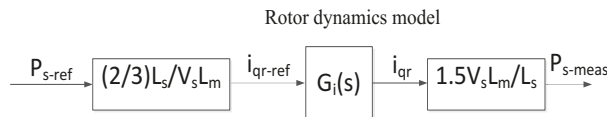


Figure 4. Control block diagram of the vector controlled DFIM for active power control loop.

Thus, plant function $G_p(s)$ is defined by multiplying $G_{ic}(s)$ with $1.5 V_s L_m / L_s$ i.e., $G_p(s) = 1.5 V_s L_m / L_s (L_r^* s + R_r)$. Accordingly, the closed loop active power control is developed as shown in Figure 5b. The PI control of $K_p(s)$ of Figure 5b processes the error signal e_p and provides the reference current i_{qr-ref} and defined by;

$$K_p(s) = \frac{P_p s + I_p}{s} \tag{18}$$

where P_p and I_p are proportional and integral gains. The open loop transfer function becomes;

$$G_{po}(s) = \left(K \frac{(P_p s + P_i)(I_p s + I_i)}{L_r^* s^3 + (R_r + I_p) s^2 + I_i s} \right) \tag{19}$$

where $K = 1.5 V_s L_m / L_s$. We used the symmetrical optimum method to determine the control gains (P_p and I_p) since the open loop transfer function has a pole at the origin. This method optimizes the system's control behavior. Thus, the inner current loop with wider bandwidth of 2.4 Hz than the outer power loop with 1.11 Hz is designed.

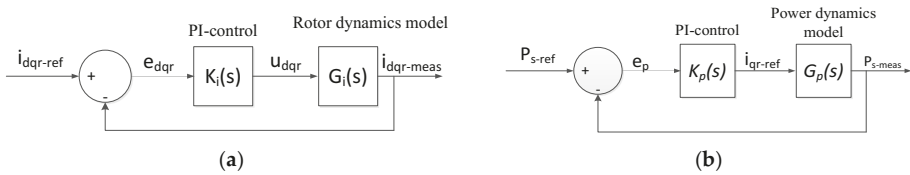


Figure 5. The PI control structure of the NPC-VSCr: (a) the current controller (inner loop); (b) the active power control (outer loop).

Permanent droop should be included in this control as active power in DFIM is controlled by the converter. In dominant wind farm power production fluctuations, the response of the power system to contingencies is highly improved if a frequency droop control scheme is included in the active power control loop. The power transfer within the DC-link can be modulated by a frequency droop control. It can be modelled as an additional signal that is added to the active power reference P_{ref} in Figure 6.

According to Figure 6, the difference between actual and reference frequency is forwarded to a proportional controller which defines permanent droop. The proportional output is added to the signal of the active power P_{set} and the optimized output power P_{opt} from the induction machine and the sum of them presents the active power reference P_{ref} for the PI active power control in the outer loop.

The optimized power P_{opt} is the very beginning reference power of the VSPS control system which is determined by considering the capacity of the hydraulic turbines of the VSPS plant along with its losses. Since the plant is a variable speed scheme, the control system enables to adjust and regulate the plant when the power variation occurs in the grid. Thus, we can add the power command $\Delta P_{wind} = P_{wind} - P_{set}$ to the VSPS power control unit and to be compensated. P_{wind} is the wind farm power measured which is subject to the fluctuation due to its intermittency. Then, it is designed for the converters to offer frequency support to the grid. This control structure provides a governor-like droop behavior through active power flow. The droop-type control is built based on the concept of power synchronization control in which grid synchronization is achieved regardless of a dedicated synchronization unit [21]. This droop-type control system provides a DC link with frequency droop characteristic. For other power generating units in the grid system, the load sharing is possible.

Hence, with the additional power command ΔP_f due to change of frequency caused by all contingencies to the VSPS active power control system, improvement of the dynamics performance of the power system can be ensured, and (20) is accordingly determined.

$$\Delta P_f = K_f (f_{ref} - f_{grid}) \tag{20}$$

where K_f is the droop constant, f_{ref} is the reference frequency in which 50 Hz applied in this paper, and f_{grid} is the grid frequency measured and estimated from the rotor speed of the synchronous machine in the same grid.

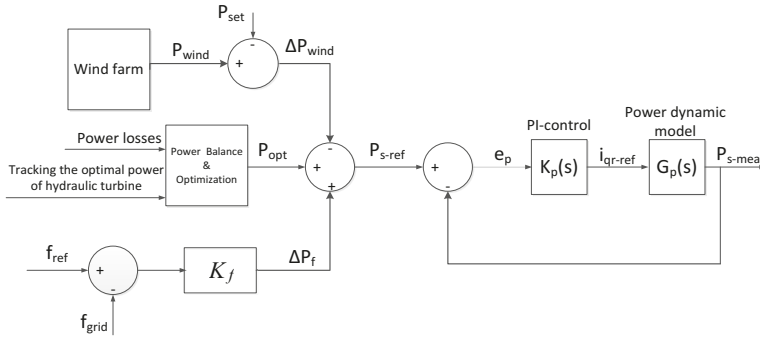


Figure 6. A rotor-side converter of active power control structure.

2.5.2. Reactive Power Control

The same procedures following as in the active power modelling section, the reactive power control system is developed. From the Equations (5), (14) and Figure 5, the model (21) is determined.

$$Q_s(s) = G_q(s)Q_{s-ref}(s) \tag{21}$$

Hence, the dynamic model for the reactive power control of rotor side converter VSC-NPCr is developed, and the PI control of $K_q(s)$ is defined in (22).

$$K_q(s) = \frac{P_q s + I_q}{s} \tag{22}$$

The rotor side converter provides the proper reactive power of stator windings as stated above. Therefore, in order to keep the AC-bus voltage constant, i.e., to adjust the generation and absorption of the reactive power in the converter, additional signal should be included to the reference reactive power. With load compensation, referring Figure 7, for parallel connected voltage control units, the magnitudes of the resulting compensated voltages can be given by

$$\begin{aligned} V_{t-SG} &= e_{SG} + k_{SG}(R_{SG} + jX_{SG})i_{SG} \\ V_{t-VSC} &= e_{VSC} + k_{VSC}(R_{VSC} + jX_{VSC})i_{VSC} \end{aligned} \tag{23}$$

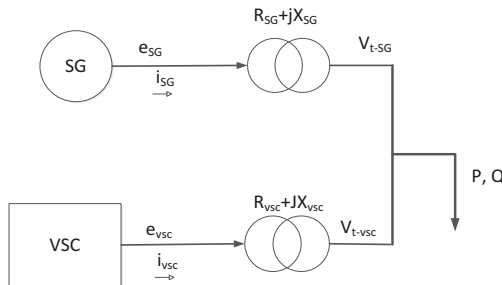


Figure 7. Voltage droop control for parallel connected voltage-control units.

In order to provide appropriate AC voltage in the network, for example, the DFIM reactive power can be properly controlled. This control can be accomplished based on the control structure presented in Figure 8. This figure indicates that the difference between actual AC voltage V_{meas} and reference AC voltage V_{ref} of the AC grid is integrated and added to the reactive power set signal Q_{set} and the sum of both signals presents the reference of the reactive power Q_{ref} for the PI reactive power control on the outer loop of the VSPS control system provided in the rotor side.

From (23), the voltage-reactive power relationship of Equation (24) with the droop constant K_{ac} is derived.

$$\Delta Q_{vsc} = K_{ac}(V_{ref} - V_{meas}) \tag{24}$$

The voltage control structure through the reactive power control loop is illustrated in Figure 8.

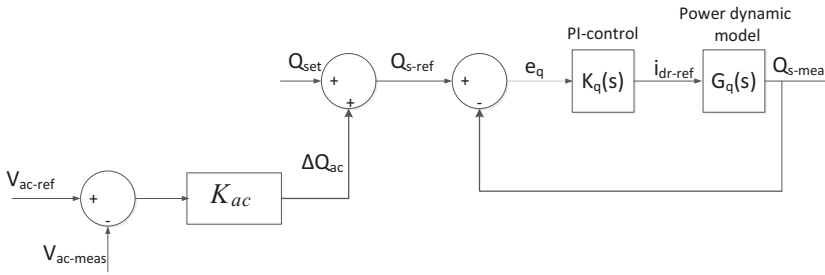


Figure 8. A rotor-side converter of reactive power control structure.

2.6. Control of Active and Reactive Power for Grid Side Converter

The reactive power on the grid side converter is controlled by a PI controller by setting its reference value zero. Whereas the proper active power exchange between the converter and grid is controlled through the PI control of DC voltage in the DC link.

For control design purposes, the d-axis is supposed to be set in phase with the voltage across the resistor. Thus, the d-component of the voltages in d-q coordinates becomes v_{dg} and zero that of v_{qg} . So, the power equations of (11) is deduced by (25).

$$\begin{aligned} P_{tg} &= 1.5v_{dg}i_{dg} \\ Q_{tg} &= -1.5v_{dg}i_{qg} \end{aligned} \tag{25}$$

Ignoring the losses and harmonics due to switching in the converter, the real power balance equation on the grid side can be given by:

$$P_{tg} = 1.5v_{dg}i_{dg} = V_{dc}I_{dc} \tag{26}$$

Equation (26) implies that the DC-bus voltage is likely and independently controlled by controlling the d-axis current i_{dg} .

The objective of the active/reactive power controller of the VSC system is to regulate the active/reactive power exchange between the converter and the AC grid. In this controller, for the sake of mathematical formulation, it is supposed to be the DC side of the VSC is connected to an ideal DC voltage source that dictates the DC-bus voltage as shown in Figure 9.

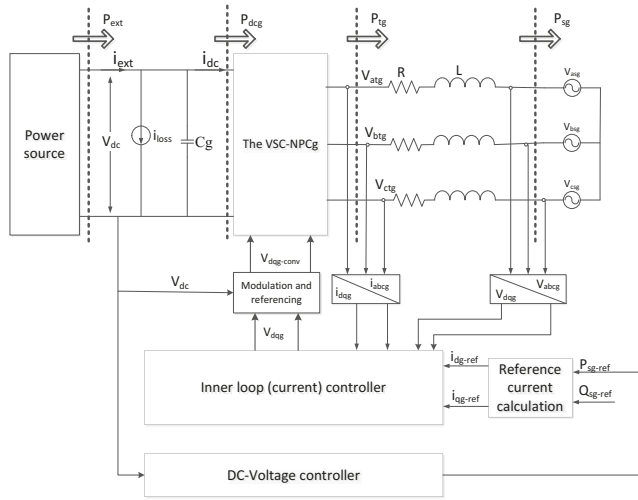


Figure 9. Simplified schematic diagram of the controlled DC-voltage power port of a three-level NPC-VSCg.

According to Figure 9, any power imbalance within the outlined area results in excursions (and potential instability) of the DC-bus voltage since there is no DC voltage source in the VSC system. Thus, the DC-voltage V_{dc} of the grid port requires proper regulation. $P_{ext}(t)$ cannot be controlled by the VSC system since it is typically an exogenous signal. Thus, to ensure the power balance exchange, P_{dcg} must be controlled through the VSC system. Based on Figure 9, the power balance is expressed by (27).

$$P_{ext} - V_{dc}i_{loss} - \frac{d}{dt} \left(\frac{1}{2} C_g V_{dc}^2 \right) = P_{dcg} = V_{dc}i_{dc} \quad (27)$$

However, for a three-level NPC-VSC, the DC bus effective capacitance is half each of its DC-side capacitors. Ignoring the power losses related to the IGBT resistance r_{on} and substituting for $P_{dcg} = P_{tg}$ and rearranging the resultant, (27) is rewritten as (28).

$$P_{ext} - \underbrace{V_{dc}i_{loss}}_{P_{loss}} - \frac{d}{dt} \left(\frac{1}{2} C_g V_{dc}^2 \right) = P_{tg} \quad (28)$$

where P_{tg} is the power at the AC-side terminal of the VSC. Equation (28) represents a power balance and describes a dynamic behavior of V_{dc} of a system in which V_{dc}^2 is the output state variable, the P_{tg} is the control input, and P_{ext} and P_{loss} are the exogenous inputs. C_g is the capacitance for smoothing the DC-bus voltage ripples.

Similarly, taking into account the system on the rotor side converter encompassing C_r , the following equation holds.

$$\frac{d}{dt} \left(\frac{1}{2} C_r V_{dc}^2 \right) = P_{dcr} - \underbrace{V_{dc}i_{lossr}}_{P_{lossr}} - P_{ext} \quad (29)$$

Ignoring the power losses related to the IGBT resistance r_{on} , AC-side terminal power is equal to the machine rotor power $P_r = P_{dcr}$. Adding (28) and (29) together, the Equation (30) is found.

$$\frac{d}{dt} \left(\frac{1}{2} C_{eq} V_{dc}^2 \right) = -P_{tg} - P_{loss} + P_{dcr} \quad (30)$$

Equation (30) describes a power-balance dynamic equation for the capacitance $C_{eq} = C_r + C_g$, which is subjected to the (relatively small) discharging power $P_{loss} = V_{dc} (i_{lossr} + i_{lossg})$ the (widely variable) charging power P_{dcr} and the (controllable) discharging power P_{tg} .

Starting with the voltage equation across the coupling inductor from Figure 6, we have

$$L \frac{di}{dt} = -Ri + V_{tg} - V_{sg} \tag{31}$$

The control input P_{tg} is expressed in terms of P_{sg} and Q_{sg} since the VSC system of Figure 9 enables to control P_{sg} and Q_{sg} . Multiplying both sides of (31) by $(3/2)i^*$ (i^* is the conjugate of i), we obtain

$$\frac{3L}{2} \text{Re} \left\{ \frac{di}{dt} i^* \right\} = -\frac{3}{2} Ri^2 + \frac{3}{2} \text{Re} \{ V_{tg} i^* \} - \frac{3}{2} \text{Re} \{ V_{sg} i^* \} \tag{32}$$

Rearranging and solving (30) for $P_{tg} = (3/2) \text{Re} \{ V_{tg} i^* \}$ and $P_{sg} = (3/2) \text{Re} \{ V_{sg} i^* \}$, we get

$$P_{tg} = P_{sg} + \frac{3}{2} Ri^2 + \frac{3L}{2} \text{Re} \left\{ \frac{di}{dt} i^* \right\} \text{ or } P_{tg} = P_{sg} + \frac{3}{2} Ri^2 + \frac{3L}{4} \frac{d\hat{i}^2}{dt} \tag{33}$$

Practically, R is a small resistance and its absorbed power is negligible compared to P_{tg} and P_{sg} . However, during transients, the power absorbed by the coupling inductor can be significant. So, L must be adequately large to suppress the switching harmonics. Furthermore, since the current controllers in dq-axis frame are fast, i can undergo rapid phase and amplitude changes, during the real/reactive-power command tracking process.

From the power equation, we have

$$P_{sg} + jQ_{sg} = \frac{3}{2} (V_{sg} i^*) \text{ or } P_{sg}^2 + Q_{sg}^2 = \frac{9}{4} \hat{V}_{sg}^2 \hat{i}^2 \tag{34}$$

Solving (34) for \hat{i}^2 and substituting in (33), Equation (35) is derived

$$P_{tg} \approx P_{sg} + \left(\frac{2L}{3\hat{V}_{sg}^2} \right) P_{sg} \frac{dP_{sg}}{dt} + \left(\frac{2L}{3\hat{V}_{sg}^2} \right) Q_{sg} \frac{dQ_{sg}}{dt} \tag{35}$$

Substituting (35) in (30), Equation (36) holds.

$$\frac{dV_{dc}^2}{dt} = \frac{2}{C_{eq}} \left[-P_{loss} + P_{dcr} - P_{sg} - \left(\left(\frac{2L}{3\hat{V}_{sg}^2} \right) P_{sg} \frac{dP_{sg}}{dt} + \left(\frac{2L}{3\hat{V}_{sg}^2} \right) Q_{sg} \frac{dQ_{sg}}{dt} \right) \right] \tag{36}$$

Equation (36) describes the dynamics of V_{dc}^2 ; P_{sg} is the control input, Q_{sg} are the disturbance inputs. Thus, to control V_{dc}^2 , one can form the control scheme shown in Figure 8, which consists of an inner control loop nested inside an outer loop. The outer loop compares V_{dc}^2 with its reference value, processes the error by a compensator, and delivers P_{sg-ref} to the inner control loop. The inner control loop is basically the current controller which regulates its reference value calculated from the P_{sg-ref} of the outer loop controller.

Since the control plant is nonlinear, Equation (36) should be linearized about the steady state real power flow operating points based on [29], and thus, designing $G_{dc}(s)$ accordingly. So, $P_{sg0} = P_{ext} - P_{loss} \approx P_{ext0}$; and (36) is linearized as

$$\frac{d\tilde{V}_{dc}^2}{dt} = \frac{2}{C_{eq}} \left[-\tilde{P}_{ext} - \tilde{P}_{sg} - \left\{ \left(\frac{2L}{3\hat{V}_{sg}^2} \right) P_{sg0} \frac{d\tilde{P}_{sg}}{dt} + \left(\frac{2L}{3\hat{V}_{sg}^2} \right) Q_{sg0} \frac{d\tilde{Q}_{sg}}{dt} \right\} \right] \tag{37}$$

where \sim denotes small-signal perturbations. The time domain of (37) is transformed into Laplace domain resulting in a control plant transfer function as

$$G_{dc}(s) = \frac{\tilde{V}_{dc}^2}{\tilde{P}_{sg}} = -\left(\frac{2}{C_{eq}}\right) \frac{\tau s + 1}{s} \tag{38}$$

where τ is the time constant defined by

$$\tau = \frac{2LP_{sg0}}{3\tilde{V}_{sg}^2} \tag{39}$$

where L , P_{sg0} and \hat{V}_{sg} are respectively the coupling inductance, (steady-state) real power flow and grid-side AC voltage magnitude.

As per Equation (39), if P_{ext0} is small, τ is insignificant and the plant is predominantly an integrator since τ is proportional to the real-power flow P_{ext0} (or P_{sg0}). τ brings a phase shift in $G_{dc}(s)$ when P_{ext0} increases. In the inverting operation mode where P_{ext0} is positive, τ is positive and adds to the phase of $G_{dc}(s)$. However, in the rectifying operation mode where P_{ext0} is negative, τ is negative and reduces the phase of $G_{dc}(s)$; a larger absolute value of P_{ext0} results in a smaller phase of $G_{dc}(s)$. Based on (38), the plant zero is $z = -1/\tau$. Therefore, a negative τ corresponds to a zero on the right-half plane, and the controlled DC-voltage VSPS represents a non-minimum-phase system in the rectifying operation mode. Thus, the phase reduction associated with the non-minimum-phase zero has a detrimental impact on the closed-loop stability.

Taking into account of system model linearization, the PI controller parameters are chosen around the operating points. For the model linearization, the point of a reference is obtained by specifying a reference input V_{dc-ref} . The control structure is depicted in Figure 10a.

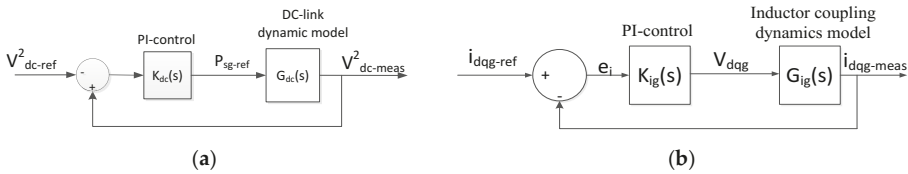


Figure 10. The control structure for grid side converter of NPC-VSC: (a) the DC-bus voltage control (outer loop) structure; (b) the current control (inner loop) structure.

The compensator $K_{dc}(s)$ is designed to guarantee an adequate stability margin even if the steady state operating point changes. It is designed based on the plant function of (36) in which V_{dc}^2 is impacted by P_{ext} and P_{loss} under the steady state and transient conditions. The feed-forward compensation can reduce the impact of P_{ext} . However, the feed-forward compensation is hardly effective to mitigate the impact of P_{loss} due to uncertainty of the measurement and estimation of P_{loss} . Therefore, $K_{dc}(s)$ must have an integral term (I_{dc}) to eliminate the steady state error of V_{dc}^2 caused by P_{loss} . Because of a presence of an integral term in the control plant and to ensure an adequate phase margin and stability, a proportional term (P_{dc}) must be included in the $K_{dc}(s)$. Hence, the PI compensation $K_{dc}(s)$ of Figure 9a is defined by (40).

$$K_{dc}(s) = \frac{P_{dc}s + I_{dc}}{s} \tag{40}$$

where P_{dc} and I_{dc} are respectively proportional and integral constants of the PI controller.

The control of the inner loops in the grid side converter is designed based on the voltage dynamics equation of (8) by following the same procedure as of the rotor side. The inner loop current controllers which are identical due to identical dynamic model are dedicated to control both active and reactive

power i_{dg} for active power and i_{qg} for reactive power. Hence, PI control structure of the inner loops shown in Figure 10b is developed.

The PI controller compensation $K_{ig}(s)$ and the inductor coupling dynamic model $G_{ig}(s)$ of Figure 9b are derived and given by (41) and (42) respectively.

$$K_{ig}(s) = \frac{P_{ig}s + I_{ig}}{s} \tag{41}$$

$$G_{ig}(s) = \frac{1}{\tau s + 1}; \tau = L/R \tag{42}$$

where P_{ig} , I_{ig} ; L and R respectively proportional and integral constants; inductance and resistance of the coupling inductor.

2.7. Measuring and Estimation of the Grid Frequency

The grid frequency can be detected or measured through a phase-locked loop (PLL) which is a nonlinear feedback system that generates an output signal whose phase is related to the phase of an input signal. A basic advantage of PLL is to synthesize the grid frequency in a power system.

In a phasor model, however, the PLL is ignored. In this method, the sinusoidal voltages and currents are replaced by phasor quantities (complex numbers) at the system nominal frequency (50 Hz). As a result, measuring of a frequency for controlling is, in a phasor model technique, critically challenging. As stated above, frequency is regulated in an open loop way through the active power control system and, in turn, the dynamic stability of the frequency during contingencies is not ensured. Therefore, a method to synthesize the frequency is proposed in this paper and presented as follows.

In the basic operation principle of a synchronous machine, the rotating magnetic field of the stator is synchronously moving with the speed of the rotor. The frequency of the power system in which the synchronous machine connected to is the number of cycles per second in an alternating current sine wave of the rotating magnetic field of the stator. Its value is practically 50 Hz or 60 Hz. The frequency and the rotor speed are linearly related in the synchronous machine. It is given as

$$f = \frac{p}{120}n \tag{43}$$

where f , p and n are respectively electrical frequency in Hz, number of poles and rotor speed of the machine in rpm

From (43), it is deduced that the per-unit (pu) values of the frequency and rotor speed are equal, i.e., $f_{pu} = n_{pu}$. Thus, taking the pu values of the rotor speed as the pu values of the frequency is practically acceptable. Therefore, the rotor speed is measured and estimated from the synchronous machine and synthesized into the input of the frequency droop controller of the VSPS plant which contains the doubly fed induction machine.

2.8. Voltage Modulation and Converter Reference Voltage

The self-commutated VSC converter is a fast and controllable converter for AC/DC interface applications. One type of VSC converters is a three-level NPC power converter which contains three arms with each four switching components with antiparallel diodes and two NPC diodes. Since this paper is engaged to validate the performance of the proposed system in accordance with the phasor model technique, the following assumptions are taken: the power losses in the converters are neglected and the switching dynamics can be also neglected because the frequency of a pulse width modulation in NPC-VSC is much greater than the frequency of the grid [30]. Hence, modulated and converter reference voltages of the VSCs in this paper are denoted by the equivalent phasor model equations and obtained accordingly.

The modulated voltages of the rotor-side converter are given in (44).

$$m_{dqr} = \left| (2/V_{dc})V_{dqr-ref} * V_{nom} \sqrt{2/3} \right| \tag{44}$$

where $V_{dqr_ref}^*$ is the feed-forward voltage in pu value and V_{nom} is the RMS nominal voltage of the VSPS plant. The converter control voltage is defined by

$$V_{dqr-cont} = |m_{dqr}| \angle(\theta_s + \theta_r + \angle V_{dqr}) \tag{45}$$

where $\angle V_{dqr}$ is an angle obtained from the feed forward voltages.

Similarly, for grid side converter, the modulated and the converter control voltages are obtained and given by the following equations.

$$\begin{aligned} m_{dqg} &= \left| (2/V_{dc}) V_{dqg-ref}^* V_{nom} \sqrt{2/3} \right| \\ V_{dqg-cont} &= |m_{dqg}| \angle(\theta_s + \angle V_{dqg}) \end{aligned} \tag{46}$$

where $V_{dqg_ref}^*$ is the feed-forward voltage in pu value and $\angle V_{dqg}$ is an angle obtained from the feed forward voltages.

Since the converters reference voltage should be fed in actual value, they are determined by

$$\begin{aligned} V_{dqr-conv} &= (1/2)\sqrt{3/2}(V_{dc}/V_{nom})V_{dqr-cont} \\ V_{dqg-conv} &= (1/2)\sqrt{3/2}(V_{dc}/V_{nom})V_{dqg-cont} \end{aligned} \tag{47}$$

where $V_{dqr-conv}$ and $V_{dqg-conv}$ are rotor side and grid side converter reference voltages respectively.

2.9. Case Study and Simulation Model

In this paper, a case-study is undertaken involving a 300 MW DFIM-based VSPS and a power grid system integrated with a wind-farm comprising of seven identical 15 MW wind turbine induction generators. To investigate the impact of wind fluctuations on the grid frequency, a medium power system model consisting of two 200 MVA hydropower plants and one 15 MVA diesel power unit with conventional synchronous generators is established. The phasor model technique in a MATLAB/Simulink platform is applied. For the conventional synchronous machines, the primary voltage regulation method in automatic voltage regulators based on the standard IEEE type I and the primary frequency regulation in turbine governors are used. The simulation network model setup is illustrated in Figure 11 with a single-line diagram.

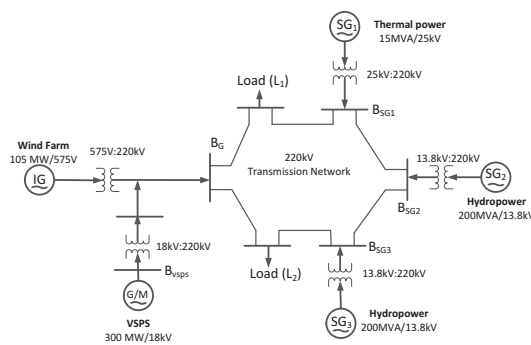


Figure 11. Single-line diagram setup of the VSPS-wind farm-grid integrated system for the case study [15].

3. Results and Discussions

The control of power in the DFIM based VSPS system is essentially the power control of the VSC fed VSPS system. The results presented in this section demonstrate the dynamics and steady-state

responses of grid frequency and AC-bus voltage control. The performances are made by comparing between the control system with and without the droop control.

3.1. VSPS Grid-Integrated Network Simulation and Implications for Regulating Grid Frequency and AC-Bus Voltage in Case of Contingencies

The control of power in the DFIM-based VSPS system with a wind farm is essentially the power control of the VSC-fed VSPS system. Figure 12 shows the evolution of the VSPS unit in the proposed network depicted in Figure 11 but excluding the wind farm and with the absence of contingencies. Generally, the reference reactive power is set to zero for a system without droop control over any operating conditions since there is no reactive power exchange between the converter and the grid. However, to show the performance of the control system, the varying active and reactive power instructional signals are given to the control system as a reference value. As shown in Figure 12a, the proposed control system tracks the power fluctuation instructions very well. A small distortion is observed while the instruction signals vary from one value to the other. A 20% overshoot is perceived during the instruction signal switches from lower to higher values. The overshoots in active power have some impact on frequency deviations. The variations in instructional signal of reactive power cause the AC voltage to deviate from its nominal value. The excursions are quickly regulated. Figure 11b shows the response of the inner loop signals when the power fluctuation instructions are imposed on the outer loop system. The response shows perfect tracking of the respective reference signals. Similarly, precise tracking of inner loop control reference signals in the droop and without droop-fed vector control of the VSPS system along with the wind power farm is also shown in Figure 13. But since the droop-fed matters to change the reference values in the dq-rotor currents, the responses between the control system with and without droop-fed in the dq-rotor currents vary. Hence, the results from Figures 12 and 13 imply that the droop-fed vector control strategy based VSPS system can adjust the grid frequency and AC voltage fluctuations caused by wind energy or other contingencies in a power grid integrated system quickly and flexibly. This is verified in the following sections.

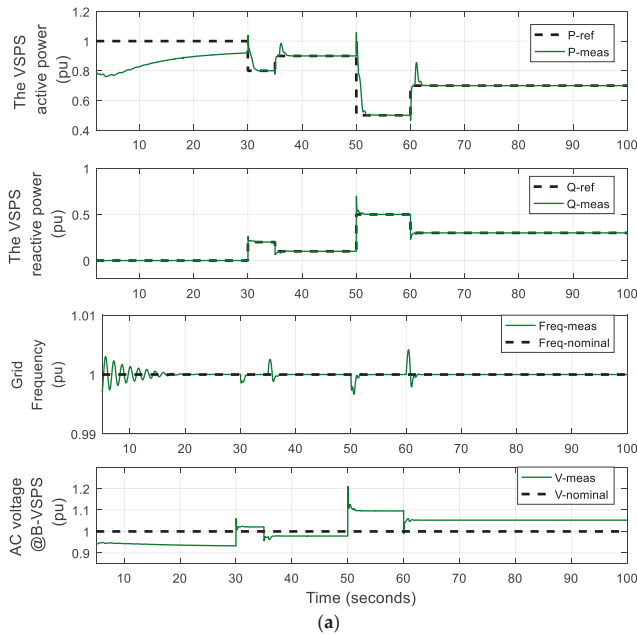


Figure 12. Cont.

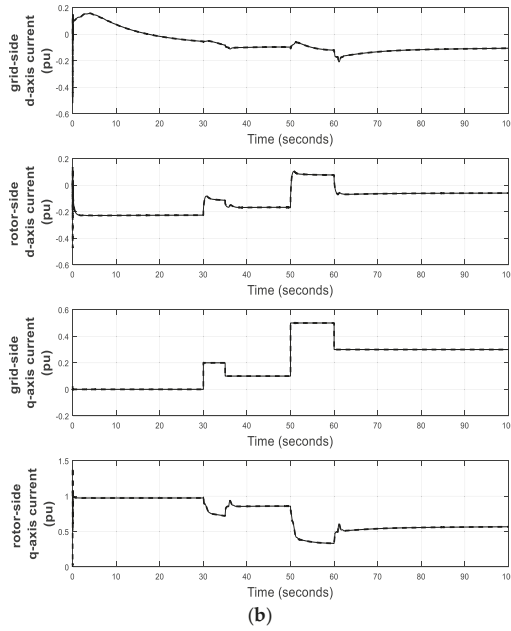


Figure 12. The droop-fed vector control based VSPS system without wind farm: (a) tracking of power instructions on outer loop control; (b) tracking of inner loop control reference signals.

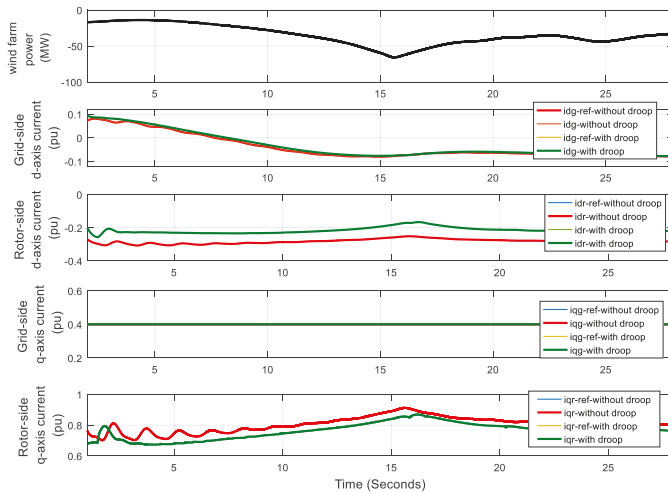


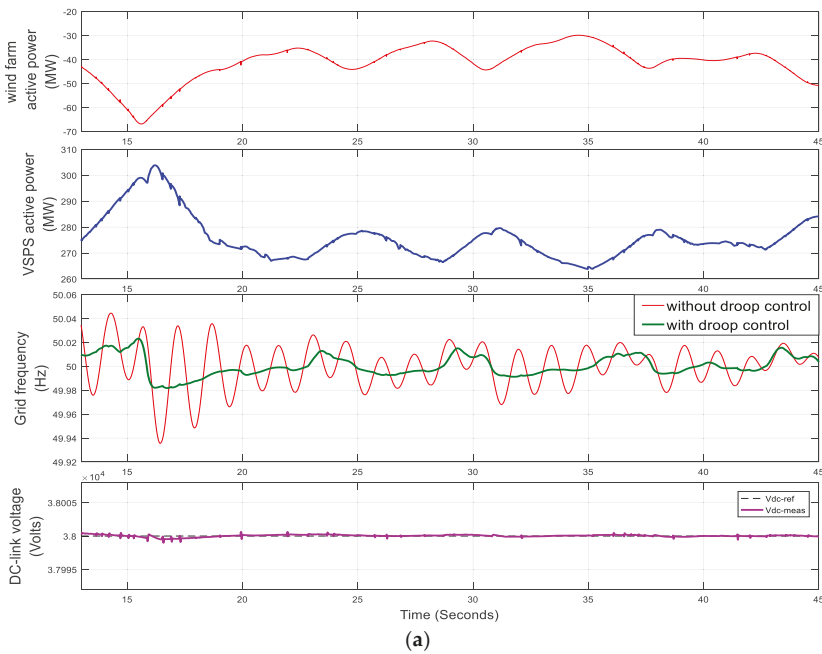
Figure 13. Tracking of inner loop control reference signals in the droop and without droop-fed vector control of the VSPS system along with wind farm.

3.2. Comparison of the Proposed Control Scheme with the Conventional Strategy

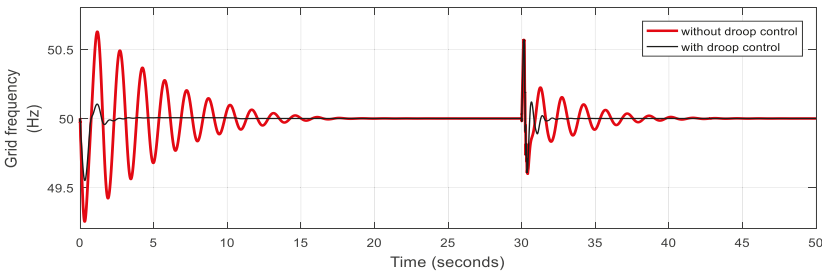
3.2.1. Grid Frequency Control and Response

Figure 14a shows the evolution of the network in grid frequency response by comparing the VSPS active power control with and without droop control and the DC-link voltage. While the power

fluctuation of the wind farm occurs in the grid, the VSPS is dedicated to compensate the fluctuations accordingly and smaller deviations in the grid frequency are recorded with droop than without droop control. The waveform of the DC voltage result shows a precise regulated dynamic response and insignificant deviations for wind power fluctuations. The difference in frequency deviations between the two control modes is more significant at a higher wind power fluctuation. It implies that the droop control system is effective for regulating the grid frequency excursions caused by large contingences. Figure 14b shows the evolution of the frequency comparison between these control modes during the start-up transient and when a three-phase fault is imposed at $t = 30$ s for nine cycles. During the start-up and fault, less excursions in frequency are observed with droop than without droop control. The time taken to dampen the frequency excursions to their nominal value without droop control is much longer than with droop. In this case, the droop control quickly and effectively regulates the frequency dynamics during grid disturbances.



(a)



(b)

Figure 14. Evolution of the network in grid frequency response comparing the VSPS active power control with and without droop control and the DC link voltage as well: (a) while the wind farm power fluctuation exists in the grid; (b) during the start-up transient and three phase fault.

3.2.2. AC-Bus Voltage Control and Response

Figure 15 shows the AC-bus voltage regulation and response of the VSPS vector control system with and without being droop-fed. Two cases with different voltage levels are considered; one at the bus terminal of the VSPS plant (B_{VSPS}), while the other at bus B_{SG3} in the grid system. In both cases, the AC bus voltage is improved to its nominal value with droop-control than without it. The AC voltage is well regulated as the equivalent reactive power is generated by the induction machine to compensate the voltage droop through the VSC based droop-fed vector control strategy. This verifies the strong known relationship between the reactive power and the AC-bus voltage stated in the load flow equation.

Figure 15 also shows the relationship between wind power fluctuations and AC voltage at buses B_{VSPS} and B_{SG3} . When the wind fluctuation is increased, as shown in Figure 15 at $t = 15.1$ s, there is greater deviation in the AC-bus voltage at both buses in the conventional vector control strategy while it remains the same in the droop-fed control mode. This is because of the direct relationship between the reactive power absorbed from the grid by the induction generator of the wind farm and its active power generation. Therefore, the fluctuation of the active power generation caused by the wind speed variation results in higher absorption of reactive power by the induction generator which leads to AC-bus voltage deviation in the grid. Hence, the VSC based droop control of the VSPS system plays a key role of balancing the generation and absorption of reactive power in the grid at varying active power from the wind farm so as to regulate the AC bus voltage.

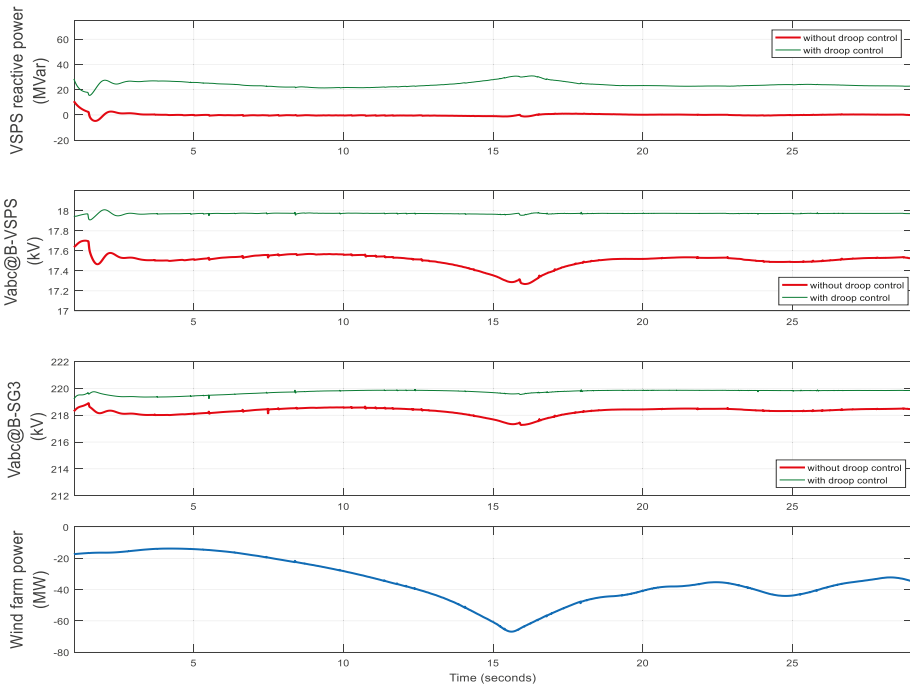


Figure 15. Evolution of the network in AC-bus voltage response of the VSPS control system considered at two buses by comparing the reactive power control with and without droop control while the wind is fluctuating.

3.3. The Frequency and AC Voltage Control and Response During Load Variations

Figure 16 demonstrates the grid frequency and AC bus voltage control and response when 20 MW load is added to the grid at $t = 20$ s and removed at $t = 40$ s in order to compare the performances of the

control modes between the droop-feed and without it. In Figure 16a, the evolution is the grid frequency associated with the active power injected at the bus B_{SG3} and the VSPS active power generation while the load is added and removed to and from the grid. The frequency tracks its nominal value very quickly with the droop control than without droop. In the absence of droop control, when the power imbalance occurs, the frequency is very sensitive for deviation and hardly to control timely. The bus power injection is also affected by the frequency fluctuation, but with the droop control, it regulates the power supply/load balance by adjusting the VSPS to increase or decrease its generation accordingly.

Figure 16b simulates the AC bus voltage control associated with the reactive power status of the VSPS plant. When the load is added to the grid, the AC bus voltage decreases more with the control system without droop mode, but in the droop mode, the voltage tracks its nominal value, because of generating more reactive power by the VSPS plant.

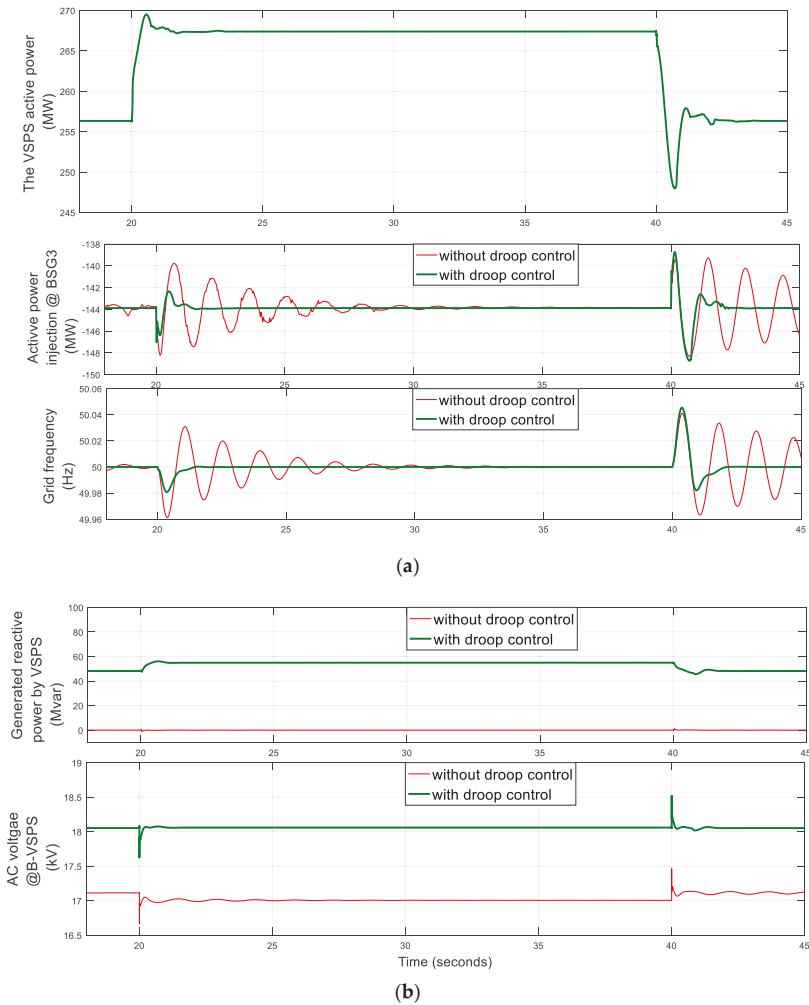


Figure 16. Evolutions of the network in the load variations; (a) in frequency control and response associated with active power; (b) AC bus voltage control and response associated with reactive power generation by the VSPS.

In general, the droop-fed vector control is quite effective to regulate the grid frequency and AC-bus voltage; in turn, it can help the stability development of the grid which are connected to a renewable energy resources.

4. Conclusions

This paper presents a study on droop-fed vector control strategy-based doubly fed induction machine VSPPS system for the reduction of wind power fluctuation impact and other contingencies on grid frequency and AC-bus voltage stability. Mathematical models based on a phasor model technique is presented. A case study of a grid system having five supplies and two loads with seven buses is conducted. The grid includes both synchronous and induction machines. Since the rotor speed rotates synchronously with the rotating magnetic field of the stator of the synchronous machine, the grid frequency is computed from the rotor speed relationship for measuring and estimating to feed the VSPPS active power control loop. The performance is validated in a MATLAB/Simulink platform. The results show that the proposed control strategy for the VSPPS system achieves better dynamic and steady state controlling responses of grid frequency and AC-bus voltage in the power system than the conventional one while the intermittent wind power, load variations three-phase fault and start-up transients are imposed to the grid with small errors in acceptable ranges in the power grid system.

Author Contributions: Conceptualization, G.T.B. and M.H.; Methodology, G.T.B.; Software, G.T.B.; Validation, G.T.B., M.H. and S.A.M.; Formal Analysis, G.T.B.; Investigation, G.T.B.; Resources, M.H.; Data Curation, G.T.B.; Writing-Original Draft Preparation, G.T.B.; Writing-Review & Editing, M.H., P.S. and S.A.M.; Visualization, G.T.B.; Supervision, M.H.; Project Administration, M.H.; Funding Acquisition, M.H.

Funding: This research received no external funding.

Acknowledgments: This work was supported by the State Key Laboratory of Smart Grid Protection and Control, "111" Project (B08013) of China.

Conflicts of Interest: The authors declare no conflict of interest.

Appendix A

The followings are the main parameters of the system used in this paper:

- A VSC DFIM based VSPPS plant; turbine rating = 300 MW; rated hydraulic head=165 m; piping area = 11.15 m²; gate opening at no load = 0.06 pu and at full load = 0.94 pu; base value is taken as a power of 333 MVA and a voltage of 220 kV
 - power capacity = 333 MVA/18 kV, stator resistance and leakage inductance $R_s = 0.0086$ pu and $L_{ls} = 0.152$ pu, rotor resistance and leakage inductance $R_r = 0.007$ pu and $L_{lr} = 0.187$ pu, magnetization inductance $L_m = 300$ pu, inertia constant, friction factor, and pairs of poles $H(s) = 10.6$, $f(\text{pu}) = 0.02$ and $p = 12$
 - Converter rating = 66 MVA/38 kV DC voltage, the DC-link equivalent capacitance $C_{eq} = 2 \times 10^{-2}$ Farad, the coupling inductor resistance and inductance $R = 0.0025$ pu and $L = 0.25$ pu
 - The rotor side controller Current loop gains ($P_i = 1.25$ and $I_i = 15$) Active power loop gains ($P_p = 1.5$ and $I_p = 20$) Reactive power loop gains ($P_q = 0.3$ and $I_q = 5.5$) Frequency droop constant ($K_f = 90$) AC voltage droop constant ($K_{ac} = 60$)
 - The grid side controller Current loop gains ($P_{ig} = 1.1$ and $I_{ig} = 9$) DC voltage loop gains ($P_{dc} = 0.001$ and $I_{dc} = 0.02$)
 - Grid connecting transformer: capacity = 350 MVA, 18 kV/220 kV, winding parameters $R_1 = R_2 = 0.0025$ pu and $L_1 = L_2 = 0.08$ pu; magnetization resistance and inductance $R_m = L_m = 500$ pu
- Two hydropower plants (synchronous generator): each has a power capacity = 200 MVA, 13.8 kV; and grid connecting transformer capacity = 350 MVA, 13.8 kV/220 kV.

- A diesel power plant (synchronous generator): Power capacity = 15 MVA, 25 kV; grid connecting transformer capacity = 20 MVA, 25 kV/220 kV.
- A wind farm with induction generator: seven turbines 15 MW capacity each, 575 V; and grid connecting transformer capacity 12 MVA, 575 V/220 kV for each wind turbine
- Load = 630 MVA and the system frequency is 50 Hz.

References

1. Global Wind Energy Council, Global Wind Energy Outlook 2014, October 2014. Available online: https://www.gwec.net/wp-content/uploads/2014/10/GWEO2014_WEB.pdf (accessed on 10 February 2018).
2. International Energy Agency & Energy Research Institute. *China Wind Energy Development Roadmap 2050*; International Energy Agency & Energy Research Institute: Paris, France, 2011.
3. Li, W.; Joós, G.; Abbey, C. Wind power impact on system frequency deviation and an ess based power filtering algorithm solution. In Proceedings of the 2006 IEEE PES Power Systems Conference and Exposition, 29 October–1 November 2006; pp. 2077–2084.
4. Chowdhury, M.A.; Hosseinzadeh, N.; Shen, W.X. Smoothing wind power fluctuations by fuzzy logic pitch angle controller. *Renew. Energy* **2012**, *38*, 224–233. [[CrossRef](#)]
5. Song, X.; Bitew, G.T.; Han, M.; Meng, Z.; Xu, J.; Wang, X. Stability and control of a grid integrated dfim based variable speed pumped storage system. In Proceedings of the 2017 International Electrical and Energy Conference (CIEEC 2017), Beijing, China, 25–27 October 2017; pp. 175–181.
6. Bocquel, A.; Janning, J. Analysis of a 300 MW variable speed drive for pump-storage plant applications. In Proceedings of the 2005 European Conference on Power Electronics and Applications, Dresden, Germany, 11–14 September 2005; pp. 1–10.
7. Furuya, S.; Taguchi, T.; Kusunoki, K.; Yanagisawa, T.; Kageyama, T.; Kanai, T. Successful achievement in a variable speed pumped storage power system at Yagisawa power plant. In Proceedings of the Conference Record of the Power Conversion Conference—Yokohama 1993, Yokohama, Japan, 19–21 April 1993; pp. 603–608.
8. Chang, X.; Han, M.; Zheng, C. Power control analysis for variable speed pumped storage with full-size converter. In Proceedings of the IECON 2015—41st Annual Conference of the IEEE Industrial Electronics Society, Yokohama, Japan, 9–12 November 2015; pp. 001327–001332.
9. Abdalla, O.H.; Han, M.; Liu, C. Multi-level converter based variable speed pump storage for wind power compensation. In Proceedings of the 2014 International Conference on Information Science, Electronics and Electrical Engineering, Sapporo, Japan, 26–28 April 2014; pp. 1497–1501.
10. Steimer, P.K.; Senturk, O.; Aubert, S.; Linder, S. Converter-fed synchronous machine for pumped hydro storage plants. In Proceedings of the 2014 IEEE Energy Conversion Congress and Exposition (ECCE), Pittsburgh, PA, USA, 14–18 September 2014; pp. 4561–4567.
11. Pronin, M.V.; Shonin, O.B.; Vorontsov, A.G.; Gogolev, G.A. Features of a drive system for pump-storage plant applications based on the use of double-fed induction machine with a multistage-multilevel frequency converter. In Proceedings of the 2012 15th International Power Electronics and Motion Control Conference (EPE/PEMC), Novi Sad, Serbia, 4–6 September 2012; pp. DS1b.7-1–DS1b.7-8.
12. Xu, L.; Cartwright, P. Direct active and reactive power control of dfig for wind energy generation. *IEEE Trans. Energy Convers.* **2006**, *21*, 750–758. [[CrossRef](#)]
13. Bourdoulis, M.K.; Alexandridis, A.T. Direct power control of dfig wind systems based on nonlinear modeling and analysis. *IEEE J. Emerg. Sel. Top. Power Electron.* **2014**, *2*, 764–775. [[CrossRef](#)]
14. Datta, R.; Ranganathan, V.T. Direct power control of grid-connected wound rotor induction machine without rotor position sensors. *IEEE Trans. Power Electron.* **2001**, *16*, 390–399. [[CrossRef](#)]
15. Bitew, G.T.; Han, M.; Simiyu, P.; Zmarrak, W.K.; Luu, K.T.; Faisal, M.S. Direct power control strategy based variable speed pumped storage system for the reduction of the wind power fluctuation impact on the grid stability. In Proceedings of the 12th IEEE International Conference on Compatibility, Power Electronics, and Power Engineering, Doha, Qatar, 10–12 April 2018.
16. Merzoug, M.; Naceri, F. Comparison of field-oriented control and direct torque control for Permanent Magnet Synchronous Motor (PMSM). *Int. J. Electr. Comput. Energy. Electron. Commun. Eng.* **2008**, *2*, 1796–1802.
17. Kundur, P. *Power System Stability and Control*; McGraw-Hill, Inc.: New York, NY, USA, 1994.

18. Maghamizadeh, M.; Fathi, S.H. Virtual flux based direct power control of a three-phase rectifier connected to an Lcl filter with sensorless active damping. In Proceedings of the 2016 7th Power Electronics and Drive Systems Technologies Conference (PEDSTC), Tehran, Iran, 16–18 February 2016; pp. 476–481.
19. Djeriri, Y.; Meroufel, A.; Massoum, A.; Boudjema, Z. A comparative study between field oriented control strategy and direct power control strategy for DFIG. *J. Electr. Eng.* **2014**, *14*, 169–178.
20. Johar, M.; Radan, A.; Miveh, M.R.; Mirsaedi, S. Comparison of dfig and synchronous machine for storage hydro-power generation. *Int. J. Pure Appl. Sci. Technol.* **2011**, *7*, 48–58.
21. MATLAB Package Center. Available online: <https://www.mathworks.com/> (accessed on 1 May 2018).
22. Gihga, R.; Wu, Q.; Nielsen, A.H. Phasor model of full scale converter wind turbine for small-signal stability analysis. *J. Eng.* **2017**, *2017*, 978–983. [[CrossRef](#)]
23. Bitew, G.T.; Han, M.; Meng, Z.; Song, X.; Xu, J.; Simiyu, P. Phasor model simulation of a grid integrated variable speed pumped storage system. *J. Eng.* **2017**, *2017*, 1002–1009.
24. Haileselassie, T.M.; Uhlen, K. Primary frequency control of remote grids connected by multi-terminal HVDC. In Proceedings of the IEEE PES General Meeting, Providence, RI, USA, 25–29 July 2010; pp. 1–6.
25. Vector Control. Available online: https://en.wikipedia.org/wiki/Vector_control/ (accessed on 3 May 2018).
26. Noguchi, T.; Tomiki, H.; Kondo, S.; Takahashi, I. Direct power control of pwm converter without power-source voltage sensors. *IEEE Trans. Ind. Appl.* **1998**, *34*, 473–479. [[CrossRef](#)]
27. Du, C.; Agneholm, E.; Olsson, G. Use of vsc-hvdc for industrial systems having onsite generation with frequency control. *IEEE Trans. Power Deliv.* **2008**, *23*, 2233–2240. [[CrossRef](#)]
28. Azbe, V.; Mihalic, R. Transient stability of doubly-fed induction machine in parallel to synchronous machine. In Proceedings of the 2015 IEEE Eindhoven PowerTech, Eindhoven, The Netherlands, 29 June–2 July 2015; pp. 1–6.
29. Yazdani, A.; Iravani, R. *Voltage-Sourced Converters in Power Systems; Modeling, Control, and Applications*; John Wiley & Sons, Inc.: Hoboken, NJ, USA, 2010.
30. Demiray, T.; Andersson, G.; Busarello, L. Evaluation study for the simulation of power system transients using dynamic phasor models. In Proceedings of the 2008 IEEE/PES Transmission and Distribution Conference and Exposition: Latin America, Bogota, Colombia, 13–15 August 2008; pp. 1–6.



© 2018 by the authors. Licensee MDPI, Basel, Switzerland. This article is an open access article distributed under the terms and conditions of the Creative Commons Attribution (CC BY) license (<http://creativecommons.org/licenses/by/4.0/>).

Article

A Virtual Micro-Islanding-Based Control Paradigm for Renewable Microgrids

Khurram Hashmi ^{1,*}, Muhammad Mansoor Khan ¹, Huawei Jiang ², Muhammad Umair Shahid ¹, Salman Habib ¹, Muhammad Talib Faiz ¹ and Houjun Tang ¹

¹ School of Electronics Information and Electrical Engineering (SEIEE), Shanghai Jiao tong University, No. 800 Dongchuan Road, Shanghai 200240, China; mkhancn@yahoo.com (M.M.K.); muhammadumairshahid@sjtu.edu.cn (M.U.S.); sams560@sjtu.edu.cn (S.H); talib_faiz@sjtu.edu.cn (M.T.F.); hjtang@sjtu.edu.cn (H.T.)

² State Grid, Wuxi Power Supply Company, Wuxi 214000, China; jiang.huawei93@outlook.com

* Correspondence: khurram_hashmi@sjtu.edu.cn; Tel.: +86-132-6290-7351

Received: 27 May 2018; Accepted: 28 June 2018; Published: 4 July 2018

Abstract: Improvements in control of renewable energy-based microgrids are a growing area of interest. A hierarchical control structure is popularly implemented to regulate key parameters such as power sharing between generation sources, system frequency and node voltages. A distributed control infrastructure is realized by means of a communication network that spans the micro-distribution grid. Measured and estimated values, as well as corrective signals are transmitted across this network to effect required system regulation. However, intermittent latencies and failures of component communication links may result in power imbalances between generation sources, deviations in node voltages and system frequency. This paper proposes a hierarchical control structure to regulate the operation of an islanded AC microgrid experiencing communication link failures. The proposed strategy aims to virtually sub-divide the microgrid into controllable “islands”. Thereafter, active power sharing, frequency and voltage restoration is achieved by competing converter systems through multi-agent consensus. The effectiveness of the proposed methodology has been verified through stability analyses using system wide mathematical small signal models and case study simulations in MATLAB, Simpower systems.

Keywords: microgrid control; distributed control; power system operation and control

1. Introduction

Recent advances in renewable energy technologies have led to a greater penetration of distributed renewable energy resources (DERs) in power distribution networks. However, due to the stochastic nature of renewable energy resources, Distributed Generation Units (DGUs) suffer from voltage deviations, frequency and power flow variations. Micro-grids (MGs) present a viable solution to the renewable energy integration problem. A micro grid is usually composed of a smaller power distribution network, energy sources, energy storages, Electric Vehicles (EV), DGUs, supervisory control and data acquisition devices. The MG behaves as a smaller isolated power system that can operate either as an energized island or in synchrony with the legacy power network. Local control measures are applied within the micro-grid to address voltage, frequency and power flow deviations [1–4].

Power conversion stages of multiple DGUs operate in parallel through the MG distribution network. Proportional sharing of power between various DGUs is required to ensure stable system operation and fair power contribution by each generation source in a microgrid. Droop control methods are employed as a simple decentralized strategy for sharing total load power among DGUs. Active and reactive power fractions proportional to frequency and amplitude respectively, are subtracted from

converter output. This method is commonly referred to as P - f and Q - E droop method and has been previously used in the control of un-interruptible power supply systems (UPS) [5–10]. Although, the droop methods provide a degree of reliability, there are certain drawbacks associated therewith. P - f / Q - E droop control works on the principle of reducing frequency and voltage by fractions to achieve power sharing. To keep the system voltage and frequency within a permissible range, a secondary control layer must be implemented to periodically correct these deviations. This can be realized through a centralized hierarchical control; composed of three or more control layers; or a decentralized control strategy where local nodes share information that modifies voltage and frequency references for inner control loops [10–14].

Most centralized control algorithms require a two-way transmission of information between DGUs throughout the system and Microgrid central controllers (MGCC). Such a control structure is often complicated and expensive to implement, in addition to being susceptible to single point of failure (SPOF). Therefore, a decentralized control approach employing consensus algorithms, has emerged as an alternate to centralized control methods [2,15–17]. Consensus-based methods model the frequency and voltage restoration goals as a multi-agent consensus problem; where, each power converter behaves as an agent regulating its voltage and frequency in combination with other agents (nodes), collectively arriving at consensus values for V and f . A virtual leader node may provide desired nominal values for controlled parameters to the micro grid controls [2,18,19].

Some researches propose a secondary voltage restoration method based on distributed cooperative control of multi-agent systems [12], wherein individual inverter units are considered as systems having non-linear internal dynamics. Input-Output feedback linearization is used to convert the secondary voltage restoration problem in such units into a second order linear tracker synchronization problem. The authors in [20] explore active power sharing in islanded AC microgrid with secondary control of frequency and voltage restoration. The inverters have been modeled as cooperative multiagent systems such that their frequency and voltage restoration be a synchronization problem. In [21], the authors present a consensus-based distributed secondary restoration control for both frequency and voltage in droop-controlled AC microgrids.

The authors in [22], present a distributed secondary control method for an inverter-based microgrid with uncertain communication links. The method discussed addresses active power flow control and restoration of frequency and voltage to nominal values. In [23], a distributed control strategy for reactive power sharing and voltage restoration in AC microgrids is presented. The strategy discussed uses small signal model of the system and sensitivity analysis to evaluate the relationship between voltage magnitude and reactive power sharing. In [24], authors have proposed a consensus-based distributed voltage control algorithm for islanded inverter-based microgrids with arbitrary meshed electrical topologies. This algorithm is based on weighted average consensus protocol that replaces traditional V-Q droop method.

The authors in [25] present a dynamic consensus algorithm (DCA) for coordinated control with an autonomous current sharing control strategy to balance discharge rate of energy storage systems (ESS) in an islanded AC microgrid. The DCA is used to share information between DG converter units to regulate output power according to ESS capacities and battery state of charge. In [26] authors propose a cooperative distributed control method for AC microgrids that discusses an alternate for the centralized secondary control and the primary-level droop mechanism of each inverter. Voltage, reactive power, and active power regulators are employed to achieve regulation of these parameters.

The work presented in [12,20,21,23,24] assumes a fault-free communication network with no broken or disrupted communication links. The communication digraph used is, therefore, time in-varying. However, the studies presented in [22,25,26] discuss scenarios with faulty communication links. The authors in [25] have represented faulty communications through a dynamically varying digraph.

This work proposes a hybrid, multi-agent consensus-based control strategy to realize power sharing, voltage and frequency regulation for an islanded AC microgrid. The method developed here addresses faults created by faulty communication links through virtually isolating portions of the

network suffering from communication faults and intermittencies. Thereafter, the control parameters are tuned to treat these isolated portions as smaller “virtual micro-grids” within the larger micro-grid. The salient contributions of this work are:

1. Identification of failed communication links.
2. Virtual segmentation of the MG network into smaller controllable islands.
3. Variation in droop and consensus control parameters to achieve power sharing, voltage and frequency restoration during communication faults.
4. Using small signal analysis to study MG system stability under the proposed control scheme.

The rest of the paper is divided as follows: Section 2 gives the microgrid network layout, derives the admittance matrix and fundamental power flow equations. Section 3 describes the hierarchical control paradigm proposed. Section 4 gives details of the communication network layer and basic graph theoretic definitions. Section 5 expounds the virtual sub islanding method used in this work. Section 6 gives small signal system derivation. Section 7 presents the results of stability analysis using eigen evolutions. Section 8 gives case study simulations and results. Section 9 concludes the paper.

2. Network Layout

This section describes the network layout and derives the admittance matrix and fundamental power flow equations. Figure 1 represents a simplified radial type three phase three wire system used in this study and the proposed four level control strategy. Buses 1 through 6 are fed through power electronic converters interfaced with the network using LC filters. The buses 2 through 6 are directly loaded with adjustable power loads whereas bus-1 is not directly loaded. This network can be operated in islanded mode. Table 1 outlines rated system parameters and Table 2 gives bus loads. All distributed renewable generators are represented by equivalent DC sources. Later sections describe the multi-level control methodology in detail.

Table 1. System parameters for microgrid control.

Parameters	Values	Parameters	Values
L_f	1.35 mH	m_p	4.5×10^{-6}
R_f	0.1 Ω	n_q	1×10^{-6}
C_f	25 μ F	K_{pf}	0.4
L_c	1.35 mH	K_{jf}	0.5
R_c	0.05 Ω	K_{pV}	0.5
R_{ime}	0.1 Ω	K_{iV}	0.3
L_{ime}	0.5 mH	F	1
f_{nom}	60 Hz	ω_c	60 Hz
V_{nom}	415 V _{L-L}		

Table 2. System loads.

Bus. No.	Directly Connected Bus Load	
	P (p.u.)	Q (p.u.)
1.	0	0
2.	0.3	0.3
3.	0.25	0.25
4.	0.25	0.25
5.	0.25	0.25
6.	0.25	0.25
7.	0	0

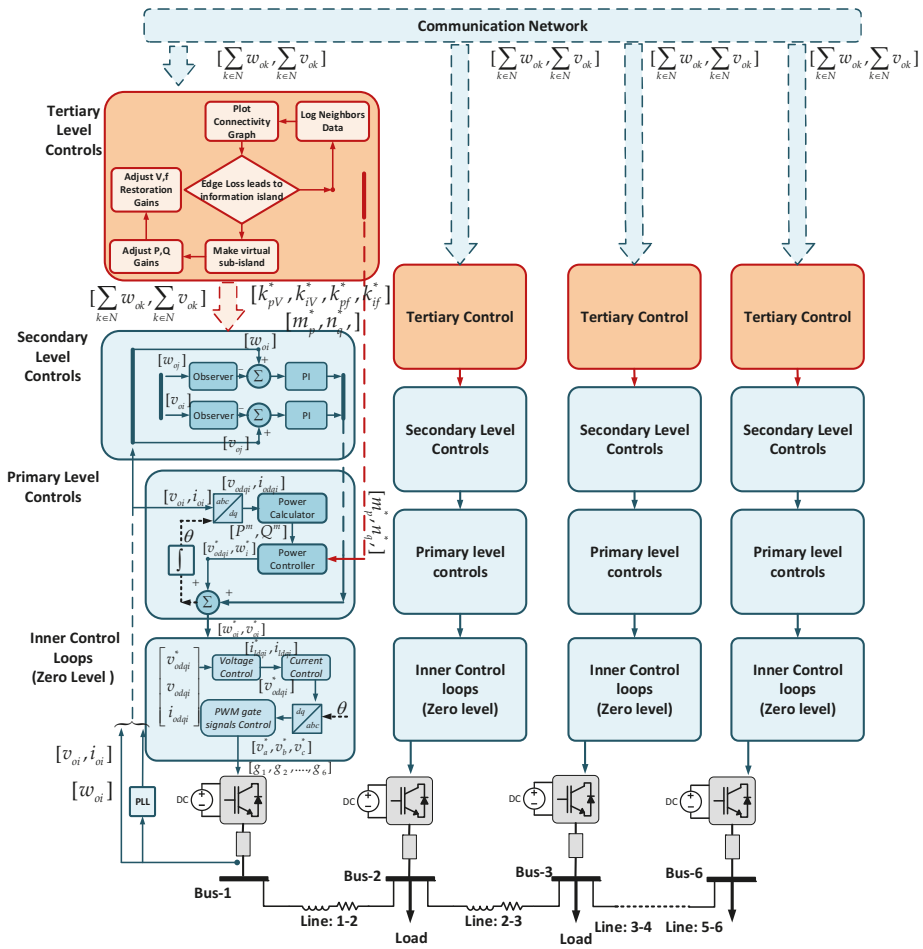


Figure 1. Distribution network and control system layout.

Equation (1) Gives the combined bus admittance matrix of micro network. Equation (2) gives the steady state model of the system.

$$Y_{busMG} = \begin{bmatrix} (Y_{s1} + Y_{17} + Y_{12}) & -Y_{12} & 0 & 0 & 0 & 0 & -Y_{17} \\ -Y_{21} & (Y_{s2} + Y_{23} + Y_{12}) & -Y_{23} & 0 & 0 & 0 & 0 \\ 0 & -Y_{32} & (Y_{s3} + Y_{32} + Y_{34}) & -Y_{34} & 0 & 0 & 0 \\ 0 & 0 & -Y_{43} & (Y_{s4} + Y_{43} + Y_{45}) & -Y_{45} & 0 & 0 \\ 0 & 0 & 0 & -Y_{54} & (Y_{s5} + Y_{54} + Y_{56}) & -Y_{56} & 0 \\ 0 & 0 & 0 & 0 & -Y_{65} & (Y_{s6} + Y_{65}) & 0 \\ -Y_{71} & 0 & 0 & 0 & 0 & 0 & (Y_{71} + Y_{s7}) \end{bmatrix} \quad (1)$$

$$[Y_{busMG}] \bullet [V_1 \ V_2 \ V_3 \ V_4 \ V_5 \ V_6 \ V_7]^T = [I_{s1} \ I_{s2} \ I_{s3} \ I_{s4} \ I_{s5} \ I_{s6} \ I_{s7}]^T \quad (2)$$

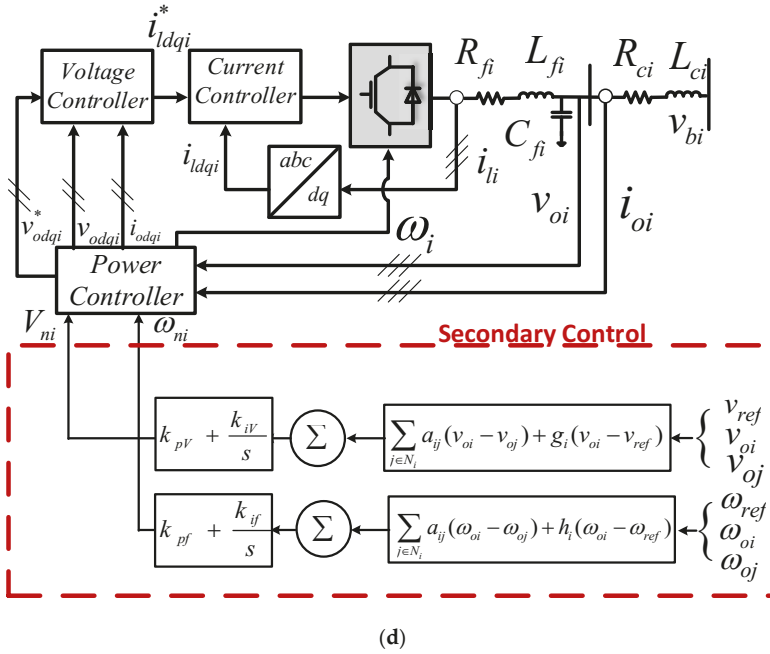


Figure 2. (a) Voltage Control loop; (b) Current Control loop; (c) Primary Control: Power Controller; (d) Secondary Control: Voltage and Frequency regulation.

3.1. Zero Level Control loops: Voltage and Current Regulation

Voltage and current control loops in d-q-0 frame form the zero level control loops for each of the power converters as shown in Figure 2a,b. dynamical equations for voltage control loop are given as (5) and (6).

$$\left. \begin{aligned} \frac{d\phi_{di}}{dt} &= \phi'_{di} = u_{odi}^* - u_{odi} \\ \frac{d\phi_{qi}}{dt} &= \phi'_{qi} = u_{oqi}^* - u_{oqi} \end{aligned} \right\} \quad (5)$$

$$\left. \begin{aligned} i_{ldi}^* &= F_i \cdot i_{odi} - \omega_b \cdot C_{fi} \cdot u_{oqi} + K_{PV_i} (u_{odi}^* - u_{odi}) + K_{IV_i} \phi_{di} \\ i_{lqi}^* &= F_i \cdot i_{oqi} - \omega_b \cdot C_{fi} \cdot u_{odi} + K_{PV_i} (u_{oqi}^* - u_{oqi}) + K_{IV_i} \phi_{qi} \end{aligned} \right\} \quad (6)$$

where, K_{PV_i} and K_{IV_i} represent the proportional and integral gains of the voltage controller. ϕ_{di} and ϕ_{qi} are auxiliary state variables for the PI controllers. F_i is the feed-forward gain. v_{oqi} , v_{odi} , i_{odi} and i_{oqi} are system measurements as seen in Figure 2d.

Similarly, (7) and (8) represent the dynamical model for current control loop at each node as shown in Figure 2b.

$$\left. \begin{aligned} \frac{d\zeta_{di}}{dt} &= \zeta'_{di} = i_{ldi}^* - i_{ldi} \\ \frac{d\zeta_{qi}}{dt} &= \zeta'_{qi} = i_{lqi}^* - i_{lqi} \end{aligned} \right\} \quad (7)$$

$$\left. \begin{aligned} u_{ldi}^* &= -\omega_b \cdot L_{fi} \cdot i_{lqi} + K_{PC_i} (i_{ldi}^* - i_{ldi}) + K_{IC_i} \zeta_{di} \\ u_{lqi}^* &= \omega_b \cdot L_{fi} \cdot i_{ldi} + K_{PC_i} (i_{lqi}^* - i_{lqi}) + K_{IC_i} \zeta_{qi} \end{aligned} \right\} \quad (8)$$

where, K_{PC_i} and K_{IC_i} represent the proportional and integral gains of the voltage controller. ζ_{di} and ζ_{qi} are auxiliary state variables for the PI controllers used. i_{lqi} and i_{ldi} are system measurements as seen in Figure 2d.

3.2. Primary Controls: Power Balancing between Distributed Sources

Power sharing control is based on so called “droop” principle [27], i.e., frequency and voltage are proportionally reduced to achieve active and reactive power sharing respectively as shown in Figure 2c. Equations (9) and (10) represent the droop controller.

$$\omega_i^* = \omega_i - m_{Pi} \cdot (P_i) \tag{9}$$

$$\left. \begin{aligned} V_{di}^* &= V_{di} - n_{Qi} \cdot (Q_i) \\ V_{qi}^* &= 0 \\ V_o &= \sqrt{V_{di}^{*2} + V_{qi}^{*2}} \end{aligned} \right\} \tag{10}$$

where, ω_i and V_0 are the nominal references of frequency and voltage for the i th inverter. P_i and Q_i correspond to active and reactive power being injected by the i^{th} power inverter at output terminals. m_{Pi} and n_{Qi} are droop gains that can be calculated as (11).

$$\left\{ \begin{aligned} m_{Pi} &= \frac{\Delta\omega}{P_{max}} \\ n_{Qi} &= \frac{\Delta V}{Q_{max}} \end{aligned} \right. \tag{11}$$

where, $\Delta\omega$ and ΔV are the maximum change permissible for converter frequency and voltage respectively. P_{max} and Q_{max} are the maximum active and reactive power the converter can deliver [12]. Primary control calculates power using two-axis theory. For accurate measurement of the fundamental power component low pass filters are used having cut off frequency of ω_{ci} . The reference frames of all inverters may be converted a common reference frame. The angle difference between i^{th} inverter and common frequency reference frame can be shown as (12)

$$\delta = \int (\omega - \omega_{com}) \cdot dt \tag{12}$$

where, ω_{com} is the MG common system frequency.

3.3. Secondary Controls: Voltage Magnitude and Frequency Restoration

Voltage magnitude and frequency restoration is achieved through multiagent consensus-based secondary control implemented at each node [28]. Figure 2d shows the distributed frequency and voltage restoration control schemes. Frequency regulation method is given by (13).

$$\left. \begin{aligned} \delta\omega_i(t) &= k_{pf}e_{\omega i}(t) + k_{if} \int e_{\omega i}(t) \cdot dt \\ e_{\omega i}(t) &= \sum_{j \in N_i} \left(\begin{aligned} &a_{ij}(\omega_{oi}(t) - \omega_{oj}(t)) \\ &+ h_i(\omega_{oi}(t) - \omega_{ref}(t)) \end{aligned} \right) \end{aligned} \right\} \tag{13}$$

where, ω_{ref} is the nominal reference frequency, ω_{oj} is the measured system frequency sensed at all nodes in the neighborhood of the i^{th} node being considered. k_{pf} and k_{if} are proportional and integral gains as shown in Figure 2d. $\delta\omega_i$ is the frequency correction applied to frequency reference of the i^{th} inverter node. h_i is pinning gain whose value is zero for primary node.

The voltage regulation method is described in (14):

$$\left. \begin{aligned} \delta V_i &= k_{pv}e_{vi} + k_{iv} \int e_{vi} dt \\ e_{vi}(t) &= \sum_{j \in N_i} \left(\begin{aligned} &a_{ij}(v_{oi}(t) - v_{oj}(t)) \\ &+ g_i(v_{oi}(t) - v_{ref}(t)) \end{aligned} \right) \end{aligned} \right\} \tag{14}$$

where, v_{nom} is the nominal reference voltage for the system in p.u., v_{oj} is the system voltage sensed at all converter nodes in the communication neighborhood of the node i being considered. k_{pv} and k_{iv} are

proportional and integral gains as shown in Figure 2d. δV_i is the voltage correction applied to voltage reference of the i^{th} inverter node. g_i is pinning gain whose value is zero for primary node.

4. Communication Network

The communication network used to exchange information between DGs can be modelled as a digraph. A digraph is usually expressed as $G_{com} = (V_g E_g A_g)$ which is composed of a non-empty, finite set of M nodes given by $V_g = \{v_1 v_2 v_3 \dots v_M\}$. The arcs that connect these nodes are given by $E_g \subset V_g \times V_g$. The associated adjacency matrix is given by $A_g = [a_{ij}] \in R^{N \times N}$. In a microgrid, the DGs can be thought of as the nodes of a communication digraph whereas the arcs represent communication links [28].

In this work, it is assumed that the communication network is initially stable and time invariant as represented in Figure 3a. However, communication links are made to break in analysis given in later sections of the paper. Channel noise has been neglected for simplifying calculations. Therefore, the representative digraph is also initially time invariant, i.e., A_g is a constant. An arc from node j to node i is denoted by (v_j, v_i) , where node j receives information from node i . a_{ij} is the weight of the arc connecting v_i to v_j . $a_{ij} > 0$, if $(v_j, v_i) \in E_g$, otherwise $a_{ij} = 0$. Node i is called a neighbor of node j , if the arc $(v_j, v_i) \in E_g$. Set of nodes neighboring the i th DGU v_i are given by $N_i = \{v_j \in V_g : (v_i, v_j) \in E_g\}$. The Laplacian Matrix $L_g = (l_{ij})_{N \times N}$ is defined as $l_{ij} = -a_{ij}$, $i \neq j$ and $l_{ii} = \sum_{j=1}^N a_{ij}$ for $i = 1, \dots, N$. Such that $L_{1N} = 0$ with $1_N = (1, \dots, 1)^T \in R^N$. The in-degree matrix can be defined as $D_G^{in} = \text{diag} \{d_i^{in}\}$, where, $d_i^{in} = \sum_{j \in N_i} (a_{ji})$ and out-degree matrix as $D_G^{out} = \text{diag} \{d_i^{out}\}$, where $d_i^{out} = \sum_{i \in N_i} (a_{ji})$. The diagonal pinning gain matrix is given by $G = \text{diag} \{g_i\}$. The system adjacency, degree and Laplacian matrix are given in Appendix C.

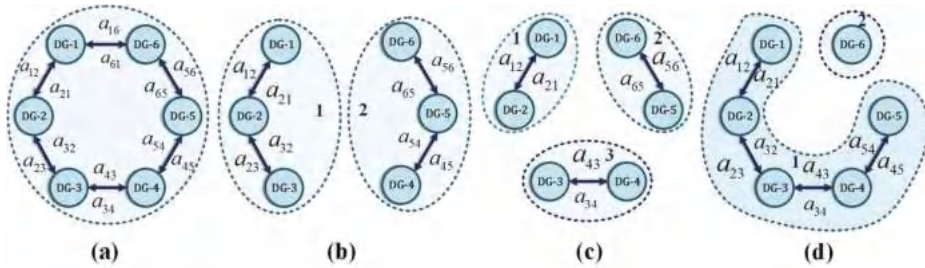


Figure 3. Communication network connectivity: (a) Full ring bidirectional connectivity; (b) Dual link failure resulting in two symmetrical sub networks; (c) Triple link failure resulting in three symmetrical sub networks; (d) Dual link failure resulting in two asymmetrical sub-networks.

The multiagent consensus algorithms implemented across the MG system converge over time according to [29]. The global system dynamics can therefore be given as (15) and (16).

$$\dot{x} = -(D_g + G_g)x + A_g x = -(D_g + G_g - A_g)x + G x_0 \tag{15}$$

where,

$$\dot{x} = -(L_g + G_g)x + G x_0 \tag{16}$$

and,

$$x_0 = 1x_0 = [x_0 \dots x_0]^T$$

5. Virtual Sub-Islanding: Tertiary Controls

In this section, tertiary controls are presented here that monitor network connectivity. When link breakage is detected the microgrid network is virtually partitioned into sub-networks determined by connectivity of healthy communication links as described in Figure 3b,d. The supervisory consensus gains in the secondary control loop and primary control droop gains are subsequently updated to regulate power sharing and frequency voltage regulation. The following subsections further elaborate these functions.

5.1. Cut Set Enumeration

Cut set enumeration is used to analyze virtual segmentation of the microgrid network into major and minor sub-islands. A cut set of a connected graph or nodes may be defined as set of edges whose removal can disconnect the graph or nodes. Therefore, a cut set divides a graph into exact components and can subsequently be used to denote a partition of the vertices [30,31]. If V_g denotes the vertex of graph G , and if P_g is the subset of vertices in one component of graph G induced by a cut set, then the cut set can be represented by, (P_g, \bar{P}_g) , where $\bar{P}_g = V_g - P_g$. The cut set space for a graph with n vertices has dimensions of $(n - 1)$.

5.2. Depth First Search Algorithm

The Depth First Search (DFS) algorithm is used to analyze graph connectivity. A graph G_{com} consists of vertices V_g and edges E_g . Initially all vertices are considered as un-visited. The DFS algorithm starts from any vertex of the graph and follows an edge until it reaches next vertex V_g . While choosing an edge to traverse, an edge emanating from an un-visited vertex is always chosen. A set of old vertices V_g with possible unvisited edges are stored in memory [32,33]. The updated Laplacian matrix then can be obtained as $L_g = D_g^{in} - A_g$ [32,34,35].

The following Lemmas elaborate the formation of cut-sets:

Lemma 1. *A vertex cut set for graph $G_{com} = (V_g, E_g)$ is a sub set of V_g , whose removal will result into a disconnected graph. The vertex connectivity of graph G_{com} , represented by $k_0(G_{com})$, is the minimum number of vertices in any of its vertex cut set. Assuming N nodes form a graph, if two sub sets become disconnected from each other, one of these sets of agents/nodes are considered lost [33]. Since there are two such sets created, the smaller of the two will be considered as lost. We can define a ratio as:*

$$\varnothing(S) = \frac{\varepsilon(S, S^c)}{\min\{card(S), card(S^c)\}} \tag{17}$$

where, $\varepsilon(S, S^c)$ is the number of disconnected nodes, $card(S)$ and $card(S^c)$ are the number of nodes in sub sets.

Cheeger’s Inequality [33] states that:

$$\varnothing(S) \geq \lambda_2(G_{com}) \geq \frac{\varnothing(G_{com})^2}{2d_{max}(G_{com})} \tag{18}$$

Lemma 2. *Let graph $G_{com} = [V_g, E_g]$, for each vertex $v \in V_g$ (node) creates a lookup table that contains all vertices w , such that $(v, w) \in E_g$. This lookup table is called adjacency matrix for vertex V_g . A set of lookup tables at each node (vertices) in graph G_{com} is called adjacent structure for graph G_{com} . A graph may have many adjacency structures because every edge around a vertex gives an adjacency structure and every structure leads to a unique arrangement of edges at each vertex.*

The Depth First Search method (DFS) described in Appendix B [32] functions efficiently using the adjacency structure producing set of edges (E_g) . DFS algorithm is here labeled depth first index,

$DFI(v)$ for every vertex V_g . Initially the value is equal to zero, whereas on the last iteration, the $DFI(v)$ is the order of last visited vertex V_g . The complexity of the algorithm is $O(\max(n, |E_g|))$. For every $v \in V$, $DFI(v)$ is called only once after it will be $DFI(v) = 0$. DFS algorithm total time proportional to $|E_g|$.

The proposed method uses each node to maintain a communication link table of all known nodes throughout the micro network. These tables are updated following an exchange of information between neighboring nodes. When one or more communication links fail partially or completely, as shown in Figure 3b–d, the proposed algorithm virtually segments the network into smaller “virtual” sub micro grids. The control parameters for these scenarios are determined by arriving at good tradeoffs between system stability and better performance for each case. Eigen evolutions are used to arrive at these optimized values that are then stored in lookup tables, as shown in Table 3, that updated droop gains (m_p^* , n_q^*) and consensus gains (K_{pV}^* , K_{iV}^* , K_{pf}^* , K_{jf}^*) accordingly.

Table 3. Controller parameters for analyzed cases.

Cases	Description	Secondary Consensus Gain			Primary Droop Gain	
1.	Full ring network	Voltage	K_{pV} K_{iV}	0.5 0.1	m_p	1.0×10^{-10}
		Frequency	K_{pf} K_{jf}	0.4 0.1	n_q	1.0×10^{-7}
2.	Two symmetrical islands formed	Voltage	K_{pV} K_{iV}	0.7 0.2	m_p	1.0×10^{-5}
		Frequency	K_{pf} K_{jf}	0.8 0.2	n_q	1.0×10^{-3}
3.	Three symmetrical islands formed	Voltage	K_{pV} K_{iV}	1.2 0.3	m_p	2.5×10^{-3}
		Frequency	K_{pf} K_{jf}	1.5 0.2	n_q	1.0×10^{-3}
4.	Two asymmetrical islands formed	Voltage	K_{pV} K_{iV}	3.0 0.5	m_p	2.0×10^{-4}
		Frequency	K_{pf} K_{jf}	2.2 0.5	n_q	1.0×10^{-4}

6. Small Signal Analysis of Microgrid System

To evaluate the performance of a proposed control method, small signal analysis of the MG system is undertaken [29,36]. Large signal dynamical equations are perturbed to obtain small signal model of the entire MG system. This section elaborates the small signal model components used in development and analysis of the control scheme.

6.1. Zero Level Converter Control Model

Small signal model for voltage control are given as in Equations (19)–(22), obtained by perturbing respective dynamical equations around quiescent point at which stability analysis is required [37,38].

$$\Delta\phi_{di} = \phi'_{di} = \Delta v_{odi}^* - \Delta v_{odi} \tag{19}$$

$$\Delta\phi_{qi} = \phi'_{qi} = \Delta v_{oqi}^* - \Delta v_{oqi} \tag{20}$$

$$\Delta i_{di}^* = F_i \cdot \Delta i_{odi} - \omega_b \cdot C_{fi} \cdot \Delta v_{oqi} + K_{pVi} (\Delta v_{odi}^* - \Delta v_{odi}) + K_{iVi} \phi_{di} \tag{21}$$

$$\Delta i_{qi}^* = F_i \cdot \Delta i_{oqi} - \omega_b \cdot C_{fi} \cdot \Delta v_{odi} + K_{pVi} (\Delta v_{oqi}^* - \Delta v_{oqi}) + K_{iVi} \phi_{qi} \tag{22}$$

where, K_{PV_i} and K_{IV_i} represent the proportional and integral gains of the voltage controller. $\Delta\phi_{di}$ and $\Delta\phi_{qi}$ are perturbations in auxiliary state variables for the PI controllers. F_i is the feed-forward gain. v_{oqi} , v_{odi} , i_{odi} and i_{oqi} are system measurements as described before.

Similarly, Equations (23)–(26) represent the small signal model for current control loop at each node as shown in Figure 2b.

$$\Delta\zeta_{di} = \zeta'_{di} = \Delta i_{ldi}^* - \Delta i_{ldi} \tag{23}$$

$$\Delta\zeta_{qi} = \zeta'_{qi} = \Delta i_{lqi}^* - \Delta i_{lqi} \tag{24}$$

$$\Delta v_{ldi}^* = -\omega_b \cdot L_{fi} \cdot \Delta i_{lqi} + K_{PCi} (\Delta i_{ldi}^* - \Delta i_{ldi}) + K_{ICi} \cdot \Delta\zeta_{di} \tag{25}$$

$$\Delta v_{lqi}^* = \omega_b \cdot L_{fi} + K_{PCi} (\Delta i_{lqi}^* - \Delta i_{lqi}) + K_{ICi} \cdot \Delta\zeta_{qi} \tag{26}$$

where, K_{PCi} and K_{ICi} represent the proportional and integral gains of the voltage controller. $\Delta\zeta_{di}$ and $\Delta\zeta_{qi}$ are perturbations in auxiliary state variables for the PI controllers used. i_{lqi} and i_{ldi} are system measurements as described before in Section 3.

6.2. Primary Power Sharing Control Model

The linearized small signal model for power controller can be written as Equations (27) and (28). The power controller provides operating frequency for the DGU (ω_i) and reference voltage (v_{odi}^* and v_{oqi}^*) for voltage control loop [12].

$$\Delta P = -\omega_{ci} \Delta P_i + \omega_{ci} (I_{od} \Delta v_{od} + I_{oq} \Delta v_{oq} + V_{od} \Delta i_{od} + V_{oq} \Delta i_{oq}) \tag{27}$$

$$\Delta Q = -\omega_{ci} \Delta Q_i + \omega_{ci} (I_{oq} \Delta v_{od} - I_{od} \Delta v_{oq} - V_{oq} \Delta i_{od} + V_{od} \Delta i_{oq}) \tag{28}$$

where I_{od} , I_{oq} , V_{od} and V_{oq} represent steady state values of i_{od} , i_{oq} , v_{od} , v_{oq} as in Figure 2c,d. ω_{ci} is the cut-off frequency for low pass filters employed in the power calculator.

Small signal model of frequency and voltage control are given by (29) and (30):

$$\left. \begin{aligned} \Delta\omega &= -m_p \cdot \Delta P \\ \Delta v_{od}^* &= -n_q \cdot \Delta Q \\ \Delta v_{oq}^* &= 0 \end{aligned} \right\} \tag{29}$$

$$\Delta\delta = \Delta\omega - \Delta\omega_{com} = -m_p \cdot \Delta P - \Delta\omega_{com} \tag{30}$$

6.3. Grid-Side Filter Model

The small signal model for the LC output filter can be given by Equations (31)–(36):

$$\Delta \dot{i}_{ldi} = -\frac{R_{fi}}{L_{fi}} \cdot \Delta i_{ldi} + \omega_i \cdot \Delta i_{lqi} + \frac{1}{L_{fi}} \cdot \Delta v_{ldi} - \frac{1}{L_{fi}} \cdot \Delta v_{odi} + I_{lq} \cdot \Delta\omega \tag{31}$$

$$\Delta \dot{i}_{lqi} = -\frac{R_{fi}}{L_{fi}} \cdot \Delta i_{lqi} - \omega_i \cdot \Delta i_{ldi} + \frac{1}{L_{fi}} \cdot \Delta v_{lqi} - \frac{1}{L_{fi}} \cdot \Delta v_{oqi} + \Delta\omega \tag{32}$$

$$\Delta \dot{v}_{odi} = \omega_i \cdot \Delta v_{oqi} + \frac{1}{C_{fi}} \cdot \Delta i_{ldi} - \frac{1}{C_{fi}} \cdot \Delta i_{odi} + V_{oq} \cdot \Delta\omega \tag{33}$$

$$\Delta \dot{v}_{oqi} = \omega_i \cdot \Delta v_{odi} + \frac{1}{C_{fi}} \cdot \Delta i_{lqi} - \frac{1}{C_{fi}} \cdot \Delta i_{oqi} - V_{od} \cdot \Delta\omega \tag{34}$$

$$\Delta \dot{i}_{odi} = -\frac{R_{ci}}{L_{ci}} \cdot \Delta i_{odi} + \omega_i \cdot \Delta i_{oqi} + \frac{1}{L_{ci}} \cdot \Delta v_{odi} - \frac{1}{L_{ci}} \cdot \Delta v_{bdi} + I_{oq} \cdot \Delta\omega \tag{35}$$

$$\Delta i_{oqi} = -\frac{R_{ci}}{L_{ci}} \cdot \Delta i_{oqi} - \omega_i \cdot \Delta i_{odi} + \frac{1}{L_{ci}} \cdot \Delta v_{oqi} - \frac{1}{L_{ci}} \cdot \Delta v_{bqi} - I_{od} \cdot \Delta \omega \quad (36)$$

The input and output parameters as shown in Figure 2d are transformed to the common reference frame using transformation matrix T_γ as in Equations (37) and (38):

$$[\Delta i_oDQ] = [T_\gamma] \cdot [i_{odq}] = \begin{bmatrix} \cos(\delta) & -\sin(\delta) \\ \sin(\delta) & \cos(\delta) \end{bmatrix} \cdot [\Delta i_{odq}] + \begin{bmatrix} -I_{od} \cos(\delta) & -I_{oq} \sin(\delta) \\ I_{od} \sin(\delta) & -I_{oq} \cos(\delta) \end{bmatrix} [\Delta \delta] \quad (37)$$

$$[\Delta u_{bdq}] = [T_\gamma^{-1}] \cdot [u_{bDQ}] = \begin{bmatrix} \cos(\delta) & \sin(\delta) \\ -\sin(\delta) & \cos(\delta) \end{bmatrix} \cdot [\Delta v_{bDQ}] + \begin{bmatrix} -U_{bD} \sin(\delta) & -U_{bQ} \cos(\delta) \\ -U_{bD} \cos(\delta) & -U_{bQ} \sin(\delta) \end{bmatrix} [\Delta \delta] \quad (38)$$

6.4. Small Signal Model of the i^{th} Inverter

The components described in previous sections can be combined to arrive at a small signal model of i^{th} distributed generation unit. This model can be written in suitable form as:

$$[\Delta \dot{x}_{invi}] = A_{invi} \cdot [\Delta x_{invi}] + B_{invi} \cdot [\Delta u_{bDQi}] + B_{iWcom} \cdot [\Delta w_{com}] \quad (39)$$

$$\begin{bmatrix} \Delta w_i \\ \Delta i_{oDQi} \end{bmatrix} = \begin{bmatrix} C_{invwi} \\ C_{invci} \end{bmatrix} \cdot [\Delta x_{invi}] \quad (40)$$

where the state vector is

$$[\Delta x_{inv}] = \begin{bmatrix} \Delta \delta_i & \Delta P_i & \Delta Q_i & \Delta \phi_{di} & \Delta \phi_{qi} & \Delta \zeta_{di} & \Delta \zeta_{qi} & \Delta i_{ldi} & \Delta i_{lqi} \\ & & & & & \Delta v_{odi} & \Delta v_{oqi} & \Delta i_{odi} & \Delta i_{oqi} \end{bmatrix}^T \quad (41)$$

The matrices A_{invi} , B_{invi} , B_{iWcom} , C_{invwi} , C_{invci} depend on component values and may be calculated as shown in appendices.

6.5. Combined Model of N Inverters

A combined model for power converters paralleled through the microgrid network is presented as in Equations (42)–(47):

$$\left. \begin{aligned} [\Delta x_{inv}] &= A_{inv} \cdot [\Delta x_{inv}] + B_{inv} \cdot [\Delta v_{bDQ}] \\ [\Delta i_{oDQ}] &= C_{inv} \cdot [\Delta x_{inv}] \end{aligned} \right\} \quad (42)$$

$$[\Delta x_{inv}] = [\Delta x_{inv1} \ \Delta x_{inv2} \ \dots \ \Delta x_{invN}]^T \quad (43)$$

$$A_{inv} = \begin{bmatrix} A_{inv1} + B_{1Wcom} C_{invw1} & 0 & 0 & 0 \\ 0 & A_{inv2} + B_{2Wcom} C_{invw2} & 0 & 0 \\ 0 & 0 & \cdot & 0 \\ 0 & 0 & 0 & A_{invN} + B_{NWcom} C_{invwN} \end{bmatrix} \quad (44)$$

$$B_{inv} = \begin{bmatrix} B_{inv1} \\ B_{inv2} \\ \cdot \\ B_{invN} \end{bmatrix} \quad (45)$$

$$[\Delta v_{bDQ}] = [\Delta v_{bDQ1} \ \Delta v_{bDQ2} \ \dots \ \Delta v_{bDQN}]^T \quad (46)$$

$$C_{inv} = \begin{bmatrix} [C_{invc1}] & 0 & 0 & 0 \\ 0 & [C_{invc2}] & 0 & 0 \\ 0 & 0 & \cdot & 0 \\ 0 & 0 & 0 & [C_{invcN}] \end{bmatrix} \quad (47)$$

6.6. Load and Network Model

A combined model for load and network, derived through Kirchhoff voltage and current laws, can be expressed in terms of line currents and node voltages as in (48) and (49):

$$[\Delta \dot{i}_{lineDQ}] = A_{NET} [\Delta i_{lineDQ}] + B_{1NET} [\Delta u_{bDQ}] + B_{2NET} \cdot \Delta \omega \quad (48)$$

$$[\Delta \dot{i}_{loadDQ}] = A_{LOAD} [\Delta i_{loadDQ}] + B_{1LOAD} [\Delta u_{bDQ}] + B_{2LOAD} \cdot \Delta \omega \quad (49)$$

where, A_{NET} , B_{1NET} , B_{2NET} and A_{LOAD} , B_{1LOAD} , B_{2LOAD} are network and load matrices, respectively, given in Appendix A.

6.7. Micro Grid Model

Finally, we can combine above described component models to express a small signal model for the complete microgrid system (50)–(55). The system used here is composed of $s = 6$ DGUs, $n = 6$ lines, $p = 5$ loads, $m = 7$ nodes. MATLAB Simulink, and Linear analysis tools (R2018a, product registered to SJTU, Shanghai, China) have been used to analyze this complex system by perturbing dynamical equations of the same.

$$[\Delta v_{bDQ}] = R_N (M_{inv} [\Delta i_{oDQ}] + M_{Load} [\Delta i_{loadDQ}] + M_{net} [\Delta i_{lineDQ}]) \quad (50)$$

$$R_N = \begin{bmatrix} r_N & & \\ & \ddots & \\ & & r_N \end{bmatrix}_{2m \times 2n} \quad (51)$$

$$M_{Load} = \begin{bmatrix} -1 & & \\ & \ddots & \\ & & -1 \end{bmatrix}_{2m \times 2p} \quad (52)$$

$$M_{net} = \begin{bmatrix} -1 & & & & \\ 0 & -1 & & & \\ 1 & 0 & -1 & & \\ & 1 & 0 & -1 & \\ & & 1 & 0 & \\ & & & 1 & \end{bmatrix}_{2m \times 2n} \quad (53)$$

$$M_{inv} = \begin{bmatrix} 1 & & & & \\ & 1 & & & \\ 0 & 0 & 0 & 0 & \\ 0 & 0 & 0 & 0 & \\ & & 1 & & \\ & & & & 1 \end{bmatrix}_{2m \times 2s} \quad (54)$$

$$\begin{bmatrix} \Delta \dot{x}_{inv} \\ \Delta \dot{i}_{lineDQ} \\ \Delta \dot{i}_{loadDQ} \end{bmatrix} = A_{MG} \begin{bmatrix} \Delta x_{inv} \\ \Delta i_{lineDQ} \\ \Delta i_{loadDQ} \end{bmatrix} \quad (55)$$

where, (53) represents the complete small signal model of the MG system used in this study. The system matrix A_{MG} is provided in the appendices.

7. Stability and Sensitivity Analysis

The small signal model of the MG given by Equations (48)–(53) is utilized to plot eigen values of the system under varying control and system parameters. Eigen values or modes are solutions to characteristic equation of the system’s linearized state matrix. Sensitivity of the system states to changes in system parameters can be determined by analyzing the system state matrix A_{MG} . A sensitivity factor rp_{ki} gives the measure of association between different state variables and their participation in modes [36,39]. Sensitivity, rp_{ki} of an eigen value λ_i , in relation to the corresponding diagonal element of state matrix a_{kk} , can be given by (56):

$$rp_{ki} = \frac{\partial \lambda_i}{\partial a_{kk}} \tag{56}$$

Eigen evolution traces are plotted to perform stability and sensitivity analyses, ascertain limits for the test MG network under the proposed control scheme. The droop gains of all inverters as well as multiagent consensus gains have been perturbed to arrive at operational limits of the system as given in Table 4. Eigen traces given in Figure 4a–d demonstrate system behavior under varying control gains. Figure 4a shows the movement of eigen values with increase in m_p , towards the right half plane. Figure 4b shows the movement of eigen values under influence of increasing proportional consensus gains, (K_{pV}, K_{pf}) , towards the right half plane. Figure 4c shows the movement of eigen values under influence of increasing integral consensus gains, (K_{iV}, K_{if}) towards the left half of the plane. Proportional consensus gains (K_{pV}, K_{pf}) tend to force the system towards early convergence, however they push the system stability to its limits. Conversely, integral consensus gains (K_{iV}, K_{if}) tend to stabilize the system. Figure 4d shows the movement of poles under influence of increasing reactive power control gains n_q , towards the right half plane. Table 4 gives operational limits of control parameters obtained from the analysis. Overall, the MG system is more sensitive towards variation in reactive power control gains n_q than active power gains m_p .

Table 4. Variation range for primary and secondary controller gains.

Sr. No.	Control Parameters		
1.	Droop Gains	Min.	Max.
	m_p	1×10^{-10}	1×10^{-3}
	n_q	1×10^{-7}	1×10^{-3}
2.	Consensus frequency		
	k_{pf}	0.4	2.5
	k_{if}	0.1	0.6
3.	Consensus voltage		
	k_{pV}	0.5	3.5
	k_{iV}	0.1	0.7

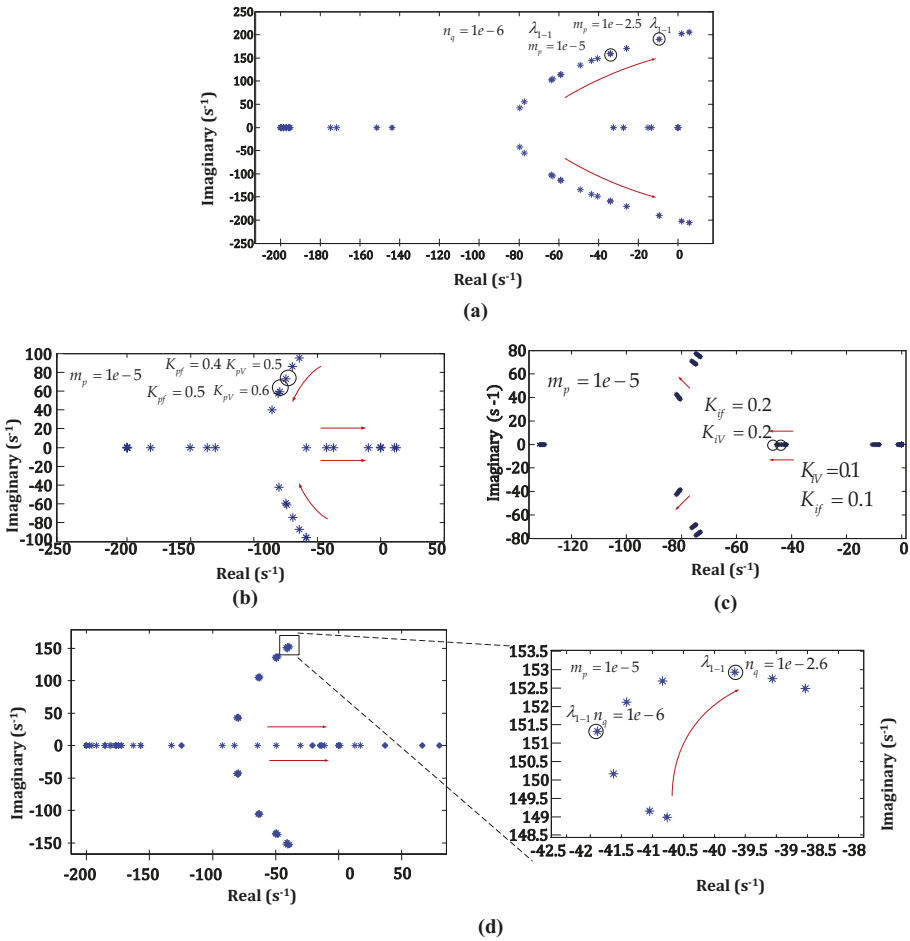


Figure 4. Observing effect of control gain variation on system stability through eigen traces: (a) effect of variation in m_p ; (b) effect of variation in tertiary controller integral gains; (c) effect of variation in tertiary controller proportional gains; (d) effect of variation in n_q .

8. Evaluation with Case Studies

This section elaborates case study simulations undertaken for scenarios resulting from multiple communication link failures. The proposed algorithm subsequently segments the microgrid network into “virtual sub islands” described as follows. Figure 5a–g gives active power sharing results for each case discussed.

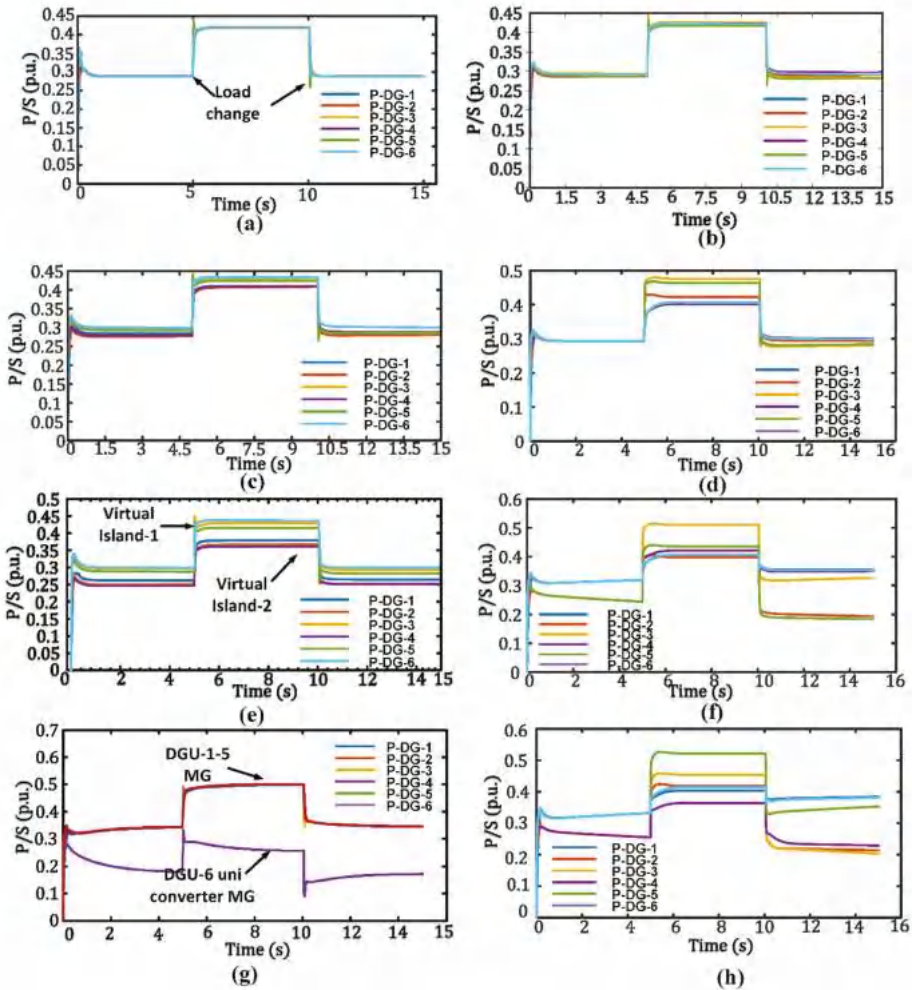


Figure 5. Comparison of active power sharing under proposed control strategy and conventional consensus-based control with varying communication network health: (a) Full ring connectivity with proposed control; (b) Full ring connectivity with consensus-based control; (c) Triple link failure, three sub-islands with proposed control; (d) Triple link failure, three sub-islands with consensus-based control (e) Dual link failure, two sub-islands with proposed control (f) Dual link failure, two sub-islands with conventional consensus-based control (g) Dual link failure, two asymmetrical sub-islands with proposed control (h) Dual link failure, two asymmetrical sub-islands with consensus-based control.

8.1. Case-1: Full Ring Sparse Connected Communication Network

In the first scenario considered, the communication network between nodes forms a complete ring digraph as represented in Figure 3a. All nodes receive information from neighboring nodes and, as such, no communication islands are formed. All converter nodes converge to proportional values of active power injection as seen in Figure 5a.

8.2. Case-2: Two Sub Groups with Equal Number of Members

This scenario is based on multiple link failures leading to the segmentation of the microgrid communication network into two virtual islands of approximately equal size. The DGUs 1 through 3 form one communication sub-island whereas DGUs 4 through 6 form another sub-island as shown in Figure 3b. Subsequently, with the aid of proposed controls, active power injected by all nodes falls within two subgroups as can be seen Figure 5c, whereas, in absence thereof, the injected powers diverge, as seen in Figure 5e.

8.3. Case-3: Three or More Sub Groups with Equal Number of Members

This considers a scenario where communication link failures divide the microgrid information network into three or more virtual sub-islands approximately equal in size viz the number of nodes in each. Accordingly, DGUs 1 and 2, 3 and 4, 5 and 6, form three virtual sub islands as shown in Figure 3c. The control algorithms within each sub-island drive the system to achieve proportional power sharing as shown in Figure 5e. Conversely, Figure 5c shows an imbalance in injected active powers when the proposed tertiary controls are absent.

8.4. Case-4: Two Sub Groups with Un-Equal Number of Members

This scenario considers an event wherein one node becomes completely isolated from the other nodes due to multiple communication link failures. The DGUs 1 through 5 correspond to one virtual sub-island. Whereas, the DGU-6 is isolated as an individual converter sub-island as shown in Figure 3d. The results obtained for this can be seen in Figure 5g. It may be observed that tertiary controls enable the power injected to fall within two subgroups accordingly, whereas, in absence thereof, the injected powers diverge.

8.5. Comparison with Previous Conventional Control Strategies

Figure 5 compares the simulation study results obtained for the proposed control strategy with results of conventional consensus-based control and distributed estimation-based methods. The left half of the figure (Figure 5: (a) (c) (e) (g)) shows the results for the proposed method, whereas, those on the right (Figure 5: (b) (d) (f) (h)) are the results of consensus-based control. It can be observed that for all cases presented, the proposed method shows better convergence than previously existing control schemes. Figure 6a,b present results for frequency and voltage restoration with the proposed control strategy, whereas, subfigures (c) and (d) present results of frequency and voltage restoration with consensus-based control under faulted communication links. Table 5 compares the proposed strategy with conventional methods previously discussed under similar testing circumstances following respective details presented. The proposed method shows early convergence under a given condition as compared with others with lesser active power mismatch between DGUs.

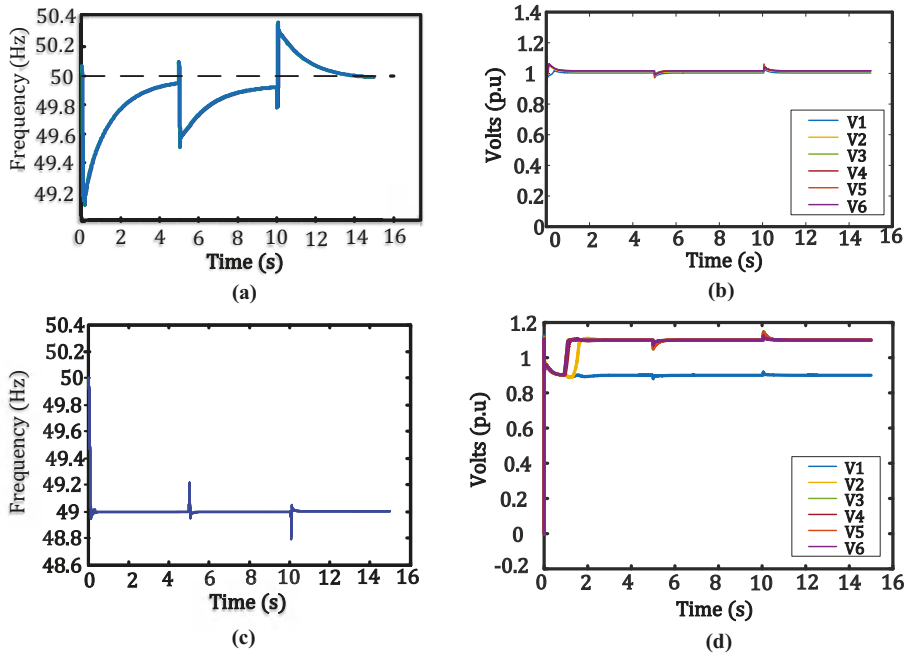


Figure 6. System performance under communication failures: (a) Frequency restoration with the proposed control strategy; (b) Voltage restoration with the proposed control strategy; (c) Frequency restoration with consensus-based control; (d) Voltage restoration with consensus-based control.

Table 5. Comparison of the proposed control strategy with existing conventional Strategies.

Sr. No.	Parameters	Proposed Method	Distributed Estimation-Based Methods [22,25,26]	Consensus-Based Methods [12,20,21,23]
1.	Maximum Active power mismatch	0.03 p.u.	0.05 p.u.	0.10 p.u.
2.	Max Voltage variation	0.01 p.u.	0.1 p.u.	0.2 p.u.
3.	Max frequency variation	0.4 Hz (4.0×10^{-5} Hz/VA)	0.2 Hz (2.0×10^{-5} Hz/VA)	1 Hz (1.0×10^{-5} Hz/VA)
4.	Convergence time (frequency)	4 s	10 s	No convergence if links severed
5.	Convergence time (voltage)	1 s	7 s	No convergence if links severed

9. Conclusions

A hierarchical multiagent consensus-based control strategy is proposed to address the coupled objectives of power balancing between generation sources, voltage and frequency restoration in islanded AC microgrids. A sparse communication network spans alongside a system distribution network and provides media for communication of estimated values and corrective signals. The proposed method mitigates system instability and power sharing imbalances when the supervisory communication network is experiencing link failures. The nodes lying inside connected communication neighborhoods form virtual “sub-islands”, wherein, power sharing, voltage and frequency regulation

control function with reference to locally available information. To verify the effectiveness of the proposed strategy, mathematical small signal models of individual components are stitched together to form an MG system model. These models are then used to analyze the performance of the said controls using eigen plots with regards to system stability and sensitivity towards variation in control parameters. Case simulation studies for different communication scenarios are undertaken. The two kinds of analyses adopted verify the effectiveness of the proposed control strategy for the given scenarios.

Author Contributions: K.H., M.U.S. and M.M.K. have contributed to the conceptualization behind this work. K.H. has prepared the write up and manuscript. M.U.S. has prepared the algorithms used in this paper, whereas, M.M.K. has helped with small signal modelling and validation. S.H. has helped with the write up, sectionalizing and appropriate referencing. H.J. and M.T.F. have helped with the software and experimental verification. This work had been jointly supervised by M.M.K. and H.T.

Funding: This research received no external funding.

Conflicts of Interest: The authors declare no conflict of interest.

Appendix A. System Matrices

$$A_{MG} = \begin{bmatrix} A_{inv} + B_{inv}R_N M_{inv} C_{inv} & B_{inv}R_N M_{net} & B_{inv}R_N M_{Load} \\ B_{1net}R_N M_{inv} C_{inv} + B_{2net}C_{inv.\omega} & A_{net} + B_{1net}R_N M_{net} & B_{1Net}R_N M_{Load} \\ B_{1Load}R_N M_{inv} C_{inv} + B_{2Load}C_{inv.\omega} & B_{1Load}R_N M_{net} & A_{Load} + B_{1Load}R_N M_{Load} \end{bmatrix}$$

$$A_{Invi} = \begin{bmatrix} A_{Pi} & 0 & 0 & B_{Pi} \\ B_{V1i}C_{Pvi} & 0 & 0 & B_{V2i} \\ B_{C1i}D_{V1i}C_{Pvi} & B_{C1i}C_{Vi} & 0 & B_{C1i}D_{V2i} + B_{C2i} \\ B_{LCL1i}D_{C1i}D_{V1i}C_{Pvi} + B_{LCL2i}[T_{Vi}^{-1}00] & B_{LCL1i}D_{C1i}C_{Vi} & B_{LCLi}C_{Ci} & A_{LCLi} + \\ B_{LCL3i}C_{Pwi} & & & B_{LCLi}(D_{C1i}D_{V2i} + D_{C2i}) \end{bmatrix}_{13 \times 13}$$

$$A_{net} = \begin{bmatrix} \frac{-R_{line1}}{L_{line1}} & \omega_0 & 0 & 0 & 0 & 0 \\ -\omega_0 & \frac{-R_{line1}}{L_{line1}} & 0 & 0 & 0 & 0 \\ 0 & 0 & \frac{-R_{line2}}{L_{line2}} & \omega_0 & 0 & 0 \\ 0 & 0 & -\omega_0 & \frac{-R_{line2}}{L_{line2}} & 0 & 0 \\ 0 & 0 & 0 & 0 & \frac{-R_{lineN}}{L_{lineN}} & \omega_0 \\ 0 & 0 & 0 & 0 & -\omega_0 & \frac{-R_{lineN}}{L_{lineN}} \end{bmatrix}$$

$$A_{load} = \begin{bmatrix} \frac{-R_{load1}}{L_{load1}} & \omega_0 & 0 & 0 & 0 & 0 \\ -\omega_0 & \frac{-R_{load1}}{L_{load1}} & 0 & 0 & 0 & 0 \\ 0 & 0 & \frac{-R_{load2}}{L_{load2}} & \omega_0 & 0 & 0 \\ 0 & 0 & -\omega_0 & \frac{-R_{load2}}{L_{load2}} & 0 & 0 \\ 0 & 0 & 0 & 0 & \frac{-R_{loadN}}{L_{loadN}} & \omega_0 \\ 0 & 0 & 0 & 0 & -\omega_0 & \frac{-R_{loadN}}{L_{loadN}} \end{bmatrix}$$

$$B_{1net} = \begin{bmatrix} \frac{1}{L_{line1}} & & & & & \\ & \frac{1}{L_{line1}} & & & & \\ & & -\frac{1}{L_{line1}} & & & \\ & & & -\frac{1}{L_{line1}} & & \\ & & & & \dots & \\ & & & & & \frac{1}{L_{lineN}} & & \\ & & & & & & -\frac{1}{L_{lineN}} & \\ & & & & & & & \frac{1}{L_{lineN}} & & \\ & & & & & & & & -\frac{1}{L_{lineN}} & \end{bmatrix}$$

Appendix C.

Appendix C.1. Adjacency Matrix

$$A_g = \begin{bmatrix} 0 & 1 & 0 & 0 & 0 & 1 \\ 1 & 0 & 1 & 0 & 0 & 0 \\ 0 & 1 & 0 & 1 & 0 & 0 \\ 0 & 0 & 0 & 0 & 1 & 0 \\ 0 & 0 & 0 & 0 & 0 & 1 \\ 1 & 0 & 0 & 0 & 1 & 0 \end{bmatrix}$$

Appendix C.2. Degree Matrix

$$D_g = \begin{bmatrix} 2 & 0 & 0 & 0 & 0 & 0 \\ 0 & 2 & 0 & 0 & 0 & 0 \\ 0 & 0 & 2 & 0 & 0 & 0 \\ 0 & 0 & 0 & 2 & 0 & 0 \\ 0 & 0 & 0 & 0 & 2 & 0 \\ 0 & 0 & 0 & 0 & 0 & 2 \end{bmatrix}$$

Appendix C.3. Laplacian Matrix

$$L_g = \begin{bmatrix} 2 & -1 & 0 & 0 & 0 & -1 \\ -1 & 2 & -1 & 0 & 0 & 0 \\ 0 & -1 & 2 & -1 & 0 & 0 \\ 0 & 0 & -1 & 2 & -1 & 0 \\ 0 & 0 & 0 & -1 & 2 & -1 \\ -1 & 0 & 0 & 0 & -1 & 0 \end{bmatrix}$$

References

1. Zeng, Z.; Yang, H.; Zhao, R. Study on small signal stability of microgrids: A review and a new approach. *Renew. Sustain. Energy Rev.* **2011**, *15*, 4818–4828. [[CrossRef](#)]
2. Han, Y.; Li, H.; Shen, P.; Coelho, E.A.A.; Guerrero, J.M. Review of active and reactive power sharing strategies in hierarchical controlled microgrids. *IEEE Trans. Power Electron.* **2017**, *32*, 2427–2451. [[CrossRef](#)]
3. Habib, S.; Kamran, M.; Rashid, U. Impact analysis of vehicle-to-grid technology and charging strategies of electric vehicles on distribution networks—A review. *J. Power Sources* **2015**, *277*, 205–214. [[CrossRef](#)]
4. Hossain, M.A.; Pota, H.R.; Issa, W.; Hossain, M.J. Overview of AC microgrid controls with inverter-interfaced generations. *Energies* **2017**, *10*, 1300. [[CrossRef](#)]
5. Guerrero, J.M.; Matas, J.; de Vicuna, L.G.; Castilla, M.; Miret, J. Decentralized control for parallel operation of distributed generation inverters using resistive output impedance. *IEEE Trans. Ind. Electron.* **2007**, *54*, 994–1004. [[CrossRef](#)]
6. Guerrero, J.M.; De Vicuña, L.G.; Matas, J.; Miret, J.; Castilla, M. Output impedance design of parallel-connected UPS inverters. *IEEE Int. Symp. Ind. Electron.* **2004**, *2*, 1123–1128. [[CrossRef](#)]
7. Guerrero, J.M.; Matas, J.; De Vicuña, L.G.; Castilla, M.; Miret, J. Wireless-control strategy for parallel operation of distributed-generation inverters. *IEEE Trans. Ind. Electron.* **2006**, *53*, 1461–1470. [[CrossRef](#)]
8. Guerrero, J.M.; Vásquez, J.C.; Matas, J.; Castilla, M.; García de Vicuna, L. Control strategy for flexible microgrid-based on parallel line-interactive UPS systems. *IEEE Trans. Ind. Electron.* **2009**, *56*, 726–736. [[CrossRef](#)]
9. De Brabandere, K.; Bolsens, B.; Van Den Keybus, J.; Woyte, A.; Driesen, J.; Belmans, R. A voltage and frequency droop control method for parallel inverters. *IEEE Trans. Power Electron.* **2007**, *4*, 1107–1115. [[CrossRef](#)]

10. Han, H.; Hou, X.; Yang, J.; Wu, J.; Su, M.; Guerrero, J.M. Review of power sharing control strategies for islanding operation of AC microgrids. *IEEE Trans. Smart Grid* **2016**, *7*, 200–215. [[CrossRef](#)]
11. Guerrero, J.M.; Chandorkar, M.; Lee, T.L.; Loh, P.C. Advanced control architectures for intelligent microgridspart I: Decentralized and hierarchical control. *IEEE Trans. Ind. Electron.* **2013**, *60*, 1254–1262. [[CrossRef](#)]
12. Bidram, A.; Member, S.; Davoudi, A.; Lewis, F.L.; Guerrero, J.M.; Member, S. Distributed cooperative secondary control of microgrids using feedback linearization. *IEEE Trans. Power Syst.* **2013**, *28*, 3462–3470. [[CrossRef](#)]
13. Kordkheili, H.; Banejad, M.; Kalat, A.; Pouresmaeil, E.; Catalão, J. Direct-lyapunov-based control scheme for voltage regulation in a three-phase islanded microgrid with renewable energy sources. *Energies* **2018**, *11*, 1161. [[CrossRef](#)]
14. Han, H.; Li, L.; Wang, L.; Su, M.; Zhao, Y.; Guerrero, J.M. A novel decentralized economic operation in islanded AC microgrids. *Energies* **2017**, *10*, 804. [[CrossRef](#)]
15. Lu, L.Y.; Chu, C.C. Consensus-based secondary frequency and voltage droop control of virtual synchronous generators for isolated AC micro-grids. *IEEE J. Emerg. Sel. Top. Circuits Syst.* **2015**, *5*, 443–455. [[CrossRef](#)]
16. Wang, X.; Zhang, H.; Li, C. Distributed finite-time cooperative control of droop-controlled microgrids under switching topology. *IET Renew. Power Gener.* **2017**, *11*, 707–714. [[CrossRef](#)]
17. Wang, H.; Zeng, G.; Dai, Y.; Bi, D.; Sun, J.; Xie, X. Design of a Fractional Order Frequency PID Controller for an Islanded Microgrid: A multi-objective extremal optimization method. *Energies* **2017**, *10*, 1502. [[CrossRef](#)]
18. Lewis, F.L.; Qu, Z.; Davoudi, A.; Bidram, A. Secondary control of microgrids based on distributed cooperative control of multi-agent systems. *IET Gener. Transm. Distrib.* **2013**, *7*, 822–831. [[CrossRef](#)]
19. Liu, W.; Gu, W.; Xu, Y.; Wang, Y.; Zhang, K. General distributed secondary control for multi-microgrids with both PQ-controlled and droop-controlled distributed generators. *IET Gener. Transm. Distrib.* **2017**, *11*, 707–718. [[CrossRef](#)]
20. Zuo, S.; Davoudi, A.; Song, Y.; Lewis, F.L. Distributed finite-time voltage and frequency restoration in islanded AC microgrids. *IEEE Trans. Ind. Electron.* **2016**, *63*, 5988–5997. [[CrossRef](#)]
21. Guo, F.; Wen, C.; Mao, J.; Song, Y.D. Distributed secondary voltage and frequency restoration control of droop-controlled inverter-based microgrids. *IEEE Trans. Ind. Electron.* **2015**, *62*, 4355–4364. [[CrossRef](#)]
22. Lu, X.; Yu, X.; Lai, J.; Guerrero, J.M.; Zhou, H. Distributed secondary voltage and frequency control for islanded microgrids with uncertain communication Links. *IEEE Trans. Ind. Inform.* **2017**, *13*, 448–460. [[CrossRef](#)]
23. Wang, Y.; Wang, X.; Chen, Z.; Blaabjerg, F. Distributed optimal control of reactive power and voltage in islanded microgrids. *IEEE Trans. Ind. Appl.* **2017**, *53*, 340–349. [[CrossRef](#)]
24. Schiffer, J.; Seel, T.; Raisch, J.; Sezi, T. Voltage stability and reactive power sharing in inverter-based microgrids with consensus-based distributed voltage control. *IEEE Trans. Control Syst. Technol.* **2016**, *24*, 96–109. [[CrossRef](#)]
25. Guan, Y.; Meng, L.; Li, C.; Vasquez, J.; Guerrero, J. A dynamic consensus algorithm to adjust virtual impedance loops for discharge rate balancing of AC microgrid energy storage units. *IEEE Trans. Smart Grid* **2017**, *3053*. [[CrossRef](#)]
26. Bidram, A.; Nasirian, V.; Davoudi, A.; Lewis, F.L. Droop-free distributed control of AC microgrids. *Adv. Ind. Control* **2017**, *31*, 141–171. [[CrossRef](#)]
27. Guerrero, J.M.; Vasquez, J.C.; Matas, J.; De Vicuña, L.G.; Castilla, M. Hierarchical control of droop-controlled AC and DC microgrids - A general approach toward standardization. *IEEE Trans. Ind. Electron.* **2011**, *58*, 158–172. [[CrossRef](#)]
28. Bidram, A.; Nasirian, V.; Davoudi, A.; Lewis, F.L. *Cooperative Synchronization in Distributed Microgrid Control*, 1st ed.; Grimble, M.J., Ed.; Springer International Publishing: Basel, Switzerland, 2017; ISBN 978-3-319-50807-8.
29. Coelho, E.A.A.; Wu, D.; Guerrero, J.M.; Vasquez, J.C.; Dragičević, T.; Stefanović, Č.; Popovski, P. Small-Signal Analysis of the Microgrid Secondary Control Considering a Communication Time Delay. *IEEE Trans. Ind. Electron.* **2016**, *63*, 6257–6269. [[CrossRef](#)]
30. Char, J.P. Circuit, cutset and path enumeration, and other applications of edge-numbering convention. *Proc. Inst. Electr. Eng.* **1970**, *117*, 532–538. [[CrossRef](#)]

31. Char, J.P. Generation and realisation of loop and cutsets. *Proc. Inst. Electr. Eng.* **1969**, *116*, 2001–2008. [[CrossRef](#)]
32. Gibbons, A. *Algorithmic Graph Theory*; Cambridge University Press: Cambridge, UK, 1985.
33. Egerstedt, M.; Mesbahi, M. *Graph Theoretic Method in Multiagent Networks*; Princeton University Press: Princeton, NJ, USA, 2010; ISBN 9780691140612.
34. Lewis, F.L.; Zhang, H.; Hengster-Movric, K.; Das, A. *Cooperative Control of Multi Agent Systems*, 1st ed.; Springer International Publishing: Basel, Switzerland, 2014; Volume 53, ISBN 9781447155737.
35. Lee, K.K.; Chen, C.E. An Eigen-based approach for enhancing matrix inversion approximation in massive MIMO systems. *IEEE Trans. Veh. Technol.* **2017**, *66*, 5483–5487. [[CrossRef](#)]
36. Mahmoud, M.S.; AL-Sunni, F.M. *Control and Optimization of Distributed Generation Systems*, 1st ed.; Springer International Publishing: Basel, Switzerland, 2015; ISBN 978-3-319-16909-5.
37. Pogaku, N.; Prodanović, M.; Green, T.C. Modeling, analysis and testing of autonomous operation of an inverter-based microgrid. *IEEE Trans. Power Electron.* **2007**, *22*, 613–625. [[CrossRef](#)]
38. Yu, K.; Ai, Q.; Wang, S.; Ni, J.; Lv, T. Analysis and optimization of droop controller for microgrid system based on small-signal dynamic model. *IEEE Trans. Smart Grid* **2016**, *7*, 695–705. [[CrossRef](#)]
39. Chen, C.-T. *Linear System Theory and Design*, 3rd ed.; Oxford University Press: New York, NY, USA, 1999; ISBN 0195117778.



© 2018 by the authors. Licensee MDPI, Basel, Switzerland. This article is an open access article distributed under the terms and conditions of the Creative Commons Attribution (CC BY) license (<http://creativecommons.org/licenses/by/4.0/>).

Article

A Control Methodology for Load Sharing System Restoration in Islanded DC Micro Grid with Faulty Communication Links

Muhammad Umair Shahid ^{1,*}, Muhammad Mansoor Khan ¹, Khurram Hashmi ¹, Salman Habib ¹, Huawei Jiang ² and Houjun Tang ¹

¹ School of Electronics, Information & Electrical Engineering (SEIEE), Smart Grid Research & Development Centre, Shanghai Jiao Tong University, Shanghai 200240, China; mkhancn@yahoo.com (M.M.K.); khurram_hashmi@sjtu.edu.cn (K.H.); iamsuliman@hotmail.com (S.H.); hjtang@sjtu.edu.cn (H.T.)

² State Grid Wuxi Power Supply Company, Wuxi 214000, China; jiang.huawei93@outlook.com

* Correspondence: MuhammadUmairShahid@sjtu.edu.cn; Tel.: +86-132-6290-7356

Received: 4 April 2018; Accepted: 31 May 2018; Published: 4 June 2018

Abstract: Communication-based distributed secondary control is extensively used in DC microgrids. Compared to centralized control, it can provide better voltage regulation and load sharing in microgrids. A conventional secondary control technique that converges the system to a common operating point is improved by using the control methodology to detect the communication link failure and stabilize the system operation during communication islanding. Recently, more robust control schemes have been proposed to improve resilience, but communication islanding has not been addressed at the secondary level control for which the system requires additional tertiary control. However, link failure is a possibility in the microgrid, so this paper proposes a control scheme at the secondary level to detect communication islanding. Communication islanding may lead the system to unpredictable behavior, which may cause the system to become unstable and may further lead to a cascading failure. The proposed control scheme sustains the stability and operation of a DC microgrid. Voltage and current observer works in a parallel manner with the proposed secondary control to achieve a correction term for global operating points. The proposed control scheme has been verified through analysis and simulation.

Keywords: DC–DC converters; multi-level control; renewable energy resources control; electrical engineering communications

1. Introduction

Microgrids are small-scale isolated distribution systems which are currently receiving increased attention due to the widespread use of renewable energy resources, energy storage batteries, and the increment of electronics-based loads that use DC current. Therefore, DC microgrids avoid cumbersome DC–AC–DC generation [1–4]. However, the usage of DC microgrids at distribution scale is increasing with the collaboration of various renewable resources due to the higher penetration of electric vehicles [5–7]. DC microgrids reduce the number of conversion units and also overcome the disadvantages of AC power, such as transformers inrush current, phase angle, frequency synchronization, reactive power, and power quality [3,8,9]. Although DC microgrids are emerging and inverter-based AC microgrids are the recent focus of research, many traditional AC loads appear in the system as DC loads when fed through inverter drive systems [8]. When studying the conventional control hierarchy for a legacy power system grid, a hierarchical control system is conventionally adopted for microgrids [10–12]. Multi-level hierarchical control is a tertiary control, which is responsible for the coordination between distributed generated units and the economic

dispatch of the units. Tertiary control adjusts the microgrid voltage for the scheduled exchange of power between the microgrid and the main grid. It adjusts the load sharing and maximum power-sharing, which increases the utilization of renewable energy, suppresses stress, and affects the aging of the microgrids [13–15]. To adjust the voltage set point of the primary controller by the tertiary and secondary controller, a primary controller is implemented locally with the droop mechanism to converge the voltage of the converters [12]. Tertiary and secondary control systems are implemented in a centralized mode in such a way that they are connected with high-speed communication networks. Communication networks used to exchange the reference values for the primary control, and any link failure of the network system may lead the affected unit to malfunction, overstressing other units, and potentially leading the system towards instability and failure [13]. A future extension for link failure in the controllability adds more complexity to the central controller. Distributed control is as an alternative to centralized systems which provides more reliability, easy scalability, and a simpler network for communication [16,17]. Structurally, it is desired to extend the distributed control in secondary and primary control levels; this control provides voltage regulation and better load sharing for DC microgrids [15].

Better load sharing is implemented using communication between converters that assign the loads according to their rated power, which equalizes the per-unit current of all nodes and reduces circulating current and overstressing of all sources [18,19]. Droop control is primarily adopted for load sharing by adding a virtual resistance to every converter. Despite the ease and simplicity in a droop control, it suffers from poor voltage regulation and current sharing. The main reason for this is the virtual impedance and output voltage mismatch between converters, which affects the real power flow between DC power systems [20–22]. Improvement in systems requires a secondary control system that has better voltage regulation and load sharing, which is done over a communication network. Secondary control may be a centralized system exchanging values over a fully connected communication network through directly connected nodes of the microgrid [15,22]. A centralized secondary control measure voltage of the microgrid calculates the restoration value of voltage for the microgrid and feeds the same value to every converter. It assumes that the voltage of every converter is the same for all the nodes in a microgrid, which is not a feasible assumption for a DC microgrid [19].

The conventional DC droop technique is used to linearly reduce the DC output voltage such that current increases, and it has limitations in line resistance in a droop control and DC bus voltage deviation increases. Droop control helps to achieve the independent operation of converters and improves current sharing [13]. The cooperative control of DC microgrids creates a distributed secondary and primary control paradigm. Secondary control adjusts set-points for the overall system, and the primary control regulates individual units employing droop control law. The controller controls the transmission line impedance and communicates with other converters in the form of a sparse technique for current sharing [14]. Using a distributed network, consensus protocol is implemented which eliminates the need for master–slave topology. Voltage regulation at a fixed point and current in per-unit are used in consensus to share the current between nodes. This involves tertiary, secondary, and primary controls. Tertiary controls the power dispatch, secondary sets the point for operation, and primary is a droop control. The controller does not require any prior knowledge of the number of converters, which makes it plug-and-play system [12]. The droop method is widely used for current or load sharing by using the virtual impedance of each converter, which prevents power sources from becoming overstressed [15]. A high droop coefficient improves the load sharing, which results in a cost for degrading voltage regulation. To achieve the required load sharing, the droop coefficient varies in the range of line impedance and line variation [16]. The communication network spans all over the microgrid for centralized control which is embedded in each converter. Node-to-node communication links are required for all sources, and any link failure makes the microgrid operation unstable. The effect of line impedance is also taken into account for the connected graph [20]. Despite improved accuracy because of the fully connected network system, any individual link failure affects the system performance. Appropriately, it is required that the average voltage over the microgrid is

directed at the global voltage set point controlled by the tertiary control, which is called global voltage regulation [21,23]. The efficiency of DC microgrids varies because of the effect of communication delays generated between the nodes to exchange values. This can cause system instability and response to load sharing of nodes [24–26]. In a bi-directional connectivity graph system, when a large amount of data is exchanged, errors in communication may occur that result in deterioration of the system performance [27,28]. Due to the intermittent nature of renewable energy resources, a fast control scheme is required [26]. A new control scheme at the secondary level is proposed with minimum data exchange to overcome the mismatch in operating reference points to in turn reduce the stress and stabilize the system. The proposed control scheme can detect communication link failure and reliable operation of the system by varying the gain for correction terms. The proposed scheme does not require the tertiary-level control which is usually used in conventional consensus-based communication control.

This paper focuses on the improvement of the secondary-level control of DC microgrids. The main features of the proposed distributed cooperative control are as follows:

1. Analysis of two-way cooperation in nodes through a communication graph by making improvements in secondary control, which can detect communication link failure and stabilize the system accordingly.
2. Each converter has a level of intelligence, which uses the proposed scheme to get correction terms and adjust the system more accurately.
3. The proposed control system does not require prior knowledge of the nodes, which gives it plug-and-play capability.
4. A sparse communication network is spanned throughout the microgrid, through which converters can communicate with their neighbors, which is completely different from the centralized control approach.

This manuscript is organized as follows: Section 2 is related to the detection of communication islanding and its impact on the system. An introduction to graph theory is presented in Section 3. Section 4 demonstrates the proposed distributed control. Section 5 presents the case studies and simulation. Finally, the conclusions of the paper are drawn in Section 6.

2. Detection of Communication Islanding and Impact

After link failure, small islands form in the DC microgrid network. The proposed scheme uses a bi-directional sparse network in which every node is connected to its neighboring nodes, as in Figure 1. In normal operation, consensus control will converge the system on global reference points. In case of communication link failure, the proposed secondary control detects and shifts the system control to primary control of the disconnected node, which overcomes the need for tertiary Control. Conventional consensus-based communication control systems use tertiary control in the case of link failure. The advantage of shifting the system to primary control is that it operates on a fixed reference value, without being unstable or generating any stress on the microgrid system. As shown in Figure 2, secondary-level control is modified to detect link failure on the basis of the values which are received from neighbors. If any value is missing or not received, a link failure is detected and the system is shifted to primary control. Otherwise, tertiary control is needed to overtake control of the system in order to remain stable. The flowchart in Figure 3 elaborates this operation. The proposed control method is modified with a logical switch, which removes the requirement for tertiary control by controlling the gain of the correction term on the secondary control of the disconnected node. Proposed Switch technique varies the gain on detecting, as an example if one side communication link failure gain becomes half or both side communication failure then gain becomes zero. The system remains stable and will not generate stress on the disconnected node.

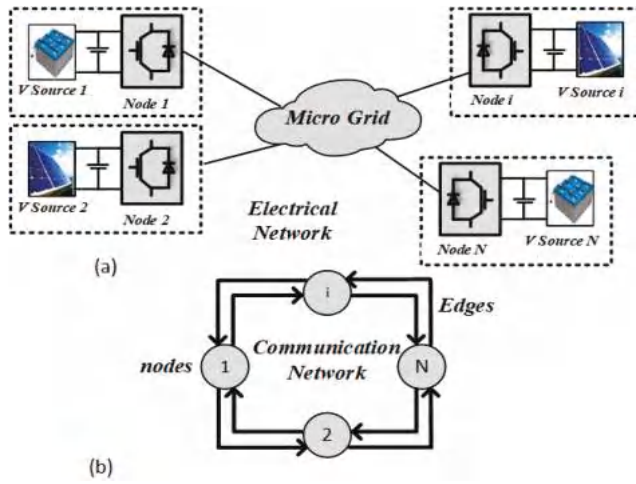


Figure 1. General layout of a micro-grid: (a) Power-supplying nodes; (b) Communication network spanned among nodes for data exchange.

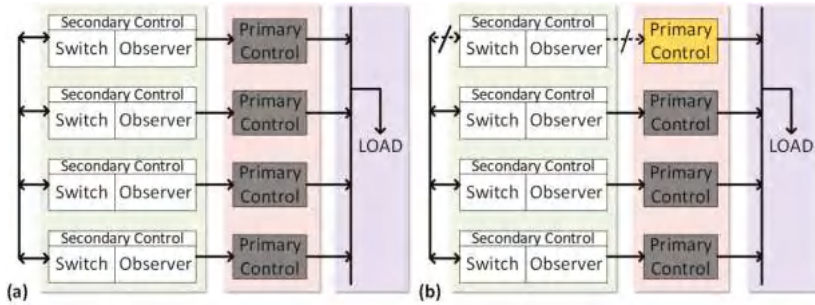


Figure 2. DC micro-grid (MG): (a) Regular 4-node DC MG; (b) Communication fault 4-node DC MG.

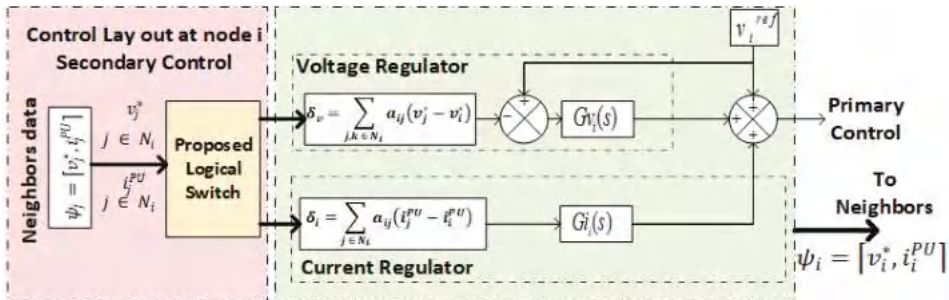


Figure 3. Proposed secondary control for a DC microgrid.

3. Review of Graph Theory

A DC microgrid (MG) system can be represented using graph theory in the form of a graph. The requirement for representing a DC MG using graph theory arises due to the increased number of nodes. So, irrespective of the communication method, the information transfer from one node

to another can be expressed graphically. Graph theory is a well-established field of mathematics which helps to study different scenarios and cases in DC MG systems for the exchange of information flow [27].

A distributed cooperative control can be represented graphically. Figure 1 shows the physical and cyber layers of the DC microgrid. Nodes represent the active sources and edges show the communication links between the nodes. The cyber layer lays the network to achieve global consensus by exchanging information with neighbors, which is an improvement upon conventional consensus systems. By exchanging values with neighbors, every agent sets its reference values according to neighbors information [28]. Thus, cooperative control offers a global consensus, provided with the help of the communication network. So, communication link failure affects the system stability in achieving convergence and generates stress on nodes [12,29].

A bi-directional communication network as in Figure 1b can be represented using graph theory. Such a graph is usually represented mathematically as a set of nodes $V_G = [V_1^g, V_2^g, V_3^g, \dots, V_N^g]$ connected through the edges $E_G \subset V_G \times V_G$. This set consists of elements such as $i, j = 1, 2, 3, \dots, n$ and $i \neq j$. When an edge exists between nodes v_i and v_j , it is called adjacent and the system creates an adjacent matrix $A_G = |a_{ij}| \in R^{N \times N}$, where N is the number of active source nodes. Adjacency matrix A_G consists of the communication weights, where $a_{ij} > 0$, if $(v_j^g, v_i^g) \in E_G$ and $a_{ij} = 0$, otherwise. a_{ij} is the coefficient of communication for transferring data from node j to node i . Here the adjacency matrix is considered with a time-invariant function. $N_i = \{j | (v_j^g, v_i^g) \in E_G\}$ denotes a set of all neighbors of point i ; that is, if $i, j \in N_i$, then v_i^g receives the information from v_j^g . The degree matrix consists of an in-degree matrix and an out-degree matrix. The in-degree matrix $D_G^{in} = diag \{d_i^{in}\}$ is a diagonal matrix, $d_i^{in} = \sum_{j \in N_i} a_{ji}$. Similarly, with the out-degree matrix $D_G^{out} = diag \{d_i^{out}\}$, $d_i^{out} = \sum_{j \in N_i} a_{ij}$. A Laplacian matrix is defined as $L_G = D_G^{in} - A_G$, whose eigenvalues adjust the global values for the microgrid. The Laplacian matrix is assumed to be balanced if the in-degree and out-degree matrices of every node are the same (i.e., $D_G^{in} = D_G^{out}$). Essentially, the in-degree matrices have a greater effect on the global dynamics of the node, which is influenced by its neighbors. In a practical system, if the graph is undirected (which means all the links are bi-directional), then the Laplacian matrix is balanced [30–32].

4. Proposed Distributed Control

The global dynamics of voltage regulation and load sharing are the primary uses of the secondary control, which requires proper set points in order for every converter to operate. The proposed distributed control technique has the ability to detect link failure and stabilize the system during communication islanding. Communication link failure affects the system’s stability and functioning. The proposed control method is modified with a control switch that can detect the communication link failure, which can be on one side or on both sides and shifts the system to primary droop control. In primary control, the system works on droop and remains stable without using any tertiary-level control. The proposed scheme is shown in Figures 3 and 4, where a node receives reference points from neighbors and in the case of failure will stop secondary control and shift to primary control. A flowchart for the proposed control method is also shown in Figure 5, which explains the proposed control method better. When the information received from a neighbor’s system converges to a common reference point, it increases cooperation for load sharing and voltage reference points. Common reference points are consistently updated through a voltage regulator and a current regulator. Node reference voltage can be expressed as [32]:

$$v_i^* = v_i^{ref} + \delta v_i + \delta i_i, \tag{1}$$

where v_i^{ref} , δv_i , and δi_i are the global voltage parameters for constant reference voltages, voltage correction term of i th node, and current correction term for i th node, respectively. Reference points are further tuned in Figure 3 using observers (Voltage and Current) on each node. In the case of any mismatch with the node’s reference point, correction terms are generated by the voltage

observer δv_i and the current observer δi_i to converge the system for better load sharing and voltage regulation. The proposed controller has a logical switch with a voltage observer and a current observer. The proposed controller detects communication link failure, whereas the voltage observer on node i senses the voltage across the microgrid to compare voltage with the global reference v_i^{ref} and converge the voltage of node i to clear any mismatch between nodes using the PI (Proportional Integral) controller $Gv_i(s)$. A distributed cooperative observer estimates the voltage and current compared with the neighbor's data for the average microgrid reference, as implemented in Figure 2. It uses the dynamic consensus framework to process the neighbors' exchange data with local data and adjust the voltage regulation for the microgrid. Figure 4 explains the main operation of the voltage observer to take global voltage averages. The voltage observer at node i receives the neighbor voltages v_j^* ($j \in N_i$), which can be written as [13]:

$$v_i^*(t) = v_i(t) + \int_0^t \sum_{j \in N_i} a_{ij} (v_j^*(\tau) - v_i^*(\tau)) d\tau. \tag{2}$$

Differentiating can be expressed as Equation (2):

$$\dot{v}_i^* = \dot{v}_i + \sum_{j \in N_i} a_{ij} (v_j^* - v_i^*) = \dot{v}_i + \sum_{j \in N_i} a_{ij} v_j^* - d_i^{in} v_i^*. \tag{3}$$

Global observer dynamics can be arranged as:

$$\dot{\bar{v}} = \dot{v} - (D_G^{in} - A_G) \bar{v} = \dot{v} - L\bar{v}. \tag{4}$$

The protocol which is used to update the set point for voltage in the voltage observer is referred to as dynamic consensus. As shown in Equation (4), the local set point (i.e., v_i) is directly input into the estimation algorithm. Thus, any change in voltage at node i 's local set point quickly responds to the situation. As a result, the new v_i^* is set in the local system and also sent to the neighbors for the reference of other nodes [33].

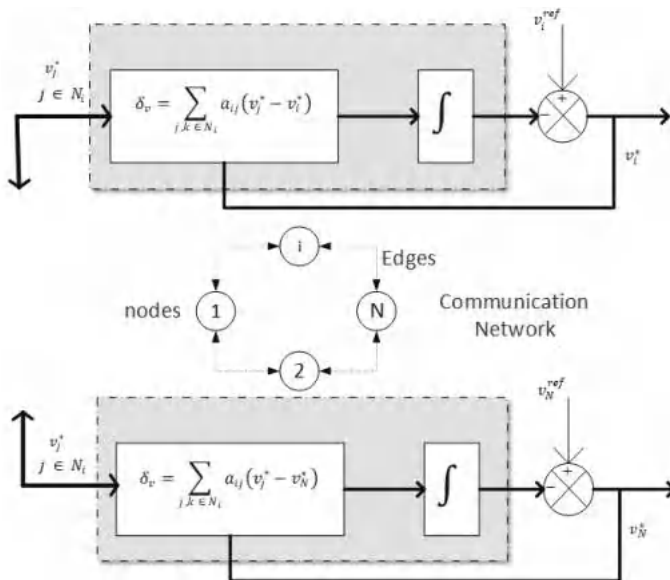


Figure 4. Voltage observer in the proposed secondary control.

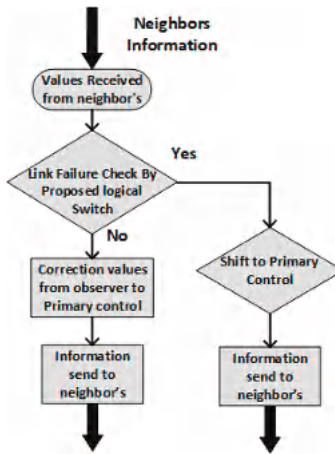


Figure 5. Proposed algorithm flow chart.

The vector for voltages $v = [v_1, v_2, \dots, v_N]^T$ carries the measured voltage for each node. Similarly, the correction estimation vector is $v^* = [v_1^*, v_2^*, \dots, v_N^*]^T$ and carries all the global voltage set points for all nodes. An equivalent equation for frequency can be expressed as:

$$s\bar{V} - \bar{v}(0) = sV - v(0) - L\bar{V}. \tag{5}$$

A current regulator of node i checks the current reference value and tries to make a correction term to ensure equal load sharing between each node. Distributed line impedance varies the droop controller performance. As on node i , it compares local per-unit i_i^{PU} current with the neighbors' weighted average current per-unit and finds the correction value for current δ_i [13].

$$\delta_i = \sum_{j \in N_i} a_{ji} (i_j^{PU} - i_i^{PU}), \tag{6}$$

where a_{ji} is the weight of the communication link, i_j^{PU} is the current from neighbors, and i_i^{PU} is the current of node i . Thus, if any mismatch between the per-unit current of the converters occurs, the current regulator will generate the correction term and adjust the current into a balanced form.

4.1. Single Converter model

DC MG systems based on multiple DC–DC converters usually have high switching frequency. Therefore, the impact of non-linearity in switching frequencies is averaged out, and owing to this fact the converters are a model based on state average modeling, and consensus control is also approximated as continuous in the time domain. However, when a connection failure occurs, the delay is very large in comparison to the normal delay in a communication network. The small signal model for a Buck converter is shown in (7) [34–36]:

$$\begin{pmatrix} \frac{di}{dt} \\ \frac{dv}{dt} \end{pmatrix} = \begin{pmatrix} 0 & -\frac{1}{L} \\ \frac{1}{C} & -\frac{1}{RC} \end{pmatrix} \begin{pmatrix} i \\ v \end{pmatrix} + \begin{pmatrix} \frac{D}{L} \\ 0 \end{pmatrix} V_g. \tag{7}$$

The transfer function for output values:

$$G_{vd} = \frac{v(s)}{d(s)} = \frac{v_g}{LCs^2 + \frac{1}{R}s + 1}, \tag{8}$$

$$G_{id} = \frac{i(s)}{d(s)} = \frac{I + V_oCs + \frac{V_o}{R}}{LCs^2 + \frac{L}{R}s + 1}. \tag{9}$$

4.2. DC MG System Modeling

Let global reference voltage $v_{ref} = [v_1^{ref}, \dots, v_n^{ref}]^T$ and actual supplied current $i = [i_1, \dots, i_n]^T$ vectors. The cooperative control of Figure 3 generates terms δv_1 and δi_i which are also represented as δv_2 at the primary control signal point [13]. Accordingly,

$$\Delta V^1 = H(V_{ref} - \bar{V}), \tag{10}$$

$$\Delta V^2 = -cGLI^{PU}. \tag{11}$$

$\Delta v^1 = [\delta v_1^1, \dots, \delta v_N^1]^T$ and $\Delta v^2 = [\delta v_1^2, \dots, \delta v_N^2]^T$ are voltage and current correction term vectors. The Laplace transforms of Δv^1 and Δv^2 are ΔV^1 and ΔV^2 . $H = diag\{H_i\}$ is the voltage controller matrix and $G = diag\{G_i\}$ is the current controller matrix. I^{PU} is the Laplace transform of i^{PU} , which is the per-unit current vector $i^{PU} = [i_1^{PU}, \dots, i_N^{PU}]^T$.

$$I^{PU} = I_{rated}^{-1}I \tag{12}$$

By, substituting (11) in (12),

$$\Delta V^2 = -cGLI_{rated}^{-1}I. \tag{13}$$

The local voltage set point for proposed controller is

$$V^* = V_{ref} + \Delta V^1 + \Delta V^2 - rI, \tag{14}$$

where $v^* = [v_1^*, \dots, v_n^*]^T$ is the vector of the local voltage set and its Laplace transform is V^* . r is the virtual resistance matrix. Substituting (10) and (13) in (14),

$$V^* = (I_N + H)V_{ref} + H\bar{V} - (cGLI_{rated}^{-1} + r)I. \tag{15}$$

The dynamic behavior of the converter with a closed loop can be expressed as:

$$V_i = G_i^c(s)V_i^*, \tag{16}$$

where V_i and V_i^* are the voltage and G_i^c is the gain of converter i . The global dynamics of the converter will be

$$V = G_c V^*, \tag{17}$$

where the transfer matrix is $G_c = diag\{G_i^c\}$. By substituting (15) in (17),

$$V = G_c \left((I_N + H)V_{ref} + H\bar{V} - (cGLI_{rated}^{-1} + r)I \right). \tag{18}$$

By rearranging (5), we can get

$$\bar{V} = s(sI_N + L)^{-1}V = H_{obs}V. \tag{19}$$

Let us suppose a delay function in the neighbor’s reference voltages. All of the delays are equal and periodic for delay value τ .

$$\bar{V} = s(sI_N + L)^{-1}V = H_{obs}V \times e^{s\tau} \tag{20}$$

For some sample of time, this function will be stable. The DC MG admittance matrix Y_{bus} is related to actual supplied current as

$$I = Y_{bus} V. \tag{21}$$

The detail of the distribution grid is contained in an admittance matrix. Therefore, (18) can be expressed as

$$\begin{cases} V = \left(G_c^{-1} + HH_{obs}^F \times e^{s\tau} + \left(cGLI_{rated}^{-1} + r \right) Y_{bus} \right)^{-1} (I_N + H) V_{ref}, \\ I = \left((Y_{bus} G_c)^{-1} + HH_{obs}^F Y_{bus}^{-1} \times e^{s\tau} + cGLI_{rated}^{-1} + r \right)^{-1} (I_N + H) V_{ref}. \end{cases} \tag{22}$$

Equation (22) describes the global dynamic with proposed controls, the system being linear. Suitable values for different gains can be found, such that poles of the system lie in the left half of the plan and the system will be stable for some open interval of delay τ .

For periodic and synchronized communication, the value of τ should be small enough such that system can achieve reasonable stability and robustness as targeted by the design specification. At the same time, it should be large enough such that it can be realized by practical means of implementation. It can safely be assumed that small variations in delay will not cause any system instability, as the bandwidth of secondary control, which depends on communication-based control, is quite a bit lower than communication rate. If the delay increases due to some uncertainty in the communication link, then the link can be considered as broken and reliance on such communication is not appropriate, as it can jeopardize system stability. A more generalized limit to this uncertain value of delay can be derived by discretizing the system and extending Lemma 1 of the agreement protocol in the presence of noise [27]. This is expressed as follows: consider the discrete time equation for agreement protocol:

$$z(k + 1) = (I - \gamma(k)L(g))z(k). \tag{23}$$

Equation (23) satisfies the following state:

$$\lim_{k \rightarrow \infty} \gamma(k) = 0, \sum_{k=1}^{\infty} \gamma(k) = \infty, \text{ and } \sum_{k=1}^{\infty} \gamma^2(k) < \infty. \tag{24}$$

Lemma 1. *For a connected graph, the system’s trajectory (23) convergences to the agreement set A w.p.1 (with probability 1) if the condition in (24) holds and for all $k \geq 1$, $\gamma(k) \leq 2/\lambda_n(g)$.*

For system convergence, a delay $\gamma(k) \leq 2/\lambda_n(g)$ with fixed boundary according to Lemma 1, So the system will converge and remain stable under such boundary that the nodes consider stable and healthy. more than this delay boundary that node consider as failed in communication network.

5. Case Studies and Simulation

A circular bi-directional communication ring was considered for the DC MG experimental setup to check the effectiveness and performance of the proposed control method by performing simulations in MATLAB, as shown in Figure 6. For the considered case study, the DC MG had a four-node radial network in a circular communication structure to support a DC resistive load connected on different nodes. For communication between nodes, an isolated RS232 was used in setup to exchange reference values. In the simulated case study, the effect of communication channel transmission delay was also considered. A detailed switch model was used for power converters to present more realistic results. The full case scenario is illustrated in Figure 6, and detailed node parameters used for the experimental setup are given in Table 1, which shows the communication links and power lines. The circular structure consisted of two-way communication with neighbors, as shown in Figure 7.

Transmission impedance effect was also considered in the experimental setup. As shown in Figures 3 and 6, the proposed control scheme detects link failure between the connected nodes and adjusts the gains according to the link failure, as explained in the flowchart in Figure 5. The detection algorithm is continuously working at every node, and if any link failure occurs, the secondary control quickly responds to the link failures and varies the gains that affect the voltage correction and current correction terms. Considering switch S2 in the experimental setup of the case study, only one node was connected with a load for the worst-case scenario with other nodes sharing the load. Consequently, the system output voltage and current sharing stabilized as shown in Figure 8a,b. The system remained stable, with variations in secondary control gain accordingly. Whenever link failure occurred in the MG as in Figure 7c, the proposed controller at the secondary level detected the link failure and it varied the voltage gain and current correction, as can be seen in Figure 8c,d. It can be seen from Equations (1) and (6) that for the correction term, the equation is dependent on the neighbor's reference values. When a link failure occurs, the reference from the neighbors in the correction equations are constant or zero, which therefore leads to sharp variations in the system correction term as in Figure 8c,d. Figure 9a,b display a conventional system without a link failure detection system that generates a correction term in absence of reference values at the voltage and current correction. This will result in the output voltage following the input voltage due to correction terms as in Figure 8c,d. The graphical representation is shown in Figure 7 for different scenarios. Bi-directional system communication links are assumed to have a balanced Laplacian matrix and adjacency matrix for communication graph weights using a_{ij} to generate correction terms. Figure 7a shows the fully connected balanced Laplacian matrix as shown in Equation (25):

$$L = \begin{pmatrix} 2 & -1 & 0 & -1 \\ -1 & 2 & -1 & 0 \\ 0 & -1 & 2 & -1 \\ -1 & 0 & -1 & 2 \end{pmatrix}. \tag{25}$$

Similarly, Figure 7b shows one communication link failure which changes the Laplacian matrix as shown in Equation (26). On the other hand, if failure of both links occurs, as shown in Figure 7c, then its Laplacian for the remaining system will be as in Equation (27):

$$L = \begin{pmatrix} 1 & -1 & 0 & 0 \\ -1 & 2 & -1 & 0 \\ 0 & -1 & 2 & -1 \\ 0 & 0 & -1 & 1 \end{pmatrix}, \tag{26}$$

$$L = \begin{pmatrix} 1 & -1 & 0 \\ -1 & 2 & -1 \\ 0 & -1 & 1 \end{pmatrix}. \tag{27}$$

During regular connectivity, all four nodes will work normally and exchange values with neighbors for correction terms as shown in Figure 6 and the first case of Figure 7a. With that correction term, the system will converge to a common reference point and share the load in a balanced form. Whereas, if one link failure occurs in any two nodes as in Figure 7b, the Laplacian will be different as in Equation (26), and consensus will work normally, in which it will vary the gain and adjust the system in order to maintain its stability and load sharing. As a result, the system has no effect on regular working of DC MG. If links fail on both sides then one node is communication islanding, whereas all other nodes can exchange information with each other. In that case, the proposed algorithm will maintain stability and load sharing by shifting the islanded node to droop by varying its gain. In contrast, the conventional secondary control would no longer be able to stabilize the system and requires tertiary control to take over the system for normal operation. The usage of the proposed control method helps

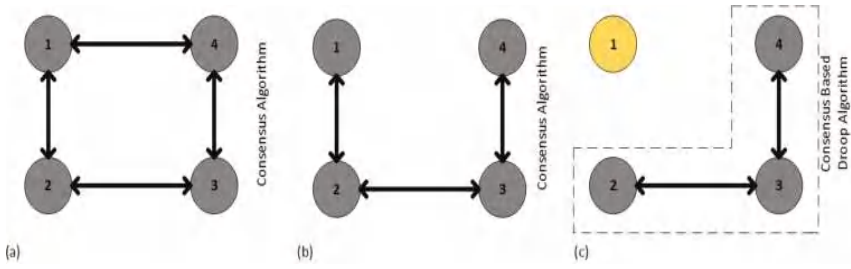


Figure 7. Different scenarios for DC MG.

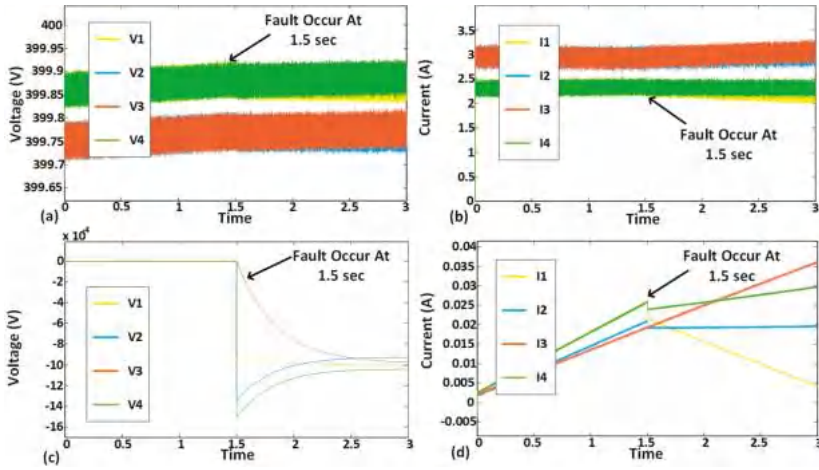


Figure 8. Results of proposed secondary control simulation: (a) node voltages; (b) node current; (c) voltage correction term; (d) current correction term.

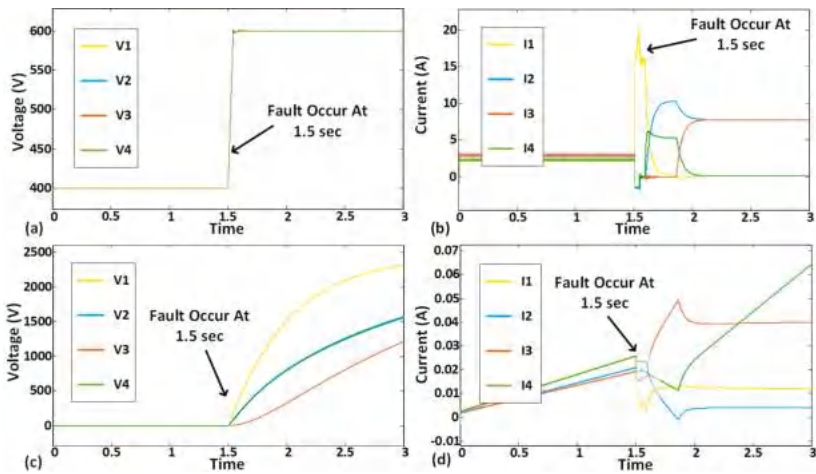


Figure 9. Results of conventional secondary control simulation: (a) node voltages; (b) node current; (c) voltage correction term; (d) current correction term.

Table 1. Parameters for single converter node in DC microgrid.

Parameters	Values
Input Voltage	600 V
Output Voltage	400 V
Droop gain (G_{Droop})	0.025
Resistive Load	80 ohm
Line Resistance	0.0005 ohm/m
Line inductance	0.50 μ H/m
Line Length	100 m
Switching Frequency	10 kHz
Filter Inductor	1 mH
Filter Capacitor	300 μ F
Communication Channel Bandwidth Delay at 20 kHz	0.15 ms
Inner loop	$K_p = 10$ $K_i = 0.05$
Outer loop	$K_p = 40$ $K_i = 0.05$
Voltage Observer	$K_p = 6$ $K_i = 0.1$
Current Observer	$K_p = 0.11$ $K_i = 0.6$

Plug-and-Play Capacity

The proposed system has plug-and-play capability. When one or more nodes’ communication links fail at any time, the proposed controls stabilize the system. Communication link failure makes communication islands of varied sizes in the system. The proposed controls work to balance the system in the case of communication islanding. The performance of the DC MG shown in Figures 8 and 9 was satisfactory under such case. A load variation test was also done on the proposed control scheme, and it performed well and balanced the system in time, as in Figure 10.

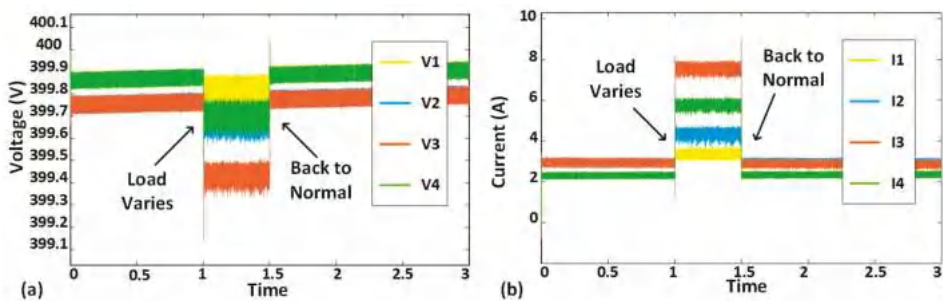


Figure 10. Load variation in the DC microgrid: (a) node voltage; (b) node current.

6. Conclusions

A distributed control scheme is proposed for a DC microgrid with some level of intelligence to check the communication link failure at the secondary level control. The proposed communication islanding algorithm scheme detects the link failure, and if any failure occurs, the proposed control scheme stabilizes the system and maintains load sharing. After detecting link failure, the proposed control scheme varies the gain of the correction term for the voltage and current observers, which stabilizes the system’s operation during communication islanding and achieves a global reference point. This study shows that the proposed secondary control scheme is effective and provides stability to the

system in the case of a communication islanding scenario. The performance of the proposed scheme in communication link failure detection and stabilizing the system operation was tested through MATLAB/Simulink.

Author Contributions: M.U.S. proposed the idea for writing the manuscript. M.M.K. and H.T. suggested the literature and supervised in writing the manuscript. K.H. helped M.U.S. in writing and formatting. S.H. helped in modifying the figures and shared the summary of various credible articles to be included in this manuscript. H.J. helped in system parameters to make the simulation test possible.

Conflicts of Interest: The authors declare no conflict of interest.

References

1. Arunkumari, T.; Indragandhi, V. An overview of high voltage conversion ratio DC-DC converter configurations used in DC micro-grid architectures. *Renew. Sustain. Energy Rev.* **2017**, *77*, 670–687. [[CrossRef](#)]
2. Tahir, S.; Wang, J.; Baloch, M.; Kaloi, G. Digital Control Techniques Based on Voltage Source Inverters in Renewable Energy Applications: A Review. *Electronics* **2018**, *7*, 18. [[CrossRef](#)]
3. Habib, S.; Kamran, M.; Rashid, U. Impact analysis of vehicle-to-grid technology and charging strategies of electric vehicles on distribution networks—A review. *J. Power Sources* **2015**, *277*, 205–214. [[CrossRef](#)]
4. Short, M.; Abugchem, F.; Abrar, U. Dependable Control for Wireless Distributed Control Systems. *Electronics* **2015**, *4*, 857–878. [[CrossRef](#)]
5. Chhaya, L.; Sharma, P.; Bhagwatikar, G.; Kumar, A. Wireless Sensor Network Based Smart Grid Communications: Cyber Attacks, Intrusion Detection System and Topology Control. *Electronics* **2017**, *6*, 5. [[CrossRef](#)]
6. Sanchez, S.; Molinas, M.; Degano, M.; Zanchetta, P. Stability evaluation of a DC micro-grid and future interconnection to an AC system. *Renew. Energy* **2014**, *62*, 649–656. [[CrossRef](#)]
7. Mishra, M.; Sahani, M.; Rout, P.K. An islanding detection algorithm for distributed generation based on Hilbert–Huang transform and extreme learning machine. *Sustain. Energy Grids Netw.* **2017**, *9*, 13–26. [[CrossRef](#)]
8. Lee, Z.; Zhu, S.; Zheng, J.; Choi, D.H.; Wei, L. *Research on Dynamic Process of DC Micro-Grid under Hierarchical Control*; IFAC: Geneva, Switzerland, 2014; Volume 47, ISBN 9783902823625.
9. Chakraborty, P.; Baeyens, E.; Khargonekar, P.P. Distributed control of flexible demand using proportional allocation mechanism in a smart grid: Game theoretic interaction and price of anarchy. *Sustain. Energy Grids Netw.* **2017**, *12*, 30–39. [[CrossRef](#)]
10. Mohamed, A.A.; Elsayed, A.T.; Youssef, T.A.; Mohammed, O.A. Hierarchical control for DC microgrid clusters with high penetration of distributed energy resources. *Electr. Power Syst. Res.* **2017**, *148*, 210–219. [[CrossRef](#)]
11. Che, L.; Shahidehpour, M. DC microgrids: Economic operation and enhancement of resilience by hierarchical control. *IEEE Trans. Smart Grid* **2014**, *5*, 2517–2526. [[CrossRef](#)]
12. Lewis, F.L.; Zhang, H.; Hengster-Movric, K.; Das, A. *Cooperative Control of Multi-Agent Systems*; Springer: London, UK, 2014; Volume 53, ISBN 978-1-4471-5573-7.
13. Nasirian, V.; Member, S.; Moayedi, S.; Member, S.; Davoudi, A.; Lewis, F.L. Distributed Cooperative Control of DC Microgrids. *IEEE Trans. Power Electron.* **2015**, *30*, 2288–2303. [[CrossRef](#)]
14. Nasirian, V.; Member, S.S.; Davoudi, A.; Lewis, F.L.; Guerrero, J.M.; Member, S.S. Distributed Adaptive Droop Control for DC Distribution Systems. *IEEE Trans. Energy Convers.* **2014**, *29*, 944–956. [[CrossRef](#)]
15. Dc, P.; Converters, D.C.; Moayedi, S.; Member, S.; Nasirian, V.; Member, S.; Lewis, F.L.; Davoudi, A. Team-Oriented Load Sharing in parallel DC–DC converters. *IEEE Trans. Ind. Appl.* **2015**, *51*, 479–490. [[CrossRef](#)]
16. Wang, P.; Xiao, J.; Setyawan, L. Hierarchical Control of Hybrid Energy Storage System in DC Microgrids. *IEEE Trans. Ind. Electron.* **2015**, *62*, 4915–4924. [[CrossRef](#)]
17. Lu, X.; Guerrero, J.M.; Sun, K.; Vasquez, J.C. An improved droop control method for dc microgrids based on low bandwidth communication with dc bus voltage restoration and enhanced current sharing accuracy. *IEEE Trans. Power Electron.* **2014**, *29*, 1800–1812. [[CrossRef](#)]

18. Jung, K.; Lim, K.; Kim, D.; Choi, J. Droop method for high-capacity parallel inverters using virtual impedance. In Proceedings of the 9th International Conference on Power Electronics—ECCE Asia: “Green World with Power Electronics”, ICPE 2015—ECCE Asia, Seoul, Korea, 1–5 June 2015; pp. 996–1002. [[CrossRef](#)]
19. Guerrero, J.M.; Vasquez, J.C.; Matas, J.; De Vicuña, L.G.; Castilla, M. Hierarchical control of droop-controlled AC and DC microgrids—A general approach toward standardization. *IEEE Trans. Ind. Electron.* **2011**, *58*, 158–172. [[CrossRef](#)]
20. Meng, L.; Shafiee, Q.; Trecate, G.F.; Karimi, H.; Fulwani, D.; Lu, X.; Guerrero, J.M. Review on Control of DC Microgrids and Multiple Microgrid Clusters. *IEEE J. Emerg. Sel. Top. Power Electron.* **2017**, *5*, 928–948. [[CrossRef](#)]
21. Moayedi, S.; Davoudi, A. Distributed Tertiary Control of DC Microgrid Clusters. *IEEE Trans. Power Electron.* **2016**, *31*, 1717–1733. [[CrossRef](#)]
22. Tanyingyong, V.; Olsson, R.; Cho, J.; Hidell, M.; Sj, P. IoT-grid: IoT Communication for Smart DC Grids. In Proceedings of the Global Communications Conference (GLOBECOM), Washington, DC, USA, 4–8 December 2016.
23. Dou, C.; Yue, D.; Guerrero, J.M.; Xie, X.; Hu, S. Multiagent System-Based Distributed Coordinated Control for Radial DC Microgrid Considering Transmission Time Delays. *IEEE Trans. Smart Grid* **2016**, *8*, 2370–2381. [[CrossRef](#)]
24. Hare, J.; Shi, X.; Gupta, S.; Bazzi, A. Fault diagnostics in smart micro-grids: A survey. *Renew. Sustain. Energy Rev.* **2016**, *60*, 1114–1124. [[CrossRef](#)]
25. Mah, D.; Hills, P.; Li, V.O.; Balme, R. *Smart Grid Applications and Developments*; Springer: London, UK, 2014; ISBN 978-1-4471-6280-3.
26. Konara, K.M.S.Y.; Kolhe, M.L. Charging management of grid integrated battery for overcoming the intermittency of RE sources. In Proceedings of the 2016 IEEE International Conference on Information and Automation for Sustainability: Interoperable Sustainable Smart Systems for Next Generation, ICIAFS 2016, Galle, Sri Lanka, 16–19 December 2016. [[CrossRef](#)]
27. Egerstedt, M.M.; Egerstedt, M. *Graph Theoretic Method in Multiagent Networks*; Princeton University Press: Princeton, NJ, USA, 2010; ISBN 978-0691140612.
28. Char, J.P. Circuit, cutset and path enumeration, and other applications of edge-numbering convention. In *Proceedings of the Institution of Electrical Engineers*; IET Digital Library: London, UK, 1970; Volume 117.
29. Char, J.P.; Sc, D.I.I.P.E. Generation and realisation of loop and cutsets. In *Proceedings of the Institution of Electrical Engineers*; IET Digital Library: London, UK, 2001; Volume 116.
30. Gibbons, A. *Algorithmic Graph Theory*; Cambridge University Press: Cambridge, UK, 1985.
31. Golub, G.H.; Van Loan, C.F.; Varga, R.S.; Götze, F.; Tikhomirov, A.; Pastur, L.; Shcherbina, M.; Nguyen, H.V.; Nguyen, V.; Shin, O.; et al. An Eigen-based Approach for Enhancing Matrix Inversion Approximation in Massive MIMO Systems. *IEEE Trans. Veh. Technol.* **2017**, *66*, 5480–5484. [[CrossRef](#)]
32. Mahmoud, M.S.; AL-Sunni, F.M. *Control and Optimization of Distributed Generation Systems*; Springer: Berlin, Germany, 2015; ISBN 978-3-319-16909-5.
33. Lewis, F.L.; Qu, Z.; Davoudi, A.; Bidram, A. Secondary control of microgrids based on distributed cooperative control of multi-agent systems. *IET Gener. Transm. Distrib.* **2013**, *7*, 822–831. [[CrossRef](#)]
34. Maksimovic, D.; Zane, R. Small-signal discrete-time modeling of digitally controlled PWM converters. *IEEE Trans. Power Electron.* **2007**, *22*, 2552–2556. [[CrossRef](#)]
35. Mahery, H.M.; Torabzad, S.; Sabahi, M.; Babaei, E. Modeling and stability analysis of buck-boost DC-DC converter based on Z-transform. In Proceedings of the India International Conference on Power Electronics, IICPE, Delhi, India, 6–8 December 2012. [[CrossRef](#)]
36. Mohan, N.; Undeland, T.M. *Power Electronics Converters, Applications and Design*, 2nd ed.; Wiley: Hoboken, NJ, USA, 1995.



© 2018 by the authors. Licensee MDPI, Basel, Switzerland. This article is an open access article distributed under the terms and conditions of the Creative Commons Attribution (CC BY) license (<http://creativecommons.org/licenses/by/4.0/>).

Article

A Novel Synchronization Technique for Wireless Power Transfer Systems

Xin Liu ¹, Nan Jin ², Xijun Yang ^{1,*}, Tianfeng Wang ¹, Khurram Hashmi ¹ and Houjun Tang ¹

¹ Key Laboratory of Control of Power Transmission and Transformation Ministry of Education, Shanghai Jiao Tong University, 800 Dongchuan RD., Shanghai 200240, China; Liu_xin@sjtu.edu.cn (X.L.); wangtf1992@163.com (T.W.); khurram_hashmi@sjtu.edu.cn (K.H.); hjtang@sjtu.edu.cn (H.T.)

² College of Electric and Information Engineering, Zhengzhou University of Light Industry, Zhengzhou 450002, China; jinnan@zzuli.edu.cn

* Correspondence: yangxijun@sjtu.edu.cn; Tel.: +86-138-1606-6208

Received: 29 September 2018; Accepted: 6 November 2018; Published: 13 November 2018

Abstract: Recently, wireless power transfer (WPT) systems with active receivers have been proposed for conduction loss reduction, bidirectional power transfer and efficiency improvement. However, the synchronization of WPT systems is complex in nature with the selection of high operating frequencies. Without proper synchronization, power oscillations appear and the system can become unstable. In this paper, a detailed analysis of different WPT systems is presented and the essence of the synchronization technique is derived as being composed of two functions: independent frequency locking and reference phase calibration. The voltage across the receiver-side compensation capacitor is divided and utilized for frequency locking, whereas the reference phase calibration is realized through software code. The proposed method is effective and easy to implement, with a lower overall cost due to its simplicity. The technique can work effectively at high frequency and withstand large variations of operating frequency, load and mutual inductance. In addition, it can address the synchronization problem of multiple active receiver WPT systems with and without cross coupling among the receiving coils. Theoretical analysis and experimental results validate the proposed technique.

Keywords: active receivers; frequency locking; reference phase calibration; synchronization; wireless power transfer

1. Introduction

Wireless power transfer (WPT) techniques can realize energy transmission through coupled coils without the need for physical contact between the transmitter and the receiver [1–3]. Considerable efforts are put into the modeling, performance analysis, design and optimization of WPT systems [4–10]. The operating frequencies of WPT systems can range from kHz to MHz. Radio frequency (RF) WPT systems operate at higher frequencies (such as 6.78 MHz and 13.56 MHz) and aim to increase the power transfer capacity [10–12]. Since the frequency is too high for digital signal processors (DSP) to control the transitions in RF WPT systems, diode rectification is widely adopted which brings about high forward voltage losses. Inductive power transfer systems with lower operating frequency (such as 85 kHz) can be used to transmit higher power levels such as in electric vehicle charging scenarios. Although inductive power transfer systems transmit power wirelessly in a shorter distance than RF systems, their overall efficiencies and power levels are higher. To avoid large transmission losses, various methods are investigated to achieve high efficiency. Recently, inductive power transfer systems with active receivers are the focus of study [13–16]. These systems can realize bidirectional power transfer [17–19] and contribute to efficiency improvement [20–22]. An active receiver in Reference [20] contributes to a maximum efficiency rise of 10% compared with traditional diode rectifiers. However,

such systems are complex in nature and some issues remain unresolved, such as the synchronization problem. The transmitter and receiver are contactless, whereas the control signals of the primary and secondary sides are in rigorous sequential relationships [23]. Although, theoretically the controllers can have the same operating frequency, the actual output frequencies may differ due to manufacturing tolerances of the devices. For DSP TMS320F28335 [24], the frequency precisions of regular pulse width modulator (PWM) and high resolution pulse width modulator (HRPWM) at 100 kHz are 0.1% and 0.002%, respectively. The corresponding maximum errors in the frequencies are in the range of 100 Hz and 2 Hz, respectively. Although the frequency deviations are much smaller as compared to the fundamental operating frequency, the WPT system becomes unstable. Without effective synchronization, the phase angles between the primary and secondary resonant voltages will change periodically, which results in power oscillations. Thus, synchronization of the WPT systems with active receivers is necessary and crucial for stable system operation.

Synchronization methods of the WPT systems can be classified into three categories as elaborated in Figure 1. The first method, as shown in Figure 1a, is introducing an external clock such as general packet radio service (GPRS), code division multiple access (CDMA) and Wi-Fi. Such systems can work only in places where the communication signals are available and stable. When the signal transfer path changes, phase error will appear due to changed time delays of different controllers. Thus, this technique cannot be easily applied to systems where the transmitter and receiver spatially move with respect to each other, such as mobile phone and electric vehicle charging scenarios [25]. The second method is, installing real-time clocks on the transmitter and receiver sides as shown in Figure 1b, which can include on-board atomic clocks and precision oscillators. This method is expensive, whereas small frequency discrepancies still exist. Cumulative error occurs during a long-time operation. The third method is, considering the transmitter as a source and synchronizing the receiver using auxiliary devices as shown in Figure 1c. The feasibility and robustness of the third scheme is greater in these methods. In References [17,18,26,27], a sense winding on the secondary side is proposed to capture the magnetic flux generated by the primary resonant current in order for synchronization. A voltage signal on the sense winding can be induced and the phase locking loop (PLL) is used to detect the primary time sequence. However, secondary magnetic flux produces an undesired voltage, which can deteriorate the synchronization performance seriously. A compensation circuit should be added to eliminate the phase error caused by this effect, whereas the circuit parameters depend heavily on the operating conditions. As reported in Reference [17], the phase error can be about 22% when the coupling factor is decreased by 50% and 15% when the primary compensation capacitance is decreased by 20%. In Reference [20], secondary current is sampled by the sensor for synchronization. Except for the cost and frequency bandwidth of the sensors, the phase error caused by the time delay of the devices is corrected by a carefully designed and parameter-sensitive phase-shift circuit. In References [28,29], the real and reactive powers produced by the receiver are utilized to estimate the position of the voltage vector induced by the primary converter. This method requires accurate samplings of secondary high-frequency resonant current and voltage, as well as a complex processing hardware circuit and calculation algorithm. In multiple active receiver applications, the magnetic field becomes more complex, which increases the difficulty in phase compensation. Previous works largely focus on the applications and contributions of multiple active receiver WPT systems [30,31], whereas, synchronization techniques have not been explored due to their complexity.

Since time delay of the synchronization signal can lead to phase errors, it can be inferred that the accuracy of the synchronization technique is closely related to the signal transmission speed. A higher speed, therefore, corresponds to a higher accuracy. Some high speed methods typically use a laser beam for synchronization [32]. However, the authors find that the essence of synchronization is frequency locking which is independent of signal transmission speed. Generally, circuit-based methods are utilized to correct the phase errors caused by the time delay and system parameter variations [17,20]. The authors find that phase calibration can be easily achieved through software code.

This paper provides a clear illustration of the synchronization technique for the WPT systems. Four specific conditions are investigated, namely: Tuned and detuned WPT systems with one active receiver, and multiple active receiver WPT systems with and without cross coupling among receiving coils. Through summarizing the analysis of different systems, the essence of the synchronization technique is deduced and presented. Then, a universal synchronization technique belonging to the third synchronization category is elaborated and verified through experimental results. The salient contributions of this work are:

- (1) Presenting a detailed analysis of the synchronization technique and clearly decomposing it into independent frequency locking and reference phase calibration based on mathematical derivations;
- (2) Proposing an effective frequency locking circuit that has strong robustness and independence of system parameters;
- (3) Achieving reference phase calibration through software code without using additional phase-shift circuits, which advances in easy realization and cost effectiveness;
- (4) Realizing the synchronization for WPT systems with multiple active receivers.

This paper is divided into five sections. Section 2 analyzes different WPT systems with active receivers, which contributes to figuring out the essence of the synchronization technique. Based on the analysis, Section 3 presents the proposed hardware circuit and software code, aiming for frequency locking and reference phase calibration, respectively. Section 4 validates the feasibility and effectiveness of the proposed systems through experiments. Section 5 concludes this paper.

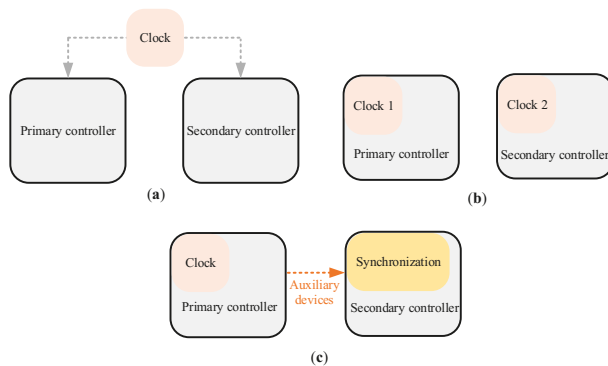


Figure 1. Synchronization methods: (a) external clock; (b) precision on-board clocks; and (c) auxiliary synchronization devices.

2. Synchronization Analysis

2.1. Tuned WPT System with One Active Receiver

The schematic of a WPT system with one active receiver is depicted in Figure 2. $V_{1,dc}$, $V_{2,dc}$, $I_{1,dc}$ and $I_{2,dc}$ are the primary and secondary dc voltages and currents, respectively. $C_{1,dc}$ and $C_{2,dc}$ are the filtering capacitors and $R_{L,2}$ is the load. L_1 and L_2 are the transmitting and receiving coils compensated by C_1 and C_2 , respectively. R_1 and R_2 are the coil resistances. Q_1 – Q_8 are eight metal-oxide-semiconductor field effect transistors (MOSFETs). v_1 and v_2 are the voltages applied on the resonant network, which contain only the odd frequency components. i_1 and i_2 are the primary and secondary resonant currents. Their fundamental frequency components are denoted as v_{11} , v_{21} , i_{11} and i_{21} , whose root-mean-square (RMS) values are V_{11} , V_{21} , I_{11} and I_{21} , respectively. Due to the band pass filtering effect by the resonant network, the fundamental frequency component contributes most to the transferred power. Therefore, i_{11} and i_{21} are nearly the same as i_1 and i_2 , respectively. The typical waveforms of the system are presented in Figure 3, where v_{21} leads i_{21} by φ_2 . $2\alpha_1$ and $2\beta_2$ represent

the phase angles of the resonant voltages. In most of the previously published papers related to WPT systems, fundamental harmonic analysis (FHA) and phasor methods are widely adopted [20–22], which can greatly simplify the analysis. In this paper, boldface letters represent the phasors and capital italic letters represent RMS values of the phasors. For example, \mathbf{V}_{11} and V_{11} represent the voltage phasor and RMS value of v_{11} , respectively.

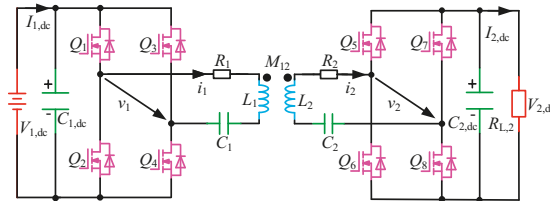


Figure 2. WPT system with one active receiver.

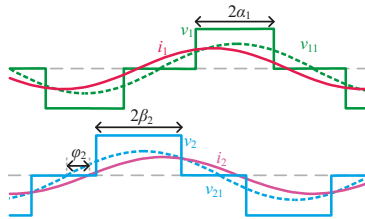


Figure 3. Typical primary and secondary waveforms of a WPT system with one active receiver.

Primary and secondary parameters are identical and the inverting angular frequency ω_1 is $\frac{1}{\sqrt{L_1 C_1}}$. Then, Equation (1) is obtained according to primary current loop.

$$\mathbf{V}_{11} = -j\omega_1 M_{12} \mathbf{I}_{21} + \mathbf{I}_{11} R_1 \tag{1}$$

Generally, the voltage across R_1 is much smaller than \mathbf{V}_{11} . Therefore, Equation (1) can be simplified into Equation (2).

$$\mathbf{I}_{21} = \frac{\mathbf{V}_{11} - \mathbf{I}_{11} R_1}{-j\omega_1 M_{12}} \approx \frac{\mathbf{V}_{11}}{-j\omega_1 M_{12}} \tag{2}$$

Neglecting the losses of the active bridge, energy conservation equation of the receiver can be derived as

$$V_{21} I_{21} \cos \varphi_2 = V_{2,dc} I_{2,dc} \tag{3}$$

According to fundamental harmonic analysis, V_{11} and V_{21} can be obtained.

$$V_{11} = \frac{2\sqrt{2} \sin \alpha_1}{\pi} V_{1,dc} \tag{4}$$

$$V_{21} = \frac{2\sqrt{2} \sin \beta_2}{\pi} V_{2,dc} \tag{5}$$

Thus, the expression of $I_{2,dc}$ can be deduced as

$$I_{2,dc} = \frac{8 \sin \alpha_1 \sin \beta_2 \cos \varphi_2}{\pi^2 \omega_1 M_{12}} V_{1,dc} \tag{6}$$

When the primary and secondary controllers operate at different frequencies (f_1 and f_2 , respectively), φ_2 is expressed as

$$\varphi_2 = 2\pi(f_1 - f_2)t + \varphi_{2,0} \tag{7}$$

where $\varphi_{2,0}$ is the initial phase of φ_2 . $\varphi_{2,0}$ is determined by controllers, whereas it may be different from the coded phase.

Then, $I_{2,dc}$ is derived by substituting Equations (7) into (6).

$$I_{2,dc} = \frac{8V_{1,dc} \sin \alpha_1 \sin \beta_2}{\pi^2 \omega_1 M_{12}} \cos[2\pi(f_1 - f_2)t + \varphi_{2,0}] \tag{8}$$

When $f_1 = f_2$, $I_{2,dc}$ is stable. Furthermore, when $\varphi_{2,0} = 0$, $I_{2,dc}$ reaches peak value which benefits power transfer.

2.2. Detuned WPT System with One Active Receiver

Figure 4 shows the equivalent circuit of an active bridge. Z_2 represents the equivalent impedance of the active bridge on the AC side, which consists of resistive and reactive components. The phase of \mathbf{I}_{21} is denoted by φ_{i_2} . Then, \mathbf{V}_{21} can be expressed as

$$\mathbf{V}_{21} = \frac{2\sqrt{2} \sin \beta_2}{\pi} V_{2,dc} e^{j(\varphi_2 + \varphi_{i_2})}. \tag{9}$$

Since $I_{2,dc} = V_{2,dc} / R_{L,2}$, Equation (3) can be deduced into Equation (10).

$$V_{21} I_{21} \cos \varphi_2 = \frac{V_{2,dc}^2}{R_{L,2}} \tag{10}$$

Therefore, I_{21} can be obtained and \mathbf{I}_{21} can be rewritten as

$$\mathbf{I}_{21} = \frac{\pi V_{2,dc} e^{j\varphi_{i_2}}}{2\sqrt{2} R_{L,2} \sin \beta_2 \cos \varphi_2}. \tag{11}$$

The expression of Z_2 can be derived as Equation (12) according to Equations (9) and (11), which is related to φ_2 .

$$Z_2 = \frac{\mathbf{V}_{21}}{\mathbf{I}_{21}} = \frac{8 \sin^2 \beta_2 \cos \varphi_2 R_{L,2} e^{j\varphi_2}}{\pi^2} \tag{12}$$

Furthermore, the relationship between $I_{2,dc}$ and I_{21} can be obtained as Equation (13).

$$I_{2,dc} = \frac{2\sqrt{2} \sin \beta_2 \cos \varphi_2}{\pi} I_{21} \tag{13}$$

The transmitter can operate at various frequencies and the dual-side parameters can be different in practice, that is, the system can be detuned. The primary and secondary reactance are expressed as Equations (14) and (15).

$$X_1 = \omega_1 L_1 - \frac{1}{\omega_1 C_1} \tag{14}$$

$$X_2 = \omega_1 L_2 - \frac{1}{\omega_1 C_2} \tag{15}$$

Therefore, the dual-side current loops can be derived as follows.

$$\mathbf{V}_{11} = -j\omega_1 M_{12} \mathbf{I}_{21} + \mathbf{I}_{11} (R_1 + jX_1) \tag{16}$$

$$0 = -j\omega_1 M_{12} \mathbf{I}_{11} + \mathbf{I}_{21} (R_2 + jX_2 + Z_2) \tag{17}$$

Then, the secondary current \mathbf{I}_{21} can be deduced as Equation (18).

$$\mathbf{I}_{21} = \frac{j\omega_1 M_{12} \mathbf{V}_{11}}{(R_1 + jX_1)(R_2 + jX_2 + Z_2) + \omega_1^2 M_{12}^2} \tag{18}$$

By combining Equations (4), (13) and (18), the following equation can be obtained.

$$I_{2,dc} = \frac{8\omega_1 M_{12} V_{1,dc} \sin \alpha_1 \sin \beta_2}{\pi^2} \frac{\cos \varphi_2}{|(R_1 + jX_1)(R_2 + jX_2 + Z_2) + \omega_1^2 M_{12}^2|} \quad (19)$$

Defining the function $g_2(\varphi_2)$ to indicate the influence of φ_2 on $I_{2,dc}$.

$$g_2(\varphi_2) = \frac{\cos \varphi_2}{|(R_1 + jX_1)(R_2 + jX_2 + Z_2) + \omega_1^2 M_{12}^2|} \quad (20)$$

By substituting Equations (7) and (20) into Equation (19), $I_{2,dc}$ can be rewritten as

$$I_{2,dc} = \frac{8\omega_1 M_{12} V_{1,dc} \sin \alpha_1 \sin \beta_2}{\pi^2} g_2(2\pi(f_1 - f_2)t + \varphi_{2,0}). \quad (21)$$

The output current is related to the frequency difference of the controllers and the initial phase. Without synchronization, φ_2 changes periodically, resulting in the variation of $g_2(\varphi_2)$. As a result, $I_{2,dc}$ will oscillate at the frequency of $(f_1 - f_2)$.

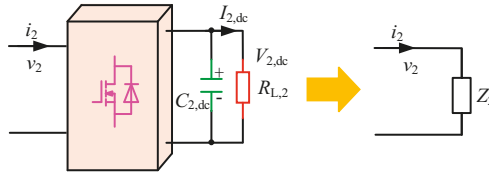


Figure 4. Equivalent circuit of active bridge.

2.3. Multiple Receivers without Cross Coupling

Figure 5 shows a multiple active receiver WPT system without cross coupling among the receiving coils, which has one transmitter and multiple receivers. The transmitting and receiving coils are coupled, whose mutual inductances are denoted as M_{1i} ($i \geq 2$). L_i , R_i , C_i , $C_{i,dc}$ and $R_{L,i}$ are the coil inductance, coil resistance, compensation capacitor, filtering capacitor and loading resistance of receiver i , respectively. v_i , i_i and $I_{i,dc}$ are the resonant voltage, resonant current and output dc current, respectively.

The phase difference between v_{i1} and i_{i1} (φ_i) can be expressed as

$$\varphi_i = 2\pi(f_1 - f_i)t + \varphi_{i,0}, \quad (22)$$

where $\varphi_{i,0}$ and f_i are the initial phase of φ_i and the operating frequency of receiver i , respectively.

Equivalent impedance Z_i and reactance X_i given by Equations (23) and (24), can be obtained according to Equations (12) and (14).

$$Z_i = \frac{8 \sin^2 \beta_i \cos \varphi_i R_{L,i} e^{j\varphi_i}}{\pi^2} \quad (23)$$

$$X_i = \omega_1 L_i - \frac{1}{\omega_1 C_i} \quad (24)$$

The source of the system described is the primary resonant voltage. The original electromotive force of each receiver coil is induced by the primary current. Therefore, the resonant current frequencies of the receivers are supposed to be identical to the primary operating frequency. The current loops of the system are given as follows.

$$\mathbf{V}_{11} = -\sum_{k=2}^n j\omega_1 M_{1k} \mathbf{I}_{k1} + \mathbf{I}_{11} (R_1 + jX_1) \tag{25}$$

$$0 = -j\omega_1 M_{1i} \mathbf{I}_{i1} + \mathbf{I}_{i1} (R_i + jX_i + Z_i) \tag{26}$$

Primary current \mathbf{I}_{11} and the receiver-side resonant current \mathbf{I}_{i1} can be deduced as Equations (27) and (28).

$$\mathbf{I}_{11} = \frac{\mathbf{V}_{11}}{R_1 + jX_1 + \sum_{k=2}^n \frac{\omega_1^2 M_{1k}^2}{R_k + jX_k + Z_k}} \tag{27}$$

$$\mathbf{I}_{i1} = \frac{j\omega_1 M_{1i} \mathbf{V}_{11}}{(R_i + jX_i + Z_i) (R_1 + jX_1 + \sum_{k=2}^n \frac{\omega_1^2 M_{1k}^2}{R_k + jX_k + Z_k})} \tag{28}$$

Thus, $I_{i,dc}$ is derived based on Equation (13).

$$I_{i,dc} = \frac{8\omega_1 M_{1i} V_{1,dc} \sin \alpha_1 \sin \beta_i}{\pi^2} \frac{\cos \varphi_i}{\left| (R_i + jX_i + Z_i) (R_1 + jX_1 + \sum_{k=2}^n \frac{\omega_1^2 M_{1k}^2}{R_k + jX_k + Z_k}) \right|} \tag{29}$$

Z_i is related to φ_i . Therefore, function $g_i(\varphi_2, \dots, \varphi_n)$ is defined to indicate the influence of φ_i on $I_{i,dc}$.

$$g_i(\varphi_2, \dots, \varphi_n) = \frac{\cos \varphi_i}{\left| (R_i + jX_i + Z_i) (R_1 + jX_1 + \sum_{k=2}^n \frac{\omega_1^2 M_{1k}^2}{R_k + jX_k + Z_k}) \right|} \tag{30}$$

By substituting Equations (22) and (30) into Equation (29), $I_{i,dc}$ can be rewritten as

$$I_{i,dc} = \frac{8\omega_1 M_{1i} V_{1,dc} \sin \alpha_1 \sin \beta_i}{\pi^2} g_i((2\pi(f_1 - f_2)t + \varphi_{2,0}), \dots, (2\pi(f_1 - f_n)t + \varphi_{n,0})). \tag{31}$$

When the cross coupling among the receiving coils is not considered, $I_{i,dc}$ is a function of the operating frequency differences $(f_1 - f_i)$ and the initial phases $(\varphi_{i,0})$.

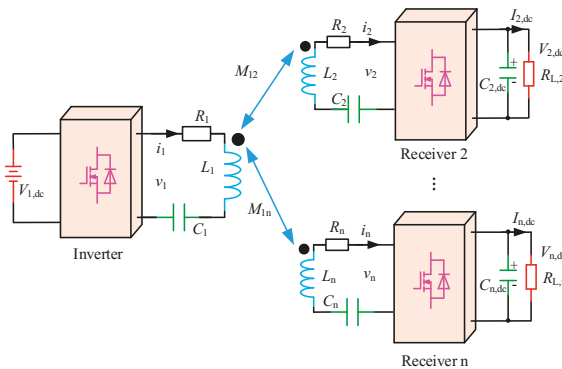


Figure 5. Schematic of a multiple active receiver WPT system without cross coupling.

2.4. Multiple Receivers with Cross Coupling

Figure 6 shows a multiple active receiver WPT system with cross coupling among the receiving coils. The cross coupling mutual inductances are denoted as M_{ij} ($i, j \geq 2$ and $i \neq j$). The current loop of receiver i can be deduced as Equation (32).

$$0 = - \sum_{j=1, j \neq i}^n j\omega_1 M_{ji} \mathbf{I}_{j1} + \mathbf{I}_{i1} (R_i + jX_i + Z_i), i \geq 2 \tag{32}$$

Then, the receiver-side resonant current \mathbf{I}_{i1} can be obtained by:

$$\mathbf{I}_{i1} = \frac{\sum_{j=1, j \neq i}^n j\omega_1 M_{ji} \mathbf{I}_{j1}}{R_i + jX_i + Z_i}, i \geq 2. \tag{33}$$

Thus, the expression of $I_{i,dc}$ is derived.

$$I_{i,dc} = \frac{2\sqrt{2} \sin \beta_i \cos \varphi_i}{\pi} \frac{\left| \sum_{j=1, j \neq i}^n j\omega_1 M_{ji} \mathbf{I}_{j1} \right|}{|R_i + jX_i + Z_i|}, i \geq 2 \tag{34}$$

The equivalent impedance of the receiver and the resonant currents are related to φ_i . Thus, function $g_i(\varphi_2, \dots, \varphi_n)$ is defined as follows.

$$g_i(\varphi_2, \dots, \varphi_n) = \frac{\left| \sum_{j=1, j \neq i}^n j\omega_1 M_{ji} \mathbf{I}_{j1} \right| \cos \varphi_i}{|R_i + jX_i + Z_i|}, i \geq 2 \tag{35}$$

$I_{i,dc}$ can be rewritten as Equation (36).

$$I_{i,dc} = \frac{2\sqrt{2} \sin \beta_i}{\pi} g_i((2\pi(f_1 - f_2)t + \varphi_{2,0}), \dots, (2\pi(f_1 - f_n)t + \varphi_{n,0})) \tag{36}$$

Regardless of their tuned or detuned conditions, having one or multiple active receivers, with or without crossing coupling, the frequency of receiver-side resonant currents should be f_1 . It is found that Equations (8), (21), (31) and (36) can be written into a similar expression as shown in Equation (37) where a_i is a constant value under a certain system configuration.

$$I_{i,dc} = a_i g_i((2\pi(f_1 - f_2)t + \varphi_{2,0}), \dots, (2\pi(f_1 - f_n)t + \varphi_{n,0})) \tag{37}$$

The synchronization target is to keep $I_{i,dc}$ constant and find the reference phase of the receivers. Thus, the synchronization of the WPT systems can be divided into two independent functions: Ensuring that $f_2 = f_3 = \dots = f_n = f_1$ and $\varphi_{2,0} = \varphi_{3,0} = \dots = \varphi_{n,0} = 0^\circ$.

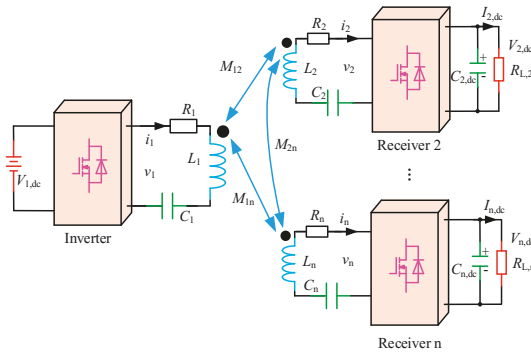


Figure 6. Schematic of a multiple active receiver WPT system with cross coupling.

3. Proposed Synchronization Technique

The synchronization system can be decomposed into independent frequency locking and reference phase calibration as analyzed in Section 2. In this paper, the frequency locking is realized by a proposed hardware circuit and the reference phase calibration is achieved through software code.

3.1. Hardware Circuit

The frequency of receiver-side resonant currents should be f_1 . i_i flows through C_i . Thus, the frequency of the voltage across C_i should be equal to f_1 as well. In this paper, the voltage across the compensation capacitor is utilized for frequency locking.

Figure 7 shows the block diagram and detailed schematic of the proposed frequency locking circuit, which produces a zero-crossing synchronization signal. The voltage across C_i is divided over the resistances, which can obtain voltage v_{ci} . The high-side resistance R_h is 2 MΩ and the low-side resistance R_l is 10 kΩ. To ensure that v_{ci} stays within a proper range, the values of the divider resistances should be configured with the power level. A bidirectional Zener diode with 6.8 V reverse breakdown voltage is used to limit the voltage. v_{ci} is sent to the comparator TLV3502 (Texas Instruments, Richardson, TX, USA) which can generate a square wave with the frequency f_1 . After passing through the isolator ISO721 (Texas Instruments, Richardson, TX, USA), the frequency locking signal v_{fi} is fed to the synchronization port of DSP such as GPIO6 in TMS320F28335 (Texas Instruments, Richardson, TX, USA). The comparator and the isolator are supplied by an isolated direct-current-to-direct-current (DC/DC) converter ADUM5000 (Analog Devices Inc., Wood, MA, USA). The resonant capacitor voltage is high and is converted into a digital signal immediately. Thus, the frequency locking circuit is insensitive to interferences. In addition, the circuit consists of a comparator, an isolator and an isolated power supply chip, which makes it cost effective and has a low power consumption.

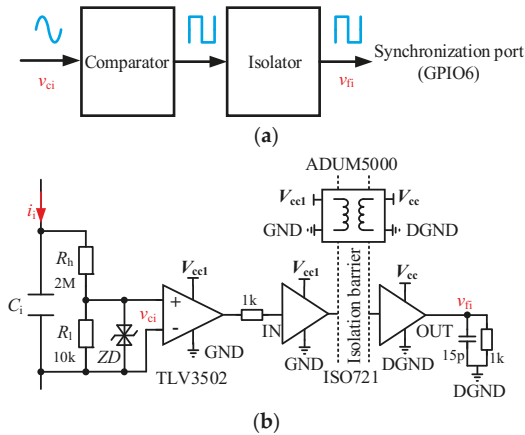


Figure 7. Proposed frequency locking circuit: (a) block diagram; and (b) detailed schematic.

3.2. Software Code

v_{ci} lags i_i by 90° . However, due to the time delay of the frequency locking and the driver circuits, $\varphi_{i,0}$ in Equation (37) is uncertain and can differ from the coded initial phase. After locking the frequency, the reference phases of the controllers should be calibrated, which is implemented by software code. The coded phase defined in the controller is φ_i' whose initial value is $\varphi_{i,0}'$. The task of reference phase calibration is to change $\varphi_{i,0}'$ to ensure $\varphi_{i,0} = 0$, that is, v_i and i_i are in phase. Figure 8 shows the reference phase calibration process. Firstly, φ_i' is set at $\varphi_{i,0}'$. v_i and i_i are captured by the oscilloscope. Then,

the system is turned on and v_i and i_i phase synchronization is observed. If v_i and i_i are not in phase, traversal algorithm can be executed to change φ_i' , where φ_i' can vary from $\varphi_{i,0}'$ to $360^\circ + \varphi_{i,0}'$. Once v_i and i_i are in phase, the reference phase is locked and $\varphi_{i,0}'$ is determined. Since the time delay remains almost unchanged for a certain circuit, the corresponding phase error is independent of the load, the mutual inductance and other system parameters. Furthermore, the reference phase calibration only needs one execution after the system is implemented and it can be completed within several minutes, which makes this synchronization technique easy for wide applications.

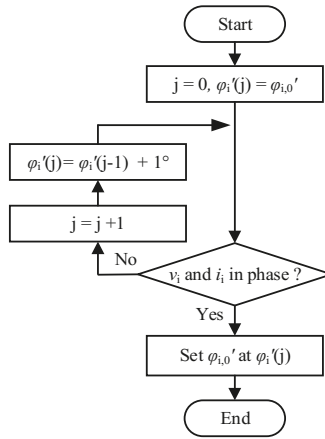


Figure 8. Reference phase calibration process.

The main flowchart of the phase calibration process has been elaborated above, whereas the register configuration details are of great importance as described below. Improper configuration can lead to the system becoming unstable.

There are three counter modes of the enhanced pulse width modulator (EPWM): count-up mode, count-down mode and count-up-down mode. For easy calculation of the register values, the count-up mode is adopted in this work. The frequency locking process in the controller is shown in Figure 9, where TBPRD1 and TBPRDi ($i \geq 2$) are the time base periods (TBPRD) of the PWM modules of the transmitter-side and receiver-side controllers, respectively. For better understanding, the time delay of the devices is not considered in this analysis. Ideally, time base periods can be the same. However, the actual output frequency will deviate from the preset value due to limited frequency precision. In practice, TBPRDi should be greater than TBPRD1. The receiver-side controller detects the frequency locking signal at first, where the counter should be equivalent to TBPRD1. Then, the counter is reset to 0. This process can ensure the frequency of v_i equal to f_1 .

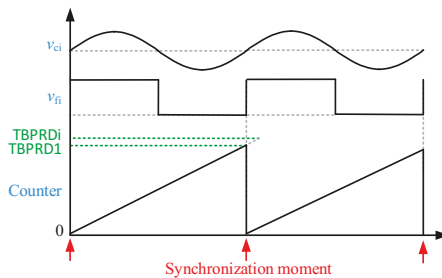


Figure 9. Synchronization process.

Faulty configurations of the reserved registers can lead to two problems. Firstly, as shown in Figure 10a, where TBPRDi is smaller than TBPRD1, the counter operates abnormally. The counter reaches TBPRDi and is reset to 0. When the frequency locking signal appears, the counter is reset to 0 again, resulting in a wrong counting sequence. Therefore, TBPRDi should be greater than TBPRD1. Secondly, as shown in Figure 10b, although the counter operates normally, an erroneous gate drive signal is generated. Comparing values of groups A and B (CMPA and CMPB) are used to generate β_i and φ_i . When CMPB (or CMPA) falls into the range of (TBPRD1, TBPRDi), wrong gate drive signals appear. The counter cannot reach the reserved register value where the control signal is supposed to be toggled. Then, the gate drive signal remains unchanged, which leads to a wrong v_i . Therefore, the maximum CMPA and CMPB should be slightly smaller than TBPRD1, which is denoted as CMP_{max} . The specific value of CMP_{max} should be determined according to the frequency precision of the controllers.

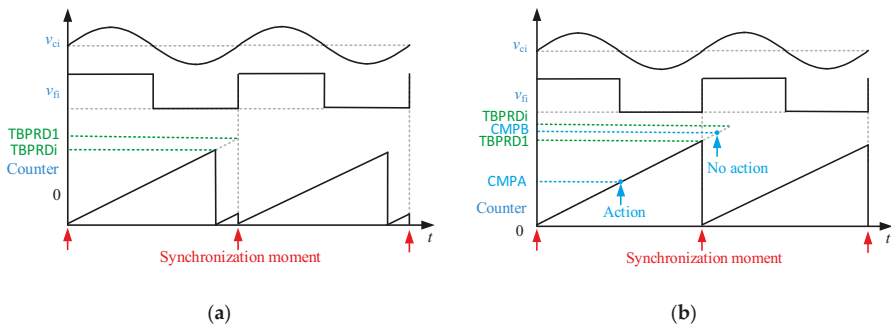


Figure 10. Faulty configuration of reserved registers: (a) wrong counting sequence; and (b) comparing value beyond the counting range.

Figure 11 shows the detailed synchronization process and corresponding relationships among the reserved register values and the phase angles. The gate drive signals of receiver i are denoted as Q_{4i-3} , Q_{4i-2} , Q_{4i-1} and Q_{4i} , whereas the comparing values of the corresponding controller are denoted as $CMPA_{2i-1}$, $CMPB_{2i-1}$, $CMPA_{2i}$ and $CMPB_{2i}$. The mathematical expressions of the register values are shown in the following equations.

$$CMPA_{2i-1} = \frac{(\varphi_{i,0'} - \varphi_i + \beta_i - 90)}{360} CMP_{max} \tag{38}$$

$$CMPB_{2i-1} = \frac{(\varphi_{i,0'} - \varphi_i + \beta_i - 270)}{360} CMP_{max} \tag{39}$$

$$CMPA_{2i} = \frac{(\varphi_{i,0'} - \varphi_i - \beta_i + 90)}{360} CMP_{max} \tag{40}$$

$$CMPB_{2i} = \frac{(\varphi_{i,0'} - \varphi_i - \beta_i - 90)}{360} CMP_{max} \tag{41}$$

Since φ_i and $\varphi_{i,0'}$ may range from 0° to 360° , according to Equations (38)–(41), the calculated CMPA and CMPB values may be beyond $[0, CMP_{max}]$. When these values are negative or greater than CMP_{max} , several times of CMP_{max} should be added or subtracted to ensure them falling in the range.

The task of reference phase calibration process is to change $\varphi_{i,0'}$ to track the point where $\varphi_i = 0$. After that, the receiver-side phase angles can be applied for impedance matching or output power regulation [20,21]. Many wireless charging devices require a constant voltage supply. Thus, Figure 12 shows the control flowchart for constant voltage power transfer, where $U_{i,dc}^*$ represents the desired voltage. If $U_{i,dc}$ is greater than $U_{i,dc}^*$ (i.e., $U_{i,dc} > U_{i,dc}^*$), β_i is decreased by 1° . Otherwise, β_i is increased by 1° . This method is effective and easy to implement.

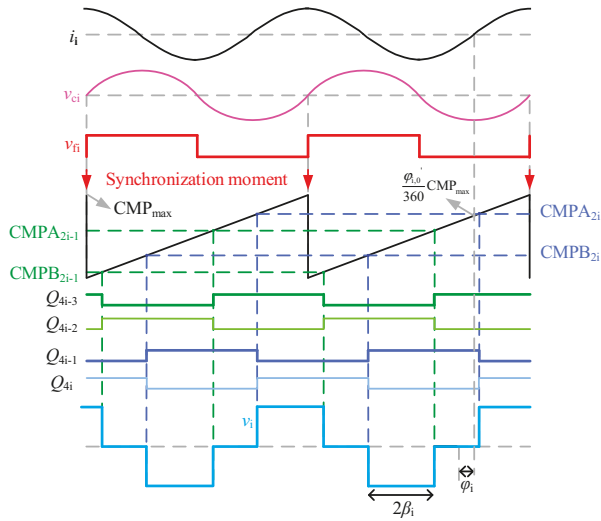


Figure 11. Detailed synchronization process and corresponding relationships among reserved register values and phase angles.

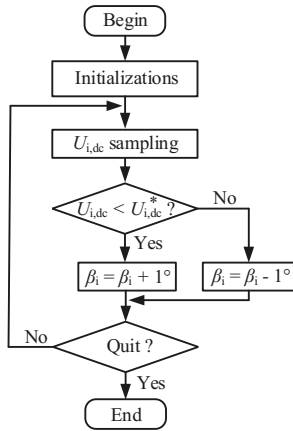


Figure 12. Flowchart of constant voltage power transfer.

3.3. System Layout

The schematic of the proposed WPT system with multiple active receivers is shown in Figure 13. A frequency locking circuit is installed on each receiver side that produces the synchronization signal for each DSP controller.

The prototype system is implemented in the following sequence: Firstly, the coded initial phase is calibrated and then the corresponding reference phase is written into the controllers. Secondly, the primary controller is turned on and the primary active bridge inverts the high frequency voltage. The frequency locking signal is generated, whereas the receiver-side controllers remain on standby and the diode rectification is used by the receivers. Thirdly, the gate drive signals of the receivers are generated. Finally, the phase angles are altered according to power transfer requirements.

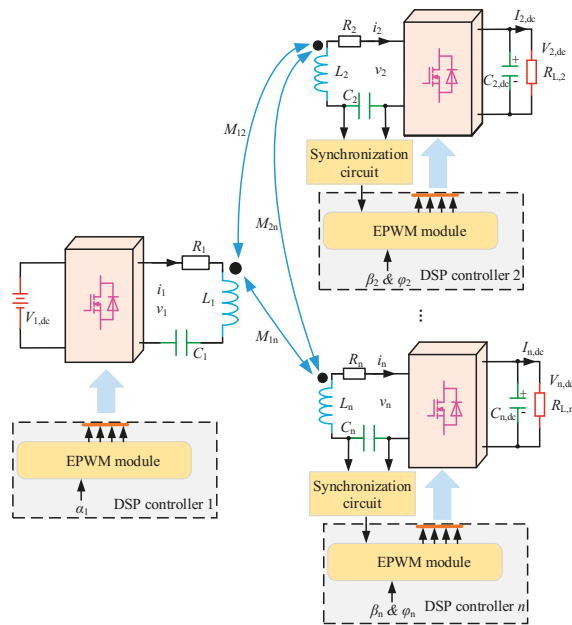


Figure 13. System schematic.

4. Experiment and Discussion

To verify the presented synchronization technique, the system is experimentally studied by using two prototypes: the first WPT system is implemented with one active receiver, whereas, the other with two active receivers. The specific parameters of the prototypes are listed in Table 1. Three independent microcontrollers and six Cree half bridges are used [33]. The coil self-inductances and mutual inductances are measured using inductance, capacitance, and resistance (LCR) meter TH2830 (RIGOL, Suzhou, China). Chroma programmable alternating-current-to-direct-current (AC/DC) electronic load model 63803 (Chroma, Marlborough, MA, USA) is utilized to vary the loading resistance. Tektronix TPS2024B Oscilloscope (Tektronix, Inc., Beaverton, OR, USA) is used to record the experimental waveforms. The experimental video is attached in Supplementary Materials.

Table 1. Key parameters of proposed system.

Symbol	Quantity	Value
L_1	coil inductance of transmitter	61 μH
L_2	coil inductance of receiver 1	61 μH
L_3	coil inductance of receiver 2	81 μH
C_1	primary compensation capacitance	0.05 μF
C_2	compensation capacitance of receiver 1	0.05 μF
C_3	compensation capacitance of receiver 2	0.04 μF

4.1. One active Receiver WPT System

Figure 14 shows the photograph of the WPT system with one active receiver. Figure 14a shows the designed DSP controller which consists of frequency locking circuit, power supply module and DSP TMS320F28335. Figure 14b shows the view of the complete system. Both the coil inductances are 61 μH , which are compensated by 0.05 μF AC capacitors. $V_{1,dc}$ is 50 V. The power transfer distance (d_{12}) is 80 mm with the mutual inductance of 16.7 μH .

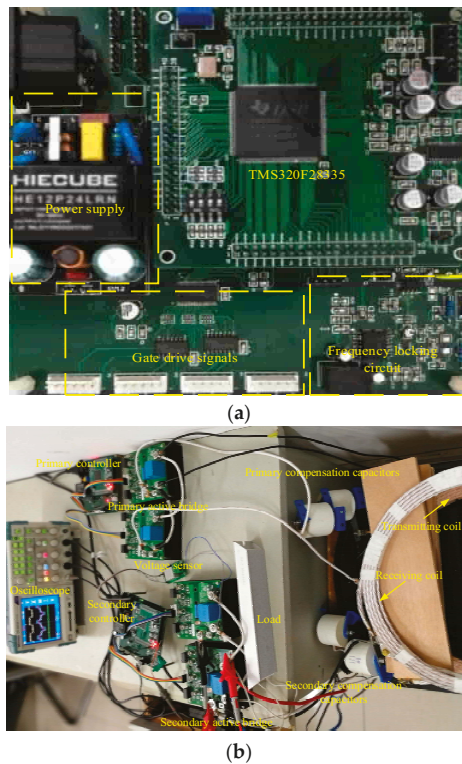


Figure 14. Photograph of WPT system with one active receiver: (a) DSP controller; and (b) overall system.

According to international standard of wireless electric vehicle charging SAE J2954 [34], the operating frequency of the WPT system ranges from 81.38 kHz to 90 kHz. The worst possible synchronization scenario is investigated in this paper, that is, when f_1 is 90 kHz. The secondary operating frequency is also set at 90 kHz. Figure 15 shows the experimental result of v_1 , v_2 , i_2 and $V_{2,dc}$ without proposed synchronization technique. Both α_1 and β_2 are 45° . $R_{L,2}$ is 50Ω . The transient process is shown in the upper portion of the figure, whereas the corresponding enlarged details are shown in the lower portion. As evident from the figure, $V_{2,dc}$ changes periodically at a frequency about 0.6 Hz. Because of the limited frequency precision of the microcontrollers, there exists 0.6 Hz frequency difference between the transmitter and the receiver. Although the frequency difference is small compared to 90 kHz operating frequency, φ_2 ranges from 0° to 360° at 0.6 Hz. Since $I_{2,dc}$ is a cosine function according to (8), power oscillations appear. When φ_2 lies within a range of $(90^\circ, 270^\circ)$, the power is transferred from the secondary side to the primary side. However, loading resistance is utilized in this experiment, which cannot provide the required power. Therefore, $V_{2,dc}$ becomes zero during this phase range as shown in the lower part of Figure 15a. When φ_2 lies within a range of $(-90^\circ, 90^\circ)$, the power is transferred to the secondary side and $V_{2,dc}$ is a cosine function. In simulations, the frequency of the gate drive signal is identical to the preset one, which can be used to verify the above experiment. A simulation in Simulink is implemented and $f_1 - f_2$ is set at 0.6 Hz. The simulated result in Figure 15b agrees well with the experiment, which validates the synchronization analysis. It can be concluded that WPT systems with active receivers cannot function normally without applying synchronization techniques.

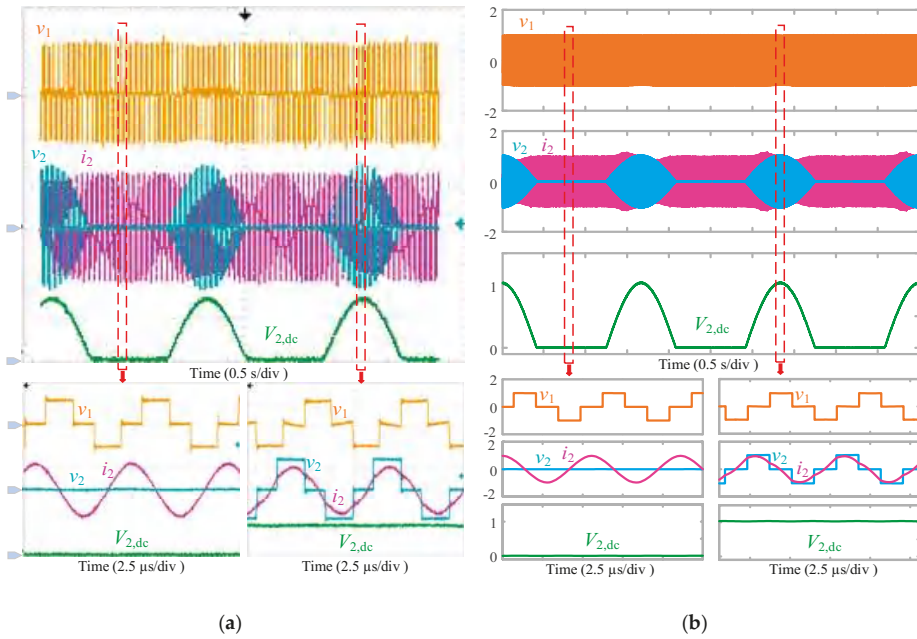


Figure 15. Power oscillations without synchronization: (a) experimental; and (b) simulated. v_1 , 50 V/div; v_2 and $V_{2,dc}$, 100 V/div; i_2 , 5 A/div.

Figure 16 shows the experimental synchronization results of the proposed technique under various conditions, including v_{f2} , v_2 , i_2 and $V_{2,dc}$. Figure 16a shows the typical experimental waveforms of the tuned WPT system. The input voltage, the phase angles and the load remain unchanged. The measured resonant frequency of the system is 91.5 kHz and the transmitter operates at this frequency. As can be seen in Figure 16a, the frequency locking signal v_{f2} is stable and v_2 is in phase with i_2 . Figure 16b shows the typical waveforms of the detuned WPT system where the operating frequency is 90 kHz. The proposed synchronization technique performs well in the detuned WPT system. Figure 16c shows the experimental result during mutual inductance variation in the detuned WPT system. d_{12} changes from 120 mm to 80 mm, where the mutual inductance changes from 11.1 μ H to 16.7 μ H. $V_{2,dc}$ decreases with the increase of mutual inductance. As evident from the enlarged details, the system is stable and v_2 is still in phase with i_2 . Figure 16d shows the experimental result during load variation in the detuned WPT system. $R_{L,2}$ changes from 50 Ω to 25 Ω by connecting the electronic load in parallel. Although $V_{2,dc}$ decreases by nearly half, v_2 and i_2 remain in phase.

The proposed synchronization system can work effectively with variations in operating frequency, coil position and load. Then, β_2 can be used to regulate the output power. Figure 17 shows the constant voltage power transfer process. The reference output voltage is set at 100 V. To guarantee the transferred power, $V_{1,dc}$ is increased to 80 V in this experiment. The load changes from 50 Ω to 25 Ω . To better record and observe the transition, β_2 is varied by 1° each 100 millisecond in this experiment. As evident from the figures, β_2 increases with decreasing $R_{L,2}$ to supply more power and $V_{2,dc}$ stabilizes at the desired 100 V within 0.25 s. The setting period can be decreased by reducing the observation time and increasing the increment or decrement to β_2 . The received power increases from 200 W to 400 W and the dc-to-dc efficiency increases from 91.5% to 92.3%. For operational convenience, a magnetic core has not been used on the receiver side. The coupling factor can be increased by installing a magnetic core, which can improve the overall efficiency.

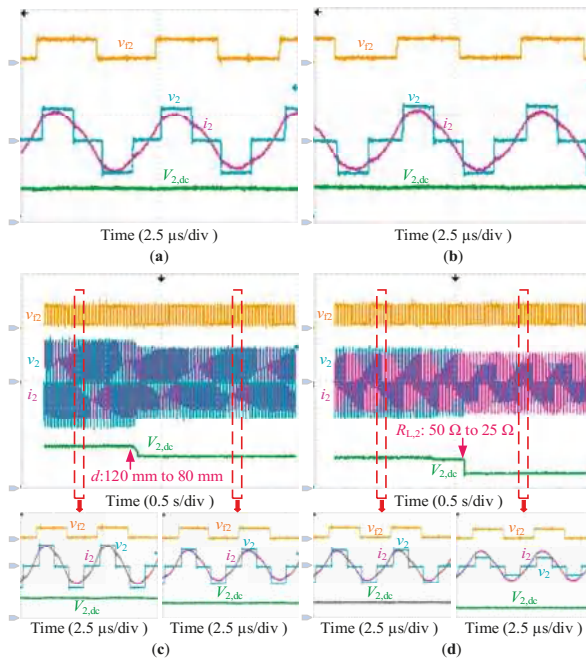


Figure 16. Experimental synchronization results of proposed technique under various conditions: (a) tuned WPT system; (b) detuned WPT system; (c) mutual inductance variation in detuned WPT system; and (d) load variation in detuned WPT system. v_{12} , 5 V/div; v_2 and $V_{2,dc}$, 100 V/div; i_2 , 5 A/div.

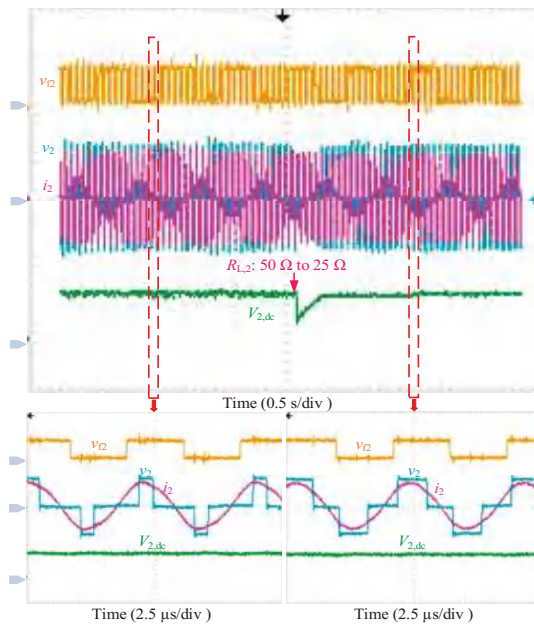


Figure 17. Constant voltage power transfer. v_{12} , 5 V/div; v_2 and $V_{2,dc}$, 100 V/div; i_2 , 10 A/div.

4.2. Multiple Active Receiver Wpt System

Figure 18a,b show the photographs of the multiple active receiver WPT systems without and with cross coupling between receiver-side coils, respectively. $V_{1,dc}$ is 50 V and α_1 is set at 45° . $R_{L,2}$ and $R_{L,3}$ are 50Ω . L_3 is $81 \mu\text{H}$, compensated by $0.04 \mu\text{F}$ AC capacitor. The calculated resonant frequency of receiver 2 is 88.5 kHz . The systems operates at 90 kHz , that is, the complex detuned condition. To confirm that the receivers can work under different conditions, β_2 is set at 45° and β_3 at 30° . In Figure 18a, the transmitting coil lies in the middle and the cross coupling between the two receiving coils is neglected. Both d_{12} and d_{13} are 80 mm . M_{12} and M_{13} are $21.2 \mu\text{H}$ and $16.7 \mu\text{H}$, respectively. In Figure 18b, the receivers are put on the above. Except for the mutual inductances among the coils, the system parameters remain the same. M_{12} , M_{13} and M_{23} are $8.9 \mu\text{H}$, $11.7 \mu\text{H}$ and $4.8 \mu\text{H}$, respectively. The cross coupling mutual inductance between the receiving coils is comparable with the mutual inductances.

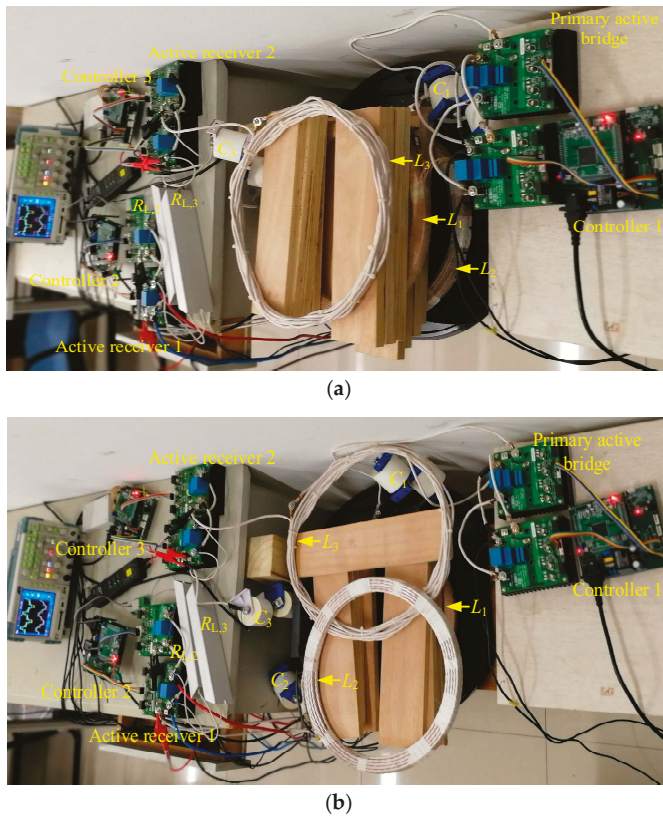


Figure 18. Multiple active receiver WPT systems without and with cross coupling between receiver-side coils: (a) without cross coupling; and (b) with cross coupling.

Figure 19a shows the typical waveforms of the successful synchronization result without crossing coupling, including v_2 , i_2 , v_3 and i_3 . As evident from the figure, v_2 and v_3 are in phase with i_2 and i_3 , respectively. The power is transferred to the active receivers successfully. Figure 19b shows the typical waveforms of the system with cross coupling between two receiver-side coils. The synchronization system performs well and the WPT system is stable. These experiments confirm the feasibility of the proposed synchronization technique in multiple active receiver WPT systems.

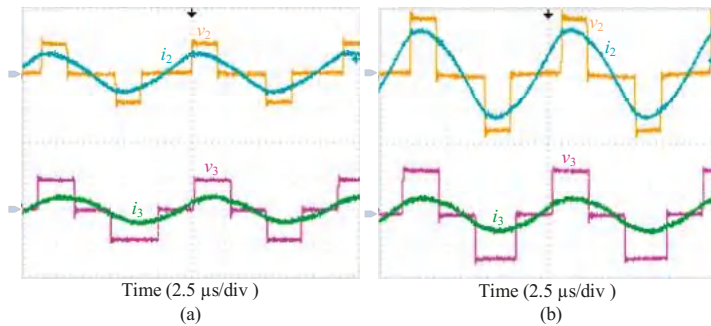


Figure 19. Successful synchronization results of multiple active receiver systems without and with cross coupling between receiver-side coils: (a) without cross coupling; and (b) with cross coupling. v_2 and v_3 , 50 V/div; i_2 and i_3 , 5 A/div.

4.3. Discussion

This paper provides a comprehensive synchronization analysis of different WPT systems and decomposes the synchronization system into independent frequency locking and reference phase calibration. Table 2 summarizes the comparisons of different synchronization techniques. The inverter’s operating frequency is 20 kHz in References [6,17], 30 kHz in Reference [20] and 85 kHz in Reference [29]. A higher operating frequency can amplify the phase errors observed in Reference [17]. Thus, the synchronization difficulty increases with the increasing frequency. The proposed system can operate at 90 kHz, validating the effectiveness of proposed frequency locking method. In addition, the proposed synchronization technique is independent of system parameters and the phase error can be calibrated in advance. Thus, it can perform well under different conditions such as frequency variation, mutual inductance variation, load variation and so forth. Usually, a critical and parameter-sensitive phase-shift circuit is needed to compensate the phase error caused by time delay. However, it is easier to achieve reference phase calibration by software code, which reduces the complexity and cost of the synchronization circuit. Although the proposed technique is validated through a resistance load, it can be effectively applied to battery charging and bidirectional power transfer systems.

Table 2. Comparisons of different synchronization techniques.

Source	Operating Frequency	Frequency Variation	Mutual Induction Variation	Load Variation	Multiple Receivers	Phase Calibration Method	Complexity
[6]	20 kHz	×	×	✓	×	N/A	N/A
[17]	20 kHz	×	✓	✓	×	Circuit-based	Complex circuit and algorithm
[20]	30 kHz	×	×	✓	×	Circuit-based	N/A
[29]	85 kHz	×	✓	✓	×	Circuit-based	Complex circuit and algorithm
This paper	90 kHz	✓	✓	✓	✓	Software Code	Simple circuit and simplified algorithm

5. Conclusions

This paper presents a detailed synchronization analysis of WPT systems with active receivers. The synchronization problem is decomposed into two independent parts: frequency locking and reference phase calibration. Based on the analysis, a novel synchronization technique is proposed where frequency locking is realized through the hardware circuit and reference phase calibration is achieved through software code, which is a great progress for synchronization system design. In experiments, frequency locking can be realized at 90 kHz and reference phase calibration only requires one execution after the system is implemented. The proposed synchronization technique adapts to multiple active

receivers under tuned and detuned conditions. In addition, the synchronization system performs well when key system parameters vary. Constant voltage power transfer can be realized with 92.3% dc-to-dc efficiency at 400 W received power. The feasibility and effectiveness of the proposed synchronization technique have been verified by theoretical analysis and experimental results.

Supplementary Materials: The following are available online at <https://zenodo.org/record/1485267#.W-qdtFLFKJ0>.

Author Contributions: X.L., H.T. and X.Y. conceptualized the main idea of this research project; X.L. designed and conducted the experiments with the help of T.W.; N.J. and X.Y. checked the results. X.L. wrote the whole paper; N.J. and K.H. reviewed and edited the paper.

Funding: This research was funded by United Foundation of NSFC-Henan, grant number U1604136. The APC was funded by Xijun Yang.

Conflicts of Interest: The authors declare no conflict of interest.

References

1. Kurs, A.; Karalis, A.; Moffatt, R.; Joannopoulos, J.D.; Fisher, P.; Soljacic, M. Wireless power transfer via strongly coupled magnetic resonances. *Science* **2007**, *317*, 83–86. [[CrossRef](#)] [[PubMed](#)]
2. Almohaimeed, A.M.; Amaya, R.E.; Lima, J.A.; Yagoub, M.C.E. An Adaptive Power Harvester with Active Load Modulation for Highly Efficient Short/Long Range RF WPT Applications. *Electronics* **2018**, *7*, 125. [[CrossRef](#)]
3. He, X.; Shu, W.; Yu, B.; Ma, X. Wireless Power Transfer System for Rotary Parts Telemetry of Gas Turbine Engine. *Electronics* **2018**, *7*, 58. [[CrossRef](#)]
4. Wang, T.; Liu, X.; Jin, N.; Tang, H.; Yang, X.; Ali, M. Wireless Power Transfer for Battery Powering System. *Electronics* **2018**, *7*, 178. [[CrossRef](#)]
5. Liu, X.; Wang, T.; Jin, N.; Habib, S.; Ali, M.; Yang, X.; Tang, H. Analysis and Elimination of Dead-Time Effect in Wireless Power Transfer System. *Energies* **2018**, *11*, 1577. [[CrossRef](#)]
6. Li, Y.; Mai, R.; Liu, Y.; He, Z. Efficiency optimising strategy for dual coupled transmitters based WPT systems. *Electron. Lett.* **2016**, *52*, 1877–1879. [[CrossRef](#)]
7. Colak, K.; Asa, E.; Bojarski, M.; Czarkowski, D.; Onar, O.C. A Novel Phase-Shift Control of Semibridgeless Active Rectifier for Wireless Power Transfer. *IEEE Trans. Power Electron.* **2015**, *30*, 6288–6297. [[CrossRef](#)]
8. Tan, L.; Guo, J.; Huang, X.; Liu, H.; Wang, W.; Yan, C.; Zhang, M.; Yan, C.; Zhang, M. Coordinated source control for output power stabilization and efficiency optimization in WPT systems. *IEEE Trans. Power Electron.* **2018**, *33*, 3613–3621. [[CrossRef](#)]
9. Fu, M.; Yin, H.; Zhu, X.; Ma, C. Analysis and tracking of optimal load in wireless power transfer systems. *IEEE Trans. Power Electron.* **2015**, *30*, 3952–3963. [[CrossRef](#)]
10. Nauryzbayev, G.; Rabie, K.M.; Abdallah, M.; Adebisi, B. On the Performance Analysis of WPT-based Dual-Hop AF Relaying Networks in α - μ Fading. *IEEE Access* **2018**, *6*, 37138–37149. [[CrossRef](#)]
11. Huang, Y.; Shinohara, N.; Mitani, T. A Constant Efficiency of Rectifying Circuit in an Extremely Wide Load Range. *IEEE Trans. Microw. Theory Tech.* **2018**, *62*, 986–993. [[CrossRef](#)]
12. Fu, M.; Zhang, T.; Zhu, X.; Ma, C. A 13.56 MHz wireless power transfer system without impedance matching networks. In Proceedings of the 2013 IEEE Wireless Power Transfer Conference (WPTC), Perugia, Italy, 15–16 May 2013; pp. 222–225.
13. Lee, J.; Han, B. A bidirectional wireless power transfer EV charger using self-resonant PWM. *IEEE Trans. Power Electron.* **2015**, *30*, 1784–1787. [[CrossRef](#)]
14. Liu, X.; Wang, T.; Yang, X.; Jin, N.; Tang, H. Analysis and Design of a Wireless Power Transfer System with Dual Active Bridges. *Energies* **2017**, *10*, 1588. [[CrossRef](#)]
15. Berger, A.; Agostinelli, M.; Vesti, S.; Oliver, J.A.; Cobos, J.A.; Huemer, M. A Wireless Charging System Applying Phase-Shift and Amplitude Control to Maximize Efficiency and Extractable Power. *IEEE Trans. Power Electron.* **2015**, *30*, 6338–6348. [[CrossRef](#)]
16. Neath, M.J.; Swain, A.K.; Madawala, U.K.; Thrimawithana, D.J. An optimal PID controller for a bidirectional inductive power transfer system using multiobjective genetic algorithm. *IEEE Trans. Power Electron.* **2014**, *29*, 1523–1531. [[CrossRef](#)]

17. Thrimawithana, D.J.; Madawala, U.K.; Neath, M. A Synchronization Technique for Bidirectional IPT Systems. *IEEE Trans. Ind. Electron.* **2013**, *60*, 301–309. [CrossRef]
18. Madawala, U.K.; Thrimawithana, D.J. A bi-directional inductive power interface for electric vehicles in V2G systems. *IEEE Trans. Ind. Electron.* **2011**, *58*, 4789–4796. [CrossRef]
19. Mohamed, A.A.S.; Berzoy, A.; Mohammed, O. Experimental validation of comprehensive steady-state analytical model of bidirectional WPT system in EVs applications. *IEEE Trans. Veh. Technol.* **2017**, *66*, 5584–5594. [CrossRef]
20. Mai, R.; Liu, Y.; Li, Y.; Yue, P.; Cao, G.; He, Z. An Active Rectifier Based Maximum Efficiency Tracking Method Using an Additional Measurement Coil for Wireless Power Transfer. *IEEE Trans. Power Electron.* **2018**, *33*, 716–728. [CrossRef]
21. Liu, X.; Wang, T.; Yang, X.; Tang, H. Analysis of Efficiency Improvement in Wireless Power Transfer System. *IET Power Electron.* **2018**, *11*, 302–309. [CrossRef]
22. Diekhans, T.; De Doncker, R.W. A dual-side controlled inductive power transfer system optimized for large coupling factor variations and partial load. *IEEE Trans. Power Electron.* **2015**, *30*, 6320–6328. [CrossRef]
23. Bac, X.N.; Vilathgamuwa, D.M.; Foo, G.H.B.; Wang, P.; Ong, A.; Madawala, U.K.; Trong, D.N. An Efficiency Optimization Scheme for Bidirectional Inductive Power Transfer Systems. *IEEE Trans. Power Electron.* **2015**, *30*, 6310–6319.
24. TI Inc. *TMS320x2833x, 2823x High Resolution Pulse Width Modulator (HRPWM) Reference Guide*; TI Inc.: Dallas, TX, USA, 2009.
25. Zhao, L.; Thrimawithana, D.J.; Madawala, U.K. Hybrid Bidirectional Wireless EV Charging System Tolerant to Pad Misalignment. *IEEE Trans. Ind. Electron.* **2017**, *64*, 7079–7086. [CrossRef]
26. Thrimawithana, D.J.; Madawala, U.K.; Neath, M.; Geyer, T. A sense winding based synchronization technique for bidirectional IPT pick-ups. In Proceedings of the 2011 IEEE Energy Conversion Congress and Exposition (ECCE), Phoenix, AZ, USA, 17–22 September 2011; pp. 1405–1410.
27. Son, Y.; Ha, J.I. Data transmission method without additional circuits in bidirectional wireless power transfer system. In Proceedings of the Applied Power Electronics Conference and Exposition (APEC), Long Beach, CA, USA, 20–24 March 2016; pp. 3717–3721.
28. Thrimawithana, D.J.; Madawala, U.K.; Neath, M. A P&Q based synchronization technique for Bi-directional IPT pick-ups. In Proceedings of the 2011 IEEE Ninth International Conference on Power Electronics and Drive Systems (PEDS), Singapore, 5–8 December 2011; pp. 40–45.
29. Tang, Y.; Chen, Y.; Madawala, U.K.; Thrimawithana, D.J.; Ma, H. A New Controller for Bi-directional Wireless Power Transfer Systems. *IEEE Trans. Power Electron.* **2018**, *33*, 9067–9087. [CrossRef]
30. Mai, R.; Ma, L.; Liu, Y.; Yue, P.; Cao, G.; He, Z. A Maximum Efficiency Point Tracking Control Scheme Based on Different Cross Coupling of Dual-Receiver Inductive Power Transfer System. *Energies* **2017**, *10*, 217. [CrossRef]
31. Swain, A.K.; Devarakonda, S.; Madawala, U.K. Modeling, sensitivity analysis, and controller synthesis of multipickup bidirectional inductive power transfer systems. *IEEE Trans. Ind. Inform.* **2014**, *10*, 1372–1380. [CrossRef]
32. Zhao, R.; Gladwin, D.T.; Stone, D.A. Phase shift control based Maximum Efficiency Point Tracking in resonant wireless power system and its realization. In Proceedings of the 42nd Annual Conference of IEEE Industrial Electronics Society (IECON), Florence, Italy, 23–26 October 2016; pp. 4541–4546.
33. Cree Inc. *KIT8020CRD8FF1217P-1 CREE Silicon Carbide MOSFET Evaluation Kit User's Manual*; Cree Inc.: Durham, NC, USA, 2014.
34. J2954™ NOV2017, SAE J2954. 2017. Available online: https://saemobilus.sae.org/content/J2954_201711 (accessed on 14 June 2018).



© 2018 by the authors. Licensee MDPI, Basel, Switzerland. This article is an open access article distributed under the terms and conditions of the Creative Commons Attribution (CC BY) license (<http://creativecommons.org/licenses/by/4.0/>).

Article

A Novel Single-switch Phase Controlled Wireless Power Transfer System

Xin Liu ¹, Nan Jin ², Xijun Yang ¹, Khurram Hashmi ¹, Dianguan Ma ^{1,*} and Houjun Tang ¹

¹ Key Laboratory of Control of Power Transmission and Transformation Ministry of Education, Shanghai Jiao Tong University, 800 Dongchuan RD., Shanghai 200240, China; Liu_xin@sjtu.edu.cn (X.L.); yangxijun@sjtu.edu.cn (X.Y.); khurram_hashmi@sjtu.edu.cn (K.H.); hjtang@sjtu.edu.cn (H.T.)

² College of Electric and Information Engineering, Zhengzhou University of Light Industry, Zhengzhou 450002, China; jinnan@zzuli.edu.cn

* Correspondence: dgma@sjtu.edu.cn; Tel.: +86-138-1758-7820

Received: 6 October 2018; Accepted: 25 October 2018; Published: 29 October 2018

Abstract: Battery charging is a fundamental application of Wireless Power Transfer (WPT) systems that requires effective implementation of Constant Current (CC) and Constant Voltage (CV) power conduction modes. DC-DC converters used in WPT systems utilize large inductors and capacitors that increase the size and volume of the system in addition to causing higher DC losses. This work proposes a novel single-switch active rectifier for phase controlled WPT systems that is smaller in volume and weight as compared to conventional WPT topologies. The proposed method simplifies the control scheme using improved Digital Phase Control (DPC) and Analog Phase Control (APC) to realize the CC and CV power transfer modes. Furthermore, it prevents forward voltage losses in Silicon Carbide (SiC) switches and shoot through states with improved switching patterns. Simulation studies and experimental results are added to verify the effectiveness of the proposed methodology.

Keywords: active rectifiers; single-switch; analog phase control; digital phase control; wireless power transfer

1. Introduction

WPT techniques can realize energy conversion without physical connections. It has gained tremendous attention in both research and industry. Recently, wireless charging is the focus of study. To improve battery life time, the system has special requirements for the charging current and voltage profiles. WPT systems can realize both CC and CV power transfer modes through either primary or secondary side control. However, primary side control requires an additional communication channel [1,2]. It is more simplified and straightforward to directly achieve the CC and CV power transfer modes through secondary side control. Therefore, various DC-DC converters [3–8] are installed on the receiver side for power regulation, including buck converter [4], boost converter [5,9,10], and buck-boost converter [6,11]. Although DC-DC converters have simpler controls, they require additional capacitors and inductors that increase the weight, volume, and cost of the receiver. In addition, more cascaded circuits result in more losses on the DC side. To address these drawbacks, researchers propose active rectifiers on the receiver side. Active rectifiers are initially put forward to reduce the conduction losses of the diode rectifier and transfer the power bi-directionally [12–19]. Recently, Phase Control (PC) method is introduced to regulate resonant currents [20–25], which can further reduce the energy consumed by parasitic resistances.

Active rectifiers proposed for WPT systems can be classified into three categories: (i) full bridge rectifier with four switches; (ii) semi-bridgeless rectifier with two switches; and (iii) single-switch rectifier. Full active bridge rectifiers are used in various applications [12–25]. Four Metal-Oxide-Semiconductor Field Effect Transistors (MOSFETs) and four isolated driver circuits are installed on

the receiver side. Short circuit may appear in the full bridge topology due to faulty operation. Such a characteristic reduces the reliability of the WPT systems, especially battery charging systems where short circuit can lead to fire and explosion. It is desirable to investigate a more cost-effective and reliable approach to achieve secondary PC. Therefore, researchers in [26–28] develop two-switch rectifiers for WPT systems. In [26,27], a semi-bridgeless topology with two MOSFETs is proposed, where two switches are installed on the lower side of the rectifier. Secondary PC can be achieved as well. In [28], two MOSFETs are in reverse connection and controlled by one signal. Duty ratio control is applied to regulate the power. Furthermore, researchers in [29–36] investigate single-switch rectifiers. In [29], a switch is connected in parallel with a resonant compensation capacitor. Power regulation can be achieved by tuning/detuning through this variable capacitor. However, this method makes the system deviate from optimal resonant point, which may cause an efficiency drop. In [30–32], a switch is connected in series with parallel resonant tank. When the switch is turned off, the receiver transfers the power only in half the period. In addition, it is difficult to obtain a stable DC voltage. In [33], an active switch is inserted into the lower phase leg of a full diode bridge. When the switch is turned on, the resonant tank is shorted in half the period and the power can be regulated by duty ratio control. In [34–36], a boost converter is directly connected after the diode bridge which reduces one filter capacitor.

Active rectifiers with two or four switches can realize PC [12–27], whereas previous single-switch rectifiers can only adopt duty ratio control [29–36]. Although duty ratio control is easier to implement, it can cause resonant current oscillations when the power transfer path is chopped. It requires larger filter capacitors to maintain the desired DC voltage. In addition, single-switch receivers in [29–33] are half-controlled, i.e., their power regulation abilities are restricted, which may fail to meet the CC and CV power transfer requirements.

This paper proposes a novel single-switch phase controlled receiver for WPT systems for the first time. With this method, the secondary side inductor is removed and only a small filter capacitor is added, thereby reducing the size of the receiver and lessening the number of switches used. The salient contributions of this work are:

- (1) The proposed methodology reduces the number of active switches and isolated driver circuits as compared to conventional phase controlled receivers.
- (2) An APC method is applied to this improved receiver that circumvents synchronization algorithms and additional programming. APC method regulates the power automatically, which reduces the difficulty in design and implementation.
- (3) Most previously discussed single-switch methods are half-controlled and use duty ratio variation. In this work, the receiver is fully controlled and has a stronger power regulation ability as compared to conventional single-switch receivers.
- (4) The proposed receiver fully utilizes the SiC MOSFET to reduce switching losses while avoiding high forward voltage losses through its intrinsic diode.

This paper is divided as follows: Section 2 shows the proposed single-switch receiver and illustrates its operating modes. Then, it presents the derivations for the CC and CV power transfer modes. Section 3 elaborates the detailed implementation techniques of the proposed DPC and APC methods. In Section 4, simulations and experiments are added to validate the feasibility and effectiveness of the proposed topology and control methods. Finally, Section 5 concludes this paper.

2. Modeling and Analysis

This section presents mathematical modeling and analysis for the proposed WPT system.

2.1. Proposed Topology

A WPT system with the proposed single-switch receiver is shown in Figure 1. U_i and U_o are the DC voltages, whereas v_p and v_s are the primary and secondary resonant voltages. L_p and L_s are the

primary and secondary coil inductances, which are compensated by C_p and C_s , respectively. S_1 – S_5 are the SiC MOSFETs, and D_1 – D_5 are the diodes. C_1 and C_o are the filter capacitors, and R_L is the load. i_1 and i_2 are the currents flowing through S_5 and D_5 , respectively. I_i and I_o denote the input and output DC currents.

The typical waveforms of the proposed topology are shown in Figure 2, where 2β presents the phase angle of v_s . According to the current directions and paths, the receiver has six operating modes as depicted in Figure 3.

Mode 1: $i_s > 0$, and S_5 is on. There exist two current loops on the receiver side: L_s – D_1 – S_5 – D_4 – C_s and C_o – R_L . The diode bridge is short-circuited by S_5 , and I_o is supplied by C_o . Thus, v_s is zero.

Mode 2: $i_s > 0$, and S_5 is turned off at the beginning of Mode 2. C_o charges, and U_o increases. Thus, the current loop is L_s – D_1 – D_5 – U_o – D_4 – C_s . v_s is basically equal to U_o .

Mode 3: $i_s > 0$, and S_5 is turned on at the beginning of Mode 3. Then, i_s flows through S_5 and v_s becomes zero. U_o is supplied by C_o , and it begins to decrease. The current loops are: L_s – D_1 – S_5 – D_4 – C_s and C_o – R_L .

Mode 4: S_5 remains on and v_s remains zero, whereas i_s changes its direction. U_o continues to decrease. The current loop of i_s becomes L_s – C_s – D_3 – S_5 – D_2 .

Mode 5: $i_s < 0$, and S_5 is turned off at the beginning of Mode 5. C_o charges via i_s , and U_o begins to increase. The current loop is L_s – C_s – D_3 – D_5 – U_o – D_2 . v_s is basically equal to $-U_o$.

Mode 6: $i_s < 0$, and S_5 is turned on at the beginning of Mode 6. The current loop of i_s becomes L_s – C_s – D_3 – S_5 – D_2 , and U_o is supplied by C_o again.

To minimize switching losses, a SiC MOSFET can be used. Since the forward voltage of the intrinsic diode of the SiC MOSFET is high, a SiC diode is connected in parallel to overcome the high forward voltage loss of the intrinsic diode. However, no current freewheels through S_5 in the proposed receiver, which means the SiC diode is not necessary in this application. Therefore, the proposed receiver can fully utilize the SiC MOSFET to reduce switching losses while avoiding its drawback of high forward voltage losses through its intrinsic diode.

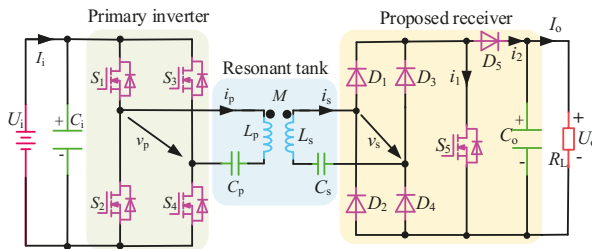


Figure 1. WPT system with proposed single-switch receiver.

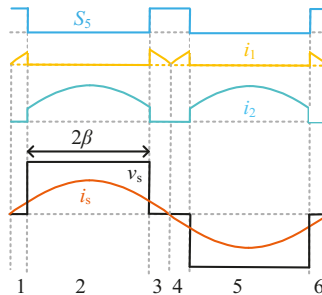


Figure 2. Typical waveforms of proposed receiver. S_5 , gate drive signal (blue line); i_1 , current flowing through MOSFET (yellow line); i_2 , current flowing through D_5 (light green line); i_s , secondary resonant current (orange line); v_s , secondary resonant voltage (black line).

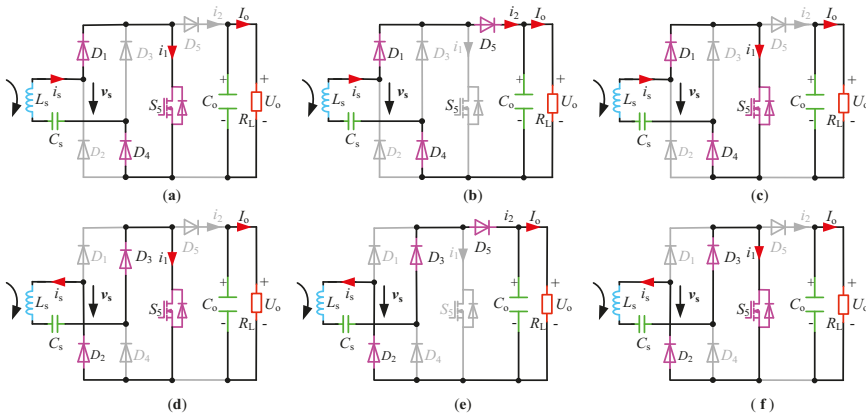


Figure 3. Operating modes of proposed receiver: (a) Mode 1; (b) Mode 2; (c) Mode 3; (d) Mode 4; (e) Mode 5; and (f) Mode 6.

2.2. Power Regulation

The CC and CV power transfer realizations are the basic requirements for battery charging systems. This section presents the theoretical analysis of secondary side control through proposed single-switch phase-controlled receiver.

The system operates at the resonant frequency, that is

$$\omega = \frac{1}{\sqrt{L_p C_p}} = \frac{1}{\sqrt{L_s C_s}} \tag{1}$$

R_p and R_s represent primary and secondary coil resistances, respectively. Then, the following equations are obtained according to Kirchoff Voltage Law (KVL).

$$v_p = -j\omega M i_s + i_p R_p \tag{2}$$

$$j\omega M i_p = v_s + i_s R_s \tag{3}$$

According to Fourier series and fundamental harmonic analysis [23–25], the root-mean-square value of v_s (V_s) can be denoted as:

$$V_s = \frac{2\sqrt{2}}{\pi} U_o \sin \beta. \tag{4}$$

Without considering the switching losses, the input and output powers of the rectifier are equal.

$$V_s I_s \simeq U_o I_o \tag{5}$$

Then, I_o versus I_s is deduced.

$$I_o \simeq \frac{2\sqrt{2} \sin \beta}{\pi} I_s \tag{6}$$

According to Equation (2), i_s can be rewritten as

$$i_s = \frac{v_p - i_p R_p}{-j\omega M} \simeq \frac{v_p}{-j\omega M} \tag{7}$$

Thus, I_o and U_o can be approximately derived as Equations (8) and (9).

$$I_o \simeq \frac{2\sqrt{2} \sin \beta}{\pi \omega M} V_p \tag{8}$$

$$U_o \simeq \frac{2\sqrt{2}R_L \sin \beta}{\pi\omega M} V_p \tag{9}$$

A larger β means a larger I_o and U_o . Therefore, β can be utilized to achieve the CC and CV power transfer modes.

3. Implementation Methods

This section presents implementation techniques for realizing DPC and APC with the proposed receiver in WPT system.

3.1. Digital Phase Control

The schematic of the DPC system is shown in Figure 4, where two independent Digital Signal Processors (DSPs) are installed. Digital control is widely used for various applications due to its flexibility. Since the controller should be isolated from the main circuit for safety consideration, isolated driver circuits as well as isolated power supplies are installed on primary and secondary sides. Furthermore, isolated current and voltage sensors are required on the receiver side for output electrical information feedback. To avoid power oscillations, the synchronization of secondary receiver is of essential importance. In [24], secondary synchronization is realized by utilizing the resonant voltage across C_s . The synchronization circuit consists of a comparator and an isolator, as shown in Figure 4, where R_h and R_l are the divider resistances. The operating frequency of the receiver-side switches in the full active bridge is equal to the current frequency, whereas it is twice that frequency in the proposed receiver. Thus, the receiver is synchronized once every two periods.

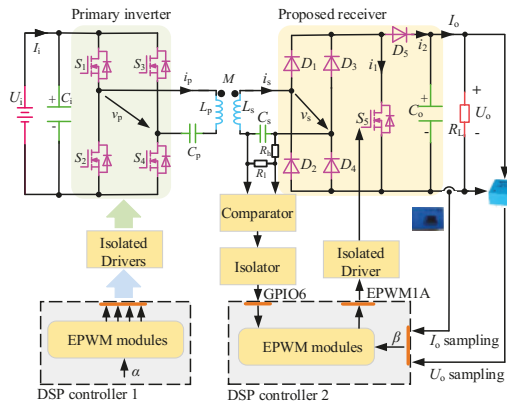


Figure 4. Schematic of DPC system.

Figure 5 shows the typical synchronization waveforms. The comparator turns the divided sinusoidal voltage into a square-wave synchronization signal. After passing a digital isolator, it is sent to the synchronization port of the DSP controller. TBPRD, CMPA, and CMPB are the time base period and comparing values of the reserved registers of the controller, respectively. The 0 and TBPRD shown in Figure 5 are the minimum and maximum values of the counter of the controller, i.e., CMPA and CMPB fall within the range of [0, TBPRD]. When the counter reaches CMPA, S_5 is turned off. When the counter reaches CMPB, S_5 is turned on. The relationships among TBPRD, CMPA, CMPB, and β are shown in Equations (10) and (11).

$$CMPA = \frac{180 - \beta}{180} TBPRD \tag{10}$$

$$CMPB = \frac{\beta}{180} TBPRD \tag{11}$$

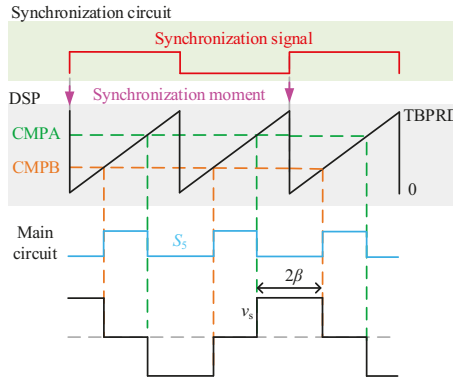


Figure 5. Typical synchronization waveforms.

TBPRD is determined by the inverter frequency, and the comparing values produce the desired β . Afterwards, the corresponding gate drive signal generates v_s in the main circuit.

As analyzed in Section 2, a larger β brings about larger I_o and U_o . Therefore, the output power regulation can be achieved by changing β . The algorithm flowchart of the CC and CV power transfer modes is shown in Figure 6, where I_o^* and U_o^* are the expected current and voltage values. Power transfer mode selection is determined by one bit, referred to as “Mode”, which is defined in the controller. The designer can initialize the Mode by setting it at 1 or 0 in the software code. When the Mode is 1, the receiver operates at the CC power transfer mode, otherwise, it operates at the CV power transfer mode. I_o is sampled for the CC power transfer mode, and U_o for the CV power transfer mode. To obtain accurate sampling values, 20 samplings of I_o or U_o are averaged. β ranges from 0° to 90° . When I_o or U_o is smaller than the desired value, β is increased by 0.1° . Otherwise, β is decreased by 0.1° . This control algorithm is simple and effective. The primary controller is turned on and the primary active bridge inverts the high frequency voltage. The frequency locking signal is generated, whereas the receiver-side controllers remain on standby and the diode rectification is used by the receiver at first. When U_o reaches the threshold value, the controller is turned on.

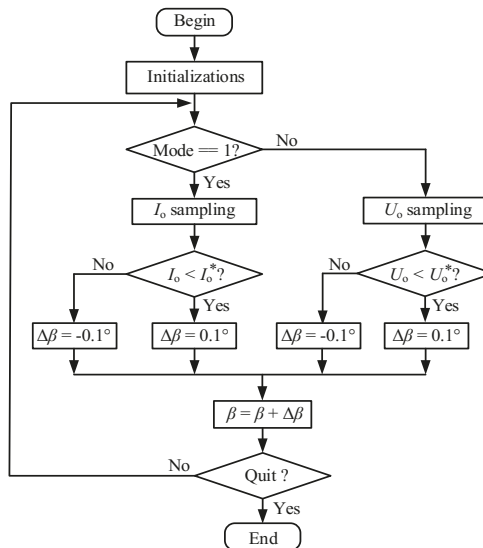


Figure 6. Algorithm flowchart of DPC receiver.

In full active bridge receivers, four gate drive signals should be controlled to generate v_s . However, β is determined by one signal in the proposed receiver, which makes the software code realization easier.

3.2. Analog Phase Control

The DPC method can achieve good control flexibility and performance. However, the receiver requires some auxiliary circuits. To further reduce the complexity and cost of the receiver, a novel APC method is presented as follows.

The schematic of the proposed APC system is shown in Figure 7. R_1 and R_2 are the divider resistances. R_3 and R_9 are the sampling resistances. The voltage across R_3 is fed back for the CC power transfer, and the divided voltage across R_2 for the CV power transfer. Since R_3 is small, and R_4 and R_5 are used to amplify the signal. In APC system, power transfer mode selection is realized by a 2:1 switch. R_1 – R_5 should satisfy Equation (12).

$$I_o^* R_3 \frac{R_4 + R_5}{R_4} = U_o^* \frac{R_2}{R_1 + R_2} \tag{12}$$

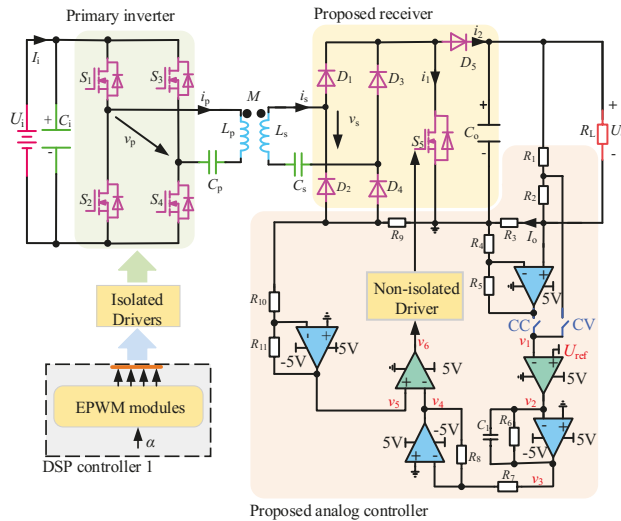


Figure 7. Schematic of APC system.

U_{ref} is a reference voltage. The relationships among U_o^* , I_o^* , and U_{ref} are given in Equations (13) and (14). Different output current and voltage can be achieved by setting U_{ref} and R_1 – R_5 .

$$I_o^* = \frac{U_{ref} R_4}{R_3 (R_4 + R_5)} \tag{13}$$

$$U_o^* = \frac{U_{ref} (R_1 + R_2)}{R_2} \tag{14}$$

R_6 and C_1 act as an integrator. Their values have a great influence on the dynamic and static performances of the system. To better demonstrate this characteristic, time constant τ is defined as Equation (15).

$$\tau = R_6 C_1 \tag{15}$$

A smaller τ brings about a faster dynamic response with a larger overshoot, whereas a larger τ corresponds to a better static performance with a slower dynamic response.

Figure 8 shows the typical waveforms of the APC receiver. When I_o (or U_o) is greater than I_o^* (or U_o^*), v_1 is greater than U_{ref} , and the comparator generates a zero v_2 . Otherwise, a positive v_2 is produced. v_3 decreases for a positive v_2 and increases for a zero v_2 . Since v_3 is negative, an inverting amplifier is used. The ratio of R_8 versus R_7 can regulate the response characteristic. i_s flows through R_9 , and the voltage drop is amplified by R_{10} and R_{11} , which obtains a half-wave voltage v_5 . Then, v_4 and v_5 are sent to a comparator, and they can produce the desired control signal. After passing the non-isolated driver circuit, the gate drive signal is fed to the switch. When S_5 is turned on, the receiver is short-circuited, which results in a zero v_s . When S_5 is turned off, v_s becomes U_o or $-U_o$. β is automatically regulated by the feedback signals.

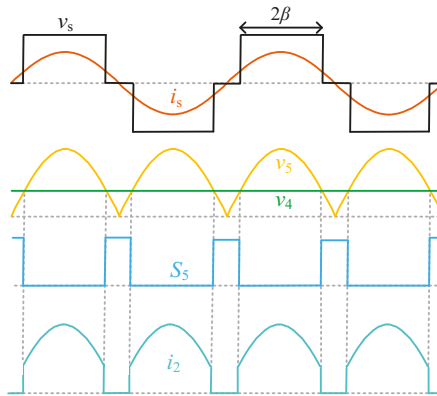


Figure 8. Typical waveforms of APC receiver. i_s , secondary resonant current (orange line); v_s , secondary resonant voltage (black line); v_4 , feedback signal (green line); v_5 , half-wave signal (yellow line); S_5 , gate drive signal (blue line); i_2 , current flowing through D_5 (light green line).

The CC and CV power transfer modes can be achieved through the proposed analog controller. Meanwhile, the receiver does not require synchronization techniques and additional programming. Thus, the proposed APC method significantly reduces the difficulty in implementation, the cost, volume, and weight of the receiver.

4. Simulation and Experiment

Results are obtained from simulation studies in PLECS and hardware prototype experiments. Both results are presented and compared to validate the feasibility of the proposed topology and control methods. The main parameters of the WPT system are listed in Table 1. L_p and L_s are 150 μH and 200 μH with a coil distance of 10 cm. The primary and secondary coils are compensated by 23 nF and 17 nF resonant capacitors, respectively. The inverting frequency of the transmitter is 85 kHz. The diodes are MUR3020PT, with a low forward voltage drop of 1 V. SiC MOSFETs are SCT3030KL. Heat sinks are installed on each diode and MOSFET.

Table 1. Main parameters of WPT system.

Symbol	Quantity	Value
L_p	coil inductance of transmitter	150 μH
L_s	coil inductance of receiver	200 μH
C_p	primary compensation capacitance	23 nF
C_s	secondary compensation capacitance	17 nF
f	inverting frequency	85 kHz

4.1. Digital Phase Control

The prototype photograph of the DPC system is shown in Figure 9. Two TMS320F28335 chips are used as the primary and secondary controllers. The transmitter inverts the DC voltage into high frequency resonant voltage v_p . Then, v_s is induced by the magnetic field generated by i_p . Afterwards, secondary resonant current i_s is rectified into DC current I_o by the proposed receiver. Finally, the power is consumed by Chroma programmable AC-DC electronic load model 63803. Current and voltage sensors are installed to sample the feedback signals for power regulation. ACPL-W346 chips are used as the isolated drivers which are supplied by isolated DC-DC converter G1212S-2W.

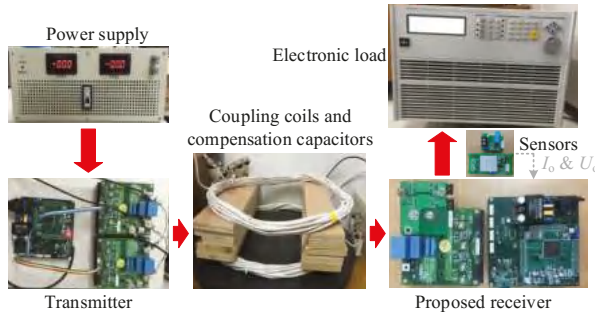


Figure 9. Prototype photograph of DPC system.

Figure 10 shows the typical waveforms of the DPC receiver. To ensure that the signal fed to the comparator stays within a proper range, the values of the divider resistances should be configured with the power level. In this paper, the high-side resistance R_h is 2 M Ω and the low-side resistance R_l is 10 k Ω . The voltage across C_p generates the synchronization signal, and it is fed to GPIO6 of the controller. v_s and i_s are controlled to be in phase. The desired output voltage or current is realized by regulating β .

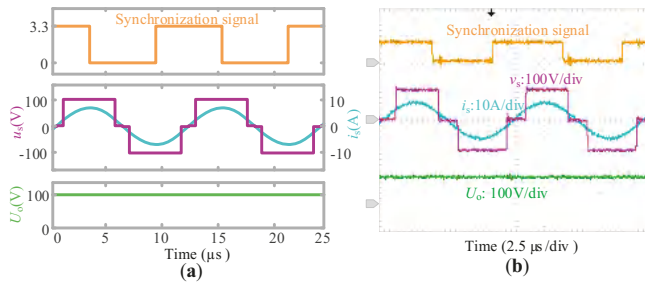


Figure 10. Typical waveforms of DPC receiver: (a) simulated; and (b) experimental. Synchronization signal (yellow lines); i_s , secondary resonant current (blue lines); v_s , secondary resonant voltage (purple lines); U_o , output voltage (green lines).

Figure 11a,b shows the simulated and experimental CC power transfer results by DPC. The reference current is set at 2 A, and R_L changes from 25 Ω to 50 Ω . When R_L is 25 Ω , the simulated and experimental values of β are 27.8° and 27.4°, respectively. The simulated and experimental output currents are 2.00 A and 1.96 A, which correspond to 83.3% and 80.8% DC-to-DC efficiencies, respectively. When R_L is 50 Ω , the simulated and experimental values of β are 28.6° and 27.5°, respectively. The simulated and experimental output currents are 1.99 A and 1.97 A, with DC-to-DC efficiencies of 90.0% and 86.2%, respectively. I_o keeps unchanged against load variations.

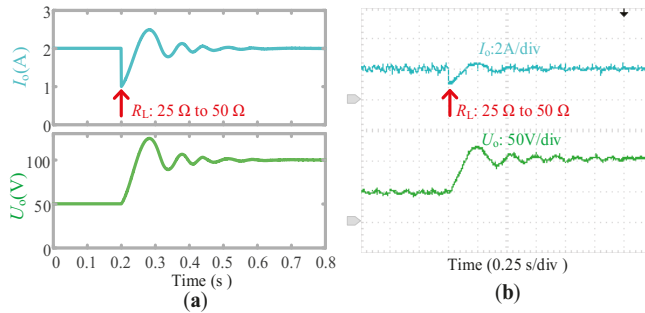


Figure 11. Simulated and experimental CC power transfer results of DPC system: (a) simulated; and (b) experimental. I_o , output current (blue lines); U_o , output voltage (green lines).

Figure 12a,b shows the simulated and experimental CV power transfer results by DPC. The reference voltage is set at 100 V. When R_L is 25 Ω , the simulated and experimental values of β are 73.9° and 73.5°, which produce 100.0 V and 101.2 V output voltages, respectively. The simulated and experimental efficiencies are 93.1% and 91.4%, respectively. When R_L is 50 Ω , the simulated and experimental values of β become 27.7° and 28.1°, respectively. The corresponding output voltages are 99.5 V and 100.5 V, with DC-to-DC efficiencies of 90.0% and 85.8%, respectively. During load variations, U_o remains at the desired level by regulating β accordingly.

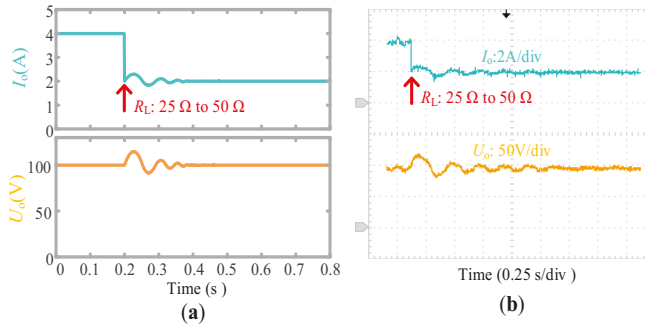


Figure 12. Simulated and experimental CV power transfer results of DPC system: (a) simulated; and (b) experimental. I_o , output current (blue lines); U_o , output voltage (yellow lines).

4.2. Analog Phase Control

A photograph of the APC receiver is shown in Figure 13. U_{ref} is set at 2.5 V. The divider resistances R_1 and R_2 are 91 k Ω and 2.2 k Ω , respectively. The sampling resistances R_3 and R_9 are 10 m Ω . R_4 and R_5 are 0.5 k Ω (1 k Ω / / 1 k Ω) and 62 k Ω , respectively. The ratios of R_7 versus R_8 and R_{11} versus R_{10} are 1 and 22, which ensures v_4 and v_5 falling within proper ranges. TLV3502 and THS4062 are used as the comparator and the operational amplifier, respectively. The configurations of the simulations are identical to the experimental prototype.

Figure 14 shows the logical waveforms of the APC receiver, including v_4 , v_5 , v_6 , and v_s . Regulation circuits are installed on the main circuit. v_4 and v_5 are sent to TLV3502 which generates the control signal. When v_5 is smaller than v_4 , v_6 becomes high level, and S_5 is turned on. Otherwise, v_6 becomes low level, and S_5 is turned off. Small oscillations appear in v_6 , which should be interferences caused by the switching processes. When I_o or U_o is smaller than the expected value, v_4 decreases which brings about a larger β . Otherwise, v_4 increases, and a smaller β is produced.



Figure 13. Photograph of APC receiver.

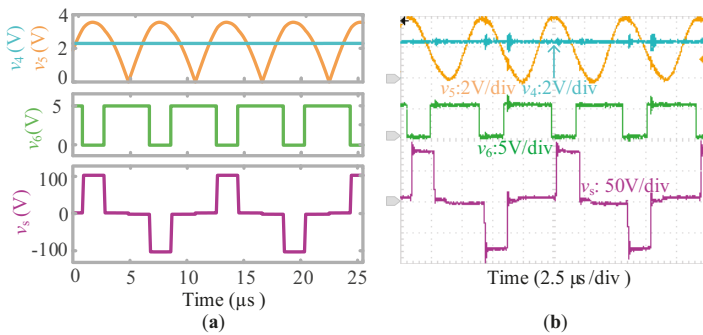


Figure 14. Logical waveforms of APC receiver: (a) simulated; and (b) experimental. v_4 , feedback signal (blue lines); v_5 , half-wave signal (yellow lines); v_6 , control signal (green lines); v_s , secondary resonant voltage (purple lines).

Figure 15 shows the typical waveforms of the APC receiver. In simulations, v_s is in phase with i_s . However, in experiments, it takes some time for the signal to go through the operational amplifier, the comparator, the DSP, and the driver circuit. This time delay results in v_s lagging i_s by some degrees. High performance devices can reduce this time delay.

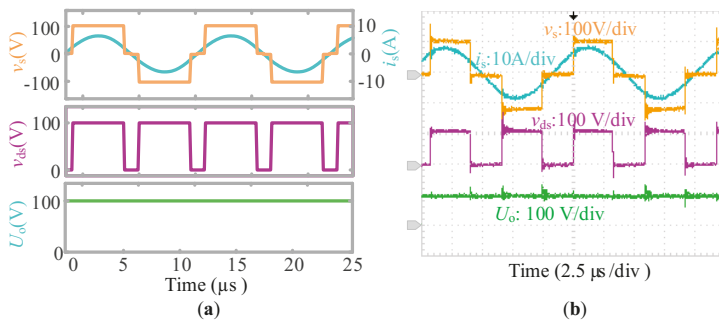


Figure 15. Typical waveforms of APC receiver: (a) simulated; and (b) experimental. i_s : secondary resonant current (blue lines); v_s , secondary resonant voltage (yellow lines); v_{ds} , voltage across S_5 (purple lines); U_o , output voltage (green lines).

Figure 16a,b shows the simulated and experimental results of the CC power transfer by APC. When R_L is 25 Ω , the simulated and experimental output currents are 1.99 A and 1.98 A, respectively.

The simulated and experimental DC-to-DC efficiencies are 82.5% and 78.2%. When R_L is 50Ω , the simulated and experimental output currents are 1.99 A and 1.94 A, which correspond to 89.5% and 85.2% DC-to-DC efficiencies, respectively. In the CC mode, I_o maintains at the desired 2 A against load variations.

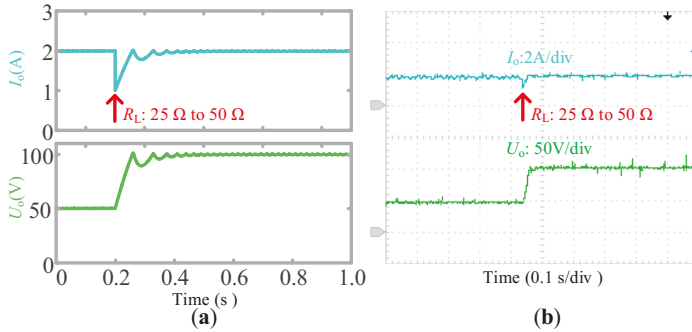


Figure 16. Simulated and experimental CC power transfer results of APC system: (a) simulated; and (b) experimental. I_o , output current (blue lines); U_o , output voltage (green lines).

Figure 17a,b shows the simulated and experimental results of the CV power transfer by APC. The reference voltage is set at 100 V. When R_L is 25Ω , the simulated and experimental output voltages are 99.7 V and 103.7 V, whose DC-to-DC efficiencies are 92.2% and 88.9%, respectively. When R_L is 50Ω , the simulated and experimental output voltages are 99.5 V and 104.6 V, respectively. The overall simulated and experimental efficiencies are 89.4% and 84.7%, respectively. In the CV mode, U_o remains unchanged against load variations.

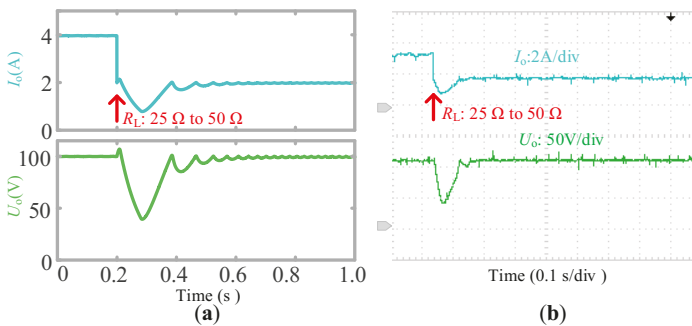


Figure 17. Simulated and experimental CV power transfer results of APC system: (a) simulated; and (b) experimental. I_o , output current (blue lines); U_o , output voltage (green lines).

Since simulations are closer to an ideal system than experiments, their efficiencies are higher than experimental ones. However, the dynamic and static performance are generally the same, which verifies the feasibility of the APC system.

4.3. Comparisons between Proposed Methods

Figure 18 shows the photograph of the two proposed controllers. The DPC controller is $9.0 \text{ cm} \times 9.0 \text{ cm} \times 2.7 \text{ cm}$, whereas the APC controller is only $2.4 \text{ cm} \times 2.0 \text{ cm} \times 0.3 \text{ cm}$. The analog controller is much smaller than the digital one. The volume, weight, and cost of the analog receiver can be significantly reduced.

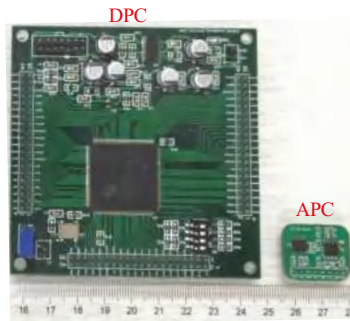


Figure 18. Photograph of two proposed controllers.

Although both the DPC and APC methods can realize the CC and CV power transfer modes, they differ in some aspects. Table 2 compares the differences of the two proposed methods. The DPC system is more complex: it requires a DSP controller, isolated power supplies and driver circuits, current and voltage sensors, and the synchronization circuit. However, the DPC system can eliminate the time delay caused by the regulation circuit and avoid additional power losses of the sampling and divider resistances in the APC receiver. The highest measured experimental efficiency of the APC system is 89.4%, whereas it is 91.4% in the DPC system. Thus, the DPC receiver contributes to a higher performance compared to the APC receiver. Furthermore, it is easier to change the received power through the software code as in the DPC system than changing the regulation resistances as in the APC system, i.e., the DPC system has a greater flexibility than the APC system. Conversely, the APC receiver is simpler since it does not require synchronization algorithms and dedicated programming. In addition, it needs fewer auxiliary devices, i.e., isolated power supplies and expensive sensors are not needed, as well as has a smaller printed circuit board layout. This makes the analog receiver lighter, more cost-effective, and compact.

Table 2. Comparisons between DPC and APC.

Methods	DPC	APC
Complexity	High	Low
Performance	Very High	Good
Flexibility	Very High	Good
Cost	High	Low
Weight	Heavy	Light
Volume	Large	Small

4.4. Comparisons among Different Topologies of WPT Receivers

Comparisons among different WPT receivers are presented in Table 3, and the advantages of the proposed topology and control methods are demonstrated below.

Table 3. Comparisons among different receivers for WPT systems.

Topologies	Capacitors	Inductors	Digital Controllers	Switches	Control Methods	Power Regulation Ability
DC-DC converters [3–8]	2	1	1	1	Duty ratio control	Full-controlled
Full bridge [12–25]	1	0	1	4	Phase control	Full-controlled
Semi-bridgeless [26,27]	1	0	1	2	Phase control	Full-controlled
Reported single-switch receivers [29–33]	1	0	1	1	Duty ratio control	Half-controlled
Proposed receiver	1	0	0 or 1	1	Phase control	Full-controlled

Compared to DC-DC converters used in the WPT systems, the proposed receiver advances in two aspects. Firstly, fewer capacitors and no inductors are required in the proposed receiver. It can reduce the volume and weight of the receiver. Secondly, AC-DC and DC-DC conversions are achieved simultaneously by the proposed receiver. Fewer cascaded circuits, therefore, bring about a higher overall efficiency.

Compared to full bridge and semi-bridgeless topologies, the proposed receiver advances in two aspects: Firstly, the proposed receiver is more cost-effective since the number of SiC MOSFETs and driver circuits used in the proposed receiver have been reduced by 75% as compared to full bridge topology, and 50% as compared to semi-bridgeless topology. In addition, a SiC diode, aiming to reduce high forward voltage, is not needed in the proposed receiver. Therefore, the cost reduction can be significant. Secondly, the proposed receiver has a higher reliability. Dead time is required to avoid short circuit in full bridge applications, whereas the proposed receiver gets rid of short circuit due to the reverse blocking of the diode.

Most reported single-switch receivers are half-controlled, which may fail to achieve the CC and CV power transfer modes. Furthermore, the receivers require a large capacitor to stabilize the output voltage due to the usage of duty ratio control. However, the proposed receiver is full-controlled and has a strong power regulation ability. Owing to the utilization of PC, a small filter capacitor is needed in the proposed receiver.

5. Conclusions

This paper presents a novel single-switch phase controlled active rectifier as receiver for WPT systems. Improved DPC and APC methods are proposed based on the receiver topology to achieve effective CC and CV power transfer modes. The proposed method prevents forward voltage losses in SiC switches and accidental shoot through states with improved switching patterns. The system is easy to implement, has a lower cost, smaller volume, lighter weight, and a higher reliability than conventional phase controlled receivers. Detailed analyses of the operating modes and implementation techniques are presented. Simulated and experimental results of a 400-W WPT system are included which show more than 91% overall efficiency and thereby demonstrate the feasibility of the proposed system.

Author Contributions: X.L., H.T., and X.Y. conceptualized the main idea of this research project; X.L. designed and conducted the experiments; N.J. and D.M. checked the results; X.L. wrote the whole paper; and N.J., D.M. and K.H. reviewed and edited the paper.

Funding: This research was funded by United Foundation of NSFC-Henan, grant number U1604136. The APC was funded by Houjun Tang.

Conflicts of Interest: The authors declare no conflict of interest.

References

1. Villa, J.L.; Sallan, J.; Osorio, J.F.S.; Llombart, A. High-misalignment tolerant compensation topology for ICPT systems. *IEEE Trans. Ind. Electron.* **2012**, *59*, 945–951. [[CrossRef](#)]
2. Ahn, D.; Hong, S. Wireless power transmission with self-regulated output voltage for biomedical implant. *IEEE Trans. Ind. Electron.* **2014**, *61*, 2225–2235. [[CrossRef](#)]
3. Wu, H.H.; Gilchrist, A.; Sealy, K.D.; Bronson, D. A High Efficiency 5 kW Inductive Charger for EVs Using Dual Side Control. *IEEE Trans. Ind. Inform.* **2012**, *8*, 585–595. [[CrossRef](#)]
4. Patil, D.; Sirico, M.; Lei, G.; Fahimi, B. Maximum Efficiency Tracking in Wireless Power Transfer for Battery Charger: Phase Shift and Frequency Control. In Proceedings of the 2016 IEEE Energy Conversion Congress and Exposition (ECCE), Milwaukee, WI, USA, 18–22 September 2016; Volume 99.
5. Li, H.; Li, J.; Wang, K.; Chen, W.; Yang, X. A maximum efficiency point tracking control scheme for wireless power transfer systems using magnetic resonant coupling. *IEEE Trans. Power Electron.* **2015**, *30*, 3998–4008. [[CrossRef](#)]

6. Zhong, W.X.; Hui, S.Y.R. Maximum energy efficiency tracking for wireless power transfer systems. *IEEE Trans. Power Electron.* **2015**, *30*, 4025–4034. [[CrossRef](#)]
7. Fu, M.; Yin, H.; Zhu, X.; Ma, C. Analysis and tracking of optimal load in wireless power transfer systems. *IEEE Trans. Power Electron.* **2015**, *30*, 3952–3963. [[CrossRef](#)]
8. Ahn, D.; Hong, S. Wireless power transfer resonance coupling amplification by load-modulation switching controller. *IEEE Trans. Ind. Electron.* **2015**, *62*, 898–909. [[CrossRef](#)]
9. Yuan, L.; Li, B.; Zhang, Y.; He, F.; Chen, K.; Zhao, Z. Maximum efficiency point tracking of the wireless power transfer system for the battery charging in electric vehicles. In Proceedings of the 2015 18th International Conference on Electrical Machines and Systems (ICEMS), Pattaya, Thailand, 25–28 October 2015; pp. 1101–1107.
10. Li, S.; Mi, C.C. Wireless Power Transfer for Electric Vehicle Applications. *IEEE J. Emerg. Sel. Top. Power Electron.* **2015**, *3*, 4–17.
11. Dai, X.; Li, X.; Li, Y.; Hu, P. Maximum Efficiency Tracking for Wireless Power Transfer Systems with Dynamic Coupling Coefficient Estimation. *IEEE Trans. Power Electron.* **2018**, *33*, 5005–5015. [[CrossRef](#)]
12. Bac, X.N.; Vilathgamuwa, D.M.; Foo, G.H.B.; Wang, P.; Ong, A.; Madawala, U.K.; Trong, D.N. An Efficiency Optimization Scheme for Bidirectional Inductive Power Transfer Systems. *IEEE Trans. Power Electron.* **2015**, *30*, 6310–6319.
13. Thrimawithana, D.J.; Madawala, U.K.; Neath, M. A Synchronization Technique for Bidirectional IPT Systems. *IEEE Trans. Ind. Electron.* **2013**, *60*, 301–309. [[CrossRef](#)]
14. Thrimawithana, D.J.; Madawala, U.K.; Yu, S. Design of a bi-directional inverter for a wireless V2G system. In Proceedings of the 2010 IEEE International Conference on Sustainable Energy Technologies (ICSET), Kandy, Sri Lanka, 6–9 September 2010; pp. 1–5.
15. Madawala, U.K.; Neath, M.; Thrimawithana, D.J. A Power–Frequency Controller for Bidirectional Inductive Power Transfer Systems. *IEEE Trans. Ind. Electron.* **2013**, *60*, 310–317. [[CrossRef](#)]
16. Madawala, U.K.; Thrimawithana, D.J. A Bidirectional Inductive Power Interface for Electric Vehicles in V2G Systems. *IEEE Trans. Ind. Electron.* **2011**, *58*, 4789–4796. [[CrossRef](#)]
17. Neath, M.J.; Swain, A.K.; Madawala, U.K.; Thrimawithana, D.J. An optimal PID controller for a bidirectional inductive power transfer system using multiobjective genetic algorithm. *IEEE Trans. Power Electron.* **2014**, *29*, 1523–1531. [[CrossRef](#)]
18. Tang, Y.; Chen, Y.; Madawala, U.K.; Thrimawithana, D.J.; Ma, H. A New Controller for Bi-directional Wireless Power Transfer Systems. *IEEE Trans. Power Electron.* **2018**, *33*, 9067–9087. [[CrossRef](#)]
19. Zhao, L.; Thrimawithana, D.; Madawala, U. A Hybrid Bi-directional Wireless EV Charging System Tolerant to Pad Misalignment. *IEEE Trans. Ind. Electron.* **2018**, *64*, 7079–7086. [[CrossRef](#)]
20. Mai, R.; Ma, L.; Liu, Y.; Yue, P.; Cao, G.; He, Z. A Maximum Efficiency Point Tracking Control Scheme Based on Different Cross Coupling of Dual-Receiver Inductive Power Transfer System. *Energies* **2017**, *10*, 217. [[CrossRef](#)]
21. Diekhans, T.; De Doncker, R.W. A dual-side controlled inductive power transfer system optimized for large coupling factor variations and partial load. *IEEE Trans. Power Electron.* **2015**, *30*, 6320–6328. [[CrossRef](#)]
22. Berger, A.; Agostinelli, M.; Vesti, S.; Oliver, J.A.; Cobos, J.A.; Huemer, M. A Wireless Charging System Applying phase-Shift and Amplitude Control to Maximize Efficiency and Extractable Power. *IEEE Trans. Power Electron.* **2015**, *30*, 6338–6348. [[CrossRef](#)]
23. Mai, R.; Liu, Y.; Li, Y.; Yue, P.; Cao, G.; He, Z. An Active Rectifier Based Maximum Efficiency Tracking Method Using an Additional Measurement Coil for Wireless Power Transfer. *IEEE Trans. Power Electron.* **2017**, *33*, 716–728. [[CrossRef](#)]
24. Liu, X.; Wang, T.; Yang, X.; Jin, N.; Tang, H. Analysis and Design of a Wireless Power Transfer System with Dual Active Bridges. *Energies* **2017**, *10*, 1588. [[CrossRef](#)]
25. Liu, X.; Wang, T.; Yang, X.; Tang, H. Analysis of Efficiency Improvement in Wireless Power Transfer System. *IET Power Electron.* **2018**, *11*, 302–309. [[CrossRef](#)]
26. Colak, K.; Asa, E.; Bojarski, M.; Czarkowski, D.; Onar, O.C. A Novel Phase-Shift Control of Semibridgeless Active Rectifier for Wireless Power Transfer. *IEEE Trans. Power Electron.* **2015**, *30*, 6288–6297. [[CrossRef](#)]
27. Mai, R.K.; Liu, Y.; Chen, Y. Studies of Efficiency Optimization Methods Based on Optimal Equivalent Load Control in IPT Systems. *Proce. CSEE* **2016**, *36*, 6468–6475.

28. Ahn, D.; Kim, S.; Moon, J.; Cho, I.K. Wireless Power Transfer with Automatic Feedback Control of Load Resistance Transformation. *IEEE Trans. Power Electron.* **2016**, *31*, 7876–7886. [[CrossRef](#)]
29. Tian, J.; Hu, A.P.; Nguang, S.K. Secondary Side Output Voltage Stabilization of an IPT System by Tuning/Detuning through a Serial Tuned DC Voltage-controlled Variable Capacitor. *J. Power Electron.* **2017**, *17*, 570–578. [[CrossRef](#)]
30. Abdolkhani, A. Single-switch soft-switched power flow controller for wireless power transfer applications. In Proceedings of the 2017 IEEE Wireless Power Transfer Conference (WPTC), Taipei, Taiwan, 10–12 May 2017; pp. 1–4.
31. Kuroda, K.; Omori, H.; Kimura, N.; Morizane, T.; Fukuda, K.; Michikoshi, H. A wireless V2H apparatus with a new SiC-MOSFET and unique bidirectional controlled single-ended converter. In Proceedings of the 2017 IEEE 3rd International Future Energy Electronics Conference and ECCE Asia (IFEEC 2017 ECCE Asia), Kaohsiung, Taiwan, 3–7 June 2017; pp. 298–303.
32. Murakami, A.; Omori, H.; Ohara, S.; Fukuda, K.; Michikoshi, H.; Kimura, N. Loss/resistance evaluation of SiC-MOSFET and Si-IGBT in a novel type of single-ended wireless V2H. In Proceedings of the 2017 IEEE PELS Workshop on Emerging Technologies: Wireless Power Transfer (WoW), Chongqing, China, 20–22 May 2017; pp. 1–6.
33. Wang, T.; Liu, X.; Jin, N.; Tang, H.; Yang, X.; Ali, M. Wireless Power Transfer for Battery Powering System. *Electronics* **2018**, *7*, 178. [[CrossRef](#)]
34. Boys, J.T.; Covic, G.A.; Xu, Y. DC analysis technique for inductive power transfer pick-ups. *IEEE Power Electron. Lett.* **2003**, *99*, 51–53. [[CrossRef](#)]
35. Green, A.W.; Boys, J.T. 10 kHz inductively coupled power transfer-concept and control. In Proceedings of the 5th 1994 Fifth International Conference on Power Electronics and Variable-Speed Drives, London, UK, 26–28 October 1994; pp. 694–699.
36. Boys, J.T.; Covic, G.A.; Green, A.W. Stability and control of inductively coupled power transfer systems. *IEEE Proc. Electr. Power Appl.* **2000**, *147*, 37–43. [[CrossRef](#)]



© 2018 by the authors. Licensee MDPI, Basel, Switzerland. This article is an open access article distributed under the terms and conditions of the Creative Commons Attribution (CC BY) license (<http://creativecommons.org/licenses/by/4.0/>).

Article

Wireless Power Transfer for Battery Powering System

Tianfeng Wang ¹, Xin Liu ¹, Nan Jin ², Houjun Tang ¹, Xijun Yang ^{1,*} and Muhammad Ali ¹

¹ School of Electronic Information and Electrical Engineering, Shanghai Jiao Tong University, Shanghai 200240, China; wangff1992@sjtu.edu.cn (T.W.); Liu_xin@sjtu.edu.cn (X.L.); hjtang@sjtu.edu.cn (H.T.); engrmak.ee@sjtu.edu.cn (M.A.)

² College of Electric and Information Engineering, Zhengzhou University of Light Industry, Zhengzhou 450002, China; jinnan@zzuli.edu.cn

* Correspondence: yangxijun@sjtu.edu.cn; Tel.: +86-021-34204604

Received: 18 August 2018; Accepted: 5 September 2018; Published: 7 September 2018

Abstract: The LCL topology (formed by an LC tank with a transmitting coil) is extensively utilized in wireless power transfer (WPT) systems with the features of a constant resonant current and ability to disconnect load abruptly. However, it requires high input voltage, which limits its utilization in battery powering scenarios (12–24 V). A current-fed inverter (CFI) is applied to the LCL-S (a compensation capacitor in series with the receiving coil) WPT systems to boost the input voltage, thereby getting a higher resonant current in the transmitting side (Tx). To facilitate the voltage regulation in the receiving side (Rx), a semi-active bridge (SAB) is introduced into the system, which further boosts the output voltage by a lower frequency switching at different duty ratios. Rigorous mathematical analysis of the proposed system is carried out and design guidelines are subsequently derived. Moreover, a power loss reduction is realized by zero voltage switch (ZVS) of the four switches in the Tx which are deduced and presented. Simulations and experiments are added to verify the proposed system. Consequently, a 93.3% system efficiency (DC-to-DC efficiency) is obtained using the proposed topology. Optimization techniques for a higher efficiency are included in this study.

Keywords: current-fed inverter; LCL-S topology; semi-active bridge; soft switching; voltage boost; wireless power transfer

1. Introduction

Nowadays, wireless power transfer (WPT) technology is a leading research field due to the wide spread electronic devices that can benefit from this technology. For instance, electric vehicles can get rid of electrical hazards caused by wire snapping and reduce on-board battery burden by dynamic charging [1–3]. Medical implants benefit from the increased power supply without the penalty of a greater bulk [4,5]. In addition, a WPT charger can power multiple loads simultaneously without lots of wires and complex connections. Accordingly, it can be predicted that WPT will be a good assistant of, or an alternative to the plug-in power transfer in various voltage rate systems. The advantages and prospects have already ignited a hot interest all over the world, and related studies are burgeoning.

In WPT systems, the compensation topologies are very crucial for high efficiency and power rates by reducing and even cancelling leakage inductance. Research on compensation topologies and their features are continually carried out and new ideas have been investigated and put forward as well [6–9]. Many research works rely on four basic topologies, namely series-series (SS), series-parallel (SP), parallel-parallel (PP), and parallel-series (PS) [10]. However, to meet special or practical requirements, such as constant current/voltage output [7,11] and the endurance of load tripping, hybrid compensation approaches like LC and LCC [12,13] have been put forward. Although, the hybrid topologies introduce more passive components into the system and may add power loss and system bulk, their benefits outweigh the shortcoming for demand and security reasons. Among

these topologies, the LCL topology, formed by an LC tank with a transmitting coil, is regarded as an ideal network used in the transmitting side (Tx), due to its ability to maintain the transmitting current constant and independent of the reflected impedance of the receivers [11,14]. Thus, the induced voltage in every receiving side (Rx) is steady. Moreover, if the disconnection happens in the four basic topologies, urgent protection would be needed, or the circuit is over-current burned. The LCL topology can endure unexpected load disconnection, so it is rather promising in practice. Accordingly, the LCL topology is applied in the Tx in this literature due to these features.

Nevertheless, this topology requires a large input voltage or small receiving coil inductance to augment the transmitting current and induce a high voltage in the Rx. Decreasing the coil inductance will lead to a small mutual inductance and a voltage decreasing in the Rx. Hence, enlarging the input voltage is recommended. The input voltage is 400 V in Ref. [9], and the input voltage of the Evatran products is 220 V. Otherwise, the output voltage can be small, only 5 V in Ref. [11] due to the small input of 26 V. For some power sources, such as photovoltaic panels and batteries, the voltage rating of each cell is very low. The output voltage of a solar cell module is around 12~24 V, and the nominal voltage of a lead-acid battery with six cells is only 12 V. Simply increasing the number of panels and cells in series can surge the system bulk, pressure and insulation requirement, thereby being impractical for solar system applications, wearable devices, and other portable equipment. In addition, the WPT technology may be adopted as an aid for safety and reliability in some internal sub-systems, where only low-voltage sources can be provided.

To extend the WPT technology and LCL topology to battery powering system and wirelessly power the loads within the 12~24 V input range, front-end boost circuits are in great need. Inserting the traditional boost circuits before the inverter is a good solution and also generally used. High efficiency of the boost circuits can be obtained due to the maturity of boost techniques. However, lots of components (an active switch, a power diode, a comparably large inductor, and a capacitor) and auxiliary circuits (control circuits and drivers) are needed. In contrast, the Z-source/quasi-Z-source networks boost the output voltage by shorting the end-rear bridge, which can be realized by the full bridge inverter itself and the extra control circuits are not required [15]. Nevertheless, two inductors and two capacitors are added so the losses caused by these components increase inevitably and the system may incur maloperations caused by the resonant networks [16–18]. On the other hand, large inductances are required in the Z-source network to suppress the ripples and prevent the discontinuous current mode [19]. Hence these two mentioned circuits will increase the bulk of the power system, which may cause difficulty in carrying or assembling.

To realize a high conversion gain and a compact size with a simpler topology, a current-fed inverter (CFI) is a good alternative in WPT systems. The CFI only contains a full bridge inverter and two identical front-end inductors so that the power conversion stages are reduced with an improvement in reliability [20,21]. Compared with the voltage source inverter (VSI) in series with a boost circuit, the CFI has a simpler circuit and easier control method. The control and response rates are also improved due to the compact stages. Compared with the Z-source inverter (ZSI), the CFI has less components and reduces the total harmonic distortion (THD) of the input current. Moreover, the switches in the CFI can operate ZVS from inductive impedance to capacitive impedance and the top-side switches can be turned OFF softly in some scenarios.

Conventionally, there are two kinds of schemes to regulate the output voltage. One scheme is to apply a diode rectifier in the Rx but conduct the optimal charge control in the Tx (the source voltage level shift, the duty ratio adjustment, etc.). This scheme predigests the Rx complexity but needs frequent and quick communications. Another scheme is to control the Rx by itself, which lowers the communication demand. Two circuits have already been proposed: inserting the buck-boost converter connected in series with the rectifier [22] or replacing the rectifier with an active bridge [23]. The former involves a large inductor and more control circuits. The latter requires a complicated controller and complex auxiliary circuits with increasing receiving volume, which is not as compact as mobile devices require. Considering the trade-off between the size and communication complexity,

an active switch replaces one diode of the rectifier and regulates the load voltage in this literature. This semi-active bridge (SAB) can regulate the output by being operated at a variable frequency and duty ratio. Specially, the SAB can boost the output, which can obtain higher voltage than the diode rectifier. Different from the switches in an active bridge that must operate at a high and precise resonant frequency, the switch in SAB can conduct at a lower frequency. Additionally, the complex control protocols and negotiation required by the active bridge [24] are not necessary for the SAB.

The paper is structured as follows: Section 2 depicts the proposed circuit diagram of the WPT system, followed by its operating principle. The capability of soft switching is also elaborated upon. Section 3 models the proposed system with mathematical analyses of the system parameters. Guidelines are provided on the configurations of the inductors, coils, and loads. In Section 4, simulations are implemented, and results are presented and compared. To further support and verify the theoretical analysis and simulation accuracy, a prototype is developed and experimental results are provided in Section 5. A 93.3% system efficiency (DC-to-DC efficiency) is achieved, and the output voltage is within twice to four times that of the input. Optimization techniques for higher efficiency are included. Finally, Section 6 concludes the paper.

2. Proposed Topology

2.1. System Composition

A block diagram of the proposed topology with one receiver is demonstrated in Figure 1. In the Tx, the CFI contains a clamp capacitor C_o , two identical front-end inductors (L_1 and L_2), and four switches ($Q_1, Q_{1a}, Q_2,$ and Q_{2a}), which can be regarded as an assembly of two boost converters [20,21]. A combination of the switching pattern and the inductors implement the boost function, and the amplitude of the output voltage is equal to the capacitor voltage V_c across C_o . For the resonant network, the LCL topology and series compensation topology is employed in the Tx and Rx, respectively. As for the Rx, the SAB supersedes the rectifier, where a bottom side diode is replaced by a controllable switch Q_s .

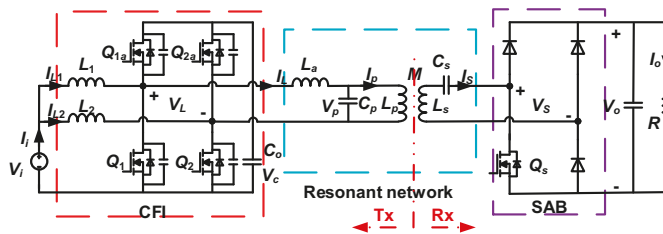


Figure 1. Proposed circuit diagram of WPT systems with one receiver.

In this paper, bold italic letters symbolize the phasors and the italic letters symbolize the real numbers or RMS values. In Figure 1, L_p and C_p represent the Tx coil inductance and its compensation capacitance. L_s and C_s represent the Rx coil inductance and its compensation capacitance. L_a and M represent the compensation inductance and mutual inductance. V_i and I_i are the input voltage and input current from the source. V_L and I_L are the output voltage and current of the CFI. V_p and I_p are the voltage across and the current through Tx coil. V_s and I_s are the input voltage of the SAB and the resonant current in the resonant tank.

2.2. Operation Patterns in Tx

Theoretically, four states exist in the full bridge. However, if the top-side switches are both ON, the charging circuits for L_1 and L_2 are broken and the voltage-boost function cannot be accomplished. Thus, three states are conducted in the CFI. Defining the duty ratio of Q_1 and Q_2 as d_s, d_s should be

above 0.5 to prevent Q_{1a} and Q_{2a} being both ON. The unequal PWM control [25] is adopted in this paper and the corresponding waveforms are depicted in Figure 2a. The four switches all conduct at a resonant frequency f_s . When Q_{1a} and Q_2 are ON, V_L is positive, L_1 is discharged but L_2 is charged, as shown in Figure 2b. When Q_{2a} and Q_1 are ON, V_L is negative, L_1 is charged but L_2 is discharged, as shown in Figure 2d. When the bottom-side switches are ON, V_L is zero, both L_1 and L_2 are charged, as shown in Figure 2c,e.

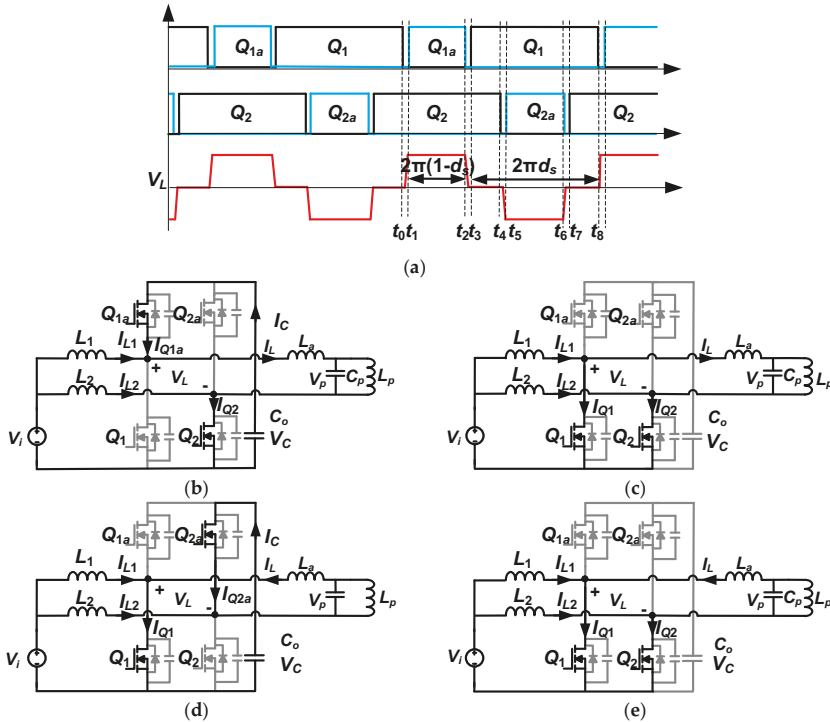


Figure 2. (a) Typical operation patterns of the CFI, (b) $t_1 \sim t_2$; (c) $t_3 \sim t_4$; (d) $t_5 \sim t_6$; (e) $t_7 \sim t_8$.

The current stress of each switches is estimated as

$$\begin{cases} I_{Q1a\max} = I_{Lm} - I_{L1\min} \\ I_{Q1\max} = I_{Lm} + I_{L1\max} \\ I_{Q2a\max} = I_{Lm} - I_{L2\min} \\ I_{Q2\max} = I_{Lm} + I_{L2\max} \end{cases} \quad (1)$$

As can be seen, the bottom-side switches suffer higher stresses than the top-side switches. According to the boost converter properties [26], the peak-to-peak current ripple and the maximum value of the inductor currents in Discontinuous Conduction Mode (DCM) are larger than those in Continuous Conduction Mode (CCM) under the same load conditions. Due to the rear-end resonant current, L_1 and L_2 will not enter DCM but quasi-CCM, where the currents through the inductors reverse their direction and the inductors are charged by the resonant network. The current ripple in quasi-CCM is large and the switches will suffer large stresses, according to Equation (1). Consequently, the CFI in this paper is recommended to operate in CCM to decrease the current stresses of the bottom switches. Thus, the two front-end inductors L_1 and L_2 should be well designed.

2.3. Operation Patterns in Rx

In the receiving side, Q_s operates at frequency f_{Q_s} . The ratio of f_s and f_{Q_s} is denoted as $n (>1)$, and the duty ratio of Q_s is denoted as d_{Q_s} . Parts of the waveforms and the corresponding patterns are illustrated in Figure 3. The direction of the dark arrow of I_s is chosen as a reference direction and the red dotted lines denote the actual current paths. When Q_s is turned OFF, it functions as a common diode. The duty ratio of Q_s is 0.5 and the corresponding waveforms of V_s , I_s , I_p are presented in Figure 3a. I_s flows as shown in Figure 3b,c, where V_s is positive and negative, respectively. When Q_s is turned ON, the anode of D_1 is directly connected with the anode of D_3 as shown in Figure 3d,e. When I_s is positive, as shown in Figure 3d, it flows straight from one end of the compensation capacitor to the end of the Tx coil, that is, the load R is cut off from the resonant source and V_s drops to zero. When I_s is negative, as shown in Figure 3e, however, it flows through D_2 and powers the parallel capacitor and the load. At that time, V_s is negative as shown in Figure 3a. Therefore, I_s resonates at f_s , while the frequency of its envelope line is f_{Q_s} . On the other hand, the amplitude of I_p can be deemed as a constant value, although the equivalent load changes frequently as mentioned. Hence, the Rx can achieve a stable induced voltage ignoring the rapid change of the equivalent impedance, which is also the reason for choosing the LCL topology as the SAB and LCL complement each other.

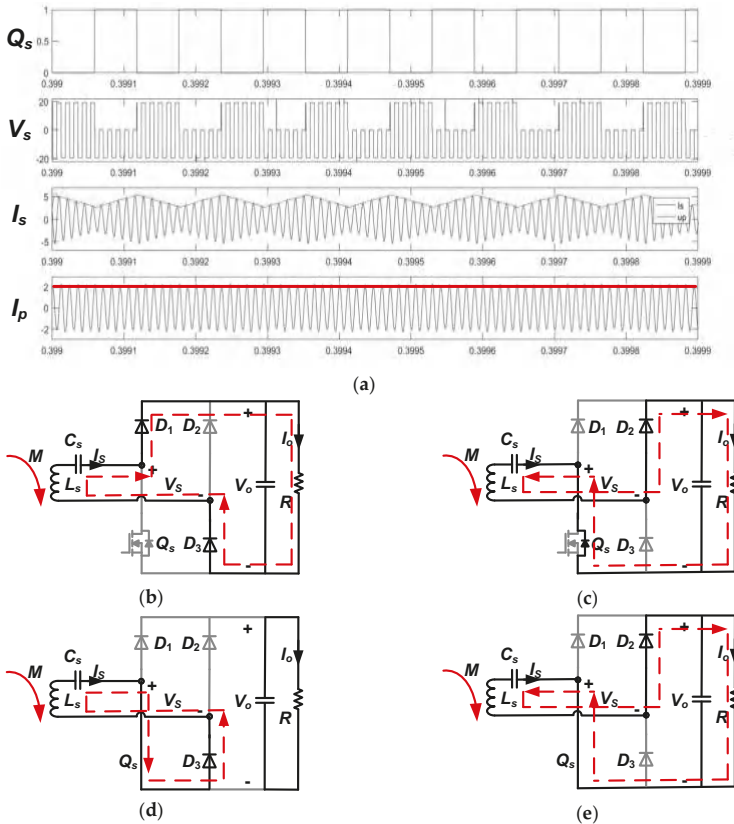


Figure 3. Typical waveforms and operation patterns of the SAB (a) waveforms of the SAB (b) current path when Q_s is OFF and I_s is positive (c) current path when Q_s is OFF and I_s is negative (d) current path when Q_s is ON and I_s is positive (e) current path when Q_s is ON and I_s is negative.

2.4. Soft-Switching Capability

In the Tx, the soft-switching operation is accomplished by the CFI and the clamp capacitor C_o . Q_1 and Q_{1a} are chosen to illustrate the soft-switching process. The analysis of Q_2 and Q_{2a} is fundamentally the same as the analysis of Q_1 and Q_{1a} due to the topology symmetry. The current paths are depicted in Figure 4.

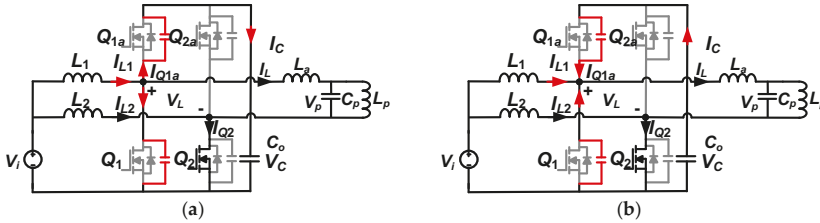


Figure 4. Current paths for CFI conducting ZVS (a) state before Q_{1a} is on $t_0 \sim t_1$; (b) state before Q_1 is on $t_2 \sim t_3$.

Figure 4a shows the state before Q_{1a} is ON, where I_{L1} reaches its maximum value. The difference between I_{L1} and I_L is positive. The current difference charges the parallel capacitor of Q_{1a} , C_{Q1a} , and discharges the parallel capacitor of Q_1 , C_{Q1} . Figure 4b shows the state before Q_1 is ON, where I_{L1} reaches its minimum value. At that time, the difference between I_{L1} and I_L is negative. Then, C_o also provides current to charge C_{Q1} and discharge C_{Q1a} . Hence, ZVS of Q_{1a} and Q_1 are achieved.

To turn OFF the top-side switches softly [27], I_{L1} should be a bit larger than I_L before Q_{1a} is OFF so that I_{Q1a} will reverse direction from Figure 5a to Figure 5b. Then, when Q_{1a} is turned OFF, the freewheeling current can flow through the parallel diode, providing a condition for the soft-switching OFF [27].

In comparison with the VSI, the inductors in the CFI can provide the current directly for soft switching, thereof getting rid of the rear-end resonant current limitation. Accordingly, the soft switching can be more likely accomplished.

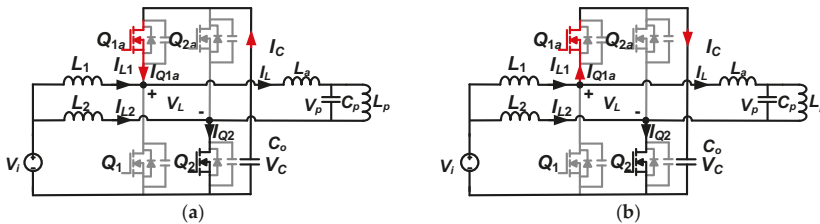


Figure 5. Current paths before turning OFF Q_{1a} (a) preclude to the hard OFF; (b) preclude to the soft OFF.

To guarantee the inductors working in CCM and the minimum value of I_{L1} larger than I_L , the inductance should be large, accompanied with the increase of the internal resistance and power loss caused by the inductors. Thus, the inductance should be set at a reasonable value.

In the Rx, the soft-switching operation [27] can also be realized by Q_s being turned ON/OFF when the current and the voltage are negative. If Q_s is turned OFF when I_s is positive and V_s is zero, the current path will suddenly change from Figure 3d to Figure 3b, leading to a surge of V_s and the hard-switching OFF Q_s . Additionally, if Q_s is turned ON when I_s and V_s are positive, the current path will suddenly change from Figure 3b to Figure 3d, leading to a plunge of V_s and the hard-switching ON of Q_s . The distortion waveform of V_s is demonstrated in Figure 6b. However, if Q_s is turned

ON/OFF when I_s is negative, the current pattern switches between Figure 3c and Figure 3e. As can be seen, the voltage output in Figure 6c is ideal and the soft-switching operation is also achieved. To prevent this distortion, Q_s should be turned ON when I_s is negative, which can be achieved alone in the Rx. In contrast, the dual active bridge (DAB) strictly demands the synchronization [28], otherwise, the system becomes unstable and power oscillations occur.

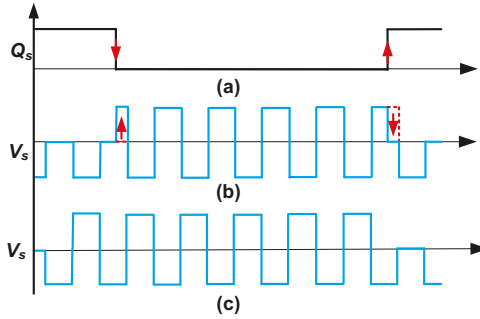


Figure 6. Difference of V_s caused by the switch time (a) Q_s switch time; (b) distortion of V_s ; (c) ideal waveform of V_s .

3. Mathematical Modeling and Configuration

3.1. Equivalent Circuit Model

To model and analyze the proposed system, an equivalent circuit is established as shown in Figure 7. Z_p , Z_{sref} , and R_{ac} denote the Tx equivalent impedance, the reflected impedance from the Rx and the equivalent ac resistance calculated in a receiving switching period, respectively. Z_{pt} , Z_{sref} , and R_{act} denote the three impedances calculated in a resonant period. r_p and r_s denote the inner resistances of the Tx coil and the Rx coil. Besides, L_a is designed to be identical to L_p . Considering the power losses, inner resistance of L_a is represented by r_{La} . In addition, r_L denotes the inner resistance of L_1 and L_2 . The Tx switching frequency and the resonant frequency are both equalized to f_s .

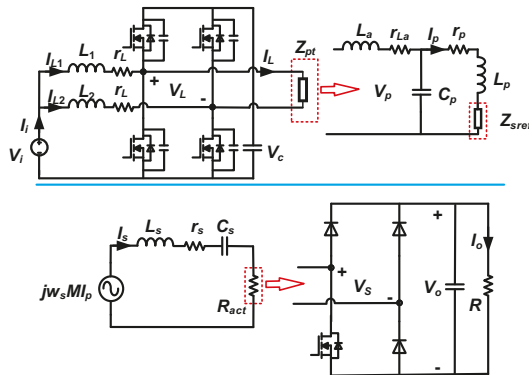


Figure 7. Equivalent circuit diagram.

Thus, Z_{pt} is resistant and deduced as:

$$Z_{pt} = j\omega_s L_a + r_{La} + \frac{(j\omega_s L_p + Z_{sref} + r_p) \frac{1}{j\omega_s C_p}}{j\omega_s L_p + Z_{sref} + r_p + \frac{1}{j\omega_s C_p}} = \frac{(\omega_s L_p)^2}{Z_{sref} + r_p} + r_{La} \approx \frac{(\omega_s L_p)^2}{Z_{sref} + r_p}, \quad (2)$$

where, Z_{srefit} is equal to

$$Z_{srefit} = \frac{(\omega_s M)^2}{R_{act} + r_s} \tag{3}$$

Based on the boost model, the amplitude of the square wave V_L is derived as:

$$V_{Lm} = V_C = \frac{V_i}{1 - d_s} \tag{4}$$

Thus, the RMS value of the fundamental harmonic of V_L is deduced as:

$$V_{L1} = 2\sqrt{2}V_i \frac{\sin \pi d_s}{\pi(1 - d_s)} \tag{5}$$

Then, the output current of CFI in a resonant period is:

$$I_L = \frac{V_{L1}}{Z_{pt}} = \frac{2\sqrt{2}V \sin \pi d_s}{\pi(1 - d_s)(\omega_s L_p)^2} \left[\frac{(\omega_s M)^2}{R_{act} + r_s} + r_p \right] \tag{6}$$

Obviously, I_L is load-dependent and its RMS value I_L will decrease with the augment of R_{act} . However, the RMS value of branch current I_p is calculated as:

$$I_p = \frac{V_{L1} \cdot (Z_{srefit} + r_p)}{(\omega_s L_p)^2} \frac{\frac{1}{j\omega_s C_p}}{\frac{1}{j\omega_s C_p} + j\omega_s L_p + Z_{srefit} + r_p} = \frac{V_{L1}}{j\omega_s L_p} \tag{7}$$

which signifies that I_p is independent of the Rx characteristics but proportional to the input voltage. Accordingly, high input voltage V_L is recommended to maintain a large resonant current. According to the mutual inductance theory, the induced voltage V_s in the Rx keeps steady if I_p is constant.

In the Rx, the model can be presented as:

$$j\omega_s M I_p = \left[j\omega_s L_s + r_s + \frac{1}{j\omega_s C_s} + R_{act} \right] I_s = [r_s + R_{act}] I_s \tag{8}$$

which implies that the induced voltage and the receiving current are in-phase.

3.2. Equivalent Resistance of SAB

To analyze the impact of duty ratio d_{Qs} and receiving switching frequency f_{Qs} ($=f_s/n$) on R_{ac} , R_{act} , and output voltage V_o , the harmonic approximation method and extended describing function are utilized. Assuming that the induced voltage $v(t)$, receiving current $i_{sL}(t)$, and compensation capacitor voltage $v_{sC}(t)$ can be approximated by fundamental terms and the former two are in same phase due to the resistive impedance, it has

$$\begin{cases} v(t) = \omega_s M I_{pm} \sin \omega_s t \\ i_{sL}(t) = i_{sL}(t) \sin \omega_s t \\ v_{sC}(t) = v_{sC}(t) \cos \omega_s t \end{cases} \tag{9}$$

where, the envelope terms are slowly time varying at f_s/n .

By utilizing the extended describing method, V_s whose waveform is depicted in Figure 3a, can be approximated as

$$v_s(t) \approx f_s(n, d_{Qs}, V_o) \sin \omega_s t \tag{10}$$

The extended describing function $f_s(n, d_{Qs}, V_o)$ can be calculated by Fourier expansions and given as

$$f_s(n, d_{Qs}, V_o) = -\frac{d_{Qs}}{2} V_o + \sum_{k=1}^{\infty} \left[a_k \cos k \frac{\omega_s}{n} t + b_k \sin k \frac{\omega_s}{n} t \right], \tag{11}$$

where the coefficients are

$$\begin{cases} a_k = \frac{V_o}{\pi k} \left[\sum_{i=1}^{2n-2d_{Qs}n} (-1)^i \sin k\varphi \left| \frac{\pi i}{\pi(i-1)/n} \right. - \sum_{i=n-d_{Qs}n}^{n-1} \sin k\varphi \left| \frac{\pi(2i+1)/n}{2\pi i/n} \right. \right] \\ b_k = \frac{V_o}{\pi k} \left[\sum_{i=1}^{2n-2d_{Qs}n} (-1)^{i-1} \cos k\varphi \left| \frac{\pi i}{\pi(i-1)/n} \right. + \sum_{i=n-d_{Qs}n}^{n-1} \cos k\varphi \left| \frac{\pi(2i+1)/n}{2\pi i/n} \right. \right] \end{cases} . \tag{12}$$

However, it is difficult to get an analytical solution on the relationship between $f_s, d_{Qs}, V_o,$ and R_{ac} , since the switching frequency is below the resonant frequency and the equivalent impedance in each resonant period is different from others, which is totally contrary to the small-signal model condition [29]. Nevertheless, a trend estimation can be conducted by analyzing the extreme cases. Since the SAB disconnects the load OFF and ON, it can be assumed that when the load is OFF, the equivalent impedance R_{ac} decreases. To validate this assumption and estimate the relation between d_{Qs} and R_{ac} , two extreme cases ($d_{Qs} = 0$ and $d_{Qs} = 1$) are considered. The corresponding waveforms are presented in Figure 8.

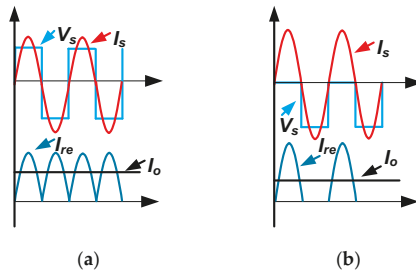


Figure 8. Typical waveforms of the Rx under different duty ratios (a) $d_{Qs} = 0$; (b) $d_{Qs} = 1$.

When Q_s stays OFF, that is $d_{Qs} = 0$, the SAB works as a diode rectifier. The typical waveforms are depicted in Figure 8a, where I_{re} represents the output current of the SAB. Thus, the equivalent ac resistance reaches the maximum as given in [30]:

$$\begin{cases} R_{act} = R_{ac} \\ R_{acmax} = \frac{8R}{\pi^2} \end{cases} . \tag{13}$$

However, when Q_s stays ON, that is $d_{Qs} = 1$, the anode of D_1 is directly connected with the anode of D_3 , waveforms change to Figure 8b and the ac load accordingly, is

$$\begin{cases} R_{act} = R_{ac} \\ R_{acmax} = \frac{2\sqrt{2}R}{\pi^2} \end{cases} . \tag{14}$$

It can be found that R_{ac} decreases when d_{Qs} increases. Besides, on basis of Equation (6), it can be drawn that the input current I_L and input power will rise as d_{Qs} increases, and the dc output V_o boost as well due to the energy principles. Thus, the voltage boost function is accomplished.

Assuming that the power loss caused by SAB can be ignored, the power fetched from the Tx is equal to the load power, that is,

$$\frac{V_o^2}{R} = I_p^2 \frac{(\omega_s M)^2}{R_{act} + r_s} \frac{R_{act}}{R_{act} + r_s}. \tag{15}$$

Hence, by substituting Equations (5), (7), (13) and (14) into Equation (15), the range of the output voltage is estimated as:

$$\frac{2\sqrt{2}\pi MR}{L_p(8R + \pi^2 r_s)} \frac{\sin \pi d_s}{(1 - d_s)} V_i \leq V_o \leq \frac{2^{0.75}\pi MR}{L_p(2\sqrt{2}R + \pi^2 r_s)} \frac{\sin \pi d_s}{(1 - d_s)} V_i, \tag{16}$$

which shows the dc load can acquire a wide range of output. Besides, the output voltage V_o can be higher than the input voltage V_i with proper configurations.

3.3. Soft-Switching Design in Tx

The power fetched from the CFI P_L during a resonant period is deduced, with Equations (5) and (6), as:

$$P_L = \frac{8V_i^2}{(\omega_s L_p)^2} \frac{\sin^2 \pi d_s}{\pi^2 (1 - d_s)^2} \left[\frac{(\omega_s M)^2}{R_{act} + r_s} + r_p \right] \geq \frac{8V_i^2}{(\omega_s L_p)^2} \frac{\sin^2 \pi d_s}{\pi^2 (1 - d_s)^2} \left[\frac{(\omega_s M)^2}{R_{acmax} + r_s} + r_p \right] = P_{Lmin}. \tag{17}$$

Assuming that the magnitude of power loss caused by the switches, L_1 , L_2 , and C_o can be ignored as compared to that of P_L , P_L is therefore equal to the DC input power P_i , which can be presented as:

$$P_i = \frac{1}{2} V_i \left[2I_{imin} + \frac{V_i}{L} (2d_s - 1) T_s \right], \tag{18}$$

where, $L = L_1 = L_2$, I_{imin} is the minimum value of the DC input current, illustrated in Figure 9, and can be calculated as

$$I_{imin} = 2I_{L1min} + \frac{V_i T_s}{2L}. \tag{19}$$

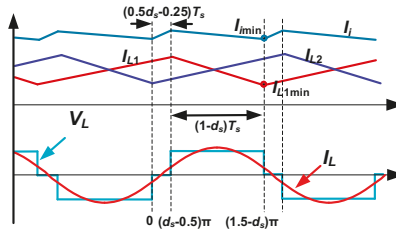


Figure 9. Typical waveforms of the CFI.

Accordingly, I_{L1min} can be calculated with Equations (17)–(19) as:

$$I_{L1min} = \frac{4V_i \sin^2 \pi d_s}{\pi^2 (1 - d_s)^2 Z_{pt}} - \frac{V_i T_s}{2L} d_s. \tag{20}$$

To prevent the system from quasi-CCM, I_{L1min} should be above zero. To make $I_{L1min} > 0$, L can be deduced from Equation (20) with Equation (2) as:

$$L > \frac{T_s d_s}{8} \frac{\sin^2 \pi d_s}{\pi^2 (1 - d_s)^2} \frac{(\omega_s L_p)^2}{\frac{(\omega_s M)^2}{R_{act} + r_s} + r_p}. \tag{21}$$

On the other hand, to complete the soft-switching OFF Q_{1a} , it demands

$$I_{L1min} > I_L|_{\varphi=1.5\pi-\pi d_s}. \tag{22}$$

Defining Q as the loaded quality factor of the Tx, Q can be calculated as:

$$Q = \frac{Z_{srefl}}{\omega_s L_p} = \frac{\omega_s k^2 L_s}{(R_{act} + r_s)}, \tag{23}$$

where k denotes the coupling coefficient.

When Q is large, the output current of CFI is sinusoidal as presented in Figure 9. To complete soft-switching OFF Q_{1a} , Equation (22) is written as:

$$I_{L1min} > \sqrt{2}I_L \sin\left(\frac{3}{2}\pi - \pi d_s\right), \tag{24}$$

that is, L is deduced from Equation (24) as:

$$L > \frac{T_s d_s}{8 \frac{\sin \pi d_s}{\pi(1-d_s)} \left[\frac{\sin \pi d_s}{\pi(1-d_s)} + \cos \pi d_s \right]} \frac{(\omega_s L_p)^2}{\frac{(\omega_s M)^2}{R_{act} + r_s} + r_p}. \tag{25}$$

Since d_s is above 0.5, the right of Equation (21) is larger than that of Equation (25) and reaches its maximum when d_s is 0.5. Hence, the inductance should meet the requirement as:

$$L > \frac{\pi^2}{64 f_s} \frac{(\omega_s L_p)^2}{\frac{(\omega_s M)^2}{R_{act} + r_s} + r_p}. \tag{26}$$

Nevertheless, considering the inner resistances and power losses of the two inductors at high input current, L cannot increase blindly otherwise the system efficiency will degrade.

However, when Q is small (i.e., $Q < 1$ according to the MATLAB and PLECS simulation), I_L distorts and I_{Q1a} can never reverse direction no matter how large L is, thereby failing soft-switching OFF Q_{1a} and Q_{2a} . In practice, the inner resistances of the coils will surge significantly with the increase of the coil inductance. On the other hand, the LCL topology requires rigorous manufacturing technique to reduce the coil resistance since the losses of the coil resistors in LCL topology far outweigh that in series compensation topology. Accordingly, L_p and M are usually small, which inevitably results in a small Q and distortion of I_L . Simply increasing L_s can reduce the receiving efficiency due to the enlarged coil resistance, leading to the system efficiency decreasing as well. Thus, there is a trade-off between the soft-switching OFF and system efficiency.

3.4. Optimal Load

To evaluate the system efficiency variation caused by the change of the equivalent impedance, the optimal load is calculated. Given that the power loss caused by the CFI is hard to theoretically calculated, the transmitting efficiency η , defined as the ratio of the CFI output power to the equivalent ac power, is presented to calculate the optimal load for the CFI and approximate the system efficiency. η can be written with Equations (3), (5)–(7) as:

$$\eta = \frac{I_p^2 Z_{srefl}}{V_{L1} I_L} = (\omega_s M)^2 \frac{R_{act}}{r_p R_{act}^2 + (\omega_s M)^2 R_{act} + 2r_s r_p R_{act} + (\omega_s M)^2 r_s + r_s^2 r_p}. \tag{27}$$

The derivative of Equation (27) is calculated as:

$$\frac{d\eta}{dt} = (\omega_s M)^2 \frac{-r_p R_{act}^2 + (\omega_s M)^2 r_s + r_s^2 r_p}{\left[r_p R_{act}^2 + (\omega_s M)^2 R_{act} + 2r_s r_p R_{act} + (\omega_s M)^2 r_s + r_s^2 r_p \right]^2}. \quad (28)$$

To obtain the highest η , Equation (28) should be equal to zero, that is,

$$R_{act} = \sqrt{\frac{(\omega_s M)^2 r_s}{r_p} + r_s^2}. \quad (29)$$

To maintain a large output voltage, L_s is deliberately designed much larger than L_p , whereas, r_s is 75 times r_p in this paper. Hence, Equation (29) can be simplified as:

$$R_{act} = \omega_s M \sqrt{r_s / r_p}. \quad (30)$$

By substituting Equation (30) into Equation (23), Equation (23) is rewritten as:

$$Q = k \sqrt{\frac{L_s r_p}{r_s L_p}}. \quad (31)$$

If R_{act} is set as the optimal value, and Equation (31) is above 1, the soft-switching OFF Q_{1a} and Q_{2a} can be achieved.

4. Simulation and Verification

To validate the analysis and the aforementioned assumptions, simulations are implemented. According to Equation (7), the Tx coil inductance L_p is set as a small value, 15.5 μH , to obtain a large current and small resistance 8 m Ω as well. The coil-to-coil gap is fixed at 10 cm and the coupling coefficient k is 0.2. Since the receiving coil adopt the series compensation topology, the coil inductance is designed to a large value and set as a large value as 274.7 μH but followed by a large resistance, 0.3 Ω . To obtain high efficiency based on Equations (27) and (29), the dc load is set as 52 Ω according to Equation (13). It is worth noting that efficiency will drop when Q_s turns ON, because R_{act} will gradually deviate from the optimum. The forward voltage drop of the diode V_F is 0.6 V and the on resistance of the MOSFET is 80 m Ω . The configurations are listed in Table 1.

Table 1. Model Parameters.

Parameter	Value	Parameter	Value
Load R	52 Ω	Input voltage E_V	24 V
Transmitting switching frequency f_s	85 kHz	Mutual inductance M	18 μH
Transmitting inductance L_p	15.5 μH	Transmitting inner resistance r_p	8 m Ω
Receiving inductance L_s	274.7 μH	Receiving inner resistance r_s	0.3 Ω
Compensation inductance L_a	15.5 μH	Compensation inner resistance r_{La}	0.04 Ω
DC inductance L_1 & L_2	51 μH	DC inner resistance r_L	0.2 Ω
Transmitting capacitance C_p	222 nF	Receiving capacitance C_s	12.8 nF
Clamp capacitance C_o	470 μF	Transmitting duty ratio d_s	0.7
Forward voltage drop of diode V_F	0.6 V	On resistance of MOSFET R_{on}	80 m Ω

4.1. Soft-Switching Realization

When Q_s operates at different duty ratios, the equivalent ac impedance varies. Thus, the variation range of the loaded quality factor is [0.14, 0.40] calculated by Equation (23). The range of the minimum of the front-end inductance L is calculated as [38.6 μH , 107.4 μH] by Equation (21). When the SAB works as a common diode rectifier, the minimum of L surges to 107.4 μH , which also means a bulky

size and large inner resistance. Although the large inductors prevent circulating current, the saved power can hardly compensate the losses caused by the inner resistance, and hence L is configured a medium value as $51 \mu\text{H}$ with 0.2Ω . Then, after Q_s operates, the circulating current will be eliminated. Simulations are fulfilled at different d_{Qs} . The simulation waveforms of Q_{1a} and I_{L1} are depicted in Figure 10. Figure 10a illustrates the waveforms where R is 52Ω and Q_s stays OFF. The whole system efficiency is 94.5%. Figure 10b illustrates the waveforms where R is 52Ω and Q_s operates as 8500 Hz with $d_{Qs} = 0.5$. The efficiency is 94.1%. Figure 10c demonstrates the waveforms where R is 52Ω and Q_s stays ON. The efficiency is 90.8%. Figure 10d demonstrates the waveforms where R is 20Ω and Q_s stays ON.

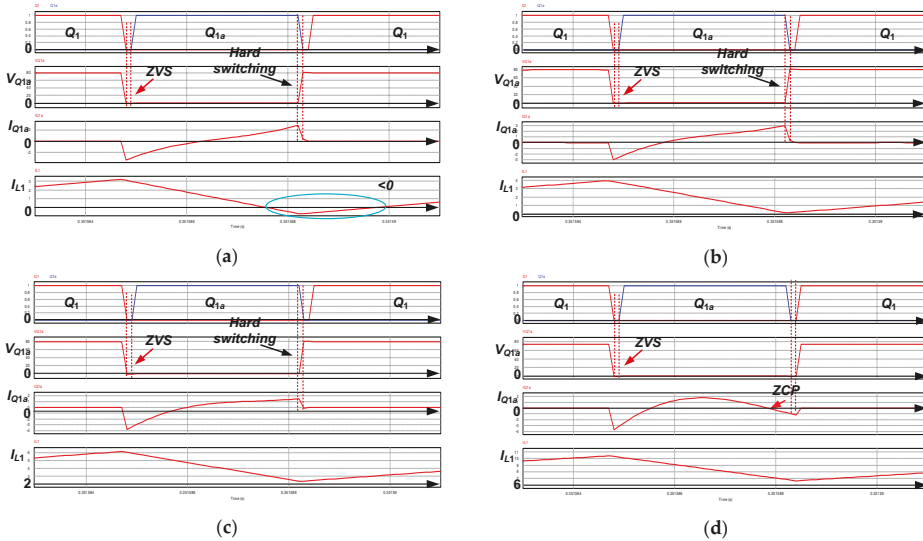


Figure 10. Typical waveforms of Q_{1a} and I_{L1} with a same L but different d_{Qs} : (a) $R = 52 \Omega$, $d_{Qs} = 0$, $\eta = 94.5\%$; (b) $R = 52 \Omega$, $d_{Qs} = 0.5$, $\eta = 94.1\%$; (c) $R = 52 \Omega$, $d_{Qs} = 1$, $\eta = 90.8\%$; (d) $R = 20 \Omega$, $d_{Qs} = 1$.

As Figure 10 shows, before Q_{1a} is ON, the voltage across Q_{1a} , V_{Q1a} , has already reached zero. Hence, ZVS is accomplished in above mentioned four cases. However, when R is 52Ω and Q is below 1, Q_{1a} is hard-switching OFF. Additionally, when R_{ac} is small, the theoretical minimum of L is above $51 \mu\text{H}$ so that the quasi-CCM occurs, and I_{L1} is below zero for a period of time, which means L_1 is charged by the resonant network and a circulation current exists in L_1 and L_2 . When R_{ac} augments, the value $51 \mu\text{H}$ satisfies Equation (21) and the circulating current is eliminated as illustrated in Figure 10b,c. Two conclusions can be drawn. Firstly, the deviation of the optimal load will reduce the efficiency comparing Figure 10b with Figure 10c. Secondly, the elimination of the circulation current can increase the efficiency as can be observed by comparing Figure 10b with Figure 10a,c. Besides, when the load decreases and Q increases above 1, a zero-cross point (ZCP) occurs before Q_{1a} is OFF and I_{Q1a} reverses its direction as Figure 5b demonstrates. Then I_{Q1a} can flow through the parallel diode for freewheeling rather than be forced to abruptly discontinue, which achieves the soft-switching OFF Q_{1a} as analyzed.

4.2. Equivalent Resistance of SAB and Variation Trend

In Section 3, the equivalent resistance of SAB R_{act} is regarded as a pure resistance according to the analysis on full-wave rectifier [30] and half-wave rectifier. To validate this assumption, we have Q_s working at 8500 Hz with $d_{Qs} = 0.5$. Waveforms of I_p , I_s , and V_s are presented in Figure 11. The purple dotted lines show that I_p lags 90° behind I_s so $j\omega_s M I_p$ is in phase with I_s which conforms to Equation

(8). Moreover, the dark dotted lines show that the fundamental voltage V_s and I_s are also in phase. These phases verify a purely resistive equivalent impedance.

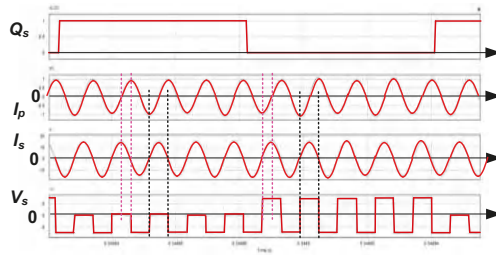


Figure 11. Phase differences in the Tx.

To further evaluate the impact of frequency ratio n and duty ratio d_{Qs} on the system, the simulation results of the output dc voltage, transferred power, and efficiency under different conditions are depicted and compared in Figure 12. Q_s works at three frequencies, 8500 Hz (i.e., $n = 10$), 17,000 Hz (i.e., $n = 5$), and 42,500 Hz (i.e., $n = 2$).

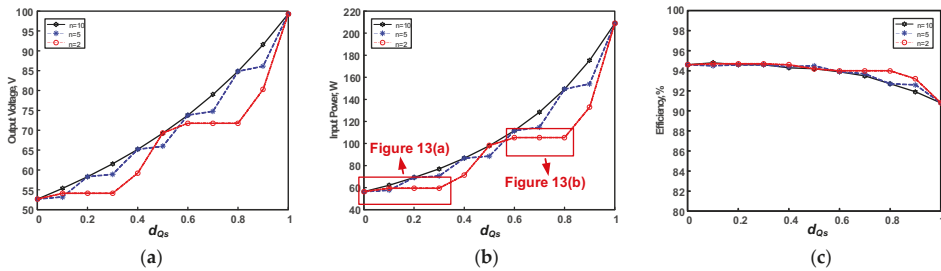


Figure 12. System performance under different frequencies and duty ratios (a) output voltage (b) input power (c) efficiency.

From Figure 12a, it is observable that the output voltage grows with the increase of d_{Qs} , which verifies the voltage boost function as claimed and also reflects the rise of R_{ac} according to Equation (15). Besides, the increase of input power can prove the negative correlation between R_{act} and I_L as already presented in Equation (6). In addition, it can be observed that the system has the same input power and output voltage once the product of n and d_{Qs} is integral and d_{Qs} stays the same. The integer of $n \cdot d_{Qs}$ means that a switching-ON period of Q_s contains an integral multiple of the resonant period, as does the switching-OFF period. On the other hand, an identical d_{Qs} means an identical proportion of the on-load time and idle time as presented in Figure 6. Accordingly, the equivalent ac load remains the same. If the switching-ON period of Q_s does not contain an integral multiple of the resonant period, the output voltage and input power may rise disproportionately as the blue line and the red line show. This phenomenon occurs because the effective proportions of the on-load time and idle time does not change. The examples in Figure 13 should suffice to demonstrate the stated where $n \cdot d_{Qs} \leq 0.5$ or $0.5 \leq n \cdot (1 - d_{Qs}) \leq 1$.

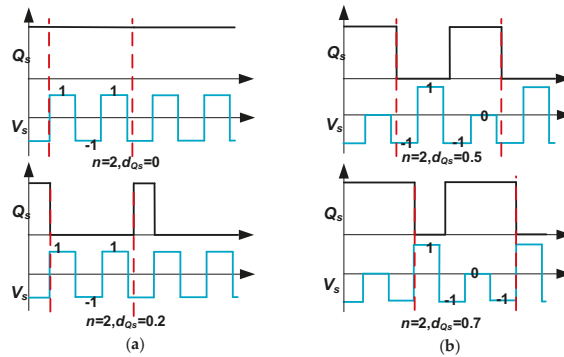


Figure 13. Impact of n and d_{Q_s} on the equivalent impedance when $n \cdot d_{Q_s}$ is small (a) $n \cdot d_{Q_s} \leq 0.5$ (b) $0.5 \leq n \cdot (1 - d_{Q_s}) \leq 1$.

Therefore, a large frequency ratio, i.e., a low operation of the receiving side, allows the power to grow in a linear fashion. However, if Q_s works at a low frequency, the ripple of the output voltage gets large, which may be unbearable for battery charging. For instance, the system output voltage, input powers, and efficiencies are totally identical when Q_s operates at 8500 Hz and 4250 Hz, theoretically. Nevertheless, the ripples at 4250 Hz operation are three times those at 8500 Hz. Thus, there is a trade-off between the system variation linearity and the output ripples considering the practical application. It is worth noting that the switching loss of the MOSFETs is not considered in the simulation, which will rise with the increase of the operating frequency. In this paper, Q_s conducts at 8500 Hz as recommended.

5. Experimental Result and Discussions

To validate and evaluate the aforementioned analyses and simulations, a practical prototype was established and tested. Figure 14 shows the laboratory prototype and its component configurations have been already tabulated in Table 1 in Section 4. However, the actual value of the load was 51.2Ω and the switching frequencies of the Tx and the Rx were 86 kHz and 8600 Hz, respectively. The DSP TMS320F28335 (San Jose, CA, USA) was used as the digital controller in this system. MPP (Ni-Fe-Mo) cores were chosen for L_1 , L_2 , and L_a for lower loss. The coil diameter is 37 cm and the coil-to-coil gap is set as 10 cm. The inductances are measured by a Keysight E4980AL (Santa Rosa, CA, USA) LCR meter under 86 kHz.

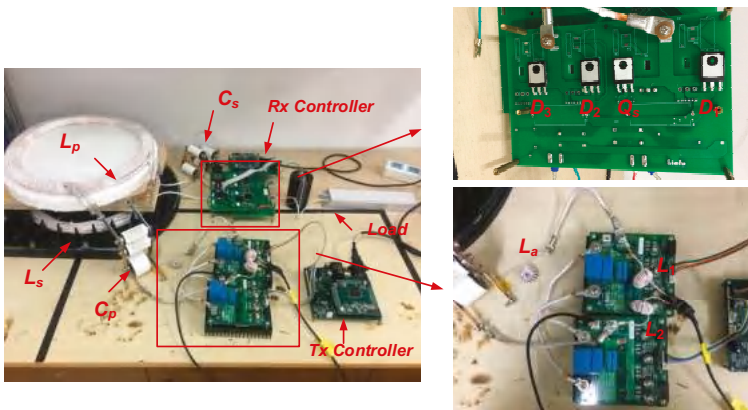


Figure 14. Prototype of the proposed system.

5.1. Soft-Switching Realization

All the four switches on the transmitter can perform ZVS under wide power variation as analyzed. The dead time is set as 2% of the resonant period. The waveforms of the four switches in three cases (Q_s stays OFF, $d_{Q_s} = 0.5$, and Q_s stays ON) are presented in Figure 15. The input power is the smallest when Q_s keeps OFF, and the output current I_L distorts as claimed in Section 3 and is presented in Figure 15b. Nevertheless, ZVS of the four switches are achieved successfully as presented in Figure 15a. After Q_s operates, both the input power and the loaded quality factor rise. When $d_{Q_s} = 0.5$, I_L is different from each other in every resonant period but I_{L1} keeps periodic variation. Hence, the current $I_{L1}-I_L$ provided for ZVS keeps changing in Figure 15d. However, ZVS of the top-side switches is still realized and ZVS of the bottom-side is also achieved most of the time as illustrated in Figure 15c. When Q_s stays on, I_L approximates to sine. As can be seen, all the switches can conduct ZVS as presented in Figure 15e. However, the soft switching-OFF for the top side switches is not achieved. The red lines in Figure 15b,d,f denote the result of I_{L1} minus I_L , and the waveforms, when Q_{1a} is going to be turned OFF, are emphasized by the ellipse. At that time, the result ΔI being negative denotes that there is a current flowing from the source electrode of Q_{1a} to its drain electrode. Therefore, the hard-switching OFF is inevitable.

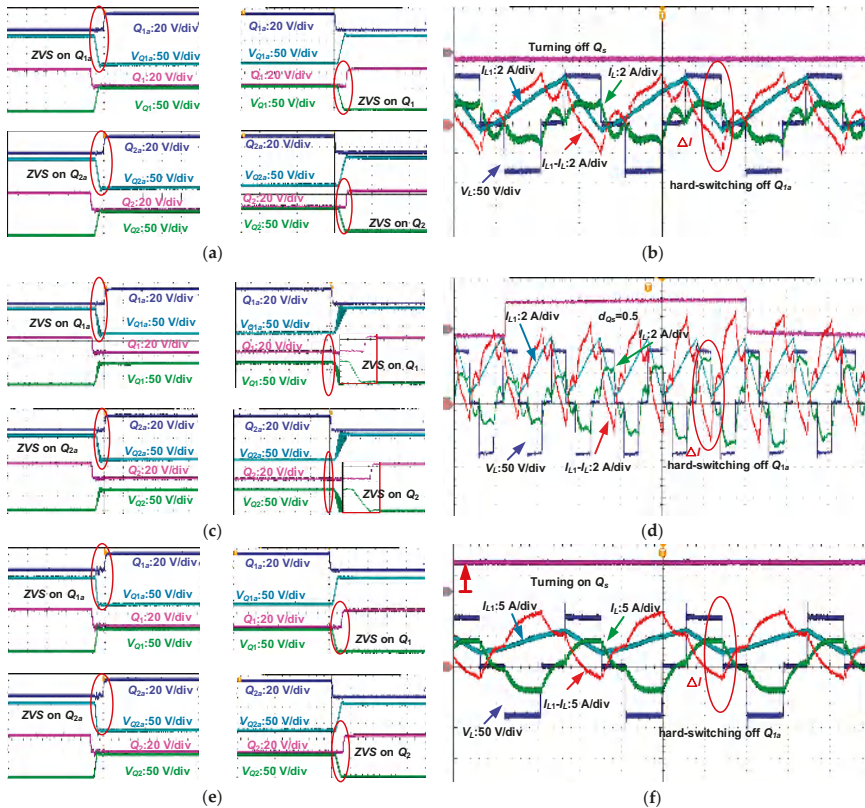


Figure 15. ZVS waveforms under different cases: (a) ZVS of four switches when $d_{Q_s} = 0$; (b) current waveforms when $d_{Q_s} = 0$; (c) ZVS of four switches when $d_{Q_s} = 0.5$; (d) current waveforms when $d_{Q_s} = 0.5$ (e) ZVS of four switches when $d_{Q_s} = 1$; (f) current waveforms when $d_{Q_s} = 1$.

On the Rx, soft switching of Q_s can also be achieved. Figure 16a,b demonstrate the waveforms of V_s and V_{Q_s} at different d_{Q_s} conditions. It can be observed that if Q_s is turned ON/OFF when V_s is negative and V_{Q_s} is zero as illustrated in Figure 3c,e, voltage distortion does not occur. Nevertheless, in practice, $n \cdot d_{Q_s}$ is not always an integer, thereby resulting in three switching situations: Q_s hard switching ON, Q_s hard switching OFF, and Q_s hard switching ON/OFF. To estimate the hard-switching impact, d_{Q_s} is set as 0.4, and n is set as 10. Then Q_s works in soft-switching ON/OFF case as shown in Figure 16c and hard-switching ON/OFF as shown in Figure 16d. When V_s and V_{Q_s} are positive, Q_s is turned ON. The current path switches from Figure 3b to Figure 3d compulsively, leading to a distortion denoted by the ellipse 1 in Figure 16d. When V_s and V_{Q_s} are positive, Q_s is turned OFF. The current path switches from Figure 3d to Figure 3b compulsively, leading to a distortion denoted by the ellipse 2 in Figure 16d. It is found that when the input power is 103.2 W, the former efficiency is 93.3%, a little higher than the latter efficiency of 92.7%, saving switching loss of 0.5 W.

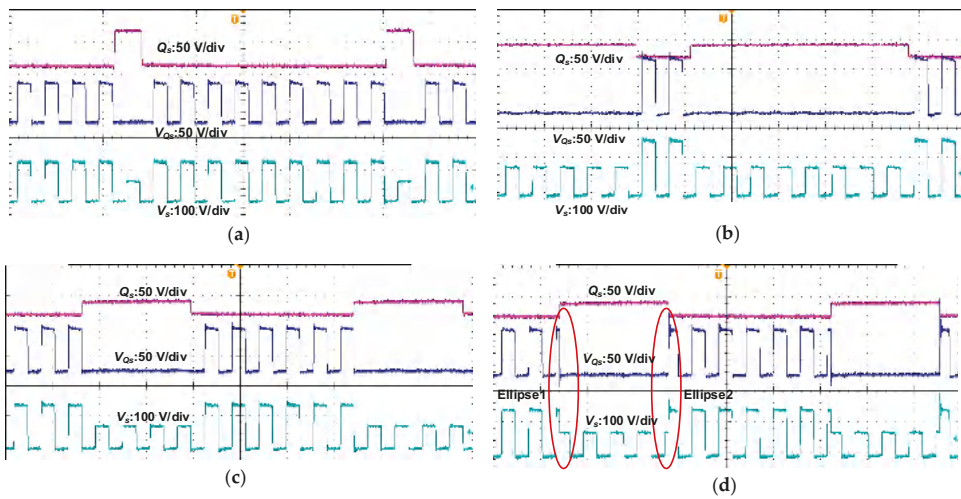


Figure 16. Waveforms of V_s and V_{Q_s} with different d_{Q_s} : (a) $d_{Q_s} = 0.1$ (b) $d_{Q_s} = 0.8$ (c) $d_{Q_s} = 0.4$ (d) $d_{Q_s} = 0.4$ but hard switching.

Additionally, I_{L1} is observed to analyze the impact of the equivalent load and the front-end inductance. At first, the value of L_1 and L_2 is set as 51 μH . When Q_s stays OFF, both the input power and the equivalent impedance are small. The inductance, 51 μH , is much less than the proposed value, 107 μH . Part of I_{L1} is below zero as depicted in Figure 17a, thereby showing a circulating current exists in L_1 and L_2 . However, with the increase of the equivalent impedance, the value of 51 μH meets the requirements. Hence, the circulating current is eliminated and I_{L1} is always above zero as presented in Figure 17b,c.

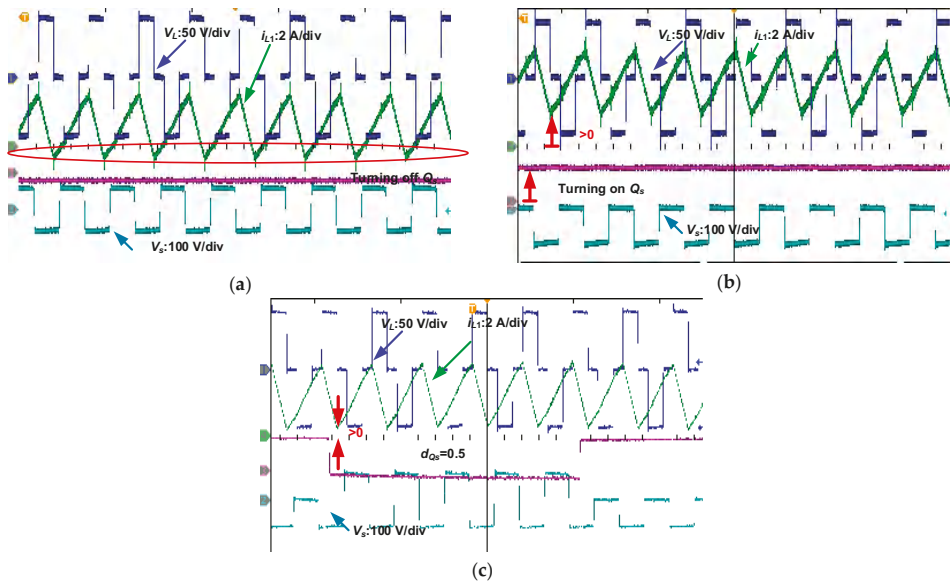


Figure 17. Waveforms of I_{L1} , V_p , and V_s : L_1 is 51 μH but the equivalent impedance R_{act} changes (a) Q_s stays OFF, R_{act} reaches the maximum, part of I_{L1} is below zero; (b) Q_s stays ON, R_{act} reaches the minimum, I_{L1} is above zero; (c) Q_s operates with $d_{Q_s} = 0.5$, I_{L1} is above zero.

5.2. Efficiency and Loss Estimation

Figure 18 demonstrates the system efficiency and the loss estimation. The blue dashed line presents the simulation result and the dark line presents the experimental result. Figure 18a shows that a higher output voltage more than the input voltage 24 V, is accomplished and boosted further after Q_s working. The results support the calculation of Equation (16). The experimental output voltage at the beginning is the same as the simulation but deviates from the theoretical value with the increasing of d_{Q_s} and system operation power. Besides, the input power of the experiment is a little higher than that of the simulation power when d_{Q_s} is below 0.5, whereas this situation reverses after d_{Q_s} becomes above 0.5. This difference is mainly caused by the modelling of the SAB in the simulations. At first, the practical forward voltage drop is not invariably 0.6 V but increase from 0.6 V to 0.8 V. The deterioration of the voltage drop can be regarded as the increase of R_{act} , thereby decreasing the practical input power according to Equation (17). In addition, the input current surging from 2.8 A to 8.7 A and the temperature rise may result in the parameter drift and the difference presented in Figure 18. High efficiency is achieved over the variation of d_{Q_s} as depicted in Figure 18c. Although the efficiency drops with d_{Q_s} rising, 88% efficiency is sustained. In general, the results of the established simulation and experimental prototype are accordant and validate the proposed topology and methods. High efficiency can still be obtained though three inductors are added into the WPT system.

Based on the data presented in Figure 18a,b, the power losses can be calculated. When Q_s stays OFF, the power loss is 5.31 W, where the losses caused by the rectifier (0.6 V drop) and the inner resistance of the front-end inductors L_1 and L_2 (0.2 Ω) are obvious and make the main percentage as presented in Figure 18d, where d_{Q_s} is 0. After Q_s operates and the power transfer rate rises, the loss ratio of the front-end inductors and the Rx coil increases as shown in Figure 18d where d_{Q_s} is 1. Hence, there are two ways to improve the system efficiency. One is decreasing the high-frequency resistance by optimizing the inductors and determining a proper value according to Equations (21) and (25). Another method is reducing the receiver coil resistance with optimal coil manufacturing. Otherwise the output rate reduces according to Equations (16) and (17).

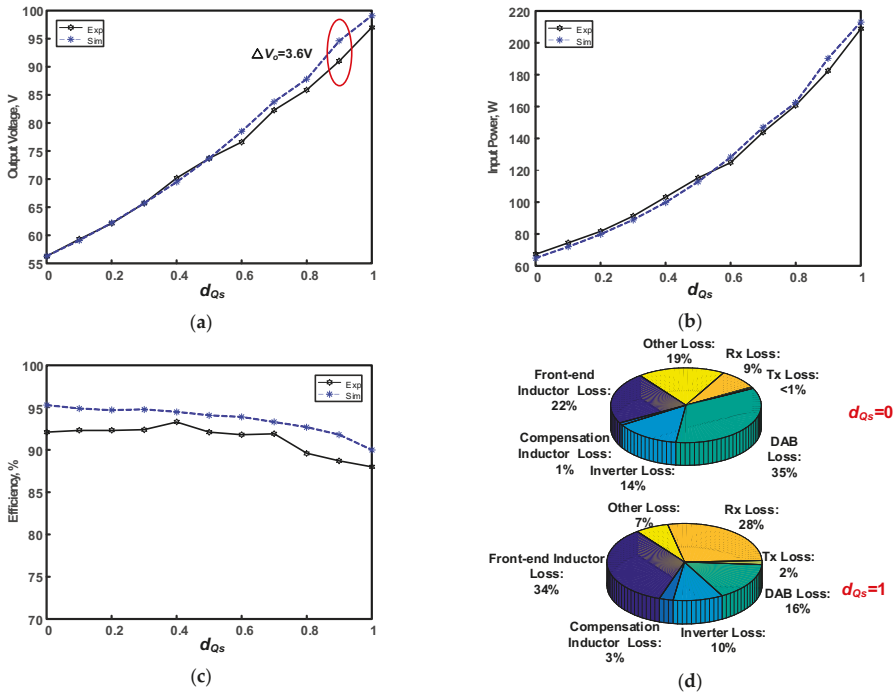


Figure 18. Efficiency and power loss comparison (a) V_o vs. d_{Qs} ; (b) P_i vs. d_{Qs} ; (c) η vs. d_{Qs} ; (d) loss analysis of extreme working cases.

5.3. Load Tripping

To further present the advantage of LCL topology to the load tripping as aforementioned, experiments are added for validation. For convenience, the Tx coil will be artificially removed to imitate the load tripping scenario. Figure 19 shows the variation of I_L and I_p . Over the working time, I_p stays constant even though the load is off, which is in accordance with the analysis of Equation (7). However, I_L varies when the load is off and on. I_L becomes small when the load is off, but becomes large again when the load is reconnected. Moreover, it can be seen that the whole system remains safe all the time.

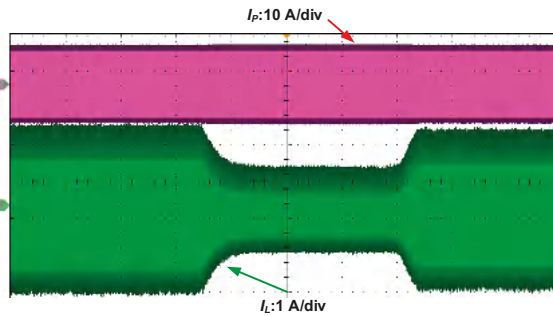


Figure 19. Waveforms of I_L and I_p when load tripping occurs.

6. Conclusions

The LCL topology is regarded as an ideal network used in the WPT systems due to its constant resonant current in the Tx coil and independence of the reflected impedance of the receivers. However, this topology requires a large source voltage to generate transmitting current and induced voltage of receivers, which limits its application in the low voltage scenarios, such as 12–24 V. This paper applied a CFI into WPT systems to boost the voltage for LCL. ZVS of the switches were accomplished under wide range of power rates and also under serious current distortion. The ability of the CFI to turn OFF the top-side switches softly was also deduced and presented in this paper.

On the receiving side, a SAB was proposed and applied to regulate and boost the output voltage and the system power. The SAB allows a lower frequency and reduces the communication requirement compared with the DAB synchronization. Higher output voltage and wide variation range were accomplished.

Guidelines on the parameter design of the front-end inductance, coils and optimal load were elaborately presented. Although more inductors were added into the system, a peak efficiency of 93.3% was obtained and the lowest efficiency was maintained at 88% with proper configuration. Both simulations and experimental results are conducted to verify the aforementioned analysis. Furthermore, optimization methods for efficiency improvement is included in this study.

Author Contributions: H.T., X.Y., and T.W. conceptualized the main idea of this research project; T.W. designed and conducted the experiments with the help of M.A. and X.L.; T.W., X.L., and N.J. checked and analyzed the results. T.W. wrote the whole paper; M.A. reviewed and edited the paper.

Funding: This work was funded by United Foundation of NSFC-Henan (U1604136).

Conflicts of Interest: The authors declare no conflict of interest.

References

1. Asheer, S.; Al-Marawani, A.; Khattab, T.; Massoud, A. Inductive power transfer with wireless communication system for electric vehicles. In Proceedings of the 2013 7th IEEE GCC Conference and Exhibition, Doha, Qatar, 17–20 November 2013; pp. 517–522.
2. Musavi, F.; Eberle, W. Overview of wireless power transfer technologies for electric vehicle battery charging. *IET Power Electron.* **2014**, *7*, 60–66. [[CrossRef](#)]
3. Song, K.; Zhu, C.; Kim Ean, K.; Imura, T.; Hori, Y. Wireless power transfer for running EV powering using multi-parallel segmented rails. In Proceedings of the 2015 IEEE PELS Workshop on Emerging Technologies: Wireless Power, Daejeon, Korea, 5–6 June 2015.
4. Yin, N.; Xu, G.; Yang, Q.; Zhao, J.; Yang, X.; Jin, J.; Fu, W.; Sun, M. Analysis of wireless energy transmission for implantable device based on coupled magnetic resonance. *IEEE Trans. Magn.* **2012**, *48*, 723–726. [[CrossRef](#)]
5. Ma, A.; Poon, A.S.Y. Midfield wireless power transfer for bioelectronics. *IEEE Circuits Syst. Mag.* **2015**, *15*, 54–60. [[CrossRef](#)]
6. Huang, C.Y.; Boys, J.T.; Covic, G.A. LCL pickup circulating current controller for inductive power transfer systems. *IEEE Trans. Power Electron.* **2013**, *28*, 2081–2093. [[CrossRef](#)]
7. Qu, X.; Han, H.; Wong, S.C.; Chi, K.T.; Chen, W. Hybrid IPT topologies with constant current or constant voltage output for battery charging applications. *IEEE Trans. Power Electron.* **2015**, *30*, 6329–6337. [[CrossRef](#)]
8. Zhang, W.; Wong, S.C.; Chi, K.T.; Chen, Q. Analysis and comparison of secondary series- and parallel-compensated inductive power transfer systems operating for optimal efficiency and load-independent voltage-transfer ratio. *IEEE Trans. Power Electron.* **2014**, *29*, 2979–2990. [[CrossRef](#)]
9. Ge, S.; Liu, C.; Li, H.; Guo, Y.; Cai, G.W. Double-LCL resonant compensation network for electric vehicles wireless power transfer: Experimental study and analysis. *IET Power Electron.* **2016**, *9*, 2262–2270.
10. Sohn, Y.H.; Choi, B.H.; Lee, E.S.; Lim, G.C.; Cho, G.H.; Rim, C.T. General unified analyses of two-capacitor inductive power transfer systems: Equivalence of current-source SS and SP compensations. *IEEE Trans. Power Electron.* **2015**, *30*, 6030–6045. [[CrossRef](#)]
11. Tan, L.; Pan, S.; Xu, C.; Yan, C.; Liu, H.; Huang, X. Study of constant current-constant voltage output wireless charging system based on compound topologies. *J. Power Electron.* **2017**, *17*, 1109–1116.

12. Li, S.; Li, W.; Deng, J.; Nguyen, T.D.; Mi, C.C. A double-sided LCC compensation network and its tuning method for wireless power transfer. *IEEE Trans. Veh. Technol.* **2015**, *64*, 2261–2273. [[CrossRef](#)]
13. Xiao, C.; Cheng, D.; Wei, K. An LCC-C compensated wireless charging system for implantable cardiac pacemakers: Theory, experiment, and safety evaluation. *IEEE Trans. Power Electron.* **2018**, *33*, 4894–4905. [[CrossRef](#)]
14. Dai, X.; Li, W.; Li, Y.; Su, Y.; Tang, C.; Wang, Z.; Sun, Y. Improved LCL resonant network for inductive power transfer system. In Proceedings of the 2015 IEEE PELS Workshop on Emerging Technologies: Wireless Power (WoW), Daejeon, Korea, 5–6 June 2015.
15. Peng, F. Z-source inverter. *IEEE Trans. Ind. Appl.* **2003**, *39*, 504–510. [[CrossRef](#)]
16. Zeng, H.; Peng, F.Z. SiC based Z-source resonant converter with constant frequency and load regulation for EV wireless charger. *IEEE Trans. Power Electron.* **2017**, *32*, 8813–8822. [[CrossRef](#)]
17. Siwakoti, Y.P.; Town, G. Improved modulation Technique for voltage fed quasi-Z-source DC/DC converter. In Proceedings of the 2014 IEEE Applied Power Electronics Conference and Exposition (APEC), Fort Worth, TX, USA, 16–20 March 2014; pp. 1973–1978.
18. Wang, T.; Liu, X.; Tang, H.; Ali, M. Modification of the wireless power transfer system with Z-source inverter. *IET Electron. Lett.* **2017**, *53*, 106–108. [[CrossRef](#)]
19. Shen, M.; Peng, F. Operation modes and characteristics of the Z-source inverter with small inductance or low power factor. *IEEE Trans. Ind. Electron.* **2008**, *55*, 89–96. [[CrossRef](#)]
20. Sha, D.; You, F.; Wang, X. A high-efficiency current-fed semi-dual-active bridge DC-DC converter for low input voltage applications. *IEEE Trans. Ind. Electron.* **2016**, *63*, 2155–2164. [[CrossRef](#)]
21. Sha, D.; Wang, X.; Chen, D. High efficiency current-fed dual active bridge DC-DC converter with ZVS achievement throughout full range of load using optimized switching patterns. *IEEE Trans. Power Electron.* **2018**, *33*, 1347–1357. [[CrossRef](#)]
22. Fu, M.; Zhang, T.; Ma, C.; Zhang, X. Efficiency and optimal loads analysis for multiple-receiver wireless power transfer systems. *IEEE Trans. Microw. Theory Tech.* **2015**, *63*, 801–812. [[CrossRef](#)]
23. Liu, X.; Wang, T.; Yang, X.; Jin, N.; Tang, H. Analysis and design of a wireless power transfer system with dual active bridges. *Energies* **2017**, *10*, 1588. [[CrossRef](#)]
24. Sanborn, G.; Phipps, A. Standards and methods of power control for variable power bidirectional wireless power transfer. In Proceedings of the 2017 IEEE Wireless Power Transfer Conference (WPTC), Taipei, Taiwan, 10–12 May 2017.
25. Sha, D.; Wang, X.; Xu, Y. Unequal PWM control for a current-fed DC-DC converter for battery application. In Proceedings of the 2017 IEEE Applied Power Electronics Conference and Exposition (APEC), Tampa, FL, USA, 26–30 March 2017; pp. 3373–3377.
26. Kazimierczuk, M.K. Boost PWM DC-DC converter. In *Pulse-Width Modulated DC-DC Power Converters*, 2nd ed.; John Wiley & Sons, Wright State University: Dayton, OH, USA, 2017; Chapter 3, pp. 85–137.
27. Mai, R.; Liu, Y.; Li, Y.; Yue, P.; Cao, G.; He, Z. An active rectifier based maximum efficiency tracking method using an additional measurement coil for wireless power transfer. *IEEE Trans. Power Electron.* **2018**, *33*, 716–728. [[CrossRef](#)]
28. Liu, X.; Wang, T.; Yang, X.; Tang, H. Analysis of efficiency improvement in wireless power transfer system. *IET Power Electron.* **2018**, *11*, 302–309. [[CrossRef](#)]
29. Yang, E.X.; Lee, F.C.; Jovanovic, M.M. Small-signal modeling of series and parallel resonant converters. In Proceedings of the 1992 Applied Power Electronics Conference and Exposition (APEC), Boston, MA, USA, 23–27 February 1992; pp. 785–792.
30. Zhang, Y.; Chen, K.; He, F.; Zhao, Z.; Lu, T.; Yuan, L. Closed-form oriented modeling and analysis of wireless power transfer system with constant-voltage source and load. *IEEE Trans. Power Electron.* **2016**, *31*, 3472–3481. [[CrossRef](#)]



Article

Simulation Model of a 2-kW IPT Charger with Phase-Shift Control: Validation through the Tuning of the Coupling Factor

Javier Vázquez ^{1*}, Pedro Roncero-Sánchez ¹ and Alfonso Parreño Torres ²

¹ Institute of Energy Research and Industrial Applications, University of Castilla-La Mancha, Campus Universitario S/N, 13071 Ciudad Real, Spain; Pedro.Roncero@uclm.es

² Institute of Industrial Development, Castilla-La Mancha Science and Technology Park, Paseo de la Innovación 1, 02006 Albacete, Spain; Alfonso.Parreno@pctclm.com

* Correspondence: Javier.Vazquez@uclm.es; Tel.: +34-926-295300

Received: 5 September 2018; Accepted: 14 October 2018; Published: 16 October 2018

Abstract: When applied to road vehicle electrification, inductive power transfer (IPT) technology has the potential to boost the transition from combustion engines to electric motors powered by a battery pack. This work focuses on the validation of a PSpice circuit model developed as a replica of a 2-kW IPT prototype with series-series compensation operating at 18.65 kHz. The laboratory prototype has the three stages commonly found in an IPT system: an inverter, controlled by the phase-shift technique, a coil coupling and a load. Simulations were run with the circuit model for three different distances between the two coils of the inductive coupling, all of which are of interest for practical chargers: 125, 150 and 175 mm. The validation approach was based on tuning the magnetic coupling factor for each distance and a set of ten load resistances, until the best match between the simulated and the experimental peak currents supplied by the inverter was found in each case. The coupling factors obtained from the simulation work are in good agreement with their experimental counterparts for the three distances, provided the duty cycle of the inverter output voltage is not too small. The circuit model developed is, therefore, able to reproduce the behavior of the laboratory prototype with sufficient accuracy over a wide range of distances between coils and loading conditions.

Keywords: electric vehicle; wireless power transfer; inductive coupling; coupling factor; phase-shift control; series-series compensation; PSpice

1. Introduction

The applications of wireless power transfer (WPT) technology, which is the contactless transmission of power by an electromagnetic field and was pioneered by Nikola Tesla over a century ago, cover an increasingly wider range of electrical goods. Some examples are cell phones, medical implants, engine telemetry, home electronic appliances, such as electric toothbrushes or some of the robot vacuum cleaners that have recently appeared, and electric vehicles (EV) [1,2]. Magnetic coupling WPT, which is a special case of non-radiative (or near-field) transmission [1,3], is suitable for power transfer over the moderate distances that are typical in EV wireless charging. For longer distances, the transmission of energy necessarily involves electromagnetic radiation. This has, in recent years, become a mature area of expertise, as evidenced by the large number of scientific papers and patent applications in the field, which began to increase considerably in 2008 and have continued to do so [4].

The electricity storage technology utilized to power an EV is, to date, arguably a major deterrent to those drivers who might be willing to make the transition from a combustion engine vehicle to a

pure EV, in the context of increasing environmental awareness. Unfortunately all battery technologies, even those currently regarded as the most advanced for use with EVs, as is the case of lithium-ion batteries [5], still lack competitiveness owing to a limited life time, a high cost, long recharging cycles and low energy density [6]. Their energy density is much lower than that of fossil fuels, which severely limits the autonomy of EVs as regards traveling long distances. While the battery performance affects all EVs equally, regardless of their charging technology (either conductive or wireless), the lack of a charging cable is an attractive feature that could promote the deployment of wireless solutions in the near future.

Charging by means of magnetic coupling WPT can be either static or dynamic. During static charging, the EV remains stationary while the battery is charged, as opposed to dynamic charging, when the EV is in motion on an energized track consisting of a sequence of road-embedded coils to which a current is supplied in synchronism with the position of the vehicle [7]. The dynamic charging exacerbates the challenges, but in turn avoids the need for a high capacity battery [8].

The core of a typical inductive power transfer (IPT) EV charger consists of a pair of loosely coupled coils. The transmitting coil, which is placed on the primary side, is driven by an alternating signal source and transfers energy to the receiving coil on the secondary side by guiding some of the magnetic flux that is generated across the air gap between both windings, just like a transformer does, by using the principle of electromagnetic induction [3]. Owing to the weakness of the magnetic coupling, a fraction of the magnetic flux generated by the primary coil fails to reach the secondary coil, giving rise to a leakage flux, which is represented by leakage inductances. The strength of the coupling, characterized by the coupling factor k , is low in IPT systems.

It is common practice to add compensation capacitors to both sides of the magnetic coupling, connected either in series or in parallel with the respective coils and designed in such a way that the transmitter and the receiver resonate at the same frequency. The resulting topologies are labeled SS, SP, PS and PP [9,10], where S stands for series and P for parallel. When the system is driven at the resonance frequency, the compensation capacitor on the transmitter side minimizes the reactive power provided by the power supply, whereas the compensation capacitor at the receiver maximizes the power transfer [11]. This resonant scheme has also been denominated as RIPT (resonant inductive power transfer) [12] or ICPT (inductively coupled power transfer) [8] in order to distinguish it from the initial non-resonant IPT scheme; in practice, however, researchers tend to use the abbreviation IPT to refer to the resonant topology, and this term is currently in widespread use.

Although each of the four basic compensation topologies have their own pros and cons, a comparative analysis in terms of efficiency, power transfer and other relevant criteria concludes that the current-source-type SS and SP compensation schemes are superior to the others [13]. One of the outstanding advantages of the SS topology for EV charging, which is not shared by any of the other three, is that the compensation capacitor on the transmitter side is independent of both the coupling factor and the load [9,14,15]. Despite some of the inherent problems of the SS topology, such as high voltages across the compensation capacitors or a drastic increase in the primary current if the secondary side is left open-circuited unintentionally [14,16], the SS topology is a usual choice when designing IPT-based EV chargers [10,14,17–23]. It should be pointed out, however, that IPT chargers cannot currently compete with conductive chargers in terms of efficiency: while conductive chargers achieve an overall efficiency of above 90%, IPT chargers fall below that figure. Reported values obtained under optimal operation conditions range from 84% to 88% [14,18,20,24]. Moreover, a mismatch in the coil alignment or an increase in the air gap contribute to a decrease in the overall efficiency.

In a practical IPT charger, the strength of the magnetic coupling is sometimes boosted with the use of ferrite cores placed on both sides of the coupling [6,18–20,25]. The stray magnetic field can be shielded with an aluminum plate placed on the receiving side and attached to the chassis of the EV [6,18,25]. The SAE-J2954 standard [26], which was released as a guideline in 2013 and issued in 2016, replaces the previous recommendation practice SAE-J1773 for EV inductively-coupled charging and establishes a nominal operating frequency for the driving signal of 85 kHz. This moderate frequency

makes magnetic coupling WPT no different from IPT [6]. Some prototypes that adhere to SAE-J2954 have recently been demonstrated [18,20,27]. It should be pointed out that SAE-J2954 was issued as a recommended practice, whose technical specifications, including the nominal frequency of operation, are pending re-evaluation after 2018.

This paper presents work whose objective is to validate a PSpice simulation model that was built as a replica of a 2-kW SS-compensated IPT prototype and which was tested experimentally in a previous work for three distances between coils that fall in the range of the expected ground clearance of light-duty EVs [14]. The validation procedure consisted of comparing the coupling factors provided by the model with their experimental counterparts for the same three air gaps and ten loading conditions for each of them. The proposed approach, based on the tuning of the coupling factor, can be readily adapted to simulate the behavior of IPT prototypes other than the one discussed in this work, including those featuring ferrite cores, which are more difficult to characterize by purely analytical methods. The simulation model can, therefore, be regarded as a practical design tool capable of providing reliable information during the development process of an IPT system. Section 2 begins with a brief analysis of the circuit of a general IPT system with SS compensation, which provides the minimum theoretical framework required to verify whether the results are in agreement. The laboratory prototype on which the simulation model is based is described in Section 3. Section 4 focuses on how the coupling factors for the air gaps under study were determined in an experimental manner using measurements carried out only in the inductive coupling stage. Section 5 contains a thorough stage-by-stage description of the circuit model developed. The definitive k factors obtained with the model are the result of a tuning process that seeks the best match between the experimental and the simulated peak amplitudes of the current waveforms supplied by the inverter. The corresponding results, which lead to the validation of the model, are analyzed in Section 6. A comparative study between the experimental and the simulated current waveforms, on which the tuning procedure is based, follows in Section 7. The conclusions are summarized in Section 8.

2. Circuit Analysis of an IPT System

The general scheme of an IPT system comprises three stages: a primary section, supplied by a grid, followed by a compensated inductive coupling with a primary and a secondary coil and finally by a secondary section that charges a battery. The primary coil is driven by an alternating signal supplied by a full-bridge inverter located in the primary section. The voltage induced across the secondary coil is, in turn, rectified and conditioned prior to feeding the battery, sometimes with the insertion of a DC/DC converter or simply with a filter capacitor. The battery is usually replaced in laboratory prototypes with a variable resistor R that reflects its state of charge (SOC) at a given time of the charging process [1]. Figure 1 depicts the three stages particularized for the SS-compensated IPT prototype used in this work.

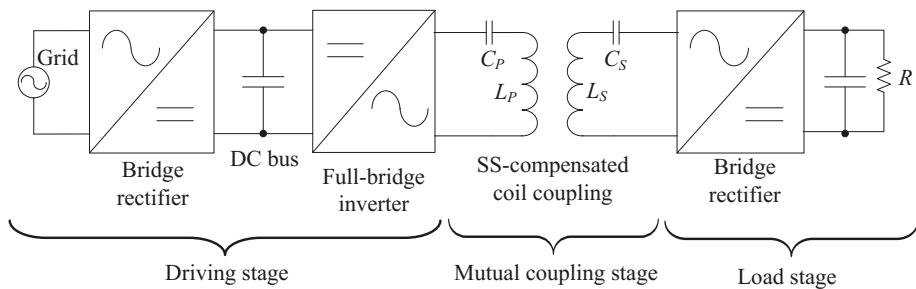


Figure 1. Constructed IPT prototype: general scheme. S, series.

A simplified equivalent circuit of the entire IPT prototype is shown in Figure 2. The circuit, which models the mutual coupling stage by means of a T-network, can be analyzed via a fundamental harmonic approximation (FHA) owing to the presence of a sinusoidal voltage source $v_p(t)$ that represents the fundamental component of the voltage that drives the primary coil generated by the inverter. FHA is a widely-used approach in the context of IPT systems that simplifies the analysis without compromising the accuracy, since the harmonic content of the resonant currents is usually low owing to the high quality factors of the resonant tanks [18].

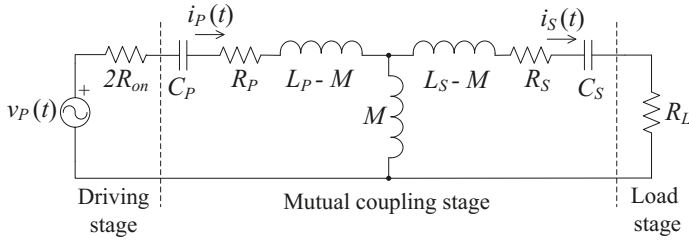


Figure 2. IPT prototype: equivalent circuit.

The conduction resistance of any of the four inverter switches is modeled with R_{on} . Since two switches are closed at any given time when an AC output is synthesized from a DC input, the circuit model includes the resistance $2R_{on}$ in series with the driving voltage. The resistance R_p results from the sum of two contributions located in the primary section and connected in series: the stray series resistance of the primary coil, R_{L_p} , and the stray series resistance of the primary capacitance, R_{C_p} . The resistance R_s is, in turn, the sum of the stray series resistances of the secondary coil, R_{L_s} , and that of the secondary capacitance, R_{C_s} . R_L accounts for the equivalent resistance of the rectifier stage and the battery. M represents the mutual inductance between the two coils, which relates to k and to the primary and secondary self-inductances L_p and L_s through the following expression:

$$M = k\sqrt{L_p L_s} \tag{1}$$

Leakage inductances on the primary and the secondary sides, L_{pk} and L_{sk} , can be expressed as a function of either k or M and the primary to secondary turns ratio $r = N_p/N_s$:

$$L_{pk} = (1 - k)L_p = L_p - rM \tag{2}$$

$$L_{sk} = (1 - k)L_s = L_s - M/r \tag{3}$$

Note that the inductances $L_p - M$ and $L_s - M$ that appear in the T-model coincide with L_{pk} and L_{sk} only if $r = 1$. Expressions (1), (2) and (3) show that IPT systems, for which k is necessarily low, have non-negligible leakage inductances.

In the phasor domain, the impedance seen from the primary side, Z_p , can be written as:

$$Z_p = \frac{\overline{V}_p}{I_p} = 2R_{on} + R_p + j(X_{L_p} + X_{C_p}) + Z_R \tag{4}$$

where Z_R is the reflected impedance, which depends on circuit elements present on the secondary side:

$$Z_R = \frac{\omega^2 M^2 [R_s + R_L - j(X_{L_s} + X_{C_s})]}{(R_s + R_L)^2 + (X_{L_s} + X_{C_s})^2} \tag{5}$$

Since the primary and secondary resonant circuits are designed to resonate at the same frequency, the common resonance frequency is given by:

$$\omega_r = \frac{1}{\sqrt{L_S C_S}} = \frac{1}{\sqrt{L_P C_P}} \tag{6}$$

When the circuit is driven at the resonance frequency, both the reactances on the primary side, X_{L_P} and X_{C_P} , and those on the secondary side, X_{L_S} and X_{C_S} , cancel each other out. Z_P is thus simplified to an expression without imaginary part, where V_P and I_P represent the peak amplitudes of their corresponding voltage and current phasors:

$$Z_P(\omega_r) = \frac{V_P}{I_P} = 2R_{on} + R_P + \frac{\omega_r^2 M^2}{R_S + R_L} \tag{7}$$

On the other hand, the power delivered to the load stage, represented by R_L , is [17,18,21]:

$$P_L = \frac{(\omega_r M V_{Prms})^2 R_L}{[(R_L + R_S)R_P + \omega_r^2 M^2]^2} \tag{8}$$

Finally, the efficiency of the mutual coupling stage can be calculated as follows: [14,17]:

$$\eta_{IPT} = \frac{R_L}{R_L + R_S + \frac{R_P(R_L + R_S)^2}{\omega_r^2 M^2}} \tag{9}$$

3. Laboratory Prototype

Figure 3 shows the three stages of the constructed prototype in a single image, along with the control electronics and the instrumentation utilized, all of which are described below.

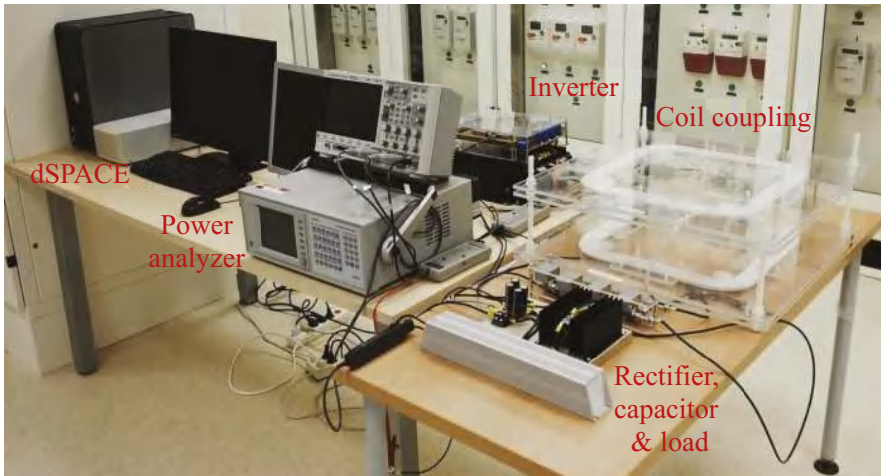


Figure 3. Laboratory prototype with control electronics and instrumentation.

3.1. Driving Stage

The driving stage, which was fed from a single-phase 230 V/50 Hz outlet of the power grid, features an AC/DC converter that provides a stable DC bus voltage V_{DC} , followed by an H-bridge inverter based on IGBT switches. The driving function was implemented using two legs of a modular three-phase inverter connected to the grid, purchased from Semikron Electronics S.L., Barcelona, Spain. It includes a bridge rectifier (ref. SK95D12), an IGBT module (ref. SK30GB128) and some additional electronics. Figure 4 depicts a simplified circuit diagram of the driving stage.

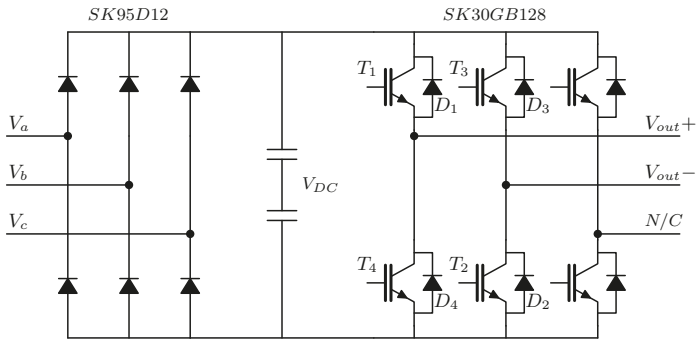


Figure 4. Driving stage: circuit diagram.

The bridge rectifier is characterized by a reverse voltage of 1200 V and a current of 95 A, whereas the IGBT switches support a collector-emitter voltage of 1200 V and a collector current of 25 A (all maximum ratings). Each of the two capacitors in Figure 4 results from a parallel arrangement of four capacitors rated at 680 μF and 400 V. The equivalent capacitance of the eight capacitors amounts thus to 1360 μF and is rated at 800 V. The features of the driving stage were expanded by means of a customized PCB attached to the top of the inverter: this includes a fiber optic interface to allow communication with a dSPACE control platform, a measurement unit of both the inverter leg currents and the DC bus voltage, and a module to protect against overcurrents.

Although the H-bridge inverter is a single-phase two-level voltage-source converter (VSC), its switching scheme is such that it does not produce a square wave output voltage, but rather a controlled one with intervals in which the output is both zero and $+V_{DC}$ and $-V_{DC}$. This controlled output with three output levels, whose duty cycle can be adjusted, is characteristic of a phase-shift control scheme. The inverter output voltage can be set to zero periodically during the so-called interval of zero voltage, whose duration can be regulated in the full range from 0 rad to 2π rad throughout each period. It is characterized by the zero-voltage angle α , which varies from 0 rad to $\pi/2$ rad. As can be seen in Figure 5, the trigger pulses V_{T1} and V_{T4} , which are applied to their respective IGBT gates located on the left leg of the inverter, are complementary. The same applies to the trigger pulses on the right leg, V_{T2} and V_{T3} . The four pulses have a duty cycle of 50%. The synchronization scheme results in a phase shift δ_{2-1} between the pulses V_{T2} and V_{T1} , on the one hand, and a second phase shift δ_{3-4} between V_{T3} and V_{T4} , on the other. Both of them are equal to 2α , whereas the interval of zero voltage is 4α throughout a period.

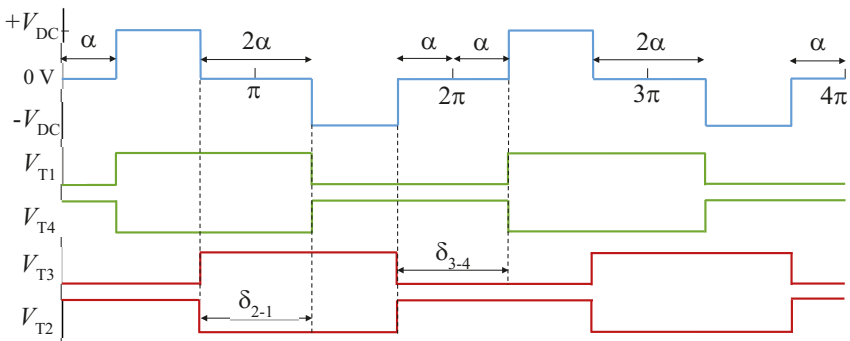


Figure 5. Phase-shift control scheme showing the displacement angles δ_{2-1} and δ_{3-4} that determine the interval of zero voltage in the inverter output voltage.

The amplitude of each harmonic that is present in the inverter output voltage waveform can be controlled by varying α , as stated in (10) [28].

$$V_n = \frac{4V_{DC}}{n\pi} \cos(n\alpha) \tag{10}$$

The inverter output rms voltage V_{rms} is, moreover, dependent on α [28]:

$$V_{rms} = V_{DC} \sqrt{1 - \frac{2\alpha}{\pi}} \tag{11}$$

The rms current supplied by the inverter to the primary coil can consequently be set to a given target value by simply selecting the appropriate angle α . An analog voltage, which is proportional to the α required, was generated by using a dSPACE 1103 (dSPACE GmbH, Paderborn, Germany) control platform. That voltage was, in turn, read by the IC UCC3895 (Texas Instruments, Dallas, TX, USA), a phase-shift PWM controller that generated the switching scheme shown in Figure 3 and is required to synchronize the trigger pulses V_{T1} to V_{T4} . The resulting inverter output voltage had a frequency of 18.65 kHz. Examples of IPT systems with an SS compensation topology featuring a phase-shift control scheme are those described in [14,20,29].

3.2. Inductive Coupling Stage with SS Compensation

Both circular and square coils have been reported in the construction of IPT prototypes. Considering that the mutual inductance M between square coils is $(4/\pi)^2$ times larger than between circular ones when the corresponding circumference is inscribed in the square [30], square rather than circular coils were chosen to design the coupling stage. The two coils, which were wound using Litz wire with a section of 6.28 mm², have 22 turns each with 11 turns piled up on top of the other 11, as Figure 6 illustrates.

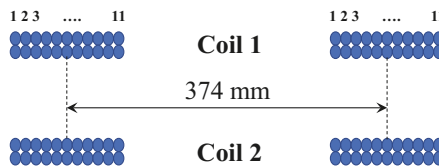


Figure 6. Constructed coils: cross-section.

Mechanical stability was achieved by sandwiching each coil between two methacrylate plates. The air gap between the coils can be manually adjusted to the desired value by means of nylon screws placed at the corners of the holding plates. The four screws also contribute to keeping the coils perfectly aligned and parallel to each other.

Each of the two compensation capacitances resulted from an arrangement composed of four branches connected in parallel and two polypropylene film capacitors connected in series per branch, with a nominal capacitance of 100 nF per capacitor (ref. MMKP386 F1230 manufactured by Vishay, Malvern, PA, USA). This arrangement is necessary to support the high voltages developed across the capacitors when the prototype operates at the resonance frequency.

3.3. Load Stage

The load stage comprises a high voltage rectifier followed by a capacitor arrangement with which to reduce the ripple current, which is in turn connected to a combination of power resistors.

The bridge rectifier was constructed by connecting two semiconductor modules (ref. STTH6006TV, ST Microelectronics, Geneva, Switzerland). Each module includes two ultrafast diodes characterized by a peak reverse voltage of 600 V and an average forward current of 30 A (absolute ratings).

The filter capacitance was the result of combining four electrolytic capacitors in an arrangement composed of two branches connected in parallel with two capacitors connected in series per branch. Each capacitor is rated at 220 μF and 450 V, with a capacitance tolerance of $\pm 20\%$.

The power resistors utilized were of a wirewound type rated at 800 W. Ten different ohmic values, from 2.5 to 40 Ω , were available from series and parallel combinations of resistors with a nominal resistance of 10 Ω .

3.4. Prototype Testing and Performance Figures

Tests were conducted for three air gaps between coils (125, 150 and 175 mm), which will henceforth be referred to as g_x , where x is the corresponding gap. The rms primary current, $I_{p\text{rms}}$, was kept at approximately 10 A via individual adjustments of the angle α for each air gap g_x and resistance R being tested. Controlling the current in the primary coil allows the series-compensated secondary side to resemble a voltage source [9].

The load power P_L depends strongly on both g_x and R . For g_{125} , the air gap for which the magnetic coupling is the strongest of all three, P_L reached 2 kW when R was 5 Ω (higher loads led to lower transferred powers). On the other hand, if the three air gaps are considered altogether, P_L was always above 1 kW for $R = 5 \Omega$ and below 500 W for $R = 30 \Omega$. The overall efficiency, computed from grid supply to load, was 82.5% for the intermediate case of g_{150} . However, if only the coil coupling stage is taken into account, it exceeded 90%. Further details regarding the prototype performance can be found in [14]. It should be noted that, according to (9), the efficiency of an SS-compensated inductive coupling stage depends, among other parameters, on the resonance frequency ω_r and the mutual inductance M , and an increase in either of them causes an increase in the efficiency. Figure 7 plots η_{IPT} calculated with (9) for the three air gaps and two different resonance frequencies (18.65 kHz and 85 kHz), with the load resistance R_L ranging from 2.5 Ω to 40 Ω . As can be seen, when the frequency is 18.65 kHz, η_{IPT} is above 90% only under certain operation conditions, in agreement with the efficiency figures found experimentally. However, for the case of 85 kHz, η_{IPT} represents a significant improvement, exceeding 95% for most of the loads and air gaps. Unfortunately, the desired increase in η_{IPT} that arises as a consequence of an increase in either M or ω_r is accompanied necessarily by a reduction in the power delivered to the load, as follows from (8). Consequently, an IPT system working at a relatively low frequency of operation, as in the case discussed in this work, is characterized by moderate efficiency figures that are compensated by an enhanced power transfer capability.

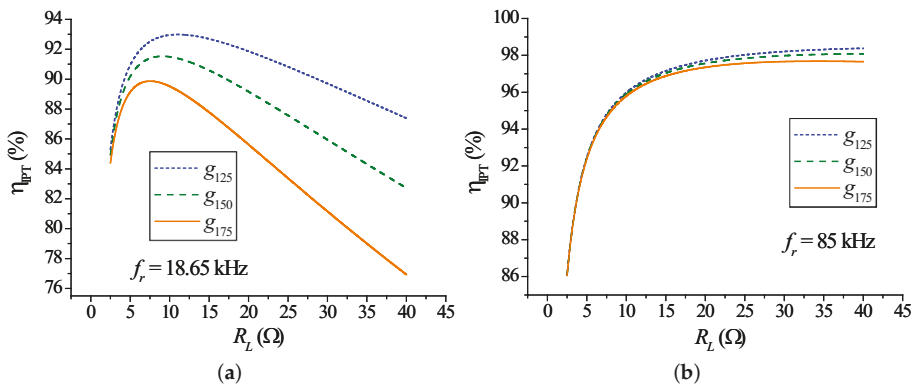


Figure 7. η_{IPT} versus R_L for two different frequencies of operation: (a) 18.65 kHz; (b) 85 kHz.

4. Experimental Determination of the Coupling Factor

A reliable figure for the coupling factor between two coupled coils can be obtained experimentally by applying the voltage ratio method, which consists of measuring the peak amplitude of the voltage waveform at each winding in open circuit conditions when a sinusoidal driving voltage is applied to the other winding [31]. The method, therefore, requires four voltage measurements for a given air gap between coils: the driving voltages at the primary and secondary windings, denoted by V_{dP} and V_{dS} , and the corresponding open circuit voltages, represented by V_{ocP} and V_{ocS} . Since the accuracy is improved if measurements are taken at a frequency at which the quality factor Q of the coils is high [31], the selected frequency of the driving voltage was 20 kHz. The experimental coupling factor obeys the following expression:

$$k_{\text{exp}} = \sqrt{\frac{V_{ocP} V_{ocS}}{V_{dS} V_{dP}}} \tag{12}$$

Considering that, for a given amplitude of the voltage applied to the driving coil, the voltage across the open-circuited coil decreases as the air gap increases, the presence of noise on the voltage signals can compromise the accuracy of the measurements, especially in the case of large air gaps. Small driving amplitudes were, therefore, avoided. In order to verify whether or not there is a threshold for the driving amplitude below which the k values obtained lack accuracy, four sets of measurements were taken for each air gap, during which the driving amplitudes V_d were set to values of around 5, 10, 15 and 20 V. The resulting k values are represented in Figure 8.

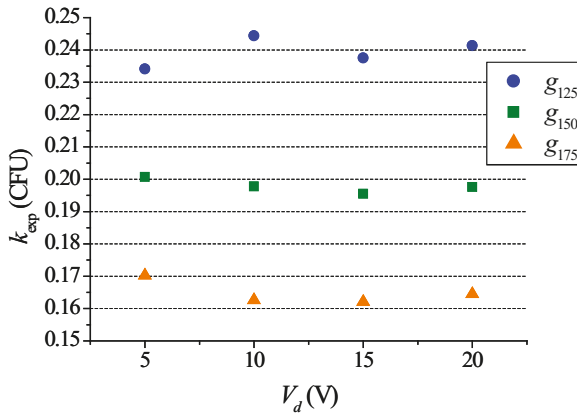


Figure 8. Determination of k_{exp} for four driving voltage amplitudes.

As can be seen, the method is able to distinguish among the three cases under study satisfactorily for every V_d . However, there is a noticeable upward deviation of the k factor obtained for g_{175} when V_d is 5 V with respect to the values that result from the other three amplitudes, which are not that different from each other. A similar deviation for 5 V, although more moderate, occurs for g_{150} . The same occurs with g_{125} , this time with a downward deviation. This analysis suggests that the driving voltage threshold sought is located somewhere between 5 and 10 V and measurements at 5 V were consequently ruled out. Although the remaining sets of measurements taken at 10, 15 and 20 V gave rise to similar k factors, the 20-V set can be regarded as the most reliable of all as its signal-to-noise ratio is the largest. The k values obtained with that set are represented in Table 1 and will be used as targets to be compared with the corresponding values resulting from the simulations.

Table 1. Coupling factors obtained experimentally ($V_d = 20$ V).

Air gap (mm)	125	150	175
k_{exp}	0.241	0.198	0.164

5. Circuit Model for Simulation

A preliminary version of the circuit model presented in this work was utilized to estimate k for the single case of g_{125} without prior knowledge of the corresponding experimental k factor to be used as a reliable reference for validation purposes [32]. This estimate of k relied on a successive approximation technique that, in turn, relied on experimental measurements of the primary peak currents for three loads (5, 10 and 20 Ω). It was not necessary to follow that approximate method here, since the experimental k values for the three air gaps were now available.

A schematic representation of the PSpice simulation model is shown in Figure 9. It has been improved when compared to the initial version, as a number of changes were made in both the inverter and the load stages. While the inverter topology remains the same, some of its parameters model the real device with more accuracy in the current version. With regard to the load stage, the refinements involve all the parts: the bridge rectifier model, the filter capacitor and the resistive load. A description of the three stages present in the circuit model follows below.

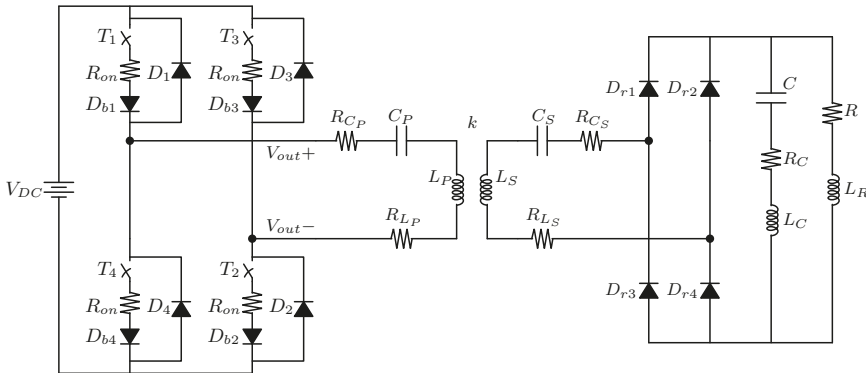


Figure 9. IPT prototype: circuit model.

5.1. Full-Bridge Inverter Stage

The four IGBTs were replaced with voltage-controlled switches denominated as T_1 to T_4 . As IGBTs carry the current in one direction and block it in the opposite one, diodes D_{b1} to D_{b4} were added to provide the blocking functionality. Considering that the switches must carry both positive and negative currents when inductive loads are driven, all switches are equipped with reverse-parallel feedback diodes D_1 to D_4 that carry the negative current during a certain time interval throughout each period.

The switch model includes a non-zero on-resistance R_{on} equal to 48 m Ω corresponding to the IGBT module SK30GB128 (Semikron S.L., Barcelona, Spain), as reported in the manufacturer’s datasheet under the name r_{CE} (typical value). The DC bus voltage V_{DC} was calculated by adding the voltage drop across the switches to the amplitude of the inverter output voltage experimental waveforms. The model parameters of the blocking diodes placed in series with the switches were purposely chosen to obtain a negligible drop in voltage across the diodes. The series resistance R_s was, therefore, set to zero and the emission coefficient n was set to 0.001. n is an empirical constant, also termed as the ideality factor, that appears in the exponential $i - v$ relationship of a diode. Reducing n makes the turn-on voltage of the diode $i - v$ characteristic to approach 0 V; however, convergence problems may arise if

n is made too small. In real diodes, n depends on both the material and the physical construction of the device [33]. Table 2 summarizes a selection of some key circuit parameters for the switch and for the two diode models present in the inverter. Other diode parameters not shown in the table adopt the default values of the PSpice Dbreak diode model.

Table 2. Inverter model: selected circuit parameters.

Switches T_1 to T_4			
$R_{on}(\Omega)$	$R_{off}(\Omega)$	$V_{on}(V)$	$V_{off}(V)$
0.048	1×10^6	1	0
Diodes D_{b1} to D_{b4}		Diodes D_1 to D_4	
$R_s(\Omega)$	n	$R_s(\Omega)$	n
0	0.001	0.1	1

5.2. Compensated Coil Coupling Stage

The inductive coupling was modeled with a PSpice device able to couple two or more coils through the corresponding coupling factors between each coil pair. The self-inductances of the primary and secondary coils, L_p and L_s , were measured using a 4294A precision impedance analyzer (by Agilent), with which the corresponding series stray resistances of the two coils, R_{L_p} and R_{L_s} , were also obtained. The two compensation capacitor arrangements were similarly measured in order to obtain both their capacitances C_p and C_s and their series stray resistances R_{C_p} and R_{C_s} , all of which are listed in Table 3.

Table 3. Compensated coil coupling model: circuit parameters.

Primary Side		Secondary Side	
C_p	186.9 nF	C_s	187.0 nF
R_{C_p}	32 m Ω	R_{C_s}	35 m Ω
L_p	393 μ H	L_s	389 μ H
R_{L_p}	369 m Ω	R_{L_s}	367 m Ω

5.3. Load Stage

The PSpice model files for the voltage rectifier STTH6006TV1 (STMicroelectronics, Geneva, Switzerland), which are available for download on the manufacturer’s website, were added to the PSpice libraries. With regard to the filter capacitor arrangement, its equivalent circuit was simplified to a series RLC combination, as electrolytic capacitors form an RLC resonant circuit with a low Q [34]. Owing to the low Q , a measurement of impedance magnitude and phase versus frequency using an impedance analyzer revealed a broad impedance minimum centered around 90 kHz rather than the sharp resonance typical of resonators with a high Q , along with a slow change in the phase rather than an abrupt transition (ideally, from -90° to $+90^\circ$ at the resonance frequency). The frequency range chosen to obtain the equivalent RLC circuit covers four decades, from 50 Hz to 500 kHz, with the objective of capturing the most significant features of the frequency response on both sides of the resonance that are necessary for the impedance analyzer to calculate reliable model parameters. With regard to the power resistor, it was initially modeled with an $RL||C$ network, which is typical for wirewound resistors, as is the case here. However, in standard resistors of this type, the capacitance is so low that it is normally ignored, since resonance effects are virtually non-existent [34]. The model adopted was, therefore, a series RL combination. Owing to the construction of wirebound resistors, their equivalent series inductance is not negligible. In the present case, it amounts to 39.20 μ H for one of the 10 Ω resistors used in the prototype. Note that if no ripple were present across the load resistor, the equivalent inductance would not play any role and it could, therefore, be safely removed from the resistor model. Since some ripple remained unfiltered on the rectified voltage signal despite the presence of the filter capacitor, the stray inductance L_R present in the power resistor was added to the model. Table 4. shows the corresponding circuit parameters.

Table 4. Load stage: circuit parameters.

Filter Capacitor		Load Resistor	
C	187.80 μF	R	10.21 Ω
R_C	718 m Ω	L_R	39.20 μH
L_C	325 nH		

6. Model Validation

Six input parameters had to be confirmed prior to running a simulation: the DC bus voltage V_{DC} , the switching frequency f , the zero-voltage angle α , the load resistance R with its series stray inductance L_R , and the coupling factor k . Simulations for each air gap were run with ten different load resistances, whose nominal values were 2.5, 5, 7.5, 10, 15, 20, 25, 30, 35 and 40 Ω . All possible combinations of different loads and air gaps led to a total of thirty angles α with which to keep I_{Prms} controlled at around 10 A. Several k values were tentatively tried for all combinations of g_x and R until the best match between the experimental and the simulated primary peak currents was found, using three decimal digits for k . Following this iterative procedure for every combination of g_x and R yielded a set of ten k values for each air gap. The results, which are compared with the experimental k values in Table 1, are shown in Figure 10.

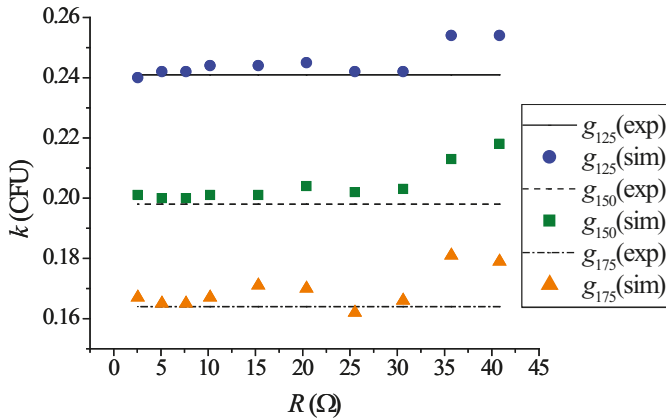


Figure 10. Coupling factors for the three air gaps and ten loads. Experimental and simulated data are represented by straight lines and discrete points, respectively.

Upon inspecting Figure 10, it is apparent that the model is capable of discriminating well among the three air gaps, although deviations from the expected k values are especially noticeable for the loads of 35 and 40 Ω . As a result of the phase-shift control action, α adopts new values as the whole range of loads is swept. Figure 11 shows that α converges to 90° as R increases, regardless of g_x . This increase in α with R makes the rms voltage at the inverter output drop in order to keep the primary current controlled for every load, as follows from (7) and (11). In practice, after a new load was connected, α was adjusted manually from the dSPACE platform until the monitored I_{Prms} was as close as possible to 10 A.

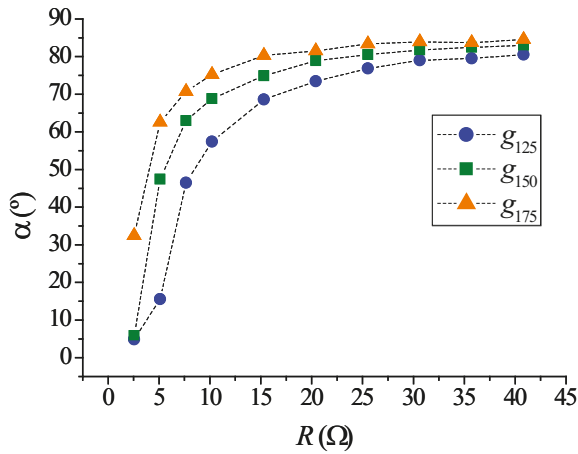


Figure 11. Convergence of α with R .

As a consequence of this gradual convergence process, the rate at which α changes has a non-linear dependence with R : a given increment in R makes α undergo a significant increase in the area of small loads; however, the same increment causes only a moderate increase in α for large loads. Although this holds for the three g_x , the effect becomes more pronounced as the air gap increases. Note that the cosine function in (10) accounts for the non-linear behavior observed.

The deviations from the experimental k factors, expressed in coupling factor units (CFU), are plotted in Figure 12 in the form of absolute errors. They reach a maximum of 7×10^{-3} CFU with the exception of the two cases mentioned previously, in which they grow remarkably larger. Overall, the area of low R (up to 10Ω) behaves best, as the deviations are 3×10^{-3} CFU or less for the three g_x . It should be noted that the absolute errors found for g_{125} are the smallest for the ten loads, ranging from 1×10^{-3} to 4×10^{-3} CFU with the exception, once again, of the two largest load resistances.

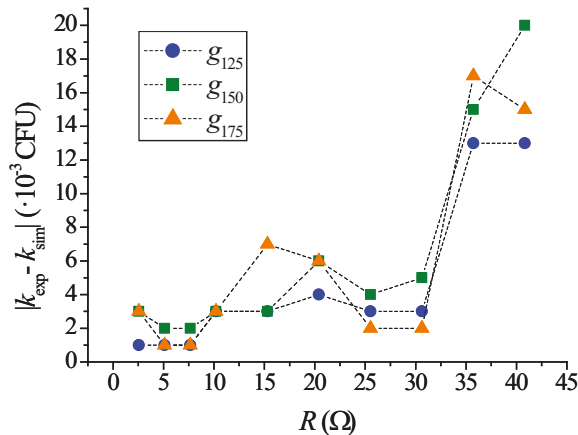


Figure 12. Absolute errors obtained in the determination of k with the circuit model.

The accuracy of every single model parameter contributes to the reliability of the circuit model, even in the case of those parameters that, in principle, play a minor role. This is the case of R_{on} : if, for a given g_x and R , R_{on} decreases from its actual value of $48 \text{ m}\Omega$ to $1 \text{ m}\Omega$ (that is, the inverter switches are

modeled as virtually ideal devices), the primary peak current increases according to (7), which in some cases alters the k obtained with the circuit model. Taking for example g_{150} , the increase in the primary current caused by that drop in R_{on} does not suffice to modify k for $R = 2.5 \Omega$. However, in the case of $R = 40 \Omega$, k undergoes an increase of 2×10^{-3} CFU, which would add to the corresponding absolute error, making the deviation from the experimental k even larger.

As stated previously, an increase in R translates into small increases in α in the area of high loads. This has important implications with regard to the sensitivity of the system and its capability to accurately determine k , since a small change in α when the prototype is loaded with a large R leads to significant variations in the peak primary current. It is, therefore, of interest to test the model response under small variations in α that may occur owing to a measurement error, as α results from time measurements of the experimental waveforms of the inverter output voltage.

Assuming that α was obtained with an error of $\pm 0.25^\circ$, and plotting k against R for g_{125} for illustration purposes, it is apparent that k undergoes an increasingly larger shift from the k factors obtained with α as R increases. As can be seen in Figure 13, the error has little or no influence on k within the low load range. However, from 10Ω onward, the shifts grow larger and larger both above and below the initial k values, reaching a maximum of 4×10^{-3} CFU for 40Ω ($k = 0.250$ for $\alpha + 0.25^\circ$ and $k = 0.258$ for $\alpha - 0.25^\circ$). If a small measurement error in the determination of α is taken into account, the capability of the system to deliver reliable figures for k consequently worsens as R increases. This may contribute to justifying the deviations found in the determination of k for the two largest loads.

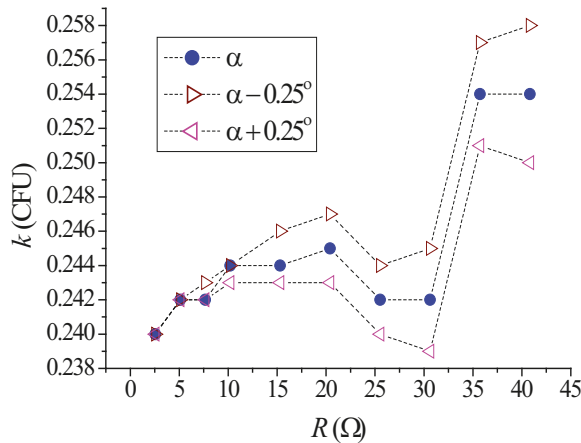


Figure 13. Influence on k of a $\pm 0.25^\circ$ error in the determination of α for g_{125} .

7. Waveform Analysis

Both experimental and simulated waveforms are shown in Figure 14 for comparison purposes. The inverter output voltages and currents are represented by blue and pink lines, respectively. A selection of three representative cases was chosen (specifically, those corresponding to 2.5, 10 and 40 Ω for the intermediate air gap g_{150}). Note that the duty cycle of the inverter output voltage is very low for 40 Ω , one of the two cases in which the circuit model behaves worst.

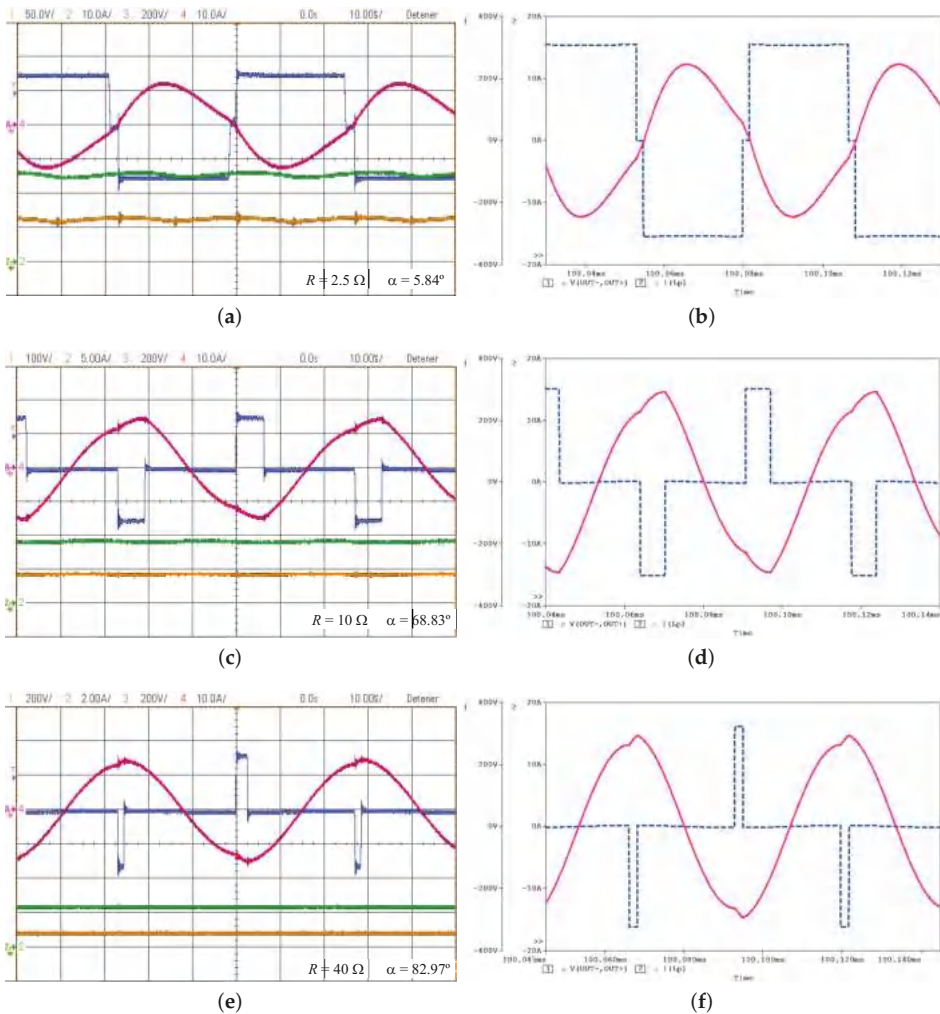


Figure 14. Selected inverter output voltage and current waveforms for g_{150} . (a,c,e) experimental prototype; (b,d,f) PSpice simulation.

A comparison of the shapes and amplitudes of the two sets of waveforms makes it possible to conclude that the simulated waveforms are very similar to their experimental counterparts. Moreover, the shape of the current waveforms is quite sinusoidal in all cases, which confirms the validity of the FHA approximation adopted before analyzing the equivalent circuit of the IPT prototype. The low harmonic content of the primary current waveforms can be understood in terms of the band-pass filtering process introduced by the resonant circuit on the primary side of the coupling. Alternatively, it can be regarded as a consequence of dealing with loosely coupled coils, which are characterized by a low k . Recall that leakage inductances are, according to (2) and (3), relatively large in the circuit model of a weak inductive coupling: a large leakage inductance effectively filters out most of the harmonic content of the current waveform, leading to the observed sinusoidal-like waveforms. Furthermore, the larger the air gap is, the larger the leakage inductance becomes, and more frequencies are consequently rejected from the spectrum of the current waveform. This effect is illustrated in

Figure 15, which represents the total harmonic distortion (THD) versus R . As can be seen, the harmonic content decreases as g_x increases, which is easier to verify for those loads in which α is similar for the three g_x (all of them, with the exception of the three smaller ones). In the case of small loads (up to $10\ \Omega$), the plot does not show the effect clearly since, for a given load, the corresponding three angles α are quite different depending on g_x . Finally, it should be pointed out that no correlation was found between the harmonic content and the deviations in k depicted in Figure 12. In fact, the THD is especially low for the two largest loads, for which the model behaves worst. It is not, therefore, possible to claim that the two estimates of k with the largest absolute errors occur as a consequence of a high harmonic content in the corresponding current waveforms.

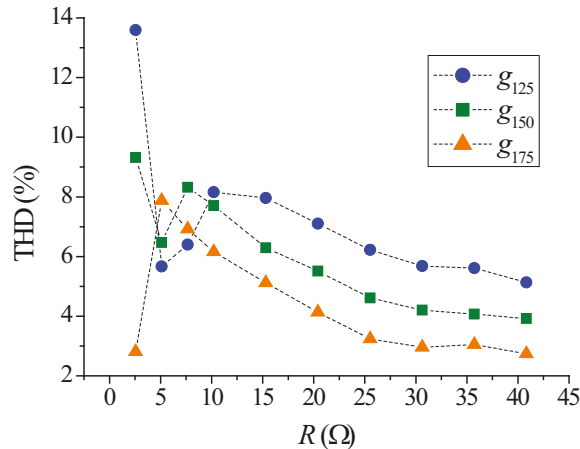


Figure 15. THD versus R .

8. Conclusions

A PSpice circuit model, developed as a replica of a 2-kW IPT charger operating at 18.65 kHz and controlled with the phase-shift technique, has been tested and validated for three air gaps of practical interest in the case of light-duty EVs: 125, 150 and 175 mm. The validation procedure was based on determining the existing deviations between the coupling factors obtained experimentally for every air gap and those delivered by the simulation model for a set of ten load resistances, ranging from $2.5\ \Omega$ to $40\ \Omega$. The results show that the deviations are within reasonable limits (below 7×10^{-3} CFU) for the three air gaps and all the loads tested with the exception of the two largest, for which the duty cycle of the inverter output voltage is especially low and accuracy is, therefore, compromised. The best agreement was found in the lower range of load resistances (up to $10\ \Omega$), in which deviations lie between 1×10^{-3} CFU and 3×10^{-3} CFU. Consequently, the overall performance of the simulation model is satisfactory, although there is evidence of a certain threshold level for the load resistance (or, equivalently, for the zero-voltage angle α) above which the reliability of the simulation model declines. Setting the threshold at the nominal resistance of $35\ \Omega$, the corresponding α angles are 79.54° , 82.46° and 83.68° for the air gaps of 125, 150 and 175 mm, respectively. Since one of the six input parameters of the circuit model is the switching frequency, the PSpice circuit developed can be readily adapted to simulate the behavior of prototypes that comply with the SAE-J2954 standard issued for EV wireless charging, which establishes a nominal switching frequency of 85 kHz.

Author Contributions: Conceptualization, J.V. Data curation, J.V., P.R. and A.P. Formal analysis, J.V. Funding acquisition, P.R. Investigation, J.V., P.R. and A.P. Methodology, J.V. Project administration, P.R. Software, J.V. and P.R. Supervision, P.R. Validation, J.V. and P.R. Writing, original draft, J.V. Writing, review and editing, P.R. and A.P.

Funding: This work has been supported by the Ministry of Economy and Competitiveness of Spain, and by the European Regional Development Fund under the research project ENE2015-71417-R (MINECO/FEDER, UE).

Acknowledgments: The authors thank the anonymous referees for their valuable suggestions and comments, which have led to the present amended version of the original manuscript.

Conflicts of Interest: The authors declare no conflict of interest. The founding sponsors had no role in the design of the study; in the collection, analyses or interpretation of data; in the writing of the manuscript; nor in the decision to publish the results.

Abbreviations

The following abbreviations are used in this manuscript:

CFU	Coupling factor unit
EV	Electric vehicle
FHA	Fundamental harmonic approximation
IC	Integrated circuit
ICPT	Inductively-coupled power transfer
IGBT	Insulated-gate bipolar junction transistor
IPT	Inductive power transfer
PCB	Printed circuit board
PWM	Pulse-width modulation
RIPT	Resonant inductive power transfer
SOC	State of charge
SS	Series-series
THD	Total harmonic distortion
VSC	Voltage-source converter
WPT	Wireless power transfer

References

1. Bi, Z.; Kan, T.; Mi, C.C.; Zhang, Y.; Zhao, Z.; Keoleian, G.A. A review of wireless power transfer for electric vehicles: Prospects to enhance sustainable mobility. *Appl. Energy* **2016**, *179*, 413–425. doi:10.1016/j.apenergy.2016.07.003. [CrossRef]
2. He, X.; Shu, W.; Yu, B.; Ma, X. Wireless power transfer system for rotary parts telemetry of gas turbine engine. *Electronics* **2018**, *7*, 58:1–58:12. doi:10.3390/electronics7050058. [CrossRef]
3. Barman, S.D.; Reza, A.W.; Kumar, N.; Karim, M.E.; Munir, A.B. Wireless powering by magnetic resonant coupling: Recent trends in wireless power transfer system and its applications. *Renew. Sustain. Energy Rev.* **2015**, *51*, 1525–1552. doi:10.1016/j.rser.2015.07.031. [CrossRef]
4. Bosshard, R.; Kolar, J. Inductive power transfer for electric vehicle charging: technical challenges and tradeoffs. *IEEE Power Electron. Mag.* **2016**, *3*, 22–30. [CrossRef]
5. Gerssen-Gondelach, S.J.; Faaij, A.P.C. Performance of batteries for electric vehicles on short and longer term. *J. Power Sources* **2012**, *212*, 111–129. doi:10.1016/j.jpowsour.2012.03.085. [CrossRef]
6. Li, S.; Mi, C.C. Wireless power transfer for electric vehicle applications. *IEEE J. Emerg. Sel. Topics Power Electron.* **2015**, *3*, 4–17. doi:10.1109/JESTPE.2014.2319453. [CrossRef]
7. Miller, J.M.; Onar, O.C.; While, C.; Campbell, S.; Coomer, C.; Seiber, L.; Sepe, R.; Steyerl, A. Demonstrating dynamic wireless charging of an electric vehicle: the benefit of electrochemical smoothing. *IEEE Power Electron. Mag.* **2014**, *1*, 12–24. [CrossRef]
8. Kalwar, K.A.; Aamir, M.; Mekhilef, S. Inductively coupled power transfer (ICPT) for electric vehicle charging—A review. *Renew. Sustain. Energy Rev.* **2015**, *47*, 462–475. doi:10.1016/j.rser.2015.03.040. [CrossRef]
9. Wang, C.S.; Stileau, O.H.; Covic, G.A. Design considerations for a contactless electric vehicle battery charger. *IEEE Trans. Ind. Electron.* **2005**, *52*, 1308–1314. doi:10.1109/TIE.2005.855672. [CrossRef]
10. Sallán, J.; Villa, J.L.; Lombart, A.; Sanz, J.F. Optimal Design of ICPT Systems Applied to Electric Vehicle Battery Charge. *IEEE Trans. Ind. Electron.* **2009**, *56*, 2140–2149. doi:10.1109/TIE.2009.2015359. [CrossRef]
11. Bosshard, R.; Mühlethaler, J.; Kolar, J.W.; Stevanovic, I. Optimized magnetic design for inductive power transfer coils. In Proceedings of the 28th Annual IEEE Applied Power Electronics Conference and Exposition (APEC), Long Beach, CA, USA, 17–21 March 2013; pp. 1812–1819. doi:10.1109/APEC.2013.6520541. [CrossRef]

12. Musavi, F.; Eberle, W. Overview of wireless power transfer technologies for electric vehicle battery charging. *IET Power Electron.* **2014**, *7*, 60–66. doi:10.1049/iet-pel.2013.0047. [[CrossRef](#)]
13. Sohn, Y.H.; Choi, B.H.; Lee, E.S.; Lim, G.C.; Cho, G.H.; Rim, C.T. General unified analyses of two-capacitor inductive power transfer systems: Equivalence of current-source SS and SP compensations. *IEEE Trans. Power Electron.* **2015**, *30*, 6030–6045. doi:10.1109/TPEL.2015.2409734. [[CrossRef](#)]
14. Del Toro García, X.; Vázquez, J.; Roncero-Sánchez, P. Design, implementation issues and performance of an inductive power transfer system for electric vehicle chargers with series-series compensation. *IET Power Electron.* **2015**, *8*, 1920–1930. doi:10.1049/iet-pel.2014.0877. [[CrossRef](#)]
15. Liu, C.; Ge, S.; Guo, Y.; Li, H.; Cai, G. Double-LCL resonant compensation network for electric vehicles wireless power transfer: experimental study and analysis. *IET Power Electron.* **2016**, *9*, 2262–2270. doi:10.1049/iet-pel.2015.0186. [[CrossRef](#)]
16. Yao, Y.; Liu, X.; Wang, Y.; Xu, D. LC/CL compensation topology and efficiency-based optimisation method for wireless power transfer. *IET Power Electron.* **2018**, *11*, 1029–1037. doi:10.1049/iet-pel.2017.0875. [[CrossRef](#)]
17. Kalwar, K.A.; Mekhilef, S.; Seyedmahmoudian, M.; Horan, B. Coil design for high misalignment tolerant inductive power transfer system for EV charging. *Energies* **2016**, *9*, 937:1–937:13. doi:10.3390/en9110937. [[CrossRef](#)]
18. Li, Z.; Zhu, C.; Jiang, J.; Song, K. A 3-kW wireless power transfer system for sightseeing car supercapacitor charge. *IEEE Trans. Power Electron.* **2017**, *32*, 3301–3316. doi:10.1109/TPEL.2016.2584701. [[CrossRef](#)]
19. Bosshard, R.; Kolar, J.W.; Mühlethaler, J.; Stevanovic, I.; Wunsch, B.; Canales, F. Modeling and η - α -Pareto optimization of inductive power transfer coils for electric vehicles. *IEEE J. Emerg. Sel. Topics Power Electron.* **2015**, *3*, 50–64. doi:10.1109/JESTPE.2014.2311302. [[CrossRef](#)]
20. Buja, G.; Bertoluzzo, M.; Mude, K.N. Design and experimentation of WPT charger for electric city car. *IEEE Trans. Ind. Electron.* **2015**, *62*, 7436–7447. doi:10.1109/TIE.2015.2455524. [[CrossRef](#)]
21. Yang, Y.; Baghdadi, M.E.; Lan, Y.; Benomar, Y.; Van Mierlo, J.; Hegazy, O. Design methodology, modeling and comparative study of wireless power transfer systems for electric vehicles. *Energies* **2018**, *11*, 1716:1–1716:22. doi:10.3390/en11071716. [[CrossRef](#)]
22. Miskiewicz, R.M.; Moradewicz, A.J. Contactless power interface for plug-in electric vehicles in V2G systems. *Bull. Pol. Acad. Sci. Tech. Sci.* **2011**, *59*, 561–568. doi:10.2478/v10175-011-0069-z. [[CrossRef](#)]
23. Zimmer, M.; Heinrich, J.; Parspour, N. Design of a 3 kW primary power supply unit for inductive charging systems optimized for the compatibility to receiving units with 20 kW rated power. In Proceedings of the 4th International Electric Drives Production Conference (EDPC), Nuremberg, Germany, 30 September–1 October 2014; pp. 318–322. doi:10.1109/EDPC.2014.6984415. [[CrossRef](#)]
24. Duan, C.; Jiang, C.; Taylor, A.; Bai, K.H. Design of a zero-voltage-switching large-air-gap wireless charger with low electric stress for electric vehicles. *IET Power Electron.* **2013**, *6*, 1742–1750. doi:10.1049/iet-pel.2012.0615. [[CrossRef](#)]
25. Budhia, M.; Covic, G.A.; Boys, J.T. Design and optimization of circular magnetic structures for lumped inductive power transfer systems. *IEEE Trans. Power Electron.* **2011**, *26*, 3096–3108. doi:10.1109/TPEL.2011.2143730. [[CrossRef](#)]
26. SAE-J2954. *Wireless Power Transfer for Light-Duty Plug-In/Electric Vehicles and Alignment Methodology*; Standard; Society of Automotive Engineers: Warrendale, PA, USA, 2017.
27. González-González, J.M.; Triviño-Cabrera, A.; Aguado, J.A. Design and validation of a control algorithm for a SAE J2954-compliant wireless charger to guarantee the operational electrical constraints. *Energies* **2018**, *11*, 604:1–604:17. doi:10.3390/en11030604. [[CrossRef](#)]
28. Hart, D.W. *Power Electronics*, international ed.; McGraw-Hill: New York, NY, USA, 2011.
29. Yang, Y.; Zhong, W.; Kiratipongvoot, S.; Tan, S.C.; Hui, S. Dynamic improvement of series-series compensated wireless power transfer systems using discrete sliding mode control. *IEEE Trans. Power Electron.* **2018**, *33*, 6351–6360. doi:10.1109/TPEL.2017.2747139. [[CrossRef](#)]
30. Raju, S.; Wu, R.; Chan, M.; Yue, C.P. Modeling of mutual coupling between planar inductors in wireless power applications. *IEEE Trans. Power Electron.* **2014**, *29*, 481–490. doi:10.1109/TPEL.2013.2253334. [[CrossRef](#)]
31. Hesterman, B. Analysis and modeling of magnetic coupling. In Proceedings of the Denver Chapter of IEEE Power Electronics Society, Fort Collins, CO, USA, 10 April 2007.

32. Vázquez, J.; Roncero-Sánchez, P.; Parreño Torres, A. Coupling factor of a weak inductive coupling in a 2-kW power transfer system with a 125-mm air gap for electric vehicle chargers. In Proceedings of the IEEE 26th International Symposium on Industrial Electronics (ISIE), Edinburgh, UK, 19–21 June 2017; pp. 670–675. doi:10.1109/ISIE.2017.8001326. [CrossRef]
33. Rashid, M.H. *Power Electronics: Circuits, Devices and Applications*, 3rd ed.; Prentice-Hall: New Delhi, India, 2004.
34. Krein, P.T. *Elements of Power Electronics*, international 2nd ed.; Oxford University Press: New York, NY, USA, 2016.



© 2018 by the authors. Licensee MDPI, Basel, Switzerland. This article is an open access article distributed under the terms and conditions of the Creative Commons Attribution (CC BY) license (<http://creativecommons.org/licenses/by/4.0/>).

Correction

Correction: Vázquez, J. et al. Simulation Model of a 2-kW IPT Charger with Phase-Shift Control: Validation through the Tuning of the Coupling Factor. *Electronics* 2018, 7, 255

Javier Vázquez ^{1,*}, Pedro Roncero-Sánchez ¹ and Alfonso Parreño Torres ²

¹ Institute of Energy Research and Industrial Applications, University of Castilla-La Mancha, Campus Universitario S/N, 13071 Ciudad Real, Spain; Pedro.Roncero@uclm.es

² Institute of Industrial Development, Castilla-La Mancha Science and Technology Park, Paseo de la Innovación 1, 02006 Albacete, Spain; Alfonso.Parreno@pctclm.com

* Correspondence: Javier.Vazquez@uclm.es

Received: 28 November 2018; Accepted: 30 November 2018; Published: 3 December 2018

The authors wish to make the following correction to our published paper [1].

There is a misprint in Equation (3) of the published paper, which expresses the leakage inductance on the secondary side, denoted by L_{Sk} , in terms of the secondary self-inductance L_S , the mutual inductance M and the turns ratio r . The term r/M is incorrect and should be replaced with M/r .

In summary, on page 4, Equation (3) should be changed from

$$L_{Sk} = (1 - k) L_S = L_S - \frac{r}{M} \quad (1)$$

to the following correct version:

$$L_{Sk} = (1 - k) L_S = L_S - \frac{M}{r} \quad (2)$$

The authors would like to apologize for any inconvenience caused to the readers by these changes. The change does not affect the scientific results. The manuscript will be updated and the original will remain online on the article webpage, with a reference to this Correction.

References

1. Vázquez, J.; Roncero-Sánchez, P.; Torres, A.P. Simulation Model of a 2-kW IPT Charger with Phase-Shift Control: Validation through the Tuning of the Coupling Factor. *Electronics* **2018**, *7*, 255. [[CrossRef](#)]



© 2018 by the authors. Licensee MDPI, Basel, Switzerland. This article is an open access article distributed under the terms and conditions of the Creative Commons Attribution (CC BY) license (<http://creativecommons.org/licenses/by/4.0/>).

Review

Magnetically Coupled Resonance WPT: Review of Compensation Topologies, Resonator Structures with Misalignment, and EMI Diagnostics

Mohamad Abou Houran, Xu Yang and Wenjie Chen *

School of Electrical Engineering, Xi'an Jiaotong University, Xi'an 710049, China; eng.horan@yahoo.com (M.A.H.); yangxu@xjtu.edu.cn (X.Y.)

* Correspondence: cwj@xjtu.edu.cn; Tel.: +86-29-82665223

Received: 11 September 2018; Accepted: 22 October 2018; Published: 2 November 2018

Abstract: Magnetically coupled resonance wireless power transfer systems (MCR WPT) have been developed in recent years. There are several key benefits of such systems, including dispensing with power cords, being able to charge multiple devices simultaneously, and having a wide power range. Hence, WPT systems have been used to supply the power for many applications, such as electric vehicles (EVs), implantable medical devices (IMDs), consumer electronics, etc. The literature has reported numerous topologies, many structures with misalignment effects, and various standards related to WPT systems; they are usually confusing and difficult to follow. To provide a clearer picture, this paper aims to provide comprehensive classifications for the recent contributions to the current state of MCR WPT. This paper sets a benchmark in order to provide a deep comparison between different WPT systems according to different criteria: (1) compensation topologies; (2) resonator structures with misalignment effects; and, (3) electromagnetic field (EMF) diagnostics and electromagnetic field interference (EMI), including the WPT-related standards and EMI and EMF reduction methods. Finally, WPT systems are arranged according to the application type. In addition, a WPT case study is proposed, an algorithm design is given, and experiments are conducted to validate the results obtained by simulations.

Keywords: compensation topology; electromagnetic field (EMF); electromagnetic field interference (EMI); misalignment; resonator structure; wireless power transfer (WPT); WPT standards

1. Introduction

Wireless power transfer (WPT) is a promising technology due to its advantages of being cordless, safe during charging, and its ability to operate in a wet and harsh environment [1]. It has gained global acceptance, and is used to supply the power for many applications in several fields, such as electric vehicles (EVs) [2–14], online electric vehicles (OLEVs) [15–17], plug-in hybrid electric vehicle (PHEVs) [18], superconducting magnetic levitation trains (maglev) [19], implantable medical devices (IMDs) [20–31], and consumer electronics [32–34]. In addition, it has been used in the charging systems of autonomous underwater vehicles (AUVs) [35], the rotary of a gas turbine [36], and Internet of Things (IoT) applications [37–39].

According to the energy transfer mechanism, the WPT technology can be divided into two categories. The first is far-field wireless transmission, which is also called electromagnetic radiation WPT. It includes microwave power transfer (MPT) [40–42], laser power transfer (LPT) [43–45], and solar power satellites (SPS) [46,47].

The second is near-field WPT (Figure 1), which can, in turn, be classified into two groups. Firstly, there is inductive power transfer, including the inductive coupled power transfer (ICPT or IPT), and magnetically coupled resonance wireless power transfer (MCR WPT); as shown in Figure 1a, T_x is

the transmitting coil and R_x is the receiving coil. Secondly, there is capacitive power transfer (CPT), as displayed in Figure 1b. Some IPT systems have presented high power transmission efficiency (PTE) of larger than 90% for transmission distances of several centimeters; however, for longer distances, efficiency will drop significantly [48–63]. Nevertheless, authors have presented an innovative IPT system to transfer power a distance of 5 m using dipole coils [64]. Most of the presented CPT systems are designed for low-power applications, including USB devices, lamps, and small robots [8,65–73], where the transmitting distance is limited to the millimeter range. High efficiency is provided by MCR WPT for a longer transferring distance [23,34,74–82].

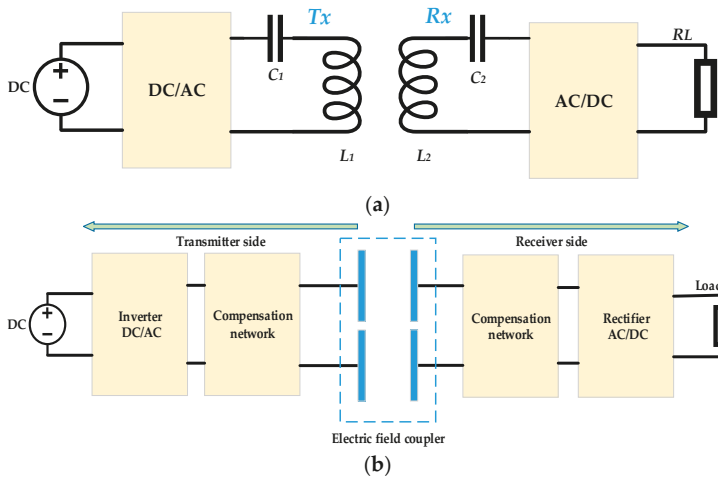


Figure 1. Near-field wireless power transfer (WPT): (a) Structure of inductive power transfer (IPT)/magnetically coupled wireless power transfer (MCR WPT); (b) Structure of capacitive power transfer (CPT).

Due to its importance and rapid development, WPT has been widely used over the last few years, offering a practical technique to transfer power wirelessly in many applications on a commercial scale. Many studies have been conducted in this area, and the literature has reported much research related to several aspects of MCR WPT, which is usually confusing and difficult to follow. To give a clear picture, this paper aims to review the recent contributions to the current state of MCR WPT systems. This paper sets a benchmark in order to provide comprehensive classifications with a deep comparison between different WPT systems according to different criteria. They are as follows:

1. Compensation topologies: Basic and hybrid compensation topologies are reported, and some commonly used topologies are compared based on application type.
2. Research work related to the resonator structure is discussed as follows:
 - Coil geometry is discussed in detail, including many resonator shapes, such as planar coils, three-dimensional (3D) structures, cavity structures, and coils with cores, etc., which are compared based on set criteria.
 - The differences between single-phase WPT and three-phase WPT systems are highlighted, and some three-phase WPT projects are reported.
 - Multi-coil systems, which are capable of charging multiple devices simultaneously, such as LEDs, are addressed.
 - Operating frequency effects on the design of coil structure.
 - Inductance of several resonator structures.

- Misalignment study: Several misalignment types are displayed and compared based on their resonator structure and effects, in addition to their advantages and disadvantages.
3. Electromagnetic field interference (EMI) diagnostics, including WPT-related standards and guidelines. In addition, EMI and EMF reduction methods are reported and compared. Moreover, advantages and disadvantages of these methods are addressed.
 4. Basic applications of WPT systems are given. Next, a WPT case study is proposed. In the proposed winding method, a bio-inspired joint made of two spherical structures is given. The algorithm design is provided, and experiments are conducted to validate the obtained results by simulation and optimization.

The paper is organized as follows. In Section 2, a benchmark is set to present the major categorizations of the WPT system. Section 3 discusses compensation topologies in detail. Section 4 classifies and reviews many resonator structures in detail. The misalignment study is presented in Section 5. WPT-related standards, electromagnetic field (EMF) mitigation methods, and EMI mitigation methods are given in Section 6. In Section 7, WPT applications are illustrated, an optimized design of a WPT system is given, and a case study is proposed and discussed. Finally, the conclusion and further areas for research are provided in Section 8.

2. Benchmark of the Research Work

In this paper, a benchmark is proposed (Figure 2) that provides various categorizations of research works related to WPT. The benchmark classifies major research areas relating to WPT, which include compensation topology, resonator structure, misalignment study, EMI and EMF diagnostics, frequency-splitting issue, impedance matching, control strategy, and WPT optimization. In this paper, a number of these issues related to WPT systems are discussed in detail. Other issues, such as impedance matching (which will be discussed in brief in Section 3) and control methods [83,84], will not be discussed for the sake of brevity.

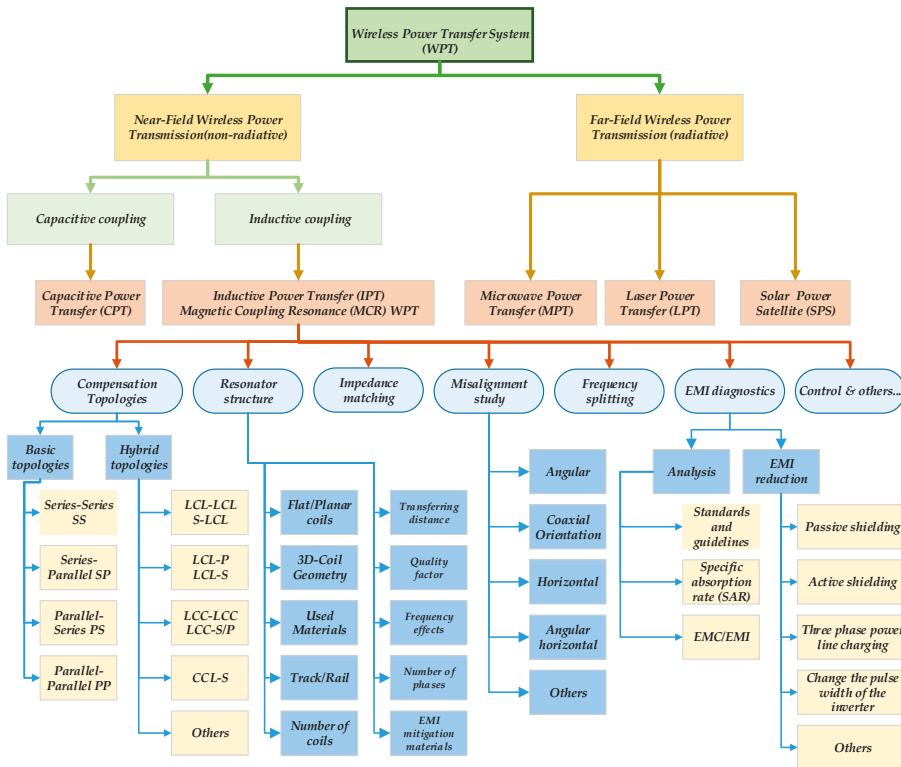


Figure 2. WPT classifications and major research areas.

3. Compensation Topologies

There are some requirements for compensation, which are as follows. (1) The compensation capacitor resonates with the primary and/or secondary inductance in order to provide reactive power, which is required for the inductances to generate an adequate magnetic field. Therefore, the basic function for the compensation of a primary coil is to minimize the volt-ampere (VA) rating of the power supply. In the secondary coil, compensation cancels the inductance to maximize the power transfer capability [85]. (2) Constant-voltage/constant-current output (CVO/CCO). (3) The maximum efficiency of a WPT system can be determined by two parameters, the coupling coefficient and quality factor [54]. (4) Bifurcation resistance, which refers to a condition where the frequency realizes a zero phase angle (ZPA) [57,85].

3.1. Basic and Hybrid Compensation Topologies

Figure 3 shows the classifications of the compensation topology. They include two groups. The first is of the four basic topologies, and the second comprises hybrid topologies, which are combinations of series and parallel topologies.

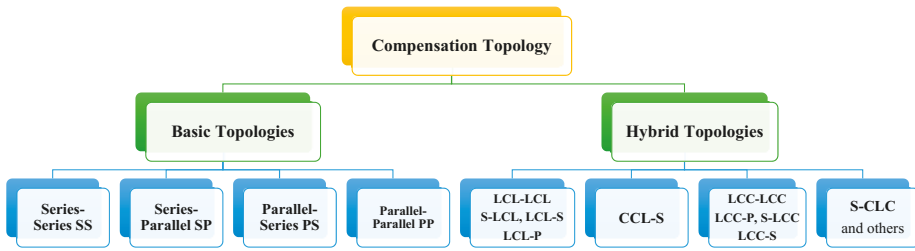


Figure 3. Classifications of the compensation topology.

Many compensation topologies have been reported. As illustrated in Figure 4, there are four basic compensation topologies: series-series (SS) [3,86–90], series-parallel (SP) [91], parallel-series (PS) [1], and parallel-parallel (PP) [92]. In Figure 4, k is the coupling coefficient, M is the mutual inductance, U_g is the input voltage on the primary side, U_2 is the load voltage, and R_L is the load. L_1, L_2, C_1 , and C_2 are the self-inductances and external compensation capacitors of the primary and secondary coils, respectively. R_1 and R_2 are the resistances of the primary and secondary coils, respectively. On the other hand, hybrid compensation topologies are investigated, such as LCC-P and LCL-P are reported in [93], where LCC and LCL are on the transmitting side, and parallel (P) is on the receiving side. Moreover, S-CLC [94], CCL-S [95], LCL-S [96], and LCC-LCC [18,97–99] are discussed. Double-sided LCC-compensated WPT (multi-LCC on the transmitter side) is presented in [100], and LCL-LCL is given in [101]. Some commonly used hybrid topologies in the research work are displayed in Figure 5. L_p and L_s are the primary and secondary inductances, respectively.

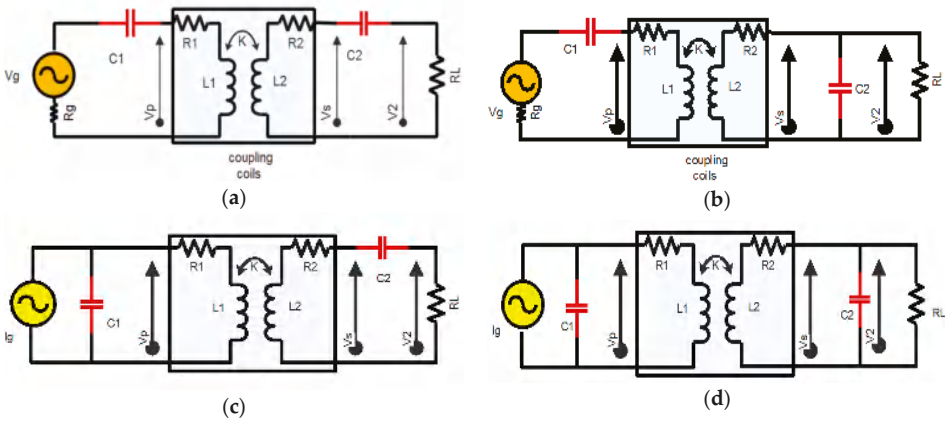


Figure 4. The basic topologies: (a) Series-Series (SS); (b) Series-Parallel (SP); (c) Parallel-Series (PS); (d) Parallel-Parallel (PP).

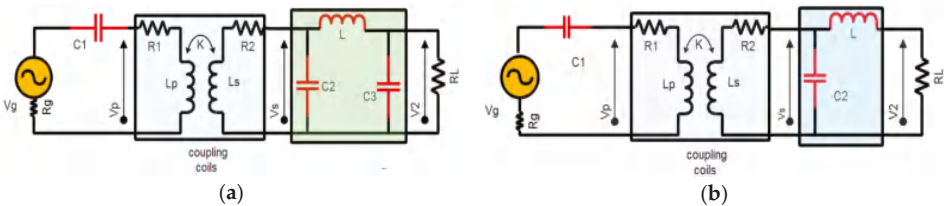


Figure 5. Cont.

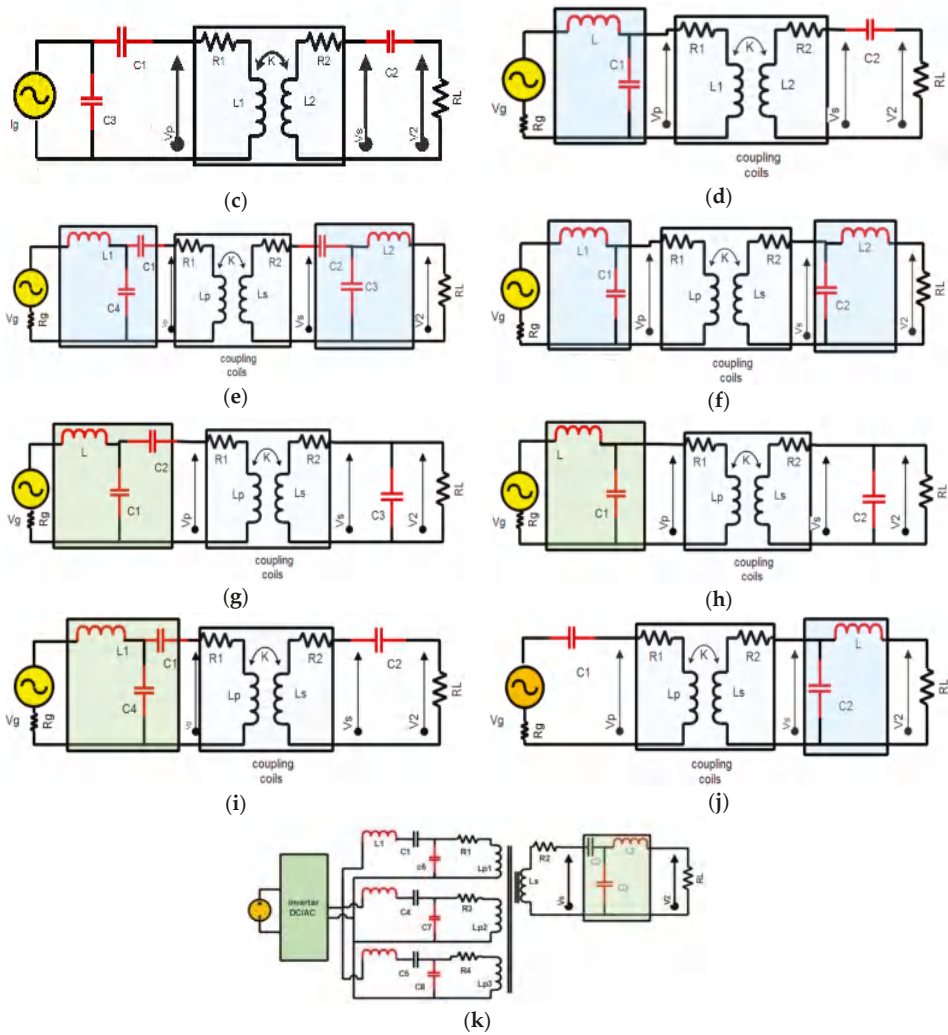


Figure 5. Hybrid compensation topologies: (a) S-CLC; (b) S-LCL; (c) CCL-S; (d) LCL-S; (e) LCC-LCC; (f) LCL-LCL; (g) LCC-P; (h) LCL-P; (i) LCC-S; (j) S-LCL; (k) Double-Sided LCC.

3.2. Review of Different WPT Systems Based on Topology and Application Type

Table 1 gives a comparison between different WPT systems based on the compensation topologies and application type (electric vehicles). The systems are easily compared considering some criteria, such as transferred power, frequency, resonators' dimensions, and transferring distance. In this table, f_0 is the resonant frequency, k is the coupling coefficient, and R_L is the load value. In addition, N_1 and N_2 are the number of turns for primary coils and secondary coils, respectively. D_1 and D_2 are the length (or diameter) and width (or diameter) of the transmitter and receiver coils, respectively. Finally, P_{out} is the output power and V_{out} is the output voltage. Table 2 reviews the WPT systems that are used in dynamic charging for EVs application.

Table 1. Review of different WPT systems based on topology and application type (such as electric vehicles, or EVs). EMI: electromagnetic field interference.

Reference and Topology	$f_0/k/R_L$ (kHz, Ω)	P_{out} , V_{out}	Efficiency	Resonators			Note
				D_1 mm Length, Diameter mm	D_2 mm width, Diameter mm	Gap mm	
[14] SS/LCC-LCC	$f_0 = 85$ $k = 0.135$ $R_L = 2, 3, 5$	1 kW 50 V	95% for SS, and 93% for LCC	500 diameter	400 diameter	200	Based on EMI, LCC-LCC topology is considered more robust to EMI exposure.
[89] SS/LCC-LCC	$f_0 = 79$	7.7 kW max. 270–405 V	For LCC: 96%	800	600	200	The LCC-LCC topology has higher efficiency when the mutual inductance is at minimum.
[101] SS/LCL-LCL	$f_0 = 85$ $k = 0.1$ $R_L = 10$	3.3 kW	93.1% for SS, 89.5% for LCC	20 × 3 layers 17 × 2 layers	240 × 240 mm ²	100	Compared to SS topology, the LCL-LCL type has a high power factor.
[98] LCC-LCC	$f_0 = 79$ $k = 0.18-0.32$ $R_L = 10-200$	7.5 kW 450 V	96%	800	600	200	Resonant frequency f_0 is independent of the coupling coefficient and load conditions.
[99] LCC-LCC	$f_0 = 95$ $k = 0.14-0.30$	5.6 kW 300–450 V	95.36%	600 200	600 200	150	The extra integration-induced couplings give more space for magnetic cores.
[87] LCC-LCC	$f_0 = 85$ $k = 0.153$ $R_L = 49.95$	3.3 kW 405.7 V	92.6%	600	300	150	Energy storage has no relation to topology type, but only with transferred power level and coupling coefficient.
[97] LCC-LCC	$f_0 = 85$ $k = 0.1877$	3 kW 300 V	95.5%	600 × 450 × 4 mm ³ 640 × 496 × 8 mm ³ 711.2 × 558.8 × 2 mm ³	400 × 300 × 4 mm ³ 480 × 352 × 8 mm ³ 508 × 406 × 2 mm ³	150	The compensated resonator design helps to eliminate or reduce the extra-coupling effects to a tiny level.

Table 2. Review of WPT systems that are used in dynamic charging for EVs and plug-in hybrid electric vehicles (PHEVs).

Reference and Topology	$f_0/k/R_L$ (kHz, Ω)	P_{out}, V_{out}	Efficiency	Coils' Dimensions and Number of Turns	Gap mm	Note
[96] LCL-S LCC-S	$f_0 = 140$ $k = 0.18-0.32$	Nominal power: 1 kW 80-90 V	Similar: LCC and LCL: 93%	Coil radius is 163 mm	100	The topology gives more robust power transfer character against the variation of k .
[100] Double-sided LCC	$f_0 = 85$ $k = 0.13$	1.4 kW 150 V	89.78%	9 turns for each transmitter, Tx coil $6 \times (388 \text{ mm} \times 400 \text{ mm})$, and for Rx: $485 \text{ mm} \times 400 \text{ mm}$	150	This paper presented a continuous dynamic WPT system, which reduces the power pulsations.
[102] LCL	$f_0 = 85$ $k = 3.7-5.4\%$	5 kW	-	The secondary: $0.35 \text{ m} \times 0.7 \text{ m}$ N87 ferrite material (each $93 \text{ mm} \times 28 \text{ mm} \times 16 \text{ mm}$). Transmitter dimensions are $10 \text{ cm} \times 75 \text{ cm}$, number of turns: nine Receiver: $25 \text{ cm} \times 20 \text{ cm}$, number of turns: 12.	240	The system is designed to supply power along the whole length of the track by activating only one primary pad.
[103] SS	$f_0 = 85$ $k = 0.4$	20 kW	80%		100	Downscale prototype operating at 85 kHz ± 2.5 kHz.
[104] SP	$f_0 = 23$ $R_L = 2$	2 kW	-	Coils diameter: 330 mm. Turns: seven turns for transmitter coil and five turns for receiver coil.	100	This paper presented technical aspects of in-motion WPTs for charging EVs and PHEVs.
[105] SS	$f_0 = 85$	-	97.6% pads length ratio is 1:1	Coil external width: 58 mm Coil inner width 38 Wire diameter 5 mm Number of turns: 8 turns.	200	Investigated the pad shape: influence of the variation of the ratio between Tx and Rx lengths with respect to the behavior of the coupling.

In PS-compensated WPT, the reactive current of the current-fed resonating converter circulates inside the parallel resonant tank without going through the switching system. Therefore, the current rating of the switching devices is reduced, and the conduction loss is reduced for a given power level. This topology has a high voltage stress on the inverter switches, especially for high power loads, and it becomes worse when the coupling coefficient is low. CCL-S is an example of hybrid topologies; as shown in Figure 5c, it has an extra series capacitor on the primary side, which leads to a lower switching loss compared to the parallel LC-S. Parallel LC-compensated WPT is preferred for low voltage gain applications. However, for higher voltage gain, CCL is preferred. S-CLC topology, which is shown in Figure 5a, provides an easier achievement of ZPA. In Figure 5k, the double-sided LCC-compensated topology was illustrated, and a continuous dynamic WPT charging system was introduced.

The output current and output voltage of SS, S-LCL, S-CLC, and SP compensation topologies are inversely proportional to the mutual inductance, and the output power is inversely proportional to the square of the mutual inductance. Regarding double-sided LCL, as well as double-sided LCC, LCL-S, LCL-P, PS, and PP compensation topologies, the output current and output voltage are proportional to the mutual inductance, and the output power is proportional to the square of the mutual inductance. Based on that, the design method of these topologies can be determined. Consider two cases. The first is an SS-compensated WPT system, which is designed to transfer a nominal power at the maximum mutual inductance, and means perfectly aligned coils. At the maximum mutual inductance, the input voltage and efficiency of the SS topology will be higher, and the current will be lower. The second is an LCC-compensated WPT system, which is designed at the minimum mutual inductance, and means a maximum misalignment between resonators.

Finally, at high-frequency circuits, there arises an impedance matching problem, where the circuit components gain a non-resistive aspect. To achieve maximum power transfer efficiency, the circuit must be impedance matched to minimize these effects [106,107]. Some impedance-matching methods were proposed, such as employing the impedance inverter only at the receiver side [108], and using a dual-band resistance compression network (RCN) as a matching network [109].

4. The Resonator Structure

Figure 6 shows the research work related to the resonator structure (geometry) including several categories, such as planar coil, 3D structures, tracks/rail, coils with cores, and the type of used materials, etc. In addition, the suitable application type for each structure is given, and the frequency ranges for some of these geometries are provided.

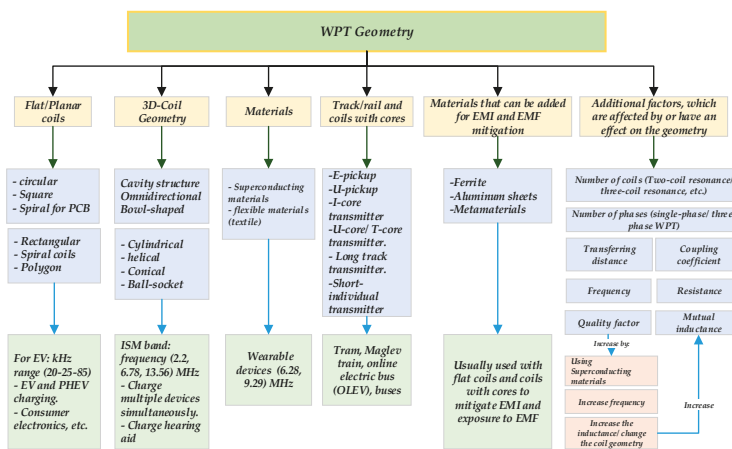


Figure 6. Classifications of resonator structure.

4.1. Shape of the Resonator

Different studies have been investigated based on the shape of resonators. They are classified as follows:

- Flat/planar-shaped coils, such as rectangular-shaped structure [89,98,110,111], octagonal resonator [101], and a double D coil (DD) [112]. In addition, defected ground structure (DGS) is presented in [113,114]. DGS means a “defect” has been integrated on the ground plane of a microwave planar circuit; this DGS technique is adopted to improve various parameters of a microwave circuit, such as low gain and narrow bandwidth [115]. Moreover, circular coils [116,117] and square coils [99,118,119] are discussed. There are planar printed spiral coils (PSC) [120–123] as well, the WPT system in the printed circuit board (PCB) [124–127], pancake coils [128], and planar shielded-loop resonators [129].
- Three-dimensional (3D) geometries are investigated, such as for instance, bowl-shaped transmitter coils [28], which are used for charging hearing aids, cylindrical coils [80], helix loop resonators [130–133], and conical coils [134]. In [135,136], the three-dimensional resonant cavity is presented, which offers a good way of charging multiple devices simultaneously. An orthogonal winding is discussed in [137], and a cylindrical cavity is given in [138]. In [139–142], the authors proposed an omnidirectional WPT system, and in [143], the authors discussed a ball joint structure.
- Coils’ materials are discussed, for example, a receiver coil made of aluminum is used in [125]. In [144], the authors proposed a helical-type coil made of superconductors in order to increase the quality factor of the coils. In [145], the authors applied an MCR WPT system (planar textile resonators, or PTRs) to wearable consumer electronics by using flexible materials.
- Coils with cores are given, such as dipole-type coils [64], which presented a WPT prototype that is capable of transferring the power up to a 5-m distance. For charging vehicles, buses, trams, and trains, long-track transmitter and short-individual tracks are used [16,17,90]. Moreover, E-core and U-core types are discussed [94,146].

Other structures were presented, for example, multiple-input multiple-output structures (MIMO) [147,148], a wirelessly powered cage system [149], transparent electrode resonators [150], domino-resonator systems [151–153], and dual-layer nested structures [154]. Moreover, the three-phase system [16,35,155] found its way to the wireless charging technology through some real applications. Finally, an L-shape transmitter was discussed in [156].

Most of the resonators are coreless, which means no iron losses (hysteresis loss, eddy current). However, the quality factor, and thus the efficiency, will be low. To overcome this problem, there are three options. The first is increasing the mutual inductance by changing the geometry or increasing the number of turns and adding ferrites. However, in some cases, ferrite cannot be added due to cost and space limitations. The second is increasing the frequency, but it could be limited by the switching speed of the semiconductors, and it might cause more switching losses. The third is using multi-transmitter WPT systems, but resonant inverters with different power rates are required.

Table 3 presents projects related to the defected ground structure (DGS). The defected ground structure (DGS) can operate at high frequencies, for example, the spiral-strips DGS operates at 50 MHz, which provides a high-quality factor and introduces a structure that mitigates the problem of a low self-inductance that is given by H-shaped DGS. Compared to H-shaped DGS, the semi-H-shaped DGS shows a better efficiency and greater transferring distance even if they have the same size. In Table 4, the three-dimensional resonant structures are reported and compared. Cylindrical, helical, and cavity structures are used to provide power for some applications, such as hearing aids, LEDs, and toys.

Table 5 displays studies related to flat structure, in which the power transferring distance is almost twice the radius/width of the coil, and the power range is within several watts to several dozen watts of power. Table 6 gives two cases of WPT systems using coils with cores. Several core types are used, especially in EV charging applications. Table 7 reports research works on domino resonator systems for low-power applications.

Table 3. Research works related to defected ground structure (DGS).

WPT System	Resonator Structure	Resonator Parameters					Efficiency	Note
		Size of the Coils/Number of the Coils	N_1/N_2 Ratio	D_1 mm	D_2 mm	Gap mm		
[113]	H-shaped DGS Semi-H-shaped DCS	Symmetrical, two-coil resonance structure	1	20 21	20 21	13 25	300 kHz/ $k = 0.025$	68%/73% Semi H-shaped DGS resonator is more robust to the coaxial orientation misalignment.
[114]	Spiral-strips DCS	Symmetrical Asymmetrical	1	50 × 50 mm ² 50 × 50 mm ²	50 × 50 mm ² 50 × 30 mm ²	50 40	50 MHz	84%/78% Spiral-strips DGS provides a better quality factor other than H-shaped or semi-H-shaped DGS.

Table 4. Research work related to three-dimensional (3D) structure.

WPT System	Resonator Structure	Size of the Coils/Number of Coils	Resonators		Gap	$f_0, R_x, P_{out}, V_{out}$, Efficiency %	Note
			Coils' Dimensions and Number of Turns	Coils' Dimensions and Number of Turns			
[80]	Structures: cylindrical for Tx, Rx1, and planar rectangular for Rx2.	Asymmetrical/four-coil resonator structure	The diameter of Tx is 350 mm, the thickness is 0.35 mm, and the coil width is 29 mm besides a one-turn driving coil. The radius of Rx1 is 80 mm, the height is 50 mm, besides a seven-turn coil that was used as the output coil. The area of Rx2 is 20.5 × 20 mm ² , and the thickness is 0.35 mm.	The diameter of Tx is 350 mm, the thickness is 0.35 mm, and the coil width is 29 mm besides a one-turn driving coil. The radius of Rx1 is 80 mm, the height is 50 mm, besides a seven-turn coil that was used as the output coil. The area of Rx2 is 20.5 × 20 mm ² , and the thickness is 0.35 mm.	150 mm Tx1 200 mm Tx2	7 MHz LED loads 80%	Tx is simply printed on the internal or external cover, or inserted in the clothes.
[132]	Helical coils	Symmetrical/three-resonator structure	The radius is 0.325 m, the pitch is 0.05 m, and the number of turns is N = 5, d12 = 6 m	The radius is 0.325 m, the pitch is 0.05 m, and the number of turns is N = 5, d12 = 6 m	2–4 m	10 MHz 90%	Compared with a single-transmitter WPT system, a higher power transfer efficiency (PTE) was achieved stably for the angular aligned and the angular misaligned.
[29]	3D structure/Bowl-shaj transmitter coil and spiral helical receiver coils	Asymmetrical/three resonator structure	The Tx bowl-shaped, which is a combination of both a spiral coil (s) and a conical-shaped coil (c) with a big diameter of 58 mm, a thickness of 9.1 mm, and turns: N5 = N6 = 7 turns. The volume of the receiver coils Rx (spiral sl + helical h) is 10.5 × 6.5 × 2.46 mm ³ with Ns1 = Nt1 = 8 turns	The Tx bowl-shaped, which is a combination of both a spiral coil (s) and a conical-shaped coil (c) with a big diameter of 58 mm, a thickness of 9.1 mm, and turns: N5 = N6 = 7 turns. The volume of the receiver coils Rx (spiral sl + helical h) is 10.5 × 6.5 × 2.46 mm ³ with Ns1 = Nt1 = 8 turns	Within 3D cavity	6.78 MHz 2.5 to 4.3 V 60%	The proposed system can uniformly charge a pouch-type LIB of a hearing aid in spite of its position or arrangement.
[131]	3D structure/Helical coils	Symmetrical/system with Relay resonator	Symmetrical relay resonator with multi load transfer and number of turns is 12	Symmetrical relay resonator with multi load transfer and number of turns is 12	-	193 MHz/0.1–2.0 Ω Several dozen watts of power, 30–40%	The WPT system transfers the same power to multiple loads over a range of distances.
[136]	The Tx is a cavity resonator and the Rx is a square coil	Asymmetrical/mult structure	The dimensions of the cavity resonator are a = 1.52 m, b = 1.42 m, and d = 1.83 m. Rx square coil has one turn 7.62 cm. (multi receivers)	The dimensions of the cavity resonator are a = 1.52 m, b = 1.42 m, and d = 1.83 m. Rx square coil has one turn 7.62 cm. (multi receivers)	91 cm	191.65 MHz 50-Ω 8-W LED 50%	The system is able to deliver power to many devices simultaneously, such as LEDs and toys in a box.
[138]	3D structure/Cylindrica cavity resonator	Asymmetrical/two-structure	The radius of the Tx coil is 30 cm, and the height is 25.4 cm; the volume of the cavity is 0.072 m ³ . The radius of Rx is 2.5 mm, and the volume of the receiver coil is 13.75 mm ³ .	The radius of the Tx coil is 30 cm, and the height is 25.4 cm; the volume of the cavity is 0.072 m ³ . The radius of Rx is 2.5 mm, and the volume of the receiver coil is 13.75 mm ³ .	10 cm	375.32 MHz 50 Ω 33%	PTE of the optimal impedance-matching (IM) system can achieve 33.88%, which is four times the 7.68% that can be achieved without an optimal IM system.

Table 5. Research work related to flat structures for low-power applications.

WPT System	Resonator Parameters				$f_0/k/R_L$	P_{out} , Efficiency %	Note
	Resonator Structure	Coils/Number of the Coils	Coils' Dimensions and Number of Turns	Gap			
[116]	Flat structure/Circular coils (44-mm inner diameter)	Symmetrical/three resonance structure	Two 76-mm diameter circular coils and a source coil with 36-mm diameter.	62 mm	684 kHz 20 Ω	12.9 W 43% At 40 mm	The maximum efficiency of the three-coil system shows a significant advantage over that of the two-coil system.
[117]	Flat structure/Circular spiral coils	Asymmetrical/foi resonance structure	Six turns for each coil. Outer diameter for Tx is 590 mm; for Rx, it is 280 mm, and the drive loop diameter is 280 mm	700 m	7.65 MHz $k = 0.1376$	12 W Laptop 50%	Presented a WPT that maximizes the quality factor of the coils; by proper loading of the drive and load loops, efficiency will be better.
[122]	Double-layer printed spiral coil PSC (square spiral coil)	Symmetrical/four resonance structure	Double-layered for each layer: 3.875 turns. Width: 288 mm, Substrate: 300 mm \times 300 mm	500 mm	4.03 MHz	150 W 50%	The printed spiral coil (PSC) has high precision, high stability, easy to design, and manufacture.

Table 6. Research work related to coil with cores structure.

WPT System	Resonators				$f_0/k/R_L$	P_{out} , V_{out} , Efficiency %	Note
	Resonator Structure	Size of the Coils/Number of Coils	Coils' Dimensions and Number of Turns	Gap			
[64]	Coil with a core/Dipoles with cores	Symmetrical/two-coil resonance structure	Number of turns for Rx: 22. Number of turns for Tx: 86. The length of the core is 3 m, and the length of the coil is 1 m.	3 m 4 m 5 m	20 kHz $k: (0.68\%, 0.39\%, 0.26\%)$ 40 Ω	1403 W 29% 471 W 16% 209 W 8%	Coils with ferrite cores will minimize parasitic effects. The optimum-stepped core structure can reduce the core loss.
[146]	Coil with a core/Resonator with EE, UU core-type	Asymmetrical/multi-coil structure	Power line modules in addition to UU, EE cores. Pick up coils for EE: five coils total, center: 64 turns, left and right: 28 turns each.	26 cm	20 kHz	100 kW 620 V 80%	The implementation cost of the power receiver unit/kW was about \$89/kW.

Table 7. Domino resonator systems.

WPT System	Resonator parameters			Note	
	Resonator Structure	Coils' Dimensions and Number of Turns	f_0/R_L		
[151,152]	Symmetrical/circular coils/domino structure/	The WPT has eight resonators, which have a radius of path r of 300/235 mm for three-resonator and four-resonator systems, respectively. The number of turns is 11.	520 kHz (11.57 ~16.94) Ω	14 W, 70.68–83%	The optimized operating frequency of this system is not the resonant frequency of the resonators.

The circular, spiral circular, square, and rectangular geometries are widely used due to their simple design and low manufacturing cost. To give a clearer picture of the circular and rectangular coils, new classifications (concluded from the above-mentioned tables) are presented in Tables 8 and 9, respectively. Comparing the size of the coils, the transferring distance, and the operating frequency, the systems will show approximate results.

Table 8. Research work on circular structures.

Case	1	2	3	4	6
A/S/iC	A/2C	S/2C	S/2C	A/2C	S/2C
Topology	SS	LCL-S LCC-S	SP	LCC-LCC	SS
Size D_1/D_2 mm	500/400	226/226	500/500	600/300	220/220
Gap mm	200	100	200	150	240
Frequency	85 kHz	140 kHz	20 kHz	85 kHz	200 kHz
Efficiency	95%	93%	93%	92.6%	85%

Note: A: asymmetrical system; S: symmetrical system; C: coil; i: number of coils.

Table 9. Research work on rectangular structures.

Case	1	2	4
A/S	S	A	S
Topology	LCC-LCC	LCC-LCC	S-SP
Size mm ²	800 × 600	600 × 450 400 × 300	500 × 600
Gap mm	200	150	100
Frequency kHz	79	85	40
Efficiency	96%	95.5%	95.2%

In EV charging application and due to space limitations, some structures, such as the helix, omnidirectional, cavity, or conical, cannot be used. However, the resonators are designed as spiral or planar coils. These geometries are printable and easy to implement at a low cost. Moreover, the dynamic charging systems are used, and according to the track length, they can be divided into two categories. The first is the long-track transmitter, which can charge multiple vehicles simultaneously. This system is simple and has a low number of components. The online electric vehicle (OLEV) with a maximum charging power up to 100 kW is one example. However, this design has a low efficiency of 74%. The second is the short-individual transmitter, where the length of the transmitter is usually within 1 m. In this system, each transmitter has a compensation circuit. Therefore, multiple short transmitters are arranged in an array to make a tracking lane, and the transmitters can be excited based on the location of the receiver. This structure is considered flexible, but requires a large number of circuit components and converters.

There are other architectures used in EVs; for example, in [104], the Oak Ridge National Laboratory (ORNL) presented an in-motion charging system for EVs/PHEVs, which transfers the power to a moving receiver coil as it passes over two transmitting coils connected in series. In this system, the coil design depends on jacketed Litz cable coils over a structure of soft ferrite. The Research Centre for Energy Resources and Consumption (CIRCE) in Spain proposed a receiver, which is longer than the transmitter [157]. In [105], the influence of the difference of the ratio between the receiver length and the transmitter length is investigated. The structure is a couple of unipolar square-shaped pads made of a copper coil, and a metallic plate, which represents the floor of the vehicle chassis, was placed 25 cm above the transmitter. In [158], the authors presented an overview of the current studies related to automotive applications, such as Korea Advanced Institute of Science and Technology (KAIST) projects on an OLEV bus, HalolPT, which developed IPT solutions in a power range of 3.3–20 kW, and WiTricity (MIT), which proposed a 3.3-kW system that has been proven. In addition, Plugless Power is a 3.3-kW IPT stationary charger, which was developed by Evatran and Bosch.

Based on the number of phases, WPT systems can be divided into two sections: single-phase systems and three-phase systems. The three-phase WPT systems that operate at symmetrical conditions and similar phase currents have two essential benefits compared to the single-phase systems: they have higher power level and better far-field EMC performance due to the three magnetic fields' superposition. In addition, they have very small power ripples on the DC output [159]. The three-phase WPT system found its way to some practical applications, for example, in [16], authors proposed a three-phase WPT system, which has six overlaid power lines and ended in two Y-points; each power line is symmetrical from its center, as a result, it can reduce the leakage magnetic field. In [35], the authors proposed a three-phase WPT, which can be used in recharging AUVs. A continuous charging system without onboard batteries was proposed [49]. In this system, charging the batteries along roadways is not required. Therefore, there was no need for complicated pickup structures. For heavy-duty applications, a tuning approach for the three-phase WPT with a long track is presented [160]. There are some high power three-phase WPT systems in operation, such as the Brunswick and Berlin buses with a maximum power of 200 kW based on Bombardier PRIMOVE technology.

4.2. Size and Number of the Resonators

Comparing the transmitter and receiver coils according to their size, they can be either symmetrical or asymmetrical. The first one is the symmetrical coils, where the transmitter and the receiver coils have the same size [94,110,117]. However, in the asymmetrical coils, the transmitter and receiver coils have a different size [80,118,136]. WPT systems can be categorized according to the number of coils, as shown in Figure 7, where they can be classified as follows: two-coil structure (2C) [64,113], three-coil structure (3C) [116,132], four-coil structure (4C) [119,122], and multi-coil structure (MC) [136,151,152]. The strongly coupled magnetic resonance (SCMR), which is a 4C system, is classified into four systems [161]: a standard SCMR system, a conformal SCMR (CSCMR system), a 3D SCMR, and a hybrid SCMR (HSCMR). Generally, the two-coil system saves more space than the other systems. However, the three-coil or four-coil systems allow transferring higher power for a longer distance.

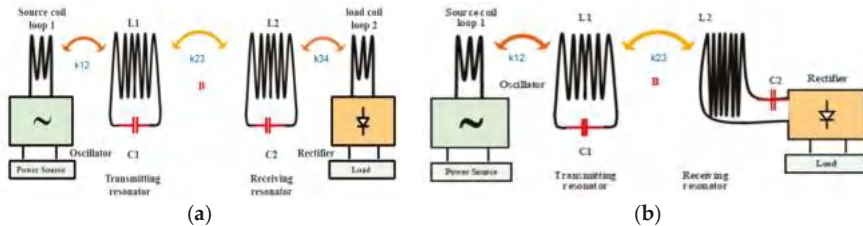


Figure 7. MCR WPT structure based on the number of the coils: (a) Four-coil MCR WPT; (b) Three-coil MCR WPT.

The multi-coil system is capable of charging multiple devices simultaneously. A WPT system that consists of a single transmitter and multiple receivers is investigated [32], and considered the influence of load and mutual inductance (the position of receivers) on the efficiency. A multi-coil transmitter array is employed to boost the power gain, which in turn allowed the application of very small receivers at a quite far distance [77]. A power transfer from a single source coil to multiple receivers through MCR WPT was demonstrated [162]. In addition, a WPT system based on the resonant cavity is proposed [136], and provided an efficient power delivery to many receivers simultaneously in an enclosed 3D volume of space (charging multiple toys that are placed randomly in a box or charging multiple LEDs). WPT systems based on the resonant cavity have the potential to enable a wide variety of new applications in many medical and industrial fields. However, this system has a problem in distributing the power uniformly to many receivers, especially in wearable devices or IMDs. To overcome this issue, a selective technique for smart power delivery to multiple receivers

is presented [163]. The method allows transferring the power to one receiver coil among multiple receivers by separating the resonant frequencies of the receivers, and isolating the cross-coupling effects between the coils.

4.3. Loop Inductance

Table 10 provides the self-inductance formula for some resonator shapes, such as square, rectangular, circular, and so on [164,165]. Table 11 gives layout dependent factors (x_i) for on-chip spiral inductors, such as square, hexagonal, octagonal, and circular [124].

Table 10. The inductance of different coreless loops.

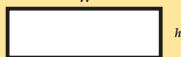
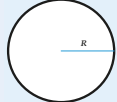
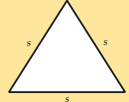
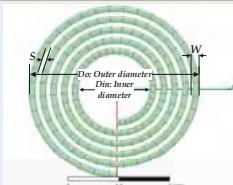
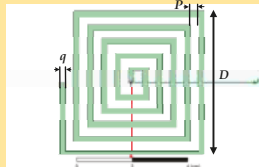
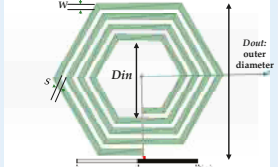
Resonator Type	Inductance	Comments
Straight conductor	$\frac{\mu_0}{2\pi} \left[\left(\ln \frac{2l}{a} \right) - \frac{3}{4} \right]$	l : Length, a : radius of the conductor.
Square loop	$2N^2 \frac{\mu_0 \mu_r w}{\pi} \left[\left(\ln \frac{w}{a} \right) - 0.774 \right]$ Where N : The number of turns.	μ_r : Relative permeability. 
Rectangular loop	$N^2 \frac{\mu_0 \mu_r w}{\pi} \left[\begin{array}{l} -2(w+h) + 2\sqrt{h^2} \\ h \ln \left(\frac{h + \sqrt{h^2 + w^2}}{w} \right) - w \ln \left(\frac{h + \sqrt{h^2 + w^2}}{h} \right) \\ h \ln \left(\frac{2h}{a} \right) + w \ln \left(\frac{2w}{a} \right) \end{array} \right]$	
Circular	$N^2 \mu_0 \mu_r R \left[\ln \left(\frac{8R}{a} \right) - 2.0 \right]$ R : radius	
Equilateral triangle	$N^2 \frac{3\mu_0 \mu_r s}{2\pi} \left[\ln \left(\frac{s}{a} \right) - 1.405 \right]$	
Pancake coil (flat spiral coil)	$(N^2 A^2) / (30A - 11D_{in})$ where: $A = (D_{in} + N(w + s)) / 2$ W : the wire diameter. S : the separation between two turns.	
Square spiral coil	$27 \cdot 10^{-10} \left(\frac{D^{8/3}}{P^{5/3}} \right) (1 + R^{-1})^{5/3}$ where $R = P/q$ q : thickness, P : the separation between turns.	
On-chip inductor spiral loops L- (nH) [124]	$N^2 \frac{x_1 D_{ave} \mu_0}{2} \left[\ln \left(\frac{x_2}{\phi} \right) + x_3 \cdot \phi + x_4 \cdot \phi^2 \right]$ where: $D_{ave} = (d_{out} + d_{in}) / 2$ $\phi = (d_{out} - d_{in}) / (d_{out} + d_{in})$ x_i —Factors from (layout depending, it is given in Table 11)	 ϕ —Fill factor

Table 11. Layout dependent factors.

Layout	x_1	x_2	x_3	x_4
Square	1.27	2.07	0.18	0.13
Hexagonal	1.09	2.23	0	0.17
Octagonal	1.07	2.29	0	0.19
Circular	1	2.46	0	0.2

Coil design is a basic step in WPT systems, since it determines the level of power transfer, efficiency, and the overall performance [104]. Therefore, the inductance is considered one of the most significant factors in the WPT system. The inductance depends on the coil geometry, which includes the size of the resonator, cross-sectional area, length, and number of turns, in addition to the separation between turns and thickness or width of copper.

4.4. Operating Frequency Effects on the Design of Coil Structure

An ideal inductor can be modeled as an inductance with no resistance, capacitance, or energy dissipation. On the other hand, for real inductors, as shown in Figure 8, the above-mentioned components are inevitable. The wire has a resistance (R_{ac}) and losses in the core materials. In addition, there are parasitic capacitances (C_{self}) caused by the electric field between the turns. The parasitic capacitance with the self-inductance can determine the self-resonant frequency (SRF) of the coil. At high frequencies, the effect of these factors will be obvious, and the AC resistance value will increase due to the skin effect. Therefore, the quality factor of the coils will drop. Due to high frequency, the current will be concentrated near the surface of the copper conductor, and as a result, the power loss will increase and cannot be ignored [166].

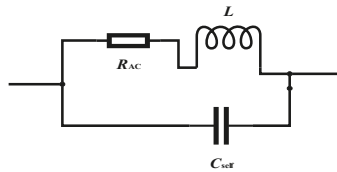


Figure 8. Equivalent circuit of the real inductor.

The inductance and skin effect are given as follows [162]: $R = r.N/d\sigma\delta$, $\delta = 1/\sqrt{\pi\sigma\mu f}$ (m), respectively. In the previous equations, r is the radius of the coil, d is the radius of the wire, and σ is the conductivity; for copper, $\sigma = 5.8 \times 10^7$ (S/m) and $\mu_0 = 4\pi \times 10^{-7}$ (H/m). Figure 9 presents a copper conductor with a 0.5-mm radius. When the frequency increases, the skin effect will be clearer. In order to reduce the AC resistance and power losses, Litz wires (multi-strand wires) are used to wind the coils. Based on the operating frequency range, the required diameter, and the number of wire gauge of the Litz wire can be determined [146]. In addition, superconducting materials were used to decrease the resistance and achieve a high-quality factor [144].

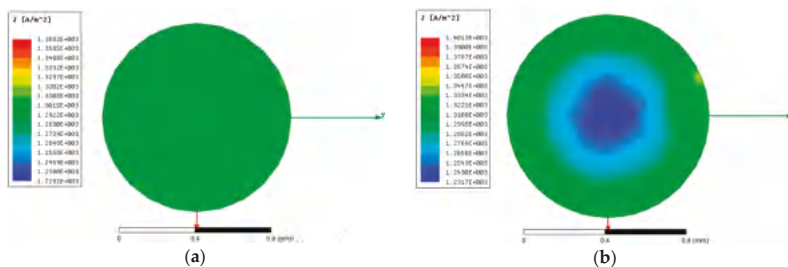


Figure 9. Cont.

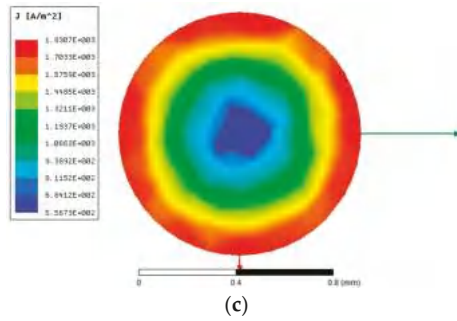


Figure 9. Skin effect (done by ANSYS Electronics 19.0.0; Canonsburg, PA, USA; 2018): (a) 60 Hz; (b) 20 kHz; (c) 85 kHz.

Finally, the frequency-splitting issue is a key point of an MCR WPT system. When moving the resonators toward each other gradually, the coupling between them becomes stronger, and if they are close enough, the resonant frequency will change. As a result, the transferred power drops sharply [167]. To clarify this case, Figure 10 shows two spherical structures for a WPT system, where the transmitting coil T_x is in blue, and the receiving coil R_x is in orange (the spherical joint structure for a WPT will be discussed in the seventh section). The coil windings are wound in different ways. In Figure 10a, T_x and R_x are located opposite to each other, and the coupling coefficient will be $k = 0.089$. Figure 10b displays the efficiency at the resonant frequency (500 kHz). In Figure 10c, T_x and R_x coils are wound in the same direction as the hemispherical structures. As a result, this model will have a short transferring distance, and the coupling coefficient will be high $k = 0.54$. Figure 10d illustrates the efficiency at the resonant frequency (500 kHz).

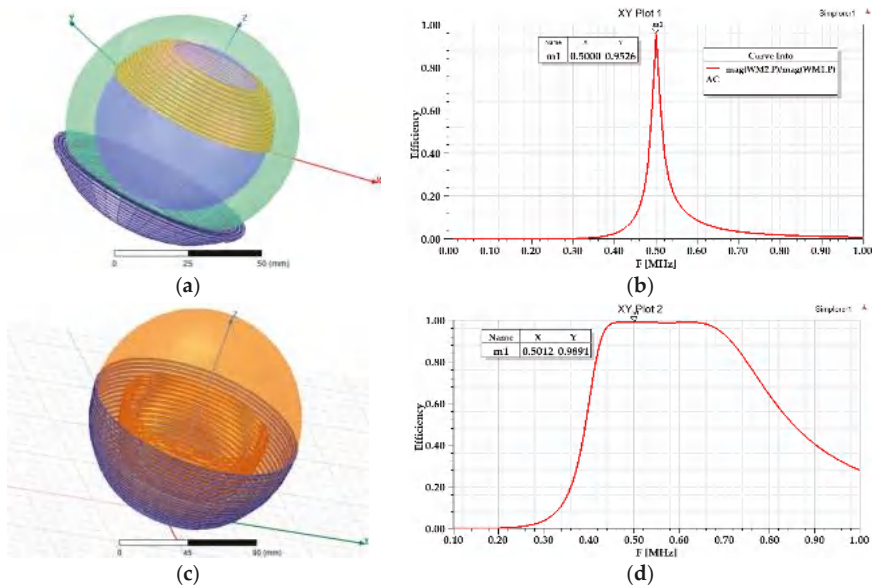


Figure 10. Efficiency at the resonant frequency (500 kHz) for two spherical structures. (a,b) $k = 0.089$; (c,d) $k = 0.54$.

To deal with the frequency-splitting issue and power transfer degradation, several methods are presented, such as an adaptive frequency tracking method, which changes the frequency in the strongly coupled region [168]. Instead, the frequency-splitting issue is suppressed by switchable configurations, such as for example, a switchable capacitor array [169], alternative multiple loops [170,171], and various load resistances [172].

5. Misalignment Study

In order to get a higher power transfer efficiency (PTE), the alignment between the WPT resonators should be perfect. However, the coils are usually misaligned [119]. There are several types of misalignment between the coils, which include the following. (1) In lateral (horizontal) misalignment, the coils are located in parallel planes, but they are offset by distance Δx . (2) In angular misalignment, the receiver coil is moved by an angle ϑ while the centers of the transmitter and receiver coils are well aligned [173]. (3) In vertical variation, the receiving coil moves vertically. (4) In planar misalignment, T_x and R_x are in parallel, and R_x rotates around the center point, but keeps the same transferring distance. (5) In angular azimuth misalignment, the transmitter is fixed, and the receiver rotates around the z-axis in the x - y plane from $\varphi = 0^\circ$ to $\varphi = 360^\circ$. (6) In angular elevation misalignment, the receiver rotates around the x -axis in the y - z plane from $\theta = 0^\circ$ to $\theta = 360^\circ$, and the transmitter is fixed [161].

Figure 11 displays different types of misalignment. This figure has shown a circular resonator to present misalignment types. However, the same misalignments apply to other structures as well, such as rectangular, square, and hexagon.

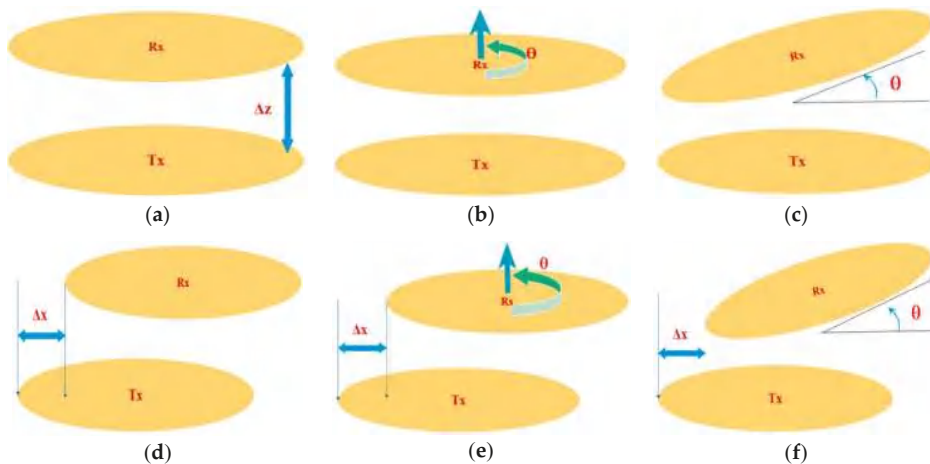


Figure 11. Types of misalignments: (a) Vertical variation; (b) Planar; (c) Angular; (d) Lateral (horizontal); (e) Planar and horizontal; (f) Angular horizontal.

Table 12 compares between different misalignments considering the coil structure and misalignment effect; some notes related to each type are given in comments.

The misalignment differs randomly under different situations and different application types. As a result, several parameters may change during the process, such as the mutual inductance, the efficiency, and output power. During the EV's charging, if there is imperfect parking, the transmitter and receiver coils will be misaligned. The transmitter coil is fixed on/under the ground, and the receiver is mounted on the bottom of the vehicle. In IMDs applications, if the patient breathes, the air gap of the WPT will change. Therefore, it is important to predict the misalignment tolerance of the WPT system in different applications. In addition, the system needs good controllability and optimization to deal with its parameter variations.

Table 12. Misalignment types: a review. SCMR: strongly coupled magnetic resonance. HSCMR: hybrid SCMR. CSCMR: conformal SCMR.

Case	The Resonator Structure	Misalignment Type	The Effect of Misalignments	Comments
[173]	Circular spiral coil	Lateral/ Angular	The values of output voltage decrease with the misalignment.	According to the test, even if the lateral and angular misalignments happen. The efficiency at a 5 cm distance is up to 50%.
[161]	Circular	Lateral/ Angular azimuth/ Angular elevation	The proposed structures: 3D SCMR, HSCMR, and CSCMR are less sensitive to the misalignments than the standard SCMR system.	The system achieves an efficiency of 40% for the entire range of 360° in case of the angular misalignment.
[1]	Helical	Lateral/ Angular general (angular horizontal)	$M = x(\Delta, \alpha) \cdot N^2$: M is the mutual inductance, which increases linearly depending on the square of the coil turns.	$x(\Delta, \alpha)$ is a variable coefficient that depends on the lateral misalignment Δ , and the angular misalignment α . The average value of the slope is (0–10 cm, 0–50°).
[99]	Double D (DD) bipolar pads	Horizontal	The efficiency is higher than 90%, even at a large misalignment in the x-direction.	For EV application, the x-misalignment is door-to-door, and the y-misalignment is front to rear.
[95]	UU type	Horizontal/Vertical	The self-inductance of the pads changes slowly with the misalignment of the coils, but the mutual inductance changes fast.	The current-fed compensation topology is a practical solution for WPT.
[132]	Helical coils	Angular	Compared to the single-transmitter WPT system, the proposed system gives a higher power transfer efficiency during the angular aligned and in case of the angular misaligned.	The paper proposed a multiple-transmitter WPT, which provides a power transfer diversity.
[113]	H-shaped DGS and semi-H-shaped	Horizontal shift/Coaxial orientation	Compared to H-shaped DGS, the semi-H-shaped DGS is more robust to misalignments.	These features boost the usage of the semi-H-shaped DGS in WPT applications.
[117]	Circular spiral coil	Angular	The case of a fixed frequency undergoes the same trend of process from the over coupled to critically coupled, and then under coupled system.	The receiver unit is placed on the axis at a fixed transferring distance of 50 cm.
[110]	Rectangular	Forward direction	Compared with SP-compensated WPT, the S/SP-compensated WPT is more robust to the misalignment.	The range of the output voltage of the SP-compensated WPT is almost double that of the S/SP-compensated WPT,

6. EMI and EMF Diagnostics in the WPT System

The electromagnetic spectrum includes two sectors. They are as follows. The first is the non-ionizing area, which means the energy of the waves is too low to ionize tissues. The second is the ionizing radiation area. MCR WPT products use electromagnetic waves within the non-ionizing area of the electromagnetic spectrum.

6.1. WPT-Related Standards, Including the Safety Issues

Regarding safety issues linked to WPT usage, there are two serious issues. The first is that long-term exposures to time-varying EMFs can harm the human body. Therefore, the International Commission on Non-Ionizing Radiation Protection (ICNIRP), expert groups, and the World Health Organization (WHO) have documented and issued some guidelines to ensure the safety of the human body. The second is a wide range of harmonics generated by inverters, which in turn create EMI issues on the other electronic devices' operations. Therefore, it is important to suppress EMF and EMI in the WPT system [174].

Based on the obvious risks that are caused by using the WPT charging systems, it is necessary to regulate the usage of the WPT systems. Therefore, many recommendations, standards, and guidelines

were issued. Table 13 provides a comprehensive review of WPT-related standards and guidelines that were issued by different international organization around the world. For example, in order to protect against any known health effects, the ICNIRP has published guidelines for maximum exposure limits. They consist of the publications from 1998 (0 Hz–300 GHz) and 2010 (0 Hz–100 kHz).

Table 14 presents the near-field WPT systems, including the frequency and power ranges under study in non-ISM bands for Japan and South Korea.

It is inevitable for the electrical circuits and the human body that are close to the WPT system to be under the influence of EMI emissions or exposure to EMFs. Therefore, it is essential to regulate the deployment of the WPT system to ensure the safety of the consumers and electrical components. The standards differ from one country to another. Therefore, the WPT system can be categorized based on the frequency, power, transferring distance, and application type. As a result, the WPT system is handled as normal equipment that follows specific restrictions, or it is considered an important case that follows tighter restrictions.

Table 13. Comprehensive review of WPT-related standards and guidelines. EMF: electromagnetic field, EU: European Union, ICPT: inductive coupled power transfer, USA: United States.

Standards	Substandard	Country	Frequency/Power	Application/Comments
Federal Communications Commission (FCC)	KDB 680106 Part 15B and part 18		Above 9 kHz are considered intentional radiators.	Radio frequency (RF) exposure wireless charging apps (wireless chargers, inductive chargers, and wireless charging pads).
Society of Automotive Engineers (SAE)	SAE J2954/J2836/61M J2847/6-J2931/6	USA	J2954 TM EVs and PHEVs use 85 kHz band.	Wireless charging task force, specific use cases, and specific protocols.
The International Special Committee on Radiofrequency	CISPR SC-B CISPR 11:2015		From 9 kHz upwards, CISPR 11 range is 150 kHz to 1.1 GHz	Household appliances, ignition systems, and fluorescent lamps. Power electronics in the industrial, scientific and medical frequency band (ISM band): RF equipment used in WPT.
International Electrotechnical Commission (IEC)	IEC 61980-1:2015, IEC 62827-2:2017, IEC PAS 63095-1:2017(E)		For IEC PAS 63095-1:2017(E) baseline power profiles are (≤ 5 W) and extended power profile is (≤ 15 W).	<ul style="list-style-type: none"> IEC 61980-1:2015: General requirements for EV WPT. IEC 62827-1:2016: justifies various functions of WPT system. IEC 62827-2:2017: Control management of multiple-device WPT. IEC PAS 63095-1:2017(E): Qi WPT and interface definitions.
International Organization for Standardization (ISO)	ISO PAS 19363, 2017-1-1, (ISO/NP 19363 under development)		Close synchronization with IEC 61980 and SAE J2954.	Magnetic field WPT, safety, and interoperability requirements.
International Commission on Non-Ionizing Radiation Protection (ICNIRP)	ICNIRP 1998 ICNIRP 2009 ICNIRP 2010	International	EM Field: (1 Hz–100 kHz)/2010 (1 Hz–300 kHz) 1998.	<ul style="list-style-type: none"> Guideline for limiting the exposure to electric fields and magnetic fields, which vary by time. ICNIRP 2010 replaces the low-frequency part of the 1998 guidelines.
European Telecommunication Standards Institute (ETSI)	ETSI EN 303 417 V1.1.0 (2017-9).	EU	For WPT systems that use frequency other than RF beam, and it has investigated ranges: [19–21 kHz, 59–61 kHz, 79–90 kHz, 100–300 kHz, and 6765–6795 kHz].	Harmonized standard, which covers the essential requirements of article 3.2 of Directive 2014/53/EU.
China Communication Standard Association (CCSA)	CCSA TC9 YD/T 2654-2013	China	Part1: General; part2: Tightly coupled (ICPT); and part3: Resonance wireless power transfer (MCR WPT).	EMF evaluation methods for WPT and EMC limit and measurements. Requirements and test methods of EMC of WPT equipment.

Table 13. *Cont.*

Standards	Substandard	Country	Frequency/Power	Application/Comments
Association of Radio Industries and Businesses (ARIB); Broadband Wireless Forum (BWF)	ARIB STD-T113 (2015)	Japan	6.78 MHz-band MCR WPT for mobile, 400 kHz-band for CPT. EV /PHEV WPT spectrum: (42 kHz~48 kHz, 52 kHz~58 kHz, 79~90 kHz, and 140.91~148.5 kHz). Power: 3 kW and 7.7 kW.	Study for WPT spectrum for all the applications and technologies. <ul style="list-style-type: none"> ▪ CPT system. ▪ MCR WPT using 6.78 MHz for mobile and portable devices. ▪ Magnetic induction WPT for home appliances and office equipment. ▪ WPT for EV /PHEV.
	BWF TR-02 Edition 1.0/2016		100 kHz, 100~500 kHz, and 6.78 MHz.	Assessment on EMI due to WPT systems.
Telecommunication Technology Association (TTA)	TTAR-06.162 (19/11/2015)	Korea	For EV in 2011, OLEV (19 kHz~21 kHz and 59 kHz~61 kHz). Normal Power: 100 kW. Frequency: 13.56 MHz band is used for 3D glasses WPT.	Efficiency measuring methods for WPT and heavy duty EVs. <ul style="list-style-type: none"> ▪ MCR WPT (magnetic resonance). ▪ WPT (magnetic induction).
Alliance for Wireless Power (A4WP)	A4WP standards	Established in 2012 (Samsung, Qualcomm and others)	6.78 MHz for power transfer and 2.4 GHz for the control signals.	Magnetic resonance WPT. <ul style="list-style-type: none"> ▪ A4WP and PMA have merged to form industry-leading organization for wireless charging standards.
Wireless Power Consortium Qi (WPC)	Qi standards Version 1.0. Version 1.1.	Industry group, since 2008	Range: 110 kHz~205 kHz. Low power in the range of (0~5) W. Medium power is up to 120 W.	Details and specifics about the Qi WPC standards. ICPT system. <ul style="list-style-type: none"> ▪ Used in cell phone, music players, Bluetooth, etc.
Power Matters Alliance (PMA)	PMA standard	Founded by Procter, Gamble and Powermat in	277 kHz~357 kHz and up to 5~10 W.	Magnetic induction technique. <ul style="list-style-type: none"> ▪ Mobile device ecosystem.
Additional standards for electromagnetic compatibility EMC, immunity tests and measurements: Radiated and conducted emissions—CISPR 11. Compliance testing of wireless power transfer products ASNI C63.30. Radiated EM immunity—ISO 11451-2:2015-06 (E).				

Table 14. Current and ongoing study frequency and power range for WPT in Japan and Korea. PCs: personal computers.

WPT System	Country	Frequency Range under Consideration	Power Range under Considerations	Application
Inductive coupling (IPT): low power	Already in Japan, Korea	Japan: 110 kHz–205 kHz. Korea: 100 kHz–205 kHz.	-	Mobile devices, portable devices, consumer electronics (CE), and industrial fields.
Inductive coupling (IPT): high power	Japan	Japan: 20.05 kHz–38 kHz, 42 kHz–58 kHz, and 62 kHz–100 kHz.	Japan: Several watts up to 1.5 kW.	Home appliances operating with high power, and office equipment.
Magnetically coupling resonant (MCR WPT)	Japan, Korea	Japan and Korea in the range of: (6.765–6.795) MHz.	Japan: Up to 100 W. Korea: Unlimited in-band emission limit	Mobile devices, tablets, note-PCs, and home appliances, which operate with low power.
Capacitive coupling (CPT)	Japan	Japan: 425 kHz–524 kHz.	Japan: Up to 100 W	Portable devices, tablets, and home appliances.

6.2. EMF and EMI Mitigation Methods

Some WPT charging applications have a large air gap, such as EVs, where it can reach 10–30 cm. This creates high levels of a stray field in the coils’ vicinities, thus arises an issue regarding the exposure to magnetic fields for people who approach the vehicle or passengers during the charging process [175]. In [175], the authors presented a pulsed magnetic fields methodology (developed according to the requirements of the International Commission on Non-Ionizing Radiation Protection (ICNIRP) guidelines), the results for the assessment applied to a 20-kW IPT system for dynamic charging of EV at the frequency of 85 kHz. The charging is performed by using several independent transmitters (each one: 1.5 m long and 0.5 m wide). When the vehicle is above them, they will be activated. In this direction, the authors investigated the human exposure to the EMFs by using a computational modeling applied to a 7-kW WPT charging system at the frequency of 85 kHz [176]. In [177], two-step scaled frequency finite-difference time-domain (SF-FDTD) methods are used to calculate the internally induced electric fields in the human body.

EMF safety can be achieved through the magnetic field level reduction in the near-field area. Therefore, several reduction methods were presented, such as using ferrite materials [14], metallic materials (aluminum) [178,179], and metamaterials (MM) [180–183]. Changing the pulse width of the inverter to decrease the harmonics of the leakage electric field was presented [184]. In [185], the authors presented three active methods that include the independent self-EMF cancelation (ISEC), the 3-dB dominant EMF cancel method (3DEC), and the linkage-free EMF cancel method (LFEC). In addition, the authors have reported other techniques, such as separating pickup rectifiers and magnetic mirror methods. In [7], the authors presented a resonant reactive shield with one coil and a capacitor. In [186], a resonant reactive shield with two coils and four capacitors was discussed. Figure 12 illustrates the above-mentioned EMF mitigation methods. On the other hand, some EMI mitigation methods are reported, for example, the spread spectrum clock technology (SSC) [187]. In [174], the authors investigated an isolation inductor scheme to reduce EMI in an automotive tightly coupled handheld resonant charging system. Moreover, EMI can be suppressed by optimizing the rise and fall times of the output voltage in high-frequency soft-switching converters [188].

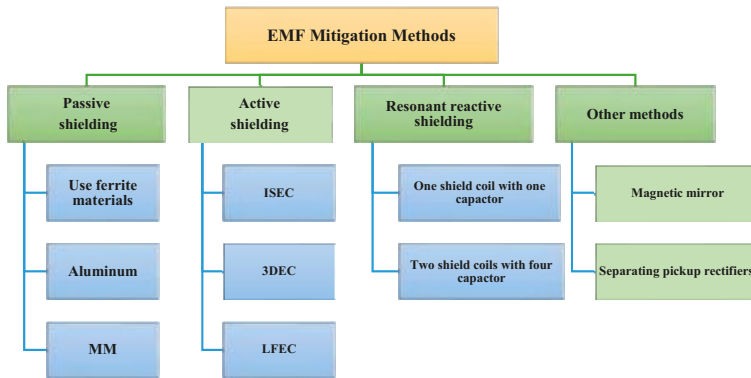


Figure 12. EMF mitigation methods.

Table 15 compares between different EMI and EMF mitigation methods, in addition to their advantages and disadvantages.

Table 15. EMF and EMI reduction methods: advantages and disadvantages. 3DEC: 3-dB dominant EMF cancel method, ISEC: independent self-EMF cancellation, LFEC: linkage-free EMF cancel method.

Case	Reduction Method	Advantages	Disadvantages	Notes
[14]	Using ferrite bars	Ferrite acts as a partial magnetic core for coupled coils, and it improves the system performance.	Ferrite bars experience hysteresis losses and have extra costs. In addition, some applications do not have enough space.	I-C-compensated topology is more effective than SS-compensated topology, and it produces a lower magnetic field in the near-field area.
	Ferrimagnetic material	It can confine and guide the magnetic flux by providing a path close to magnetic field sources.	Using the ferrimagnetic material could be limited for some applications due to its cost, occupied space, and weight.	The EMF noise that is produced by CSPP topology is higher and worse than that of the CSSR noise.
[178]	Metallic shielding (Aluminum), same case in [179]	The metallic shielding induces eddy currents, which result in magnetic fields cancellation. Therefore, the total magnetic field near the material is reduced.	Ferrite and metallic shields block a wide band of electromagnetic spectrum. Consequently, they have a lower power transfer efficiency, in addition to the thermal stress caused by eddy currents.	CSPP means constant current CCO, series resonance for Tx, parallel resonance for Rx, and a resistive load (R). CSSR: constant current source
[180]	Near-field metamaterial zero-permeability shield	It does not cause significant extra losses, and it blocks the near-field radiation only at an exact frequency.	If the metamaterial is not placed between the coils, it will work as a shield, so it does not enhance the coupling.	The selective frequency technique blocks specific frequencies and allows other fields to pass. Consequently, this method could be used for human safety.
[16]	Three-phase power line to reduce the leakage EMF	The current circulates in two wires for each phase. Therefore, the side and center parts of the power lines cancel each other.	The three-phase system has a higher input current compared to the single-phase system.	This system uses six overlaid power lines (three in the center and three to the side); they are ended to two Y-connections.
[185]	Active shielding	It generates counter magnetic fields from the EMF cancel coil. In addition, it is suitable for high-power application, such as EVs, PHEVs, and road-powered type EVs.	Requires extra components, extra coils, and a power supply.	The linear time-invariant steady-state system, which means that the cores are unsaturated and the circuit parameters are constant.
[7186, 189]	Reactive resonant (with one or two shielding coils)	The cancellation magnetic field is generated from the original magnetic field noise. Therefore, it does not require any power source.	Requires shielding coils and capacitors.	The shielding coils are connected to each other so that the primary shield coil can supply enough shield current for the second shield coil. Consequently, the leakage magnetic field is reduced.
[187]	Spread spectrum clock technology (SSC)	This method reduces the current spectrum, and as a result, the EMI is suppressed.	EMI mitigation methods It requires a power supply, which occupies more space and weight. In addition, it is not simple to design.	Triangular modulation; the peak deviation $\pm 1\%$ and the modulation frequency is 156.25 Hz.
[174]	The isolation inductor scheme to reduce EMI	The magnitude of the input impedance is increased at higher frequencies. At the resonant frequency, no change at the magnitude of the input impedance.	Due to the coil and core losses of the isolation inductor.	Isolation inductors of Tx and Rx are made of shell-type ferrite cores' coils.

7. WPT Applications: An Optimized Case Study

Figure 13 summarizes many applications of a WPT charging system, and shows that the WPT became an important part of some basic fields. First, in transportation, wireless power transfer for electric vehicles is a promising technology. Secondly, in the implantable medical devices (IMDs), it gives a convenient, reliable, and safe way to supply the power wirelessly without any pain to patients. Thirdly, in the field of consumer electronic applications, WPT is used in LED TVs, charging portable devices, such as cell phones, tablets, and other smart building appliances, where the WPT technology reflects the development of this kind of buildings. Moreover, the WPT system is used in IoT applications. Finally, WPT systems are used in LED lights, underwater detection, military defense systems, space applications, etc.



Figure 13. WPT applications.

To give a clear picture about the design method for a certain application, a 3D structured WPT that transfers the power wirelessly in a robotic application is proposed. The system is a bio-inspired joint for the WPT system. The joint consists of a movable spherical structure that rotates inside a big sphere using a mechanical stud (0° – 85°). The transmitter coil (T_x) is wound on a hemispherical structure, as shown in Figure 14a, or wound on a spherical structure (with a slot), as shown in Figure 14c. In this case, the mechanical stud can rotate the small sphere up to 45° . The receiver coil (R_x) is wound on the small sphere structure. α is the displacement angle (degrees) between the vertical axes of the joint structures.

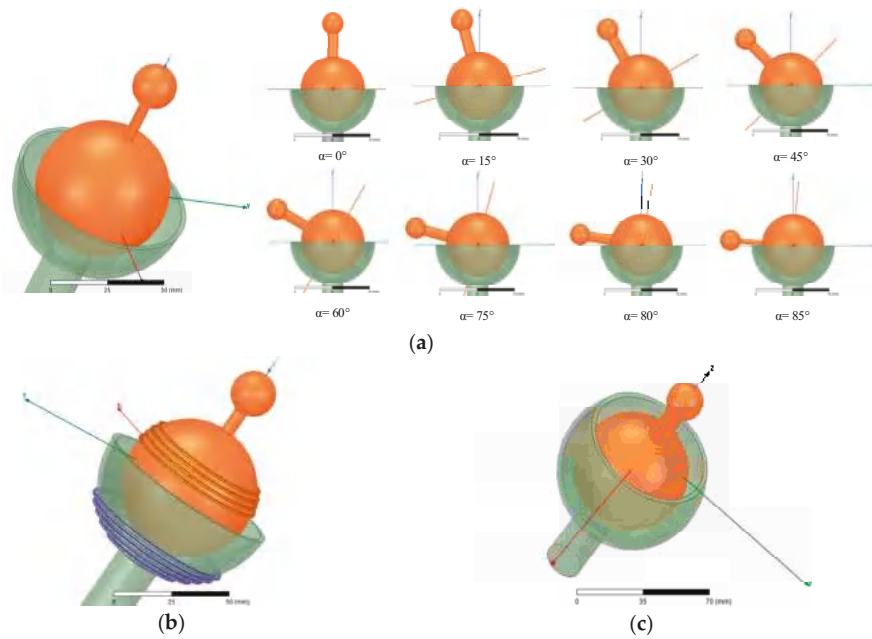


Figure 14. Joint-WPT: (a) Displacement angle (0° – 85°); (b) An example of winding Tx and Rx coils; (c) Spherical model (0° – 45°).

To design the WPT system, Figure 15 is illustrated. Considering the transferred power, frequency, structure, and other parameters, the purpose of the WPT system should be determined. The application type has two types of constraints, which include the structure and electrical constraints. The structure constraints include the size, volume, and gap. The electrical constraints comprise the compensation topology and its parameters, the required power to be transferred, and the operating frequency. On the other hand, several variables are parameterized to optimize the WPT, such as for example, the mutual inductance M , the output power, and the efficiency. WPT optimization is achieved by simulation and calculation, and experiments are put forward to validate the obtained results. Other factors can be considered during the design, such as suitable EMI and EMF mitigation methods (based on the application type).

2. Initialize z_i , β , and θ as 0. Initialize $z_j = 10$ mm (start z-position for Rx), $N_1 = 0$, $N_2 = 0$, $m = 0$, and $n = 0$.
3. Enter the radius of the transmitter coil $r_s = 38.5$ mm, the radius of the receiver coil $r_b = 28.5$ mm, and the pitch between turns P .
4. Enter β and θ . // Measured in radian.
5. Count: $\theta = \theta + (1/36) \pi$, $\beta = \beta + (1/36) \pi$, $N_1 = N_1 + 1$, $N_2 = N_2 + 1$, $z_{im} = z_{im} + P$, and $z_{jn} = z_{jn} + P$, n addition to $m = m + 1$ and $n = n + 1$. // Increment angles to determine the z-position and r for each turn of the transmitter and receiver coils. ((1/36) π is the assumed step). Increment N_1 and N_2 to find the number of turns for both coils. Move the turns in the z-direction with the pitch between coils equal to 0.5 mm. The number of turns can be calculated by $N_1 = z_{im}/P$ and $N_2 = z_{jn}/P$.
6. Calculate $r_{im} = r_s \sin(\theta)$, $r_{jn} = r_b \sin(\beta)$, $z_{im} = r_s (1 - \cos(\theta))$, and $z_{jn} = r_b (1 - \cos(\beta))$. // mm (based on angles).
7. Calculate L_1 and L_2 : the self-inductances of the transmitter coil and receiver coil, respectively. Calculate and maximize the mutual inductance M and the coefficient coupling k , and determine the required capacitors C_1 , C_2 . // In order to maximize the mutual inductance, the inductances will be adjusted based on the number of turns and the space between turns (pitch). The transferring distance between Tx and Rx will determine the coupling coefficient, which should be less than a certain value k_s .
8. With the available values of the frequency and coil resistance, calculate the quality factor, transferred power, and efficiency.
9. Sweep the frequency and mutual inductance to maximize the efficiency and transferred power.
10. Is $k < k_s$, if yes, go to 11, or else go to step 13. The coupling coefficient should stay within a certain range to avoid cases with very low values or cases with very high coupling between Tx and Rx.
11. Is $\theta < \pi/2$, if yes, go to step 12, or else go to step 13.
12. Is $\beta < \pi$, if yes, go to step 3, or else proceed to step 13.
13. End.

Figure 17 illustrates a flowchart that represents the algorithm design.

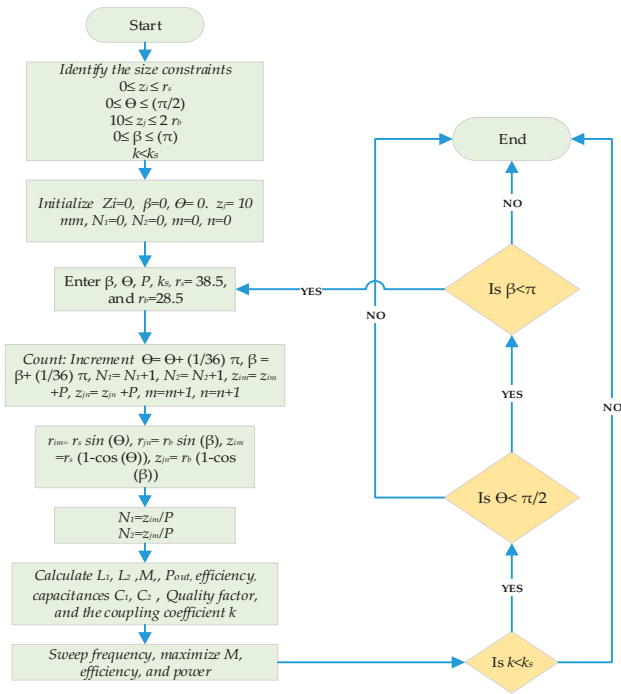


Figure 17. Flowchart represents the algorithm design of the joint WPT.

7.2. Simulations

The simulation of the joint WPT system is conducted by ANSYS electronics 19.0.0, USA, 2018. The optimization process has resulted in cases with high coupling coefficient values and others with low values. As shown in Figure 18, two cases are considered. The first is the hemisphere winding with a high coupling coefficient ($k = 0.54$). The second is the optimized model with $k = 0.089$. The obtained parameters are given in Table 16.

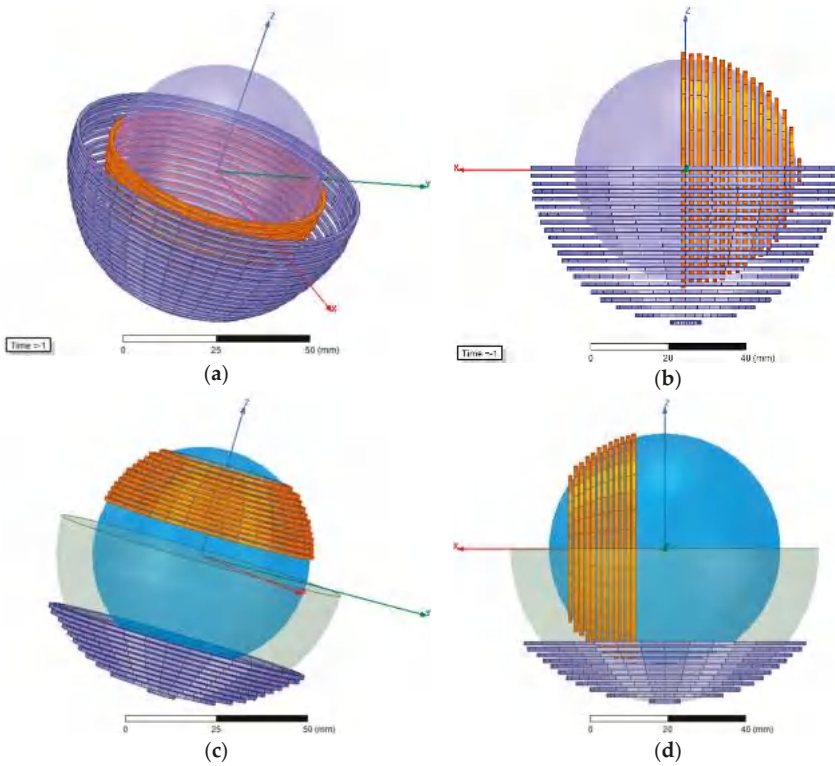


Figure 18. Two case studies: (a) Hemisphere winding at 0°; (b) Hemisphere winding at 90°; (c) Optimized design at 0°; (d) Optimized design at 90°.

Table 16. Parameters of case studies.

WPT	f_0	N_1/N_2	L_1/L_2 (μH)	Resistances: R_1, R_2 (Ω)	Mutual Inductance M	Coupling Coefficient k	C_1/C_2 (nF)
Hemisphere (a)	500 kHz	21/16	21.14/7.8156	0.23/0.13	7.478 μH	0.54	4.79/12.96
Optimized model (b)		34/22	50.699/31.83	0.19/0.1	3.6117 μH	0.089	2/3.18

Figure 19 shows that the mutual inductance and coupling coefficient for the hemisphere-winding drop rapidly with the angular misalignment, which can, in turn, lead to low efficiency. However, with the optimized solution, the fluctuation of M and k is reduced, and the performance of the WPT system is improved. Therefore, the receiver can rotate inside the transmitter from zero degrees (perfectly aligned coils) up to 90 degrees (practically 85°) while keeping high efficiency. Figure 20 shows the relation between the efficiency, load, and resonant frequency. For the hemispherical winding at a load of $R_L = 20 \Omega$, the efficiency was up to 96% at $\alpha = 0^\circ$. However, at $\alpha = 85^\circ$, the efficiency dropped to lower than 10%. On the other hand, for the optimized WPT with the same load, the efficiency was up to 95.75% at $\alpha = 0^\circ$ and 96% at $\alpha = 85^\circ$ (the mutual inductance at 85° is higher than that at 0°).

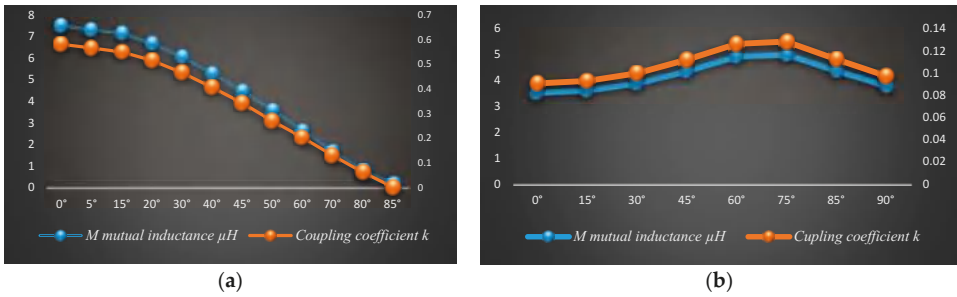


Figure 19. The mutual inductance and coupling coefficient: (a) Hemisphere winding; (b) Optimized design.

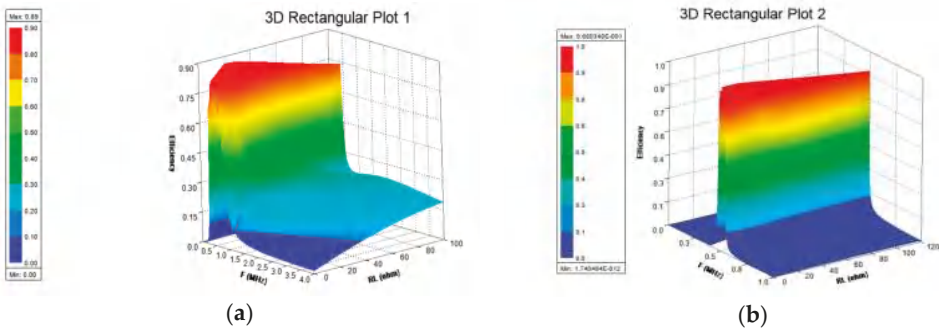


Figure 20. WPT efficiency: (a) Hemisphere winding; (b) Optimized design.

Figure 21 presents the magnetic field density for the optimized and hemisphere models. The magnetic field density is given by $B = \mu H$, where H is the magnetic field strength (intensity) measured by (A/m). In Figure 21a, at $\alpha = 0^\circ$, the yellow area (within 12-cm diameter) shows that B is around $86 \mu T$, which is higher than the allowed level by ICNIRP 2010 (should not exceed $27 \mu T$). In Figure 21b, the magnetic field density is concentrated in the close area around the coils. These cases require attention if the WPT is deployed close to the human body or other sensitive circuits. EMI and EMF mitigation methods can be selected based on the cost, weight, and size constraints of the joint. For instant, choosing ferrites is not a good choice, since it will put more pressure on the robotic arm. Based on the simulation results, a thin light sheet of aluminum can reduce the magnetic field density around the joint WPT to a safe level.

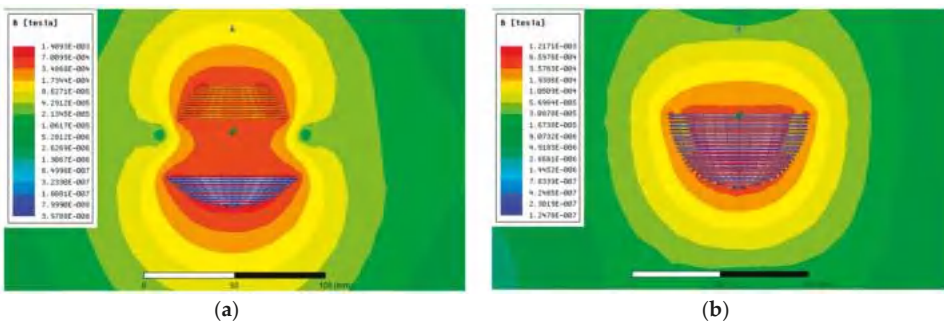


Figure 21. The magnetic field density (B vector/cross section): (a) Optimized design; (b) Hemisphere winding.

7.3. Experiments of the Proposed WPT and Measurements

The WPT system is fabricated to validate the calculated and simulated results. Figure 22 presents the experimental setup, where a multi-strand Litz wire was used to wind the coils. Radio frequency (RF) Mica-type capacitors CDE (CD15FA102JO3F) and a half-bridge inverter were used. The system is SS-compensated WPT, and the experiments included two models, as presented in Table 16.

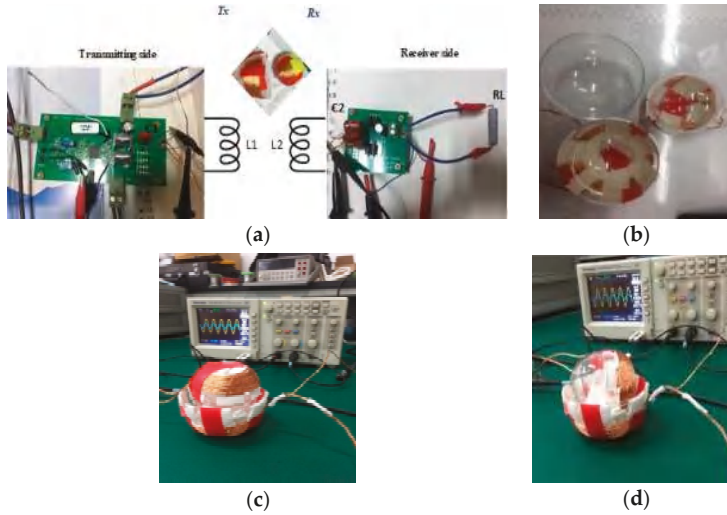


Figure 22. Experimental setup: (a) Circuits; (b) Hemisphere windings; (c) Optimized design at $\alpha = 0^\circ$; (d) Optimized design at $\alpha = 90^\circ$.

Figure 23 shows the input and output voltages at the resonant frequency (496 kHz) for the hemisphere-winding in Figure 23a, and the optimized model in Figure 23b.

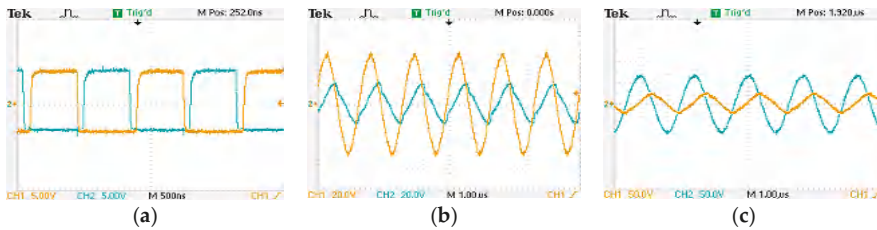


Figure 23. (a) Pulse-width modulation (PWM) signal; (b) Input/output voltages for the hemisphere case; (c) Input/output voltages for the optimized model.

The angular misalignment effects on the input and output voltages are given in Figures 24 and 25. In this structure, the receiver coil can rotate up to 85° . At $\alpha = 85^\circ$, for the hemisphere-winding, the output voltage will drop to values close to zero. However, for the optimized model, even at $\alpha = 85^\circ$, the output voltage keeps a high value.

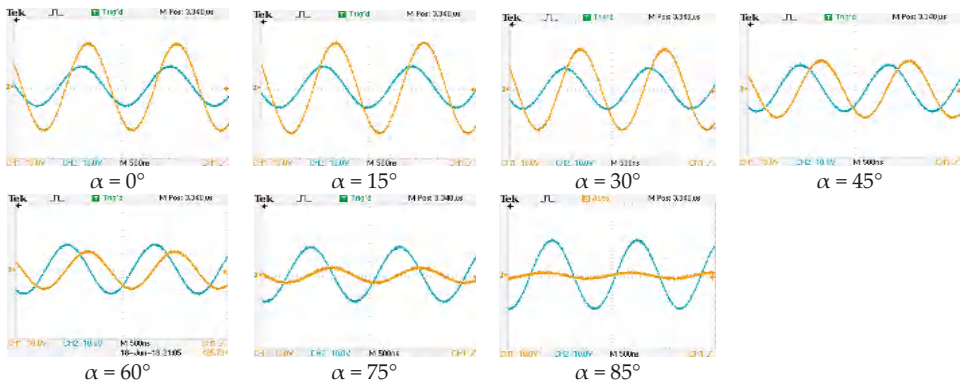


Figure 24. Input (blue) and output (orange) coil-to-coil voltages for the hemisphere winding.

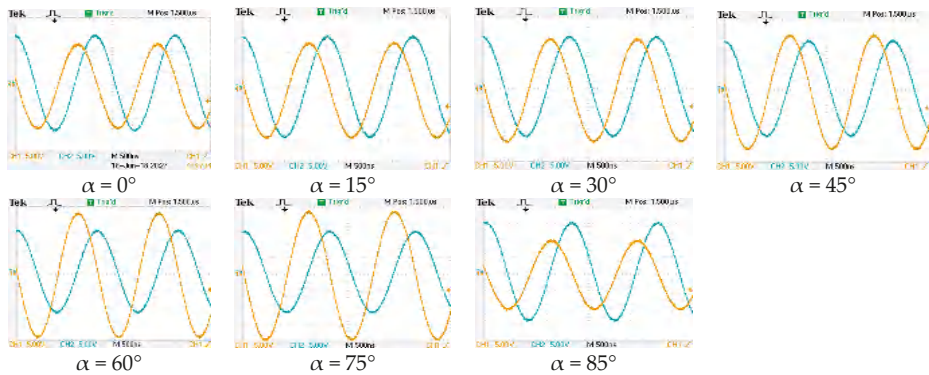


Figure 25. Input (blue) and output (orange) coil-to-coil voltages for the optimized model.

7.4. Cost Assessment of WPT Systems

The cost assessment of the WPT system can be done by considering the number of required components, such as inverter switches, diodes, Litz wires, resistors, capacitances, etc. In general, compared to hybrid topologies, the SS, SP, PS, and PP compensation topologies require fewer components. At kHz-range frequencies, high output power could be needed, and the power converters are added. As a result, the total cost is increased, such as EV charging applications that operate at 20 kHz and 85 kHz. At high frequencies, the output power could be very low, and the system does not require additional components such as IMDs that use the ISM band (2.2 MHz and 6.78 MHz).

8. Conclusions and Future Research

This paper has comprehensively reviewed the recent progress of the MCR WPT system including several aspects, such as compensation topologies, resonator structures, and misalignment analysis. In addition, EMI and EMF diagnostics were discussed, and the WPT-related standards were reviewed. Moreover, several EMI and EMF mitigation methods were reported and compared. Furthermore, a wide range of WPT applications was presented. Finally, a WPT case study was proposed. In the proposed winding method, a bio-inspired joint made of two spherical structures was given. The design process and algorithm design were provided, and experiments were conducted to validate the obtained results by simulation.

As shown in Figure 26, to work toward an optimum design of WPT, there are some factors that have an impact on the design process and thus should be considered during the design and

manufacturing process. The application type is determined by considering the size or volume, the transferring distance, the required power to be transferred, and the operating frequency. After that, inductances, resistances, quality factors, and mutual inductance are obtained. Choosing a proper compensation topology is another basic step. Other factors are considered, such as suitable EMI and EMF mitigation methods. Therefore, a good combination of the above-mentioned factors has to be considered. Even though many studies have been investigated, research related to new topologies, novel structures, new materials, and mitigation methods, in addition to system stability under misalignments, impedance matching, control strategy, and cost-effective assessment should be done.

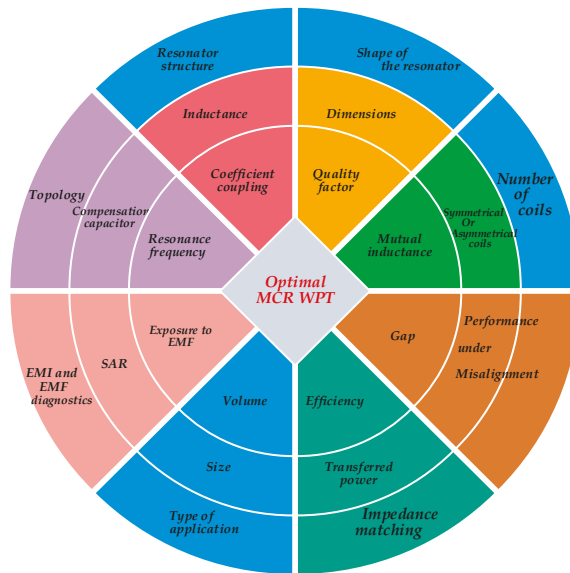


Figure 26. Influencing factors in order to get an optimal WPT.

Author Contributions: M.A.H. conducted the review and wrote the manuscript. X.Y. and W.C. Guided and contributed in discussions and supervision.

Funding: This research received no external funding.

Acknowledgments: The authors would like to thank the anonymous reviewers for their constructive comments.

Conflicts of Interest: The authors declare no conflict of interest.

References

1. Liu, F.; Yang, Y.; Jiang, D.; Ruan, X.; Chen, X. Modeling and Optimization of Magnetically Coupled Resonant Wireless Power Transfer System with Varying Spatial Scales. *IEEE Trans. Power Electron.* **2017**, *32*, 3240–3250. [CrossRef]
2. Miller, J.M.; Onar, O.C.; Chinthavali, M. Primary-side power flow control of wireless power transfer for electric vehicle charging. *IEEE J. Emerg. Sel. Top. Power Electron.* **2015**, *3*, 147–162. [CrossRef]
3. Hsieh, Y.C.; Lin, Z.R.; Chen, M.C.; Hsieh, H.C.; Liu, Y.C.; Chiu, H.J. High-Efficiency Wireless Power Transfer System for Electric Vehicle Applications. *IEEE Trans. Circuits Syst. II Exp. Briefs* **2017**, *64*, 942–946. [CrossRef]
4. Mou, X.; Groling, O.; Sun, H. Energy efficient and adaptive design for wireless power transfer in electric vehicles. *IEEE Trans. Ind. Electron.* **2017**, *64*, 7250–7260. [CrossRef]
5. García, D.T.; Vázquez, J.; Roncero-Sánchez, P. Design, implementation issues and performance of an inductive power transfer system for electric vehicle chargers with series-series compensation. *IET Power Electron.* **2015**, *8*, 1920–1930. [CrossRef]

6. Li, S.; Mi, C. Wireless power transfer for electric vehicle applications. *IEEE J. Emerg. Sel. Top. Power Electron.* **2015**, *3*, 4–17.
7. Kim, S.; Park, H.H.; Kim, J.; Kim, J.; Ahn, S. Design and analysis of a resonant reactive shield for a wireless power electric vehicle. *IEEE Trans. Microw. Theory Tech.* **2014**, *62*, 1057–1066. [[CrossRef](#)]
8. Zhang, H.; Lu, F.; Hofmann, H.; Liu, W.; Mi, C. A Four-Plate Compact Capacitive Coupler Design and LCL-Compensated Topology for Capacitive Power Transfer in Electric Vehicle Charging Application. *IEEE Trans. Power Electron.* **2016**, *31*, 8541–8551.
9. Dai, J.; Ludois, D.C. Capacitive power transfer through a conformal bumper for electric vehicle charging. *IEEE J. Emerg. Sel. Top. Power Electron.* **2016**, *4*, 1015–1025. [[CrossRef](#)]
10. Choi, S.Y.; Gu, B.W.; Jeong, S.Y.; Rim, C.T. Advances in wireless power transfer systems for roadway-powered electric vehicles. *IEEE J. Emerg. Sel. Top. Power Electron.* **2015**, *3*, 18–36. [[CrossRef](#)]
11. Mi, C.C.; Buja, G.; Choi, S.Y.; Rim, C.T. Modern advances in wireless power transfer systems for roadway powered electric vehicles. *IEEE Trans. Ind. Electron.* **2016**, *63*, 6533–6545. [[CrossRef](#)]
12. Zeng, H.; Yang, S.; Peng, F.Z. Design Consideration and Comparison of Wireless Power Transfer via Harmonic Current for PHEV and EV Wireless Charging. *IEEE Trans. Power Electron.* **2016**, *32*, 5943–5952. [[CrossRef](#)]
13. Do Chung, Y.; Lee, C.Y.; Kang, H.; Park, Y.G. Design considerations of superconducting wireless power transfer for electric vehicle at different inserted resonators. *IEEE Trans. Appl. Supercond.* **2016**, *26*, 1–5. [[CrossRef](#)]
14. Campi, T.; Cruciani, S.; Maradei, F.; Feliziani, M. Near-Field Reduction in a Wireless Power Transfer System Using LCC Compensation. *IEEE Trans. Electromag. Compat.* **2017**, *59*, 686–694. [[CrossRef](#)]
15. Lee, W.Y.; Huh, J.; Choi, S.Y.; Thai, X.V.; Kim, J.H.; Al-Ammar, E.A.; El-Kady, M.A.; Rim, C.T. Finite-width magnetic mirror models of mono and dual coils for wireless electric vehicles. *IEEE Trans. Power Electron.* **2013**, *28*, 1413–1428. [[CrossRef](#)]
16. Kim, M.; Kim, H.; Kim, D.; Jeong, Y.; Park, H.H.; Ahn, S. A Three-Phase Wireless-Power-Transfer System for Online Electric Vehicles with Reduction of Leakage Magnetic Fields. *IEEE Trans. Microw. Theory Tech.* **2015**, *63*, 3806–3813. [[CrossRef](#)]
17. Ko, Y.D.; Jang, Y.J. The optimal system design of the online electric vehicle utilizing wireless power transmission technology. *IEEE Trans. Intell. Transp. Syst.* **2013**, *14*, 1255–1265. [[CrossRef](#)]
18. Li, W.; Zhao, H.; Li, S.; Deng, J.; Kan, T.; Mi, C.C. Integrated LCC Compensation Topology for Wireless Charger in Electric and Plug-in Electric Vehicles. *IEEE Trans. Ind. Electron.* **2015**, *62*, 4215–4225. [[CrossRef](#)]
19. Do Chung, Y.; Lee, C.Y.; Kim, D.W.; Kang, H.; Park, Y.G.; Yoon, Y.S. Conceptual Design and Operating Characteristics of Multi-Resonance Antennas in the Wireless Power Charging System for Superconducting MAGLEV Train. *IEEE Trans. Appl. Supercond.* **2017**, *27*, 1–5. [[CrossRef](#)]
20. Mirbozorgi, S.A.; Yeon, P.; Ghovanloo, M. Robust Wireless Power Transmission to mm-Sized Free-Floating Distributed Implants. *IEEE Trans. Biomed. Circuits Syst.* **2017**, *11*, 692–702. [[CrossRef](#)] [[PubMed](#)]
21. Liu, Z.; Zhong, Z.; Guo, Y.X. In Vivo High-Efficiency Wireless Power Transfer with Multisine Excitation. *IEEE Trans. Microw. Theory Tech.* **2017**, *65*, 3530–3540. [[CrossRef](#)]
22. Li, X.; Tsui, C.Y.; Ki, W.H. A 13.56 MHz wireless power transfer system with reconfigurable resonant regulating rectifier and wireless power control for implantable medical devices. *IEEE J. Solid-State Circuits* **2015**, *50*, 978–989. [[CrossRef](#)]
23. Das, R.; Yoo, H. A Multiband Antenna Associating Wireless Monitoring and Nonleaky Wireless Power Transfer System for Biomedical Implants. *IEEE Trans. Microw. Theory Tech.* **2017**, *65*, 2485–2495. [[CrossRef](#)]
24. Kim, D.; Kim, J.; Park, Y.J. Optimization and Design of Small Circular Coils in a Magnetically Coupled Wireless Power Transfer System in the Megahertz Frequency. *IEEE Trans. Microw. Theory Tech.* **2016**, *64*, 2652–2663. [[CrossRef](#)]
25. Tang, S.C.; Lun, T.L.T.; Guo, Z.; Kwok, K.W.; McDannold, N.J. Intermediate Range Wireless Power Transfer with Segmented Coil Transmitters for Implantable Heart Pumps. *IEEE Trans. Power Electron.* **2017**, *32*, 3844–3857. [[CrossRef](#)]
26. Li, X.; Li, Y.P.; Tsui, C.Y.; Ki, W.H. Wireless Power Transfer System with $\Sigma\Delta$ Modulated Transmission Power and Fast Load Response for Implantable Medical Devices. *IEEE Trans. Circuits Syst. II Exp. Briefs* **2017**, *64*, 279–283. [[CrossRef](#)]

27. Xiao, C.; Wei, K.; Cheng, D.; Liu, Y. Wireless charging system considering eddy current in cardiac pacemaker shell: Theoretical modeling, experiments, and safety simulations. *IEEE Trans. Ind. Electron.* **2017**, *64*, 3978–3988. [[CrossRef](#)]
28. Campi, T.; Cruciani, S.; Palandrani, F.; De Santis, V.; Hirata, A.; Feliziani, M. Wireless power transfer charging system for AIMDs and pacemakers. *IEEE Trans. Microw. Theory Tech.* **2016**, *64*, 633–642. [[CrossRef](#)]
29. Kim, J.; Kim, D.H.; Choi, J.; Kim, K.H.; Park, Y.J. Free-positioning wireless charging system for small electronic devices using a bowl-shaped transmitting coil. *IEEE Trans. Microw. Theory Tech.* **2015**, *63*, 791–800. [[CrossRef](#)]
30. Chen, Q.; Wong, S.C.; Tse, C.K.; Ruan, X. Analysis, design, and control of a transcutaneous power regulator for artificial hearts. *IEEE Trans. Biomed. Circuits Syst.* **2009**, *3*, 23–31. [[CrossRef](#)] [[PubMed](#)]
31. Lee, B.; Dukju, A.; Ghovanloo, M. Three-phase time-multiplexed planar power transmission to distributed implants. *IEEE J. Emerg. Sel. Top. Power Electron.* **2016**, *4*, 263–272. [[CrossRef](#)] [[PubMed](#)]
32. Fu, M.; Zhang, T.; Ma, C.; Zhu, X. Efficiency and optimal loads analysis for multiple-receiver wireless power transfer systems. *IEEE Trans. Microw. Theory Tech.* **2015**, *63*, 801–812. [[CrossRef](#)]
33. Moon, J.; Hwang, H.; Jo, B.; Shin, H.A.; Kim, S.W. Design of a 5-W power receiver for 6.78 MHz resonant wireless power transfer system with power supply switching circuit. *IEEE Trans. Consum. Electron.* **2016**, *62*, 349–354. [[CrossRef](#)]
34. Kang, S.H.; Choi, J.H.; Jung, C.W. Magnetic resonance wireless power transfer using three-coil system with single planar receiver for laptop applications. *IEEE Trans. Consum. Electron.* **2015**, *61*, 160–166.
35. Kan, T.; Mai, R.; Mercier, P.P.; Mi, C.C. Design and Analysis of a Three-Phase Wireless Charging System for Lightweight Autonomous Underwater Vehicles. *IEEE Trans. Power Electron.* **2018**, *33*, 6622–6632. [[CrossRef](#)]
36. He, X.; Shu, W.; Yu, B.; Ma, X. Wireless Power Transfer System for Rotary Parts Telemetry of Gas Turbine Engine. *Electronics* **2018**, *7*, 58. [[CrossRef](#)]
37. Xie, L.; Shi, Y.; Hou, Y.T.; Lou, A. Wireless power transfer and applications to sensor networks. *IEEE Wirel. Commun.* **2013**, *20*, 140–145.
38. Minnaert, B.; Thoen, B.; Plets, D.; Joseph, W.; Stevens, N. Wireless energy transfer by means of inductive coupling for dairy cow health monitoring. *Comput. Electron. Agric.* **2018**, *152*, 101–108. [[CrossRef](#)]
39. Yao, W.; Li, M.; Wu, M.Y. Inductive charging with multiple charger nodes in wireless sensor networks. In *Asia-Pacific Web Conference*; Springer: Berlin, Germany, 2006; pp. 262–270.
40. Caldeirinha, R.F.S.; Fernandes, T.R.; Richter, J.; Al-Nuaimi, M.O. Simplified RET model derived from path loss and directional spectrum measurements in vegetation media at 11.2 and 20 GHz. *IET Microw. Antennas Propag.* **2016**, *11*, 136–143. [[CrossRef](#)]
41. Nariman, M.; Shirinfar, F.; Papio Toda, A.; Pamarti, S.; Rofougaran, A.; De Flaviis, F. A Compact 60-GHz Wireless Power Transfer System. *IEEE Trans. Microw. Theory Tech.* **2016**, *64*, 2664–2677. [[CrossRef](#)]
42. Li, X.; Zhou, J.; Duan, B.; Yang, Y.; Zhang, Y.; Fan, J. Performance of Planar Arrays for Microwave Power Transmission with Position Errors. *IEEE Antennas Wirel. Propag. Lett.* **2015**, *14*, 1794–1797. [[CrossRef](#)]
43. Valenta, C.R.; Durgin, G.D. Harvesting wireless power: Survey of energy-harvester conversion efficiency in far-field, wireless power transfer systems. *IEEE Microw. Mag.* **2014**, *15*, 108–120.
44. Zhou, W.; Ke, J. Optimal Photovoltaic Array Configuration under Gaussian Laser Beam Condition for Wireless Power Transmission. *IEEE Trans. Power Electron.* **2016**, *32*, 3662–3672. [[CrossRef](#)]
45. Zhou, W.; Ke, J. Efficiency Evaluation of Laser Diode in Different Driving Modes for Wireless Power Transmission. *IEEE Trans. Power Electron.* **2015**, *30*, 6237–6244. [[CrossRef](#)]
46. Wang, R.; Ye, D.; Dong, S.; Peng, Z.; Salamin, Y.; Shen, F.; Huangfu, J.; Li, C.; Ran, L. Optimal matched rectifying surface for space solar power satellite applications. *IEEE Trans. Microw. Theory Tech.* **2014**, *62*, 1080–1089. [[CrossRef](#)]
47. Sato, D.; Noboru, Y.; Koji, T. Thermal Design of Photovoltaic/Microwave Conversion Hybrid Panel for Space Solar Power System. *IEEE J. Photovolt.* **2016**, *7*, 374–382. [[CrossRef](#)]
48. Dai, X.; Li, L.; Yu, X.; Li, Y.; Sun, Y. A Novel Multi-degree Freedom Power Pickup Mechanism for Inductively Coupled Power Transfer System. *IEEE Trans. Magn.* **2017**, *53*, 8600107. [[CrossRef](#)]
49. Covic, G.A.; Boys, J.T.; Kissin, M.L.G.; Lu, H.G. A three-phase inductive power transfer system for roadway-powered vehicles. *IEEE Trans. Ind. Electron.* **2007**, *54*, 3370–3378. [[CrossRef](#)]
50. Kissin, M.L.G.; Boys, J.T.; Covic, G.A. Interphase mutual inductance in polyphase inductive power transfer systems. *IEEE Trans. Ind. Electron.* **2009**, *56*, 2393–2400. [[CrossRef](#)]

51. McDonough, M. Integration of inductively coupled power transfer and hybrid energy storage system: A multiport power electronics interface for battery-powered electric vehicles. *IEEE Trans. Power Electron.* **2015**, *30*, 6423–6433. [[CrossRef](#)]
52. Villa, J.L.; Sallan, J.; Sanz Osorio, J.F.; Llombart, A. High-misalignment tolerant compensation topology for ICPT systems. *IEEE Trans. Ind. Electron.* **2012**, *59*, 945–951. [[CrossRef](#)]
53. Sallan, J.; Villa, J.L.; Llombart, A.; Sanz, J.F. Optimal design of ICPT systems applied to electric vehicle battery charge. *IEEE Trans. Ind. Electron.* **2009**, *56*, 2140–2149. [[CrossRef](#)]
54. Pinuela, M.; Yates, D.C.; Lucyszyn, S.; Mitcheson, P.D. Maximizing DC-to-load efficiency for inductive power transfer. *IEEE Trans. Power Electron.* **2013**, *28*, 2437–2447. [[CrossRef](#)]
55. Aldhafer, S.; Luk, P.C.K.; Whidborne, J.F. Electronic tuning of misaligned coils in wireless power transfer systems. *IEEE Trans. Power Electron.* **2014**, *29*, 5975–5982. [[CrossRef](#)]
56. Fotopoulou, K.; Flynn, B.W. Wireless power transfer in loosely coupled links: Coil misalignment model. *IEEE Trans. Magn.* **2011**, *47*, 416–430. [[CrossRef](#)]
57. Pantic, Z.; Bai, S.; Lukic, S.M. ZCS LCC-compensated resonant inverter for inductive-power-transfer application. *IEEE Trans. Ind. Electron.* **2011**, *58*, 3500–3510. [[CrossRef](#)]
58. Inagaki, N. Theory of image impedance matching for inductively coupled power transfer systems. *IEEE Trans. Microw. Theory Tech.* **2014**, *62*, 901–908. [[CrossRef](#)]
59. Mercier, P.P.; Chandrakasan, A.P. Rapid wireless capacitor charging using a multi-tapped inductively-coupled secondary coil. *IEEE Trans. Circuits Syst. I* **2013**, *60*, 2263–2272. [[CrossRef](#)]
60. Safaei, A.; Woronowicz, K. Time-Domain Analysis of Voltage-Driven Series–Series Compensated Inductive Power Transfer Topology. *IEEE Trans. Power Electron.* **2017**, *32*, 4981–5003. [[CrossRef](#)]
61. Ye, Z.H.; Sun, Y.; Dai, X.; Tang, C.S.; Wang, Z.H.; Su, Y.G. Energy efficiency analysis of U-Coil wireless power transfer system. *IEEE Trans. Power Electron.* **2016**, *31*, 4809–4817. [[CrossRef](#)]
62. Buja, G.; Bertoluzzo, M.; Mude, K.N. Design and experimentation of WPT charger for electric city car. *IEEE Trans. Ind. Electron.* **2015**, *62*, 7436–7447. [[CrossRef](#)]
63. Abdolkhani, A.; Hu, A.P.; Tian, J. Autonomous Polyphase Current-Fed Push–Pull Resonant Converter Based on Ring Coupled Oscillators. *IEEE J. Emerg. Sel. Top. Power Electron.* **2015**, *3*, 568–576. [[CrossRef](#)]
64. Park, C.; Lee, S.; Cho, G.H.; Rim, C.T. Innovative 5-m-off-distance inductive power transfer systems with optimally shaped dipole coils. *IEEE Trans. Power Electron.* **2015**, *30*, 817–827. [[CrossRef](#)]
65. Lu, F.; Zhang, H.; Hofmann, H.; Mi, C.C. A Double-Sided LC Compensation Circuit for Loosely-Coupled Capacitive Power Transfer. *IEEE Trans. Power Electron.* **2018**, *33*, 1633–1644. [[CrossRef](#)]
66. Lu, F.; Hua, Z.; Hofmann, H.; Mi, C.C. An inductive and capacitive combined wireless power transfer system with LC-compensated topology. *IEEE Trans. Power Electron.* **2016**, *31*, 8471–8482. [[CrossRef](#)]
67. Huang, L.; Hu, A.P. Defining the mutual coupling of capacitive power transfer for wireless power transfer. *Electron. Lett.* **2015**, *51*, 1806–1807. [[CrossRef](#)]
68. Dai, J.; Ludois, D.C. A survey of wireless power transfer and a critical comparison of inductive and capacitive coupling for small gap applications. *IEEE Trans. Power Electron.* **2015**, *30*, 6017–6029. [[CrossRef](#)]
69. Zhang, H.; Lu, F.; Hofmann, H.; Liu, W.; Mi, C. A Six-Plate Capacitive Coupler to Reduce Electric Field Emission in Large Air-Gap Capacitive Power Transfer. *IEEE Trans. Power Electron.* **2017**, *33*, 665–675. [[CrossRef](#)]
70. Li, S.; Liu, Z.; Zhao, H.; Zhu, L.; Shuai, C.; Chen, Z. Wireless power transfer by electric field resonance and its application in dynamic charging. *IEEE Trans. Ind. Electron.* **2016**, *63*, 6602–6612. [[CrossRef](#)]
71. Jegadeesan, R.; Agarwal, K.; Guo, Y.X.; Yen, S.C.; Thakor, N.V. Wireless Power Delivery to Flexible Subcutaneous Implants Using Capacitive Coupling. *IEEE Trans. Microw. Theory Tech.* **2016**, *65*, 280–292. [[CrossRef](#)]
72. Mishra, S.K.; Adda, R.; Rathore, A.K.; Sekhar, S.; Joshi, A. Power transfer using portable surfaces in capacitively coupled power transfer technology. *IET Power Electron.* **2016**, *9*, 997–1008. [[CrossRef](#)]
73. Lu, F.; Zhang, H.; Mi, C. A Review on the Recent Development of Capacitive Wireless Power Transfer Technology. *Energies* **2017**, *10*, 1752. [[CrossRef](#)]
74. Wake, K.; Laakso, I.; Hirata, A.; Chakarothai, J.; Onishi, T.; Watanabe, S.; Santis, V.D.; Feliziani, M.; Taki, M. Derivation of Coupling Factors for Different Wireless Power Transfer Systems: Inter-and Intralaboratory Comparison. *IEEE Trans. Electromagn. Compat.* **2017**, *59*, 677–685. [[CrossRef](#)]

75. Hu, H.; Georgakopoulos, S.V. Multiband and Broadband Wireless Power Transfer Systems Using the Conformal Strongly Coupled Magnetic Resonance Method. *IEEE Trans. Ind. Electron.* **2017**, *64*, 3595–3607. [[CrossRef](#)]
76. Assawaworrarit, S.; Yu, X.; Fan, S. Robust wireless power transfer using a nonlinear parity–time-symmetric circuit. *Nature* **2017**, *546*, 387–390. [[CrossRef](#)] [[PubMed](#)]
77. Zhao, B.; Kuo, N.C.; Niknejad, A.M. A Gain Boosting Array Technique for Weakly-Coupled Wireless Power Transfer. *IEEE Trans. Power Electron.* **2017**, *32*, 7130–7139. [[CrossRef](#)]
78. Kuo, N.C.; Bo, Z.; Niknejad, A.M. Bifurcation analysis in weakly-coupled inductive power transfer systems. *IEEE Trans. Circuits Syst. I Regul. Pap.* **2016**, *63*, 727–738. [[CrossRef](#)]
79. Kurs, A.B.; Karalis, A.; Moffatt, R.; Joannopoulos, J.D.; Fisher, P.H.; Soljacic, M. Wireless Power Transfer via Strongly Coupled Magnetic Resonances. *Science* **2007**, *317*, 83–86. [[CrossRef](#)] [[PubMed](#)]
80. Zhang, F.; Liu, J.; Mao, Z.; Sun, M. Mid-range wireless power transfer and its application to body sensor networks. *Open J. Appl. Sci.* **2012**, *2*, 35–46. [[CrossRef](#)]
81. Liu, Z.; Chen, Z.; Li, J. A Magnetic Tank System for Wireless Power Transfer. *IEEE Microw. Wirel. Compon. Lett.* **2017**, *27*, 443–445. [[CrossRef](#)]
82. Moghadam, M.R.; Zhang, R. Node placement and distributed magnetic beamforming optimization for wireless power transfer. *IEEE Trans. Signal Inf. Process. Netw.* **2018**, *4*, 264–279. [[CrossRef](#)]
83. Ahn, D.; Kim, S.; Moon, J.; Cho, I.K. Wireless power transfer with automatic feedback control of load resistance transformation. *IEEE Trans. Power Electron.* **2016**, *31*, 7876–7886. [[CrossRef](#)]
84. Iguchi, S.; Yeon, P.; Fuketa, H.; Ishida, K.; Sakurai, T.; Takamiya, M. Wireless power transfer with zero-phase-difference capacitance control. *IEEE Trans. Circuits Syst. I* **2015**, *62*, 938–947. [[CrossRef](#)]
85. Zhang, W.; Mi, C.C. Compensation topologies of high-power wireless power transfer systems. *IEEE Trans. Veh. Technol.* **2016**, *65*, 4768–4778. [[CrossRef](#)]
86. Cheng, L.; Ki, W.H.; Lu, Y.; Yim, T.S. Adaptive on/off delay-compensated active rectifiers for wireless power transfer systems. *IEEE J. Solid-State Circuits* **2016**, *51*, 712–723.
87. Zhang, W.; Wong, S.C.; Tse, C.K.; Chen, Q. Analysis and comparison of secondary series- and parallel-compensated inductive power transfer systems operating for optimal efficiency and load-independent voltage-transfer ratio. *IEEE Trans. Power Electron.* **2014**, *29*, 2979–2990. [[CrossRef](#)]
88. Zhang, W.; White, J.C.; Malhan, R.K.; Mi, C.C. Loosely Coupled Transformer Coil Design to Minimize EMF Radiation in Concerned Areas. *IEEE Trans. Veh. Technol.* **2016**, *65*, 4779–4789. [[CrossRef](#)]
89. Li, W.; Zhao, H.; Deng, J.; Li, S.; Mi, C.C. Comparison study on SS and double-sided LCC compensation topologies for EV/PHEV wireless chargers. *IEEE Trans. Veh. Technol.* **2016**, *65*, 4429–4439. [[CrossRef](#)]
90. Lee, S.H.; Lee, B.S.; Lee, J.H. A New Design Methodology for a 300-kW, Low Flux Density, Large Air Gap, Online Wireless Power Transfer System. *IEEE Trans. Ind. Appl.* **2016**, *52*, 4234–4242. [[CrossRef](#)]
91. Jegadeesan, R.; Guo, Y.X. Topology selection and efficiency improvement of inductive power links. *IEEE Trans. Antennas Propag.* **2012**, *60*, 4846–4854. [[CrossRef](#)]
92. Hariri, A.O.; Youssef, T.; Elsayed, A.; Mohammed, O. A Computational Approach for a Wireless Power Transfer Link Design Optimization Considering Electromagnetic Compatibility. *IEEE Trans. Magn.* **2016**, *52*, 1–4. [[CrossRef](#)]
93. Liu, F.; Zhang, Y.; Chen, K.; Zhao, Z.; Yuan, L. A comparative study of load characteristics of resonance types in wireless transmission systems. In Proceedings of the 2016 IEEE Asia-Pacific International Symposium on Electromagnetic Compatibility (APEMC), Shenzhen, China, 17–21 May 2016; Volume 1, pp. 203–206.
94. Wang, Y.; Yao, Y.; Liu, X.; Xu, D. S/CLC Compensation Topology Analysis and Circular Coil Design for Wireless Power Transfer. *IEEE Trans. Transp. Electr.* **2017**, *3*, 496–507. [[CrossRef](#)]
95. Samanta, S.; Rathore, A.K. A New Current-Fed CLC Transmitter and LC Receiver Topology for Inductive Wireless Power Transfer Application: Analysis, Design, and Experimental Results. *IEEE Trans. Transp. Electr.* **2015**, *1*, 357–368. [[CrossRef](#)]
96. Feng, H.; Cai, T.; Duan, S.; Zhao, J.; Zhang, X.; Chen, C. An LCC-Compensated Resonant Converter Optimized for Robust Reaction to Large Coupling Variation in Dynamic Wireless Power Transfer. *IEEE Trans. Ind. Electron.* **2016**, *63*, 6591–6601. [[CrossRef](#)]
97. Kan, T.; Nguyen, T.D.; White, J.C.; Malhan, R.K.; Mi, C.C. A New Integration Method for an Electric Vehicle Wireless Charging System Using LCC Compensation Topology: Analysis and Design. *IEEE Trans. Power Electron.* **2017**, *32*, 1638–1650. [[CrossRef](#)]

98. Li, S.; Li, W.; Deng, J.; Nguyen, T.D.; Mi, C.C. A double-sided LCC compensation network and its tuning method for wireless power transfer. *IEEE Trans. Veh. Technol.* **2015**, *64*, 2261–2273. [[CrossRef](#)]
99. Deng, J.; Li, W.; Nguyen, T.D.; Li, S.; Mi, C.C. Compact and efficient bipolar coupler for wireless power chargers: Design and analysis. *IEEE Trans. Power Electron.* **2015**, *30*, 6130–6140. [[CrossRef](#)]
100. Lu, F.; Zhang, H.; Hofmann, H.; Mi, C.C. A dynamic charging system with reduced output power pulsation for electric vehicles. *IEEE Trans. Ind. Electron.* **2016**, *63*, 6580–6590. [[CrossRef](#)]
101. Park, M.; Nguyen, V.T.; Yu, S.D.; Yim, S.W.; Park, K.; Min, B.D.; Kim, S.D.; Cho, J.G. A study of wireless power transfer topologies for 3.3 kW and 6.6 kW electric vehicle charging infrastructure. In Proceedings of the 2016 IEEE Transportation Electrification Conference and Expo (ITEC Asia-Pacific), Busan, South Korea, 1–4 June 2016; pp. 689–692.
102. Zaheer, A.; Neath, M.; Beh, H.Z.Z.; Covic, G.A. A dynamic EV charging system for slow moving traffic applications. *IEEE Trans. Transp. Electrif.* **2017**, *3*, 354–369. [[CrossRef](#)]
103. Cirimele, V.; Freschi, F.; Guglielmi, P. Wireless power transfer structure design for electric vehicle in charge while driving. In Proceedings of the International Conference on Electrical Machines (ICEM), Berlin, Germany, 2–5 September 2014; pp. 2461–2467.
104. Onar, O.C.; Miller, J.M.; Campbell, S.L.; Coomer, C.; White, C.P.; Seiber, L.E. A novel wireless power transfer for in-motion EV/PHEV charging. In Proceedings of the IEEE Applied Power Electronics Conference and Exposition (APEC), Twenty-Eighth Annual, Long Beach, CA, USA, 17–21 March 2013; pp. 3073–3080.
105. Cirimele, V.; Pichon, L.; Freschi, F. Electromagnetic modeling and performance comparison of different pad-to-pad length ratio for dynamic inductive power transfer. In Proceedings of the IECON 2016-42nd IEEE Annual Conference of the Industrial Electronics Society, Florence, Italy, 23–26 October 2016; pp. 4499–4503.
106. Liao, C.; Li, J.; Li, S. Design of LCC impedance matching circuit for wireless power transfer system under rectifier load. *CPSS Trans. Power Electron. Appl.* **2017**, *2*, 237–245. [[CrossRef](#)]
107. Imura, T.; Hori, Y. Maximizing air gap and efficiency of magnetic resonant coupling for wireless power transfer using equivalent circuit and Neumann formula. *IEEE Trans. Ind. Electron.* **2011**, *58*, 4746–4752. [[CrossRef](#)]
108. Koh, K.E.; Beh, T.C.; Imura, T.; Hori, Y. Impedance matching and power division using impedance inverter for wireless power transfer via magnetic resonant coupling. *IEEE Trans. Ind. Appl.* **2014**, *50*, 2061–2070. [[CrossRef](#)]
109. Niotaki, K.; Georgiadis, A.; Collado, A.; Vardakas, J.S. Dual-band resistance compression networks for improved rectifier performance. *IEEE Trans. Microw. Theory Tech.* **2014**, *62*, 3512–3521. [[CrossRef](#)]
110. Hou, J.; Chen, Q.; Wong, S.C.; Tse, C.K.; Ruan, X. Analysis and control of series/series-parallel compensated resonant converter for contactless power transfer. *IEEE J. Emerg. Sel. Top. Power Electron.* **2015**, *3*, 124–136.
111. Ahn, D.; Hong, S. A transmitter or a receiver consisting of two strongly coupled resonators for enhanced resonant coupling in wireless power transfer. *IEEE Trans. Ind. Electron.* **2014**, *61*, 1193–1203. [[CrossRef](#)]
112. Zhang, W.; White, J.C.; Abraham, A.M.; Mi, C.C. Loosely coupled transformer structure and interoperability study for EV wireless charging systems. *IEEE Trans. Power Electron.* **2015**, *30*, 6356–6367. [[CrossRef](#)]
113. Hekal, S.; Abdel-Rahman, A.B.; Jia, H.; Allam, A.; Barakat, A.; Pokharel, R.K. A Novel Technique for Compact Size Wireless Power Transfer Applications Using Defected Ground Structures. *IEEE Trans. Microw. Theory Tech.* **2017**, *65*, 591–599. [[CrossRef](#)]
114. Hekal, S.; Abdel-Rahman, A.B.; Allam, A.; Jia, H.; Barakat, A.; Pokharel, R.K. Asymmetric wireless power transfer systems using coupled DGS resonators. *IEICE Electron. Express* **2016**, *13*, 20160591. [[CrossRef](#)]
115. Khandelwal, M.K.; Kanaujia, B.K.; Kumar, S. Defected ground structure: Fundamentals, analysis, and applications in modern wireless trends. *Int. J. Antennas Propag.* **2017**, *2017*, 2018527. [[CrossRef](#)]
116. Zhang, J.; Yuan, X.; Wang, C.; He, Y. Comparative Analysis of Two-Coil and Three-Coil Structures for Wireless Power Transfer. *IEEE Trans. Power Electron.* **2017**, *32*, 341–352. [[CrossRef](#)]
117. Sample, A.P.; Meyer, D.A.; Smith, J.R. Analysis, experimental results, and range adaptation of magnetically coupled resonators for wireless power transfer. *IEEE Trans. Ind. Electron.* **2011**, *58*, 544–554. [[CrossRef](#)]
118. Cabrera, F.L.; De Sousa, F.R. Achieving Optimal Efficiency in Energy Transfer to a CMOS Fully Integrated Wireless Power Receiver. *IEEE Trans. Microw. Theory Tech.* **2016**, *64*, 3703–3713. [[CrossRef](#)]
119. Moon, S.; Moon, G.W. Wireless Power Transfer System with an Asymmetric Four-Coil Resonator for Electric Vehicle Battery Chargers. *IEEE Trans. Power Electron.* **2016**, *31*, 6844–6854.

120. Koohestani, M.; Zhadobov, M.; Ettore, M. Design methodology of a printed WPT system for HF-band mid-range applications considering human safety regulations. *IEEE Trans. Microw. Theory Tech.* **2017**, *65*, 270–279. [[CrossRef](#)]
121. Jolani, F.; Yu, Y.; Chen, Z. A planar magnetically coupled resonant wireless power transfer system using printed spiral coils. *IEEE Antennas Wirel. Propag. Lett.* **2014**, *13*, 1648–1651. [[CrossRef](#)]
122. Chen, K.; Zhao, Z. Analysis of the double-layer printed spiral coil for wireless power transfer. *IEEE J. Emerg. Sel. Top. Power Electron.* **2013**, *1*, 114–121. [[CrossRef](#)]
123. Lee, W.S.; Son, W.I.; Oh, K.S.; Yu, J.W. Contactless energy transfer systems using antiparallel resonant loops. *IEEE Trans. Ind. Electron.* **2013**, *60*, 350–359. [[CrossRef](#)]
124. Mohan, S.S. The Design, Modeling and Optimization of On-Chip Inductor and Transformer Circuits. Ph.D. Thesis, Stanford University, Stanford, CA, USA, 1999.
125. Song, J.; Kim, S.; Bae, B.; Kim, J.J.; Jung, D.H.; Kim, J. Design and analysis of magnetically coupled coil structures for PCB-to-active interposer wireless power transfer in 2.5 D/3D-IC. In Proceedings of the IEEE Electrical Design of Advanced Packaging & Systems Symposium (EDAPS), Bangalore, India, 14–16 December 2014; pp. 1–4.
126. Sandoval, F.S.; Delgado, S.M.; Moazenzadeh, A.; Wallrabe, U. Nulls-Free Wireless Power Transfer with Straightforward Control of Magnetoinductive Waves. *IEEE Trans. Microw. Theory Tech.* **2017**, *65*, 1087–1093. [[CrossRef](#)]
127. Kim, S.; Jung, D.H.; Kim, J.J.; Bae, B.; Kong, S.; Ahn, S.; Kim, J.; Kim, J. High-efficiency PCB-and package-level wireless power transfer interconnection scheme using magnetic field resonance coupling. *IEEE Trans. Compon. Packag. Manuf. Technol.* **2015**, *5*, 863–878.
128. Yi, Y.; Buttner, U.; Fan, Y.; Foulds, I.G. Design and optimization of a 3-coil resonance-based wireless power transfer system for biomedical implants. *Int. J. Circuit Theory Appl.* **2015**, *43*, 1379–1390. [[CrossRef](#)]
129. Tierney, B.B.; Grbic, A. Planar shielded-loop resonators. *IEEE Trans. Antennas Propag.* **2014**, *62*, 3310–3320. [[CrossRef](#)]
130. Yang, C.; Tsunekawa, K. A Novel Parallel Double Helix Loop Resonator for Magnetic Coupled Resonance Wireless Power Transfer. In Proceedings of the PIERS Proceedings, Guangzhou, China, 25–28 August 2014; pp. 466–470.
131. Zhang, Y.; Lu, T.; Zhao, Z.; Chen, K.; He, F.; Yuan, L. Wireless power transfer to multiple loads over various distances using relay resonators. *IEEE Microw. Wirel. Compon. Lett.* **2015**, *25*, 337–339. [[CrossRef](#)]
132. Lee, K.; Cho, D.H. Diversity analysis of multiple transmitters in wireless power transfer system. *IEEE Trans. Magn.* **2013**, *49*, 2946–2952. [[CrossRef](#)]
133. Zhang, Y.; Zhao, Z.; Lu, T. Quantitative analysis of system efficiency and output power of four-coil resonant wireless power transfer. *IEEE J. Emerg. Sel. Top. Power Electron.* **2015**, *3*, 184–190. [[CrossRef](#)]
134. Hadadtehrani, P.; Kamalinejad, P.; Molavi, R.; Mirabbasi, S. On the use of conical helix inductors in wireless power transfer systems. In Proceedings of the 2016 IEEE Canadian Conference on Electrical and Computer Engineering (CCECE), Vancouver, BC, Canada, 15–18 May 2016; pp. 1–4.
135. Chabalko, M.J.; Sample, A.P. Resonant cavity mode enabled wireless power transfer. *Appl. Phys. Lett.* **2014**, *105*, 243902. [[CrossRef](#)]
136. Chabalko, M.J.; Sample, A.P. Three-dimensional charging via multimode resonant cavity enabled wireless power transfer. *IEEE Trans. Power Electron.* **2015**, *30*, 6163–6173. [[CrossRef](#)]
137. Chow, J.P.W.; Chen, N.; Chung, H.S.H.; Chan, L.L.H. An investigation into the use of orthogonal winding in loosely coupled link for improving power transfer efficiency under coil misalignment. *IEEE Trans. Power Electron.* **2015**, *30*, 5632–5649. [[CrossRef](#)]
138. Mei, H.; Huang, Y.W.; Thackston, K.A.; Irazoqui, P.P. Optimal wireless power transfer to systems in an enclosed resonant cavity. *IEEE Antennas Wirel. Propag. Lett.* **2016**, *15*, 1036–1039. [[CrossRef](#)]
139. Ng, W.M.; Zhang, C.; Lin, D.; Hui, S.R. Two- and three-dimensional omnidirectional wireless power transfer. *IEEE Trans. Power Electron.* **2014**, *29*, 4470–4474. [[CrossRef](#)]
140. Zhang, C.; Lin, D.; Hui, S.Y. Basic control principles of omnidirectional wireless power transfer. *IEEE Trans. Power Electron.* **2016**, *31*, 5215–5227.
141. Ha-Van, N.; Seo, C. Analytical and Experimental Investigations of Omnidirectional Wireless Power Transfer using a Cubic Transmitter. *IEEE Trans. Ind. Electron.* **2017**, *65*, 1358–1366. [[CrossRef](#)]

142. Lin, D.; Zhang, C.; Hui, S.R. Mathematic Analysis of Omnidirectional Wireless Power Transfer—Part-II Three-Dimensional Systems. *IEEE Trans. Power Electron.* **2017**, *32*, 613–624. [[CrossRef](#)]
143. Zhang, C.; Lin, D.; Hui, S.Y. Ball-Joint Wireless Power Transfer Systems. *IEEE Trans. Power Electron.* **2018**, *33*, 65–72. [[CrossRef](#)]
144. Jeong, I.S.; Jung, B.I.; You, D.S.; Choi, H.S. Analysis of S-Parameters in Magnetic Resonance WPT Using Superconducting Coils. *IEEE Trans. Appl. Supercond.* **2016**, *26*, 1–4. [[CrossRef](#)]
145. Kang, S.H.; Jung, C.W. Textile Resonators with Thin Copper Wire for Wearable MR-WPT System. *IEEE Microw. Wirel. Compon. Lett.* **2017**, *27*, 91–93. [[CrossRef](#)]
146. Shin, J.; Shin, S.; Kim, Y.; Ahn, S.; Lee, S.; Jung, G.; Jeon, S.; Cho, D.H. Design and implementation of shaped magnetic-resonance-based wireless power transfer system for roadway-powered moving electric vehicles. *IEEE Trans. Ind. Electron.* **2014**, *61*, 1179–1192. [[CrossRef](#)]
147. Huang, Y.; Clerckx, B. Relaying strategies for wireless-powered MIMO relay networks. *IEEE Trans. Wirel. Commun.* **2016**, *15*, 6033–6047. [[CrossRef](#)]
148. Yang, G.; Moghadam, M.R.V.; Zhang, R. Magnetic MIMO Signal Processing and Optimization for Wireless Power Transfer. *IEEE Trans. Signal Process.* **2017**, *65*, 2860–2874. [[CrossRef](#)]
149. Mirbozorgi, S.A.; Jia, Y.; Canales, D.; Ghovanloo, M. A Wirelessly-Powered Homecare with Segmented Copper Foils and Closed-Loop Power Control. *IEEE Trans. Biomed. Circuits Syst.* **2016**, *10*, 979–989. [[CrossRef](#)] [[PubMed](#)]
150. Lee, H.H.; Kang, S.H.; Jung, C.W. Transparent electrode resonators for MR-WPT. In Proceedings of the IEEE URSI Asia-Pacific Radio Science Conference (URSI AP-RASC), Seoul, Korea, 21–25 August 2016; pp. 716–718.
151. Zhong, W.X.; Lee, C.K.; Hui, S.Y. Wireless power domino-resonator systems with noncoaxial axes and circular structures. *IEEE Trans. Power Electron.* **2012**, *27*, 4750–4762. [[CrossRef](#)]
152. Lee, C.K.; Zhong, W.X.; Hui, S.Y.R. Effects of magnetic coupling of nonadjacent resonators on wireless power domino-resonator systems. *IEEE Trans. Power Electron.* **2012**, *27*, 1905–1916. [[CrossRef](#)]
153. Zhong, W.X.; Lee, C.K.; Hui, S.Y.R. General analysis on the use of tesla's resonators in domino forms for wireless power transfer. *IEEE Trans. Ind. Electron.* **2013**, *60*, 261–270. [[CrossRef](#)]
154. Zhang, X.; Ho, S.L.; Fu, W.N. Analysis and optimization of magnetically coupled resonators for wireless power transfer. *IEEE Trans. Magn.* **2012**, *48*, 4511–4514. [[CrossRef](#)]
155. Fu, X.; Liu, F.; Chen, X. Optimization of coils for a three-phase magnetically coupled resonant wireless power transfer system oriented by the zero-voltage-switching range. In Proceedings of the Applied Power Electronics Conference and Exposition (APEC), Tampa, FL, USA, 26–30 March 2017; pp. 3708–3713.
156. Liu, Z.; Chen, Z.; Li, J.; Guo, Y.; Xu, B. A Planar L-Shape Transmitter for a Wireless Power Transfer System. *IEEE Antennas Wirel. Propag. Lett.* **2017**, *16*, 960–963. [[CrossRef](#)]
157. Villa, J.; Sanz, J.; Peri, J.; Acerete, R. Victoria project: Static and dynamic wireless charging for electric buses. In Proceedings of the Business Intelligence on Emerging Technologies IDTechEX Conference, Berlin, Germany, 27–28 April 2016.
158. Cirimele, V.; Freschi, F.; Mitolo, M. Inductive power transfer for automotive applications: State-of-the-art and future trends. In Proceedings of the IEEE Industry Applications Society Annual Meeting, Portland, OR, USA, 2–6 October 2016; pp. 1–8.
159. Safaee, A.; Woronowicz, K. Tuning Scheme for Three-Phase Wireless Power Transfer Systems with Long Primary. In Proceedings of the International Conference on Smart Energy Grid Engineering (SEGE), Oshawa, ON, Canada, 11–13 August 2014; pp. 1–9.
160. Safaee, A.; Woronowicz, K.; Dickson, T. Reactive power compensation in three-phase high output inductive power transfer. In Proceedings of the IEEE Electrical Power and Energy Conference (EPEC), London, ON, Canada, 26–28 October 2015; pp. 375–380.
161. Liu, D.; Hu, H.; Georgakopoulos, S. Misalignment Sensitivity of Strongly Coupled Wireless Power Transfer Systems. *IEEE Trans. Power Electron.* **2016**, *32*, 5509–5519. [[CrossRef](#)]
162. Cannon, B.L.; Hoburg, J.F.; Stancil, D.D.; Goldstein, S.C. Magnetic resonant coupling as a potential means for wireless power transfer to multiple small receivers. *IEEE Trans. Power Electron.* **2009**, *24*, 1819–1825. [[CrossRef](#)]
163. Kim, Y.J.; Ha, D.; Chappell, W.J.; Irazoqui, P.P. Selective wireless power transfer for smart power distribution in a miniature-sized multiple-receiver system. *IEEE Trans. Ind. Electron.* **2016**, *63*, 1853–1862. [[CrossRef](#)]

164. Thompson, M.C. *Inductance Calculation Techniques-Part II: Approximations and Handbook Methods*; CiteSeer: University Park, PA, USA, 1991.
165. Grover, F.W. *Inductance Calculations: Working Formulas and Tables*; Courier Corporation: Washington, DC, USA, 2004.
166. Hui, S.Y.; Zhong, W.; Lee, C.K. A critical review of recent progress in mid-range wireless power transfer. *IEEE Trans. Power Electron.* **2014**, *29*, 4500–4511. [[CrossRef](#)]
167. Lyu, Y.L.; Meng, F.Y.; Yang, G.H.; Che, B.J.; Wu, Q.; Sun, L.; Erni, D.; Li, J.L. A method of using nonidentical resonant coils for frequency splitting elimination in wireless power transfer. *IEEE Trans. Power Electron.* **2015**, *30*, 6097–6107. [[CrossRef](#)]
168. Park, J.; Tak, Y.; Kim, Y.; Nam, S. Investigation of adaptive matching methods for near-field wireless power transfer. *IEEE Trans. Antennas Propag.* **2011**, *59*, 1769–1773. [[CrossRef](#)]
169. Beh, T.C.; Kato, M.; Imura, T.; Oh, S.; Hori, Y. Automated impedance matching system for robust wireless power transfer via magnetic resonance coupling. *IEEE Trans. Ind. Electron.* **2013**, *60*, 3689–3698. [[CrossRef](#)]
170. Kim, J.; Jeong, J. Range-adaptive wireless power transfer using multiloop and tunable matching techniques. *IEEE Trans. Ind. Electron.* **2015**, *62*, 6233–6241. [[CrossRef](#)]
171. Lee, G.; Waters, B.H.; Shin, Y.G.; Smith, J.R.; Park, W.S. A reconfigurable resonant coil for range adaptation wireless power transfer. *IEEE Trans. Microw. Theory Tech.* **2016**, *64*, 624–632. [[CrossRef](#)]
172. Fu, M.; Yin, H.; Zhu, X.; Ma, C. Analysis and tracking of optimal load in wireless power transfer systems. *IEEE Trans. Power Electron.* **2015**, *30*, 3952–3963. [[CrossRef](#)]
173. Wang, J.; Li, J.; Ho, S.L.; Fu, W.N.; Li, Y.; Yu, H.; Sun, M. Lateral and angular misalignments analysis of a new PCB circular spiral resonant wireless charger. *IEEE Trans. Magn.* **2012**, *48*, 4522–4525. [[CrossRef](#)]
174. Song, C.; Kim, H.; Jung, D.H.; Kim, J.J.; Kong, S.; Ahn, S.; Kim, J.; Kim, J. Low EMF and EMI Design of a Tightly Coupled Handheld Resonant Magnetic Field (HH-RMF) Charger for Automotive Battery Charging. *IEEE Trans. Electromagn. Compat.* **2016**, *58*, 1194–1206. [[CrossRef](#)]
175. Cirimele, V.; Freschi, F.; Giaccone, L.; Pichon, L.; Repetto, M. Human exposure assessment in dynamic inductive power transfer for automotive applications. *IEEE Trans. Magn.* **2017**, *53*, 1–4. [[CrossRef](#)]
176. Laakso, I.; Hirata, A.; Fujiwara, O. Computational dosimetry for wireless charging of an electrical vehicle. In Proceedings of the International Symposium on Electromagnetic Compatibility EMC, Tokyo, Japan, 12–16 May 2014; pp. 202–205.
177. Zang, M.; Clemens, M.; Cimala, C.; Streckert, J.; Schmuelling, B. Simulation of Inductive Power Transfer Systems Exposing a Human Body with Two-Step Scaled-Frequency FDTD Methods. *IEEE Trans. Magn.* **2017**, *53*, 7201804. [[CrossRef](#)]
178. Kim, J.; Kim, H.; Song, C.; Kim, I.M.; Kim, Y.; Kim, J. Electromagnetic interference and radiation from wireless power transfer systems. In Proceedings of the 2014 IEEE International Symposium on Electromagnetic Compatibility (EMC), Raleigh, NC, USA, 4–8 August 2014; pp. 171–176.
179. Wen, F.; Huang, X. Optimal magnetic field shielding method by metallic sheets in wireless power transfer system. *Energies* **2016**, *9*, 733. [[CrossRef](#)]
180. Besnoff, J.; Chabalko, M.; Ricketts, D.S. A Frequency-Selective Zero-Permeability Metamaterial Shield for Reduction of Near-Field Electromagnetic Energy. *IEEE Antennas Wirel. Propag. Lett.* **2016**, *15*, 654–657. [[CrossRef](#)]
181. Oh, T.; Lee, B. Analysis of wireless power transfer using metamaterial slabs made of ring resonators at 13.56 MHz. *J. Electromagn. Eng. Sci.* **2013**, *13*, 259–262. [[CrossRef](#)]
182. Cho, Y.; Kim, J.J.; Kim, D.-H.; Lee, S.; Kim, H.; Song, C.; Kong, S.; Kim, H.; Seo, C.; Ahn, S.; et al. Thin PCB-Type Metamaterials for Improved Efficiency and Reduced EMF Leakage in Wireless Power Transfer Systems. *IEEE Trans. Microw. Theory Tech.* **2016**, *64*, 353–364. [[CrossRef](#)]
183. Cho, Y.; Lee, S.; Kim, D.H.; Kim, H.; Song, C.; Kong, S.; Park, J.; Seo, C.; Kim, J. Thin Hybrid Metamaterial Slab with Negative and Zero Permeability for High Efficiency and Low Electromagnetic Field in Wireless Power Transfer Systems. *IEEE Trans. Electromagn. Compat.* **2017**, *60*, 1001–1009. [[CrossRef](#)]
184. Jo, M.; Sato, Y.; Kaneko, Y.; Abe, S. Methods for reducing leakage electric field of a wireless power transfer system for electric vehicles. In Proceedings of the IEEE Energy Conversion Congress and Exposition (ECCE), Pittsburgh, PA, USA, 14–18 September 2014; pp. 1762–1769.
185. Choi, S.Y.; Gu, B.W.; Lee, S.W.; Lee, W.Y.; Huh, J.; Rim, C.T. Generalized active EMF cancel methods for wireless electric vehicles. *IEEE Trans. Power Electron.* **2014**, *29*, 5770–5783. [[CrossRef](#)]

186. Moon, H.; Kim, S.; Park, H.H.; Ahn, S. Design of a resonant reactive shield with double coils and a phase shifter for wireless charging of electric vehicles. *IEEE Trans. Magn.* **2015**, *51*. [[CrossRef](#)]
187. Kim, J.; Kim, H.; Ahn, S.; Kim, I.; Kim, I.M.; Kim, Y.I.; Kim, J. Spread spectrum technology to reduce the EMI from the constant voltage source type wireless power transfer system. In Proceedings of the International Symposium on Antennas and Propagation, Jeju, Korea, 25–28 October 2011.
188. Monteiro, R.; Borges, B.; Anunciada, V. EMI reduction by optimizing the output voltage rise time and fall time in high-frequency soft-switching converters. In Proceedings of the IEEE 35th Annual PESC 04, Aachen, Germany, 20–25 June 2004; Volume 2, pp. 1127–1132.
189. Park, J.; Kim, D.; Hwang, K.; Park, H.H.; Kwak, S.I.; Kwon, J.H.; Ahn, S. A Resonant Reactive Shielding for Planar Wireless Power Transfer System in Smartphone Application. *IEEE Trans. Electromagn. Compat.* **2017**, *59*, 695–703. [[CrossRef](#)]



© 2018 by the authors. Licensee MDPI, Basel, Switzerland. This article is an open access article distributed under the terms and conditions of the Creative Commons Attribution (CC BY) license (<http://creativecommons.org/licenses/by/4.0/>).

MDPI
St. Alban-Anlage 66
4052 Basel
Switzerland
Tel. +41 61 683 77 34
Fax +41 61 302 89 18
www.mdpi.com

Electronics Editorial Office
E-mail: electronics@mdpi.com
www.mdpi.com/journal/electronics



MDPI
St. Alban-Anlage 66
4052 Basel
Switzerland

Tel: +41 61 683 77 34
Fax: +41 61 302 89 18

www.mdpi.com



ISBN 978-3-03921-021-3